Parameter Estimation on Interference-Imposed Satellite Channels

Michael Bergmann

A dissertation submitted in partial fulfilment
of the requirements for the degree

Doctor in Engineering Sciences (Dr. techn.)

Supervisor: Univ.-Prof. Dipl.-Ing. Dr. Otto Koudelka
Advisor: Ass. Prof. Dipl.-Ing. Dr. Wilfried Gappmair

Institute of Communication Networks and Satellite Communications
Graz University of Technology
Austria

November 2012

“All truths are easy to understand once discovered; the point is to discover them”

(Galileo Galilei)

“To live effectively is to live with adequate information”

(Norbert Wiener)

STATUTORY DECLARATION

I hereby declare that I have authored this dissertation independently, that I have not used other than the revealed sources / resources and that I have explicitly marked all material which has been quoted either literally or by content from the used sources.

Graz, November 7th, 2012 …….

(Dipl.-Ing. Michael Bergmann)

to my family

ACKNOWLEDGEMENTS

First of all the author likes to thank Prof. Otto Koudelka, the head of the Institute of Communication Networks and Satellite Communications and prime reviewer of this thesis, for his continuous and helpful support.

The author wishes to thank Prof. Wiley Larson, professor at the Stevens Institute of Technology and well known author of prominent space systems books, as co-reviewer of this thesis for his advice and comments.

The author also acknowledges gratefully to all people who contributed in different ways to this thesis:

Wilfried Gappmair for sharing his vast knowledge in communications and mathematics, his continuous and helpful mentoring and advice which substantially contributed to the quality of this thesis.

The project authorities and partners, especially Riccardo De Gaudenzi, Nader Alagha and Stefano Cioni (all ESA) as well as Carlos Mosquera and Jesús Arnau Yañez (both University of Vigo), of the *Satellite Communication Network of Experts III* activity – ESA contract no. 12859/09/NL/CLP and 23089/10/NL/CPL launched by ESA for advanced research in satellite communications – for their appreciated collaboration and helpful remarks.

Prof. Otto Koudelka and all colleagues at his Institute for creating and maintaining a positive, professional and inspiring work atmosphere.

Barbara Süsser-Rechberger for her contributions to Chapter 4 carried out in the context of her Bachelor thesis.

Finally, I want to give my sincere thanks to my family for their unconditional support and love.

ABSTRACT

Efficient utilization of bandwidth resources is not novel in the realm of satellite communications due to evolutions towards higher frequencies, spot beam architectures and mobile users.

Spot beam architectures split the service regions into smaller and smaller cells whilst reusing the dedicated frequency bands more and more. This often causes a significant level of interference in the system with a serious impact on the achievable data throughput. Appropriate methods can baffle this detrimental interference, but require the awareness of the channel state.

Another layer of complexity is imposed by mobile terminals accessing the satellite network; to keep the system efficient, appropriate adaptive coding and modulation schemes are indispensable, requiring timely and accurate channel state information, which is not a simple task in the context of long round-trip times and time-variant channels.

In the context mentioned above this thesis focusses on parameter estimation in such highly interference-imposed scenarios as defined by the *European Space Agency* (ESA) in the framework of the *Satellite Communication Network of Experts III* activity; the research presented herein was carried out under the ESA framework enhanced by further proactive investigations.

ZUSAMMENFASSUNG

Eine möglichst effiziente Ausnutzung der zur Verfügung stehenden Bandbreite ist kein neuer Anspruch in der Satellitenkommunikation, sondern gelebte Praxis im Zusammenhang mit der Einführung höherer Frequenzbereiche, *Spot-Beam* Architekturen und mobilen Anwendern.

Bei modernen *Spot-Beam* Architekturen tendiert man dazu das Versorgungsgebiet in immer kleinere Zellen zu teilen. Die dabei zugewiesenen Frequenzbänder werden immer öfter wiederverwendet, was schlussendlich zu hohen Interferenzen mit negativen Auswirkungen auf den Gesamtdatendurchsatz führt. Durch passende Maßnahmen kann die Interferenz vermindert werden, jedoch muss der aktuelle Zustand des Übertragungskanals bekannt sein.

Werden mobile Stationen in einem Satellitennetzwerk betrieben, so bedeutet dies zusätzliche Komplexität. Um das Gesamtsystem effizient zu halten, sind adaptive Modulations- und Codierverfahren unabdingbar, welche den aktuellen Kanalzustand akkurat kennen müssen. Letzteres ist keine einfache Aufgabe im Zusammenhang mit langen Signallaufzeiten und sich rasch veränderlichen Kanälen.

Im Zusammenhang mit dem oben Genannten beschäftigt sich diese Dissertation mit der Parameter Schätzung in solch stark interferenzgestörten Szenarien, wie von der europäischen Weltraumagentur ESA im Kontext der *Satellite Communication Network of Experts III* Aktivität definiert. Die in dieser Arbeit präsentierten Forschungsergebnisse wurden daher im Zusammenhang mit der genannten ESA Aktivität erarbeitet und durch eigene weitergehende Forschung ergänzt.

CONTENTS

LIST OF FIGURES

LIST OF TABLES

1 Introduction

Communication satellites are one of the game-changing technologies developed in the middle of the last century; they were first envisioned by the Austrian Hermann Potocnik in 1929 but not widely published. His idea became reinvented in 1945 by the well-known science-fiction author Arthur C. Clarke publishing an article in the magazine *Wireless World*, which actually didn't even make it to the headline at the time. In his article Clarke postulated launching humanly operated "space stations" – three of their kind – in an equatorial orbit at an altitude of 35786 km above the Earth so as to provide worldwide communications; today this orbit is well-known as the *geostationary Earth orbit* (GEO) providing coverage to areas below latitudes of about 74° [1][3, pp. 537-538].

Just 19 years after Clarke's article and after some established experience from launching communication satellites in *low* and *medium Earth orbits* (LEO, MEO) the *National Aeronautics and Space Administration* (NASA) put the *Syncom-3* satellite successfully on a GEO [4][5]. Only one year later (1965) the first commercial GEO satellite *Early Bird* (Intelsat-1) of the *Communications Satellite Cooperation* was put in operation providing relay services at a bandwidth of a single television channel [6].

Up to now (2012), a broad range of commercial communication satellites has been designed, built, launched, operated and some already decommissioned. The communication satellite market is now an evolving multi-billion Euro market. For Europe this can be quantified by a few impressive numbers: about 80% of launches with European rockets are telecommunication satellites; *fixed satellite service* (FSS) transponders including direct broadcasting systems and *mobile satellite service* (MSS) transponders produce annual revenues exceeding 6.85 billion and 1.5 billion Euros, respectively. Annual turnovers for manufacturing and launching account for 5 billion Euros, whereas ground-segment manufacturing and satellite-related services produce revenues of about 25 and 50 billion Euro [7].

LEO and MEO satellites and satellite constellations (*e.g.* Iridium, Globalstar, and Orbcomm) benefit from relatively short round-trip times (RTT) and inherently less signal attenuation compared to GEO ones, but they also require for continuous coverage multiple satellites to be deployed and operated which significantly adds to the overall mission costs. Hand-held devices have limited bandwidth. Broadband systems require tracking antennas making user terminals more expensive and complex [3, pp. 537-539]. Modern GEO communication satellite systems already contain substantial on-board processing capabilities whilst implementing digital spot beam technologies combined

with frequency reuse schemes. The service region is divided into cells, thus the system can achieve a significantly higher throughput at a given bandwidth resource [8, pp. 9-12]. Prominent examples of such systems providing FSS and MSS are *TerreStar-1*, *ViaSat-1*, *SpaceWay-3*, *Hylas-2*, and *KA-SAT* as detailed in Table 1 [9-15].

Satellite:	*TerreStar-1*	*ViaSat-1*	*SpaceWay-3*	*Hylas-2*	*KA-SAT*
Operator:	TerreStar Networks (US)	ViaSat (US)	Hughes (US)	Avanti Communications (EU)	Eutelsat (EU)
Prime Contractor:	Space Systems /Loral (US)	Space Systems /Loral (US)	Hughes (US)	Orbital Science Corporation (US)	EADS Astrium (EU)
Service:	S-band MSS	Ka-band FSS	Ka-band FSS	Ka-band FSS	Ka-band FSS
Comm.:	500 dynamically configurable spot beams	72 spot beams; ~ 130 Gbit/s	24 Ka-band hopping spot beams; 112 uplink cells, 784 downlink microcells ~ 10 Gbit/s	24 fixed spot beams, 1 steerable beam;	82 spot beams; ~ 70 Gbit/s
Coverage Area:	Continental US, Canada, Puerto Rico	Continetal US, Canada, Alaska, Hawaii	North America	Europe, Middle East, Africa	Europe, Middle East, North Africa, VAE
Launch:	Q3, 2009	Q4, 2011	Q3, 2007	Q2, 2012	Q4, 2010
Mass:	6910 kg	6740 kg	5993 kg	3325 kg	6150 kg
Orbit:	GEO	GEO	GEO	GEO	GEO
	15 years	15 years	12.5 years	15 years	15 years

Table 1: Reference data of TerreStar-1, ViaSat-1, SpaceWay-3, Hylas-2 and KA-Sat

In the end the business case weighing between the user needs, legal restrictions and the expected overall mission costs versus expectable revenues governs the decisions on the system topology. Furthermore, competitors such as terrestrial wireless and cable service providers are not to be forgotten in the planning, thus requiring diversification strategies and low unit costs for a transferred data bit. For the latter it is indispensable to put effort in designing communication satellite systems that are versatile, reliable and exploit the available bandwidth very efficiently.

Since nowadays most of the satellite communication is done digitally, appropriate protocols and algorithms incorporating the efficiency paradigm are inevitable. Considering bi-directional data communications over satellite, burst-mode transmissions are typically applied, which in turn require appropriate ancillary information (overhead) incorporating preambles, training sequences, as well as relevant transmission parameters in order to synchronize transmitter and receiver. All the required overhead lowers the efficiency. Developing appropriate synchronization techniques capable to handle the chal-

lenges of modern interference-imposed satellite channels at a minimum investment of side information is a relevant part of today's communication sciences. In that respect, the work presented throughout this Doctoral Thesis aims at enhancing knowledge regarding selected topics in this realm. Therefore, the rest of this Doctoral Thesis is organized as follows:

Fundamental basics are presented in Chapter 2, whereas Chapter 3 is focused on channel estimation on *multiple-input multiple-output* (MIMO) satellite links; inspired by that Chapter 4 investigates possible improvements of MIMO channel estimation considering deterministic dependencies leveraged through location awareness. The Chapters 5 and 6 study parameter estimations on mobile satellite channels, whereas Chapter 5 investigates estimation methods using a simplified channel model as test bench. Chapter 6 employs the candidate techniques identified in Chapter 5 on a *land-mobile satellite* (LMS) link and discusses their performance. Finally, Chapter 8 identifies tasks and topics established by the fundamental work presented in this thesis which should find attention in future research activities.

(This page is intentionally left blank)

2 Fundamentals

This chapter briefly wraps up fundamentals which are key to the introduced research work in subsequent chapters aiming to ease the understanding for the reader.

In the sequel, modern burst mode data communications via satellite and their inherent need for appropriate synchronization algorithms is discussed; upon digital signal processing in the context of synchronization and channel parameter estimation it is expanded further on, followed by considerations about theoretical lower bounds for estimator benchmarking.

2.1 Preface

It is to be noticed, that the fundamentals presented in this chapter are selected according to the topics discussed throughout this thesis. It is refrained from providing all-encompassing elaborations since this would be a book-filling effort. However, the interested reader may retrieve additional information from the used sources. If there is no statement to the contrary the described fundamentals consider digital signal processing techniques and models since they conveniently model modern digital receiver architectures.

2.2 Satellite Data Communications

In a general sense satellite communications are not based on a different model than their terrestrial counterparts, whereas it is well known that they are primarily affected by long transmission distances leading to long *round-trip times* (RTTs) and high path losses. However, considering channel coding and modulations only, a classical decomposition of the baseband model is sketched in Figure 2.1 [16, p.11]. Synchronizing the receiver to the transmitter is evidently imperative for coherent demodulation and decoding so as to efficiently retrieve the transmitted user data. In that context, parameter estimations play a vital role by delivering the relevant channel parameters necessary for the synchronization task.

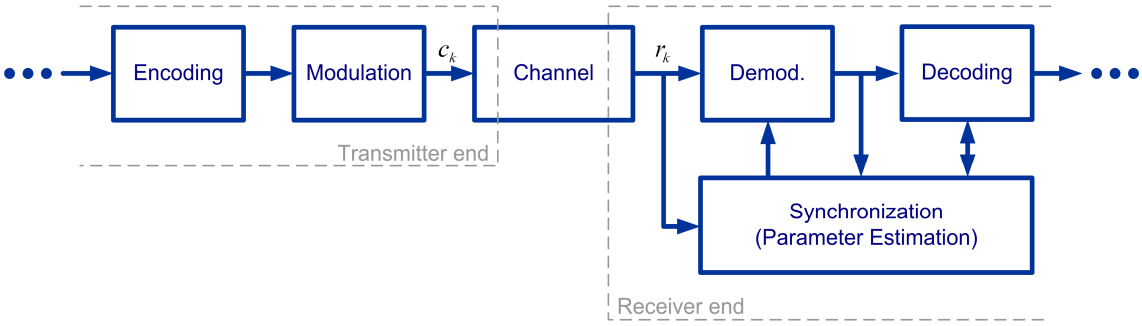

Figure 2.1: Classical baseband model of a communication system

As already mentioned, parameter estimations are required for synchronization and to provide an insight into the current channel state. The channel itself in the above presented model embraces effects introduced by the analogue front-ends of transmitter and receiver in addition to the effects of the physical propagation path.

When considering bi-directional data services, such as for example in the *second generation* of the *Digital Video Broadcasting over Satellite* standard (DVB-S2) [17] and the *second generation* of the *Digital Video Broadcasting Return Channel over Satellite* (DVB-RCS2) standard [18] of the *European Telecommunications Standards Institute* (ETSI), it is clear that *time division multiple access* (TDMA) schemes play an important role to share the bandwidth of a carrier amongst users. Burst mode transmission is employed, whereas each burst typically consists of a *header* field accumulating training sequences for carrier and timing recovery (coherent demodulation) as well as signalling and network management information, and a *data field* containing data and eventually interspersed pilot sequences for tracking purposes [8, pp. 158-163]. Furthermore, satellite communication systems today resort to highly-efficient coding schemes, such as *low-density parity-check* (LDPC) codes [17] and Turbo codes [18], which build upon estimated channel parameters such as the *signal-to-noise ratio* (SNR). It is to be noticed, that iterative decoding algorithms can also be appropriately enhanced so as to jointly deliver data and parameter estimates [16, p.11][19][20].

2.3 Synchronization

As already mentioned synchronization plays a critical role in communications. Failures in synchronization may result in erroneous data transmission diminishing the system performance. It basically comprises two steps, *acquisition*, representing the initial synchronization at the start of a burst, and *tracking*, representing a control loop to maintain synchronization. Synchronization basically aims at finding the optimum of an object function. This optimization problem is often tackled by applying the *maximum likeli-*

hood (ML) principle, which in general yields algorithms exhibiting (quasi) optimum performances. In that respect, three estimator principles are distinguished [21][22, pp.1-4][23, pp. 271-273]:

1 Data-aided (DA) estimation
2 Decision-directed (DD) estimation
3 Non-DA (NDA) estimation

For DA estimations the relevant *unique words* (UWs) or equivalently training sequences are known to the receiver, whereas for DD estimations only a detected sequence is available. NDA algorithms on the other hand, as their name suggests, perform the estimations without presence of training data or decisions [21][23, pp. 271-273].

Synchronization algorithms can furthermore be distinguished in *feed-forward* and *feedback* algorithms; the former derive the estimate before it is corrected whereas the second does it vice versa by feeding back an error signal to an interpolator or phase rotator, respectively. For obvious reasons feedback algorithms can only be applied for tracking purposes in the context of burst mode reception, because for initial acquisition the time constraints are rather stringent [21][23, pp. 271-401].

Within the following timing recovery as well as carrier frequency and phase error correction are discussed in the context of a discrete Gaussian channel. It is refrained from introducing specific estimation algorithms which can be found in [22] and [23] and elsewhere in the open literature. Assuming a memory-less discrete Gaussian baseband channel model, the received signal is furnished as

$$\tilde{r}(t) = a \cdot e^{j(2\pi\Delta f t+\theta)} \cdot \sum_{m} c_m \cdot h(t - mT - \tau) + n(t), \tag{2.1}$$

where the following notations apply:

- a …signal amplitude
- Δf …carrier frequency offset
- θ …carrier phase offset[1]
- T …sampling period
- c_m …symbol out of an arbitrary alphabet, $E[|c_m|^2] = 1$
- $h(\cdot)$ …*root-raised cosine* (RRC) filter response
- τ …timing error

[1] It is to be noticed, in order to account for phase noise, θ can be replaced by $\theta(t)$, which is typically modeled as Wiener process [16, p. 10].

- $n(t)$…zero-mean circular-complex Gaussian noise $\sim\mathcal{N}_c(0,\sigma_{n_c}^2)$.

First, the correct *timing* has to be established through an appropriate estimation of τ; assuming that the estimate was good enough such that the remaining error is negligible, *i.e.* $|\tau-\hat{\tau}|\ll 1$, hence (2.1) resolves by means of the matched filter $h^*(-t)$ to[2]

$$\tilde{r}_k' = \tilde{r}(t) * h^*(-t)|_{t=kT+\tau} = a\cdot e^{j(2\pi k v+\theta)}\cdot c_k + n_k', \tag{2.2}$$

where the operator "$*$" indicates convolution, v represents the carrier frequency offset normalized by the sampling period and $n_k' = n(t) * h^*(-t)|_{t=kT+\tau}$, which is the k-th instance of a band-limited circular-complex zero-mean Gaussian noise process. The filter process in (2.2) vanished, because the 2nd *Nyquist theorem* is yet fulfilled expressed by

$$g([k-n]T) = \begin{cases} 1, & k=n \\ 0, & k\neq n \end{cases}, \tag{2.3}$$

with $g(t)=h(t)*h^*(-t)$ [23, pp. 505-523][24, pp. 621-622].

It is worth mentioning that the matched filter is typically applied before the timing error is estimated, so the convolution in (2.2) practically consists of a procedure performing in consecutive order matched filtering, timing estimation, and timing correction [22, pp. 353-368].

After having discussed the timing recovery, the carrier frequency and phase error can now be tackled. Presuming proper estimates of both instances, *i.e.* $\hat{v}$ and $\hat{\theta}$, respectively, where it may be assumed that the estimation was successful such that $|v-\hat{v}|\ll 1$ and $\left|\theta-\hat{\theta}\right|\ll 1$, the corrected signal is established as $r_k=\tilde{r}_k'\cdot e^{-j(2\pi k\hat{v}+\hat{\theta})}$ which results in

$$r_k = a\cdot c_k + n_k. \tag{2.4}$$

By close inspection of the abovementioned derivation which ended up in (2.4) it is clear that $n_k\sim\mathcal{N}_c(0,\sigma_{n_c}^2)$.

---

[2] In the context of matched filtering with RRC filters it is $h^*(-t)\equiv h(t)$, where * denotes the conjugate-complex.

2.4 Channel Parameter Estimation

Parameter estimations may fulfil several tasks in a communication system such as revealing the current channel state compiled as *channel state information* (CSI) which typically forms part of modern decoding schemes [25, pp. 110-113] or of *adaptive coding and modulation* (ACM) concepts. It is to be noticed that synchronization also relies on parameter estimation in the end, but the term *channel parameter estimation* as used here is confined to the above mentioned context.

In general there are three basic estimation approaches to extract parameters from a set of observations:

- Heuristic approach
- ML approach
- Bayesian approach

Estimators following heuristic or partially heuristic principles can hardly be explained in a structured manner, in contrast to ML and Bayesian approaches [22, p. 37].

ML approaches are predominantly used as analytical framework for estimators, whereas also the Bayesian theory is of significant importance in the realm of communications. The latter is exemplified by Turbo decoders implementing the maximum *a posteriori* principle in an iterative manner so as to detect the sent data vector given the received, yet perturbed samples. Bayesian estimators typically come into play when *a priori* information can be exploited (*e.g.* Turbo codes) and/or when a ML approach cannot be found or turns out being too intricate. ML approaches maximize the likelihood function for the estimation parameter; asymptotically speaking, they are in general unbiased, achieve the theoretical lower bounds (see Section 2.5) and exhibit a Gaussian *probability density function* (PDF) [25, pp. 110-171][26, pp. 157-309].

By removing the data modulation from (2.4), which is obtained by multiplying with the complex-conjugate data symbols c_k^* such that

$$z_k = c_k^* \cdot r_k = a + c_k^* \cdot n_k, \tag{2.5}$$

where the term $c_k^* \cdot n_k \sim \mathcal{N}_c(0, \sigma_{n_c}^2)$, a ML DA estimator for the signal powers can easily be found using (2.6) and (2.7) below:

$$E[z_k] = a\,, \tag{2.6}$$

$$E[|z_k|^2] = a^2 + \sigma_{n_c}^2. \tag{2.7}$$

By linear combination of (2.6) and (2.7) and by the fact that the zero-mean circular-complex Gaussian noise process can be broken up into mutually independent in-phase and quadrature-phase zero-mean Gaussian random processes, *i.e.* $\sigma_{n_c}^2 = 2\sigma_n^2$, the power parameters are established for signal and noise as

$$S = a^2, \tag{2.8}$$

$$N = 2\sigma_n^2. \tag{2.9}$$

From above, the SNR is obtained as

$$SNR = \varrho = \frac{S}{N} = \frac{a^2}{2\sigma_n^2}. \tag{2.10}$$

It is to be noticed that relevant criteria assessing the quality of any estimator involve its behaviour regarding *estimation bias*, *jitter variance* and *consistency* (no bias, with increased observation length the jitter variance decreases) as well as *practically relevant issues* such as its implementation complexity and computational requirements [21].

2.5 Theoretical Estimation Bounds

Generally speaking, all the information about the parameter to be estimated is accumulated in the observation data. The achievable accuracy with which the parameter can be estimated thus strictly depends on how much the parameter influences the observed data, or more precisely, how dominantly it shapes the PDF of the observed data [26, p. 28].

The theoretical accuracy with which a parameter can be extracted from observations can be analytically described. Therefore theoretical bounds are derived to benchmark the jitter variance of the developed (suboptimal) estimation algorithms. In the glance of parameter estimation and synchronization the *Cramer-Rao lower bound* (CRLB) or its modified version, the *modified Cramer-Rao bound* (MCRB), are prominently used for that purpose. It is to be noticed that the MCRB is generally looser than the CRLB, *i.e.* [22, p. 53][26, p. 27][27]

$$MCRB(\lambda) \leq CRLB(\lambda), \tag{2.11}$$

whereas λ denotes the parameter to be estimated.

In the subsequent paragraphs the CRLB and MCRB are discussed with simple examples.

To introduce the concept of CRLBs a simple discrete *additive white Gaussian noise* (AWGN) channel model is given as

$$r_k = a \cdot c_k + w_k, \tag{2.12}$$

where a denotes the deterministic received signal amplitude, c_k is the k-th modulated symbol with $|c_k| = 1$ and w_k represents AWGN. A generic DA estimator is assumed delivering $\hat{a}$ by means of a training sequence of length L; the data symbols can be removed, such that the observation sequence develops as

$$z_k = c_k^* \cdot r_k \mathrel{\widehat{=}} a + w_k, \tag{2.13}$$

because the statistical properties of $w_k \sim \mathcal{N}(0, \sigma_w^2)$ equal those of $c_k^* \cdot w_k \sim \mathcal{N}_c(0, \sigma_w^2)$. From that the CRLB can be derived using [26, pp. 30-32]

$$CRLB(a) = \frac{1}{-E\left[\frac{\partial^2 \ln(p(\mathbf{z}|\, a))}{\partial a^2}\right]}, \tag{2.14}$$

$$p(\mathbf{z}|\, a) = \prod_{k=0}^{L-1} p(\mathrm{z}_k|\, a)\,, \tag{2.15}$$

where

$$p(\mathrm{z}_k|\, a) = \frac{1}{2\pi {\sigma_w}^2} \exp\left[-\frac{|z_k - a|^2}{2{\sigma_w}^2}\right]. \tag{2.16}$$

With (2.15) and (2.16) and after some straightforward algebra the second derivative leads to a constant, *i.e.*

$$\frac{\partial^2 \ln\big(p(\mathbf{z}|\, a)\big)}{\partial a^2} = -\frac{L}{{\sigma_w}^2}, \tag{2.17}$$

so the CRLB in that case is simply furnished as

$$CRLB(a) = \frac{{\sigma_w}^2}{L}. \tag{2.18}$$

The calculation of (2.15) is represented in more general terms as

$$p(\mathbf{z}|\lambda) = \int_{-\infty}^{\infty} p(\mathbf{z}|\mathbf{u}, \lambda) p(\mathbf{u}) d\mathbf{u}, \tag{2.19}$$

where $\mathbf{z}$, $\mathbf{u}$ and λ denote the observation sequence, the vector of unwanted (nuisance) parameters and the wanted parameter, respectively. Determining $p(\mathbf{z}|\lambda)$ often is hard yet impossible; this can also hold true for calculations of the expectation in (2.14). Because $p(\mathbf{z}|\mathbf{u}, \lambda)$ is easily available, the MCRB can be employed in such cases, *i.e.* [22, pp. 54-55][27]

$$MCRB(\lambda) = \frac{1}{E_{\mathbf{z},\mathbf{u}}\left[\left(\frac{\partial \ln\big(p(\mathbf{z}|\mathbf{u},\lambda)\big)}{\partial \lambda}\right)^2\right]}. \tag{2.20}$$

Considering a multiple of parameters to be jointly estimated which is represented by a parameter vector $\boldsymbol{\lambda} = \{\lambda_1, \lambda_2, \dots, \lambda_n\}$, the CRLB is achieved as

$$CRLB(\lambda_i) = \mathrm{J}_{ii}(\boldsymbol{\lambda})^{-1}, \tag{2.21}$$

with $\mathrm{J}_{ii}(\boldsymbol{\lambda})$ denoting the i-th diagonal element of the *Fisher information matrix* (FIM); $i = \{1,2, \dots, n\}$. The entities in the FIM are furthermore established as

$$\mathrm{J}_{ij}(\boldsymbol{\lambda}) = -E\left[\frac{\partial^2 \ln p(\mathbf{z}|\boldsymbol{\lambda})}{\partial\lambda_{\mathrm{i}}\partial\lambda_j}\right]. \tag{2.22}$$

2.6 Summary

Satellite communications differ from their terrestrial counterparts primarily by long transmission distances leading to long round-trip times and path losses. By considering a classical communication model it was pointed out that synchronization is of paramount importance for communications, especially when considering burst mode transmissions.

After having discussed the ways of synchronization in terms of presence and absence of training sequences with respect to acquisition and tracking, synchronization was elucidated in the context of a discrete Gaussian channel model.

Channel parameter estimations were introduced providing channel state information necessary for different purposes in communications systems exemplified by adaptive coding and modulation schemes or Turbo decoders. Whilst comparing different approaches it was stipulated that maximum likelihood estimation is most prominently used in that context. Continuing on the Gaussian channel example amongst others an amplitude estimator was elaborated.

Finally the analytical framework of theoretical lower bounds focusing on (modified) Cramer-Rao lower bounds was presented. Single estimation parameters as well as vectors of estimation parameters were elucidated; considering the former, the lower bound for amplitude estimation was derived.

(This page is intentionally left blank)

3 Channel Estimation on MIMO Satellite Links

The work presented in this chapter was mainly carried out in the framework of the *Satellite Communication Network of Experts III* (SatNEx III) *Call off-Order* (CoO) 1 project supported by the *European Space Agency* (ESA). SatNEx III is a follow up initiative from the *Satellite Communication Network of Excellence I and II* (SatNEx I, II) programs initially supported by the *European Union* (EU). CoO 1 focuses on next generation satellite systems including investigations on techniques necessary for Terabit-per-second communication satellites, hybrid space/ground signal processing techniques and novel network protocol techniques for communication satellites [28].

Findings and results, created by the author throughout the SatNEx III CoO 1 study, were already integrated in technical notes and reports [29 – 33] and partially published in [34][35]. However, they are not explicitly quoted in the following to avoid confusion and to support the readability of this thesis. Quotations on the listed documents refer to results and findings not or not only created by the author himself.

The subsequent sections after an introductive section focus on the generic *multiple-input multiple-output* (MIMO) SatNEx III satellite scenario, called *DigiSat*, on channel estimation on the *forward* and *return links* (*i.e.* the *forward link* the link between gateway, satellite and *user terminals* and the *return link* the link between user terminal, satellite and gateway).

3.1 Preface

To handle the rapidly growing bulk of transmitted data, the next generation broadband satellite systems must offer versatile and efficient communication to users at competitive prices. Both, FSS and MSS have to increase their overall throughput significantly in that respect. Besides evolutions towards higher frequencies, efforts in better exploitation of the available bandwidth are needed. Promising with respect to significant capacity enhancements are multi-beam satellite systems configured in a (multi-)star topology, *i.e.* all communication with users is done from one or more central gateways throughout a multi-beam satellite acting as relay (star network topology). However, the overall increase of throughput basically originates from the spatial diversity achieved by the multi-beam space borne antenna system. Appropriate measures to mitigate interference from neighbouring spot beams operated at the same frequency band are inevitable (see Figure 3.1). The latter require different technologies with respect to the forward and

return link. Most attractive for the MIMO concept are *precoding* and *beam forming* techniques on the forward link and *multi-user detection* (MUD) using *interference cancellation* (IC) methods on the return link [36]. However, Figure 3.1 depicts the footprint consisting of 100 beams/cells of the antenna as provided by ESA [37] for the SatNEx III project. The used colour coding of four different colours (green, orange, blue, and grey) exemplifies a frequency reuse factor of four, *i.e.* every fourth cell applies the same frequency band. Interference in terms of co-channel interference may be neglected at first, because *multiple access interference* (MAI), caused by emission of interfering signals to neighbouring cells, imposes.

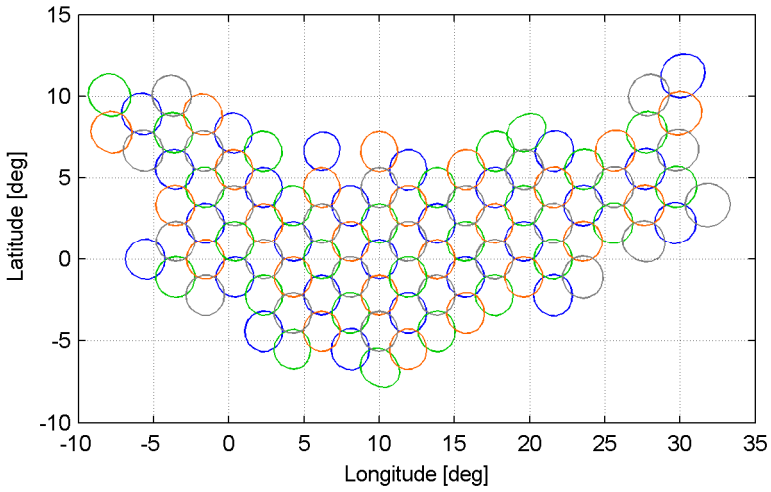

Figure 3.1: Footprint of antenna beams with a frequency reuse factor of four

Not surprisingly, the amount of interference highly depends on the number of neighbouring cells operated at the same frequency. Thus, high frequency reuse factors boost the impairments and challenge the system design to the benefit of an increased overall throughput and bandwidth efficiency.

3.2 The DigiSat Scenario

To meet capacity and throughput requirements of next generation satellite systems, the SatNEx III DigiSat scenario addresses a MIMO satellite system targeting aggressive design goals. These comprise full frequency reuse throughout all 100 cells and the ability to serve one user terminal per cell per timeframe. Hence, TDMA within cells applies. Figure 3.2 depicts the cell pattern formed by the spot beams. It furthermore details the beam/cell numbering, as used within simulations, and indicates the -3 dB contours

by red boundaries. Appropriate interference mitigation techniques on both forward and return link are mandatory. Those comprise beamforming, precoding and MUD techniques based on hybrid space-ground signal processing [34][35].

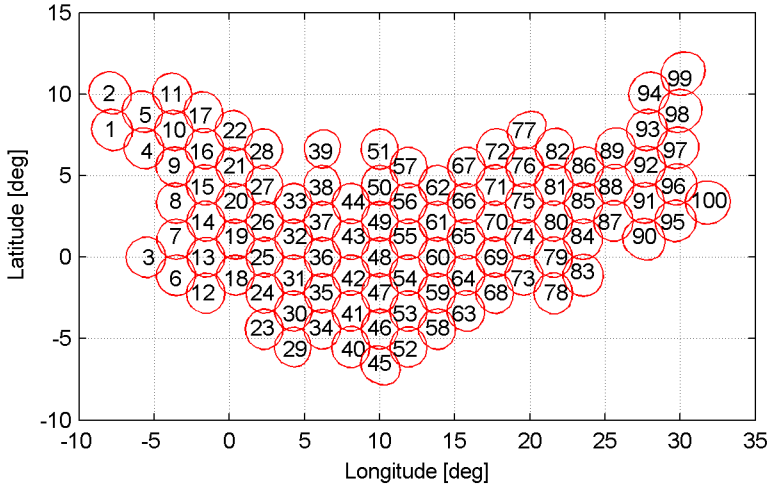

Figure 3.2: Footprint of the numbered antenna beams with full frequency reuse

The DigiSat scenario is foreseen to be implemented as a star network, *i.e.* every user terminal directly communicates with the gateway via the satellite. A digital feeder *uplink* of 2 GHz bandwidth in either Ka-band for an MSS scenario or Q/V-band for an FSS scenario is required between gateway and the satellite. The MIMO *downlinks* between the satellite and the user terminals are implemented in either S-band or K/Ka-band utilizing a bandwidth of 30 MHz for MSS and 500 MHz for FSS, respectively [33, p. 9].

3.2.1 Beamforming

As already mentioned, the antenna footprint of the DigiSat scenario is shaped by 100 beams. In this particular case, these beams are formed by 155 feeds. Figure 3.3 shows the -3 dB contours of the antenna feeds, their respective numbers and heading. The contribution of each feed is already directional, thus the aim of beamforming is to provide uniform cell coverage by tuning clusters of approximately 20 feeds in amplitude and phase. It is further important that the emitted energy in the respective cell is maximized whilst minimizing emissions outside. An *array fed reflector* (AFR) antenna with a reflector size of > 18 m for MSS or > 2.5 m for FSS is envisaged for DigiSat in that regard [37][32, pp. 14-18].

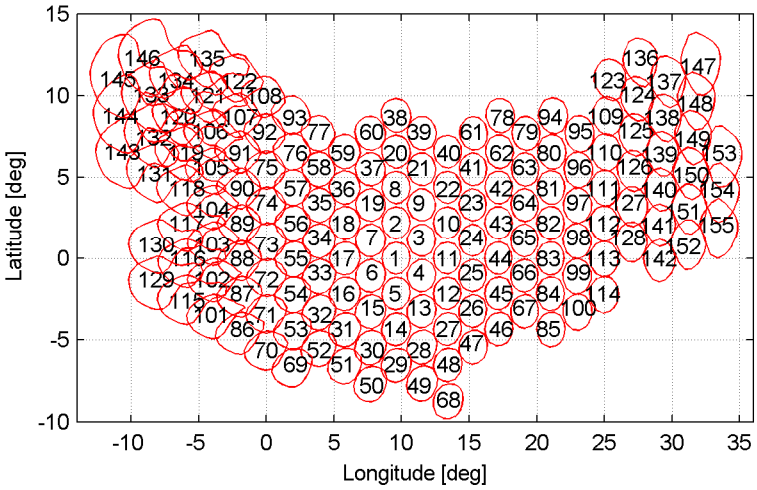

Figure 3.3: Footprint of 155 antenna feeds

For a single beam, as exemplified with beam 48 in Figure 3.5, a number of about 20 feeds (see Figure 3.4) are appropriately weighted, corrected in phase and summed up. Those tuning factors are represented in (3.1) by the beamforming matrix **B**, an $N \times K$ matrix relating the feed and beam space:

$$\mathbf{x}_f = \mathbf{B} \cdot \mathbf{x}_b. \tag{3.1}$$

The signal vectors $\mathbf{x}_f$ $(N \times 1)$ and $\mathbf{x}_b$ $(K \times 1)$ represent the signal stack in feed and in beam space, respectively [32, p. 41][35].

The mentioned directivity of the feed patterns can be seen in Figure 3.4 below. By comparing the radiation patterns of Figure 3.4 with those in Figure 3.5, a significant benefit for beams in the main lobe to side lobe ratio can be observed, thus helping to suppress interference from adjacent cells. For the sake of completeness, Figure 3.6 shows the three dimensional beam pattern of the DigiSat antenna comprising all beams.

Classical beamforming networks typically consist of high frequency elements such as phase shifters, combiners, splitters, attenuators, etc. only allowing for little flexibility. *Digital beamforming* (DBF) can provide dynamic pattern control including software formed, shaped, and steered beams, thus facilitating individual beams for users as well as real time adaptive beamforming. The complexity of DBF relates to the numbers of feeds and beams, as well as to the overall system bandwidth [38].

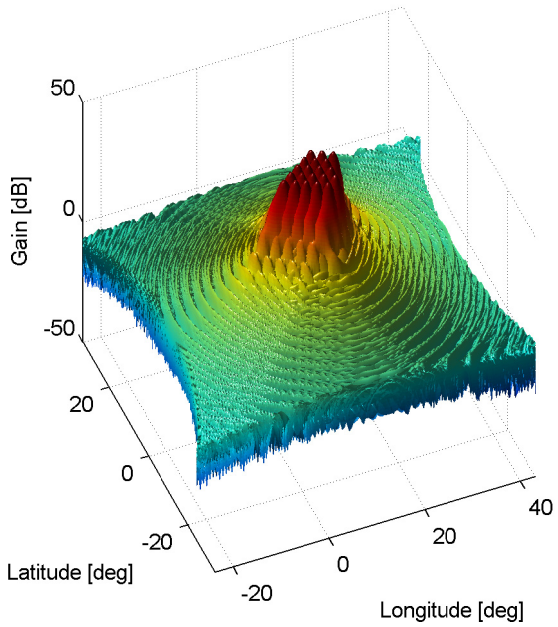

Figure 3.4. 3D radiation pattern of the feeds forming beam 48

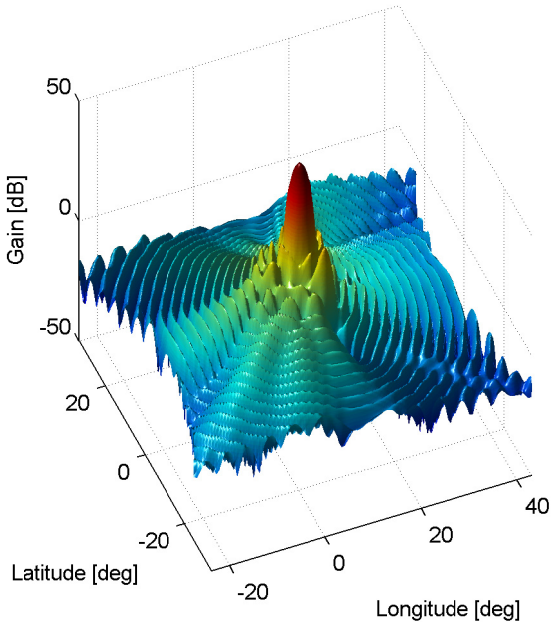

Figure 3.5: 3D beam radiation pattern of beam 48

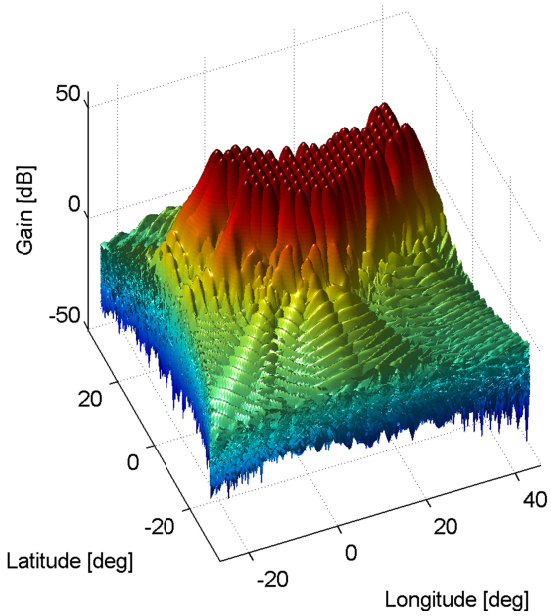

Figure 3.6: 3D radiation pattern of all beams of the DigiSat antenna

3.2.2 Hybrid Space Ground Processing

Space processing, on the one hand, inflicts a high level of payload complexity on the space segment involving increased power requirements and costs. Beamforming is done

on-board, thus potentially reducing the required bandwidth for the feeder uplink to a minimum. *Ground processing*, on the other hand, requires higher bandwidth at the feeder link, but benefits from sufficiently available processing power. In addition, satellite development times and risks are reduced [35][39].

Hybrid space ground processing techniques, as foreseen for DigiSat, are a trade-off between performance and complexity by splitting the computational load between gateway and satellite. While *ground and space processing* demand the highest and lowest feeder link bandwidth, respectively, *hybrid space ground processing* resides in-between [35]. Reducing the required feeder link capacity is the main motivation to evolve from pure *ground processing* systems towards *hybrid* systems; for a fixed number of gateways this goal can only be achieved by reducing the amount of transmitted information on the feeder link [39]. Furthermore, by using wave digitization for the feeder link, calibration is not required in contrast to analogue present day systems [35].

By introducing *hybrid space ground processing*, (3.1) can be rewritten as

$$\mathbf{x}_f = \mathbf{B}_S \cdot \mathbf{B}_G \cdot \mathbf{x}_b, \tag{3.2}$$

where $\mathbf{B}_S$ represents an $N \times M$ coarse beamforming matrix on board the satellite and $\mathbf{B}_G$ represents an $M \times K$ beamforming matrix on ground. With $N > K$, $M \in \mathbb{N}$, $N \geq M \geq K$ the processing in the space segment gives

$$\mathbf{x}_f = \mathbf{B}_S \cdot \mathbf{x}'_f, \tag{3.3}$$

where $\mathbf{x}'_f$ in an $(M \times 1)$ signal stack representing the *compressed feed signal subspace*. The coarse beamforming matrix $\mathbf{B}_S$ can be achieved through singular value decomposition. With $\mathbf{B}_S$ being fixed, adaptive beamforming is done through $\mathbf{B}_G$ on ground. However, the required bandwidth on the feeder link is proportional M, but the overall system performance in terms of throughput decreases as M decreases, hence there is a trade-off between performance, compression, and bandwidth utilization [32, pp. 71-73].

Figure 3.7 depicts the architecture as envisaged for DigiSat [35][39], where the functional blocks follow the logic of the return link. After digitization at feed level (wave field digitization), coarse beamforming takes place reducing the feed signals to a feed signal subspace. The compressed feed subspace signals become efficiently coded, modulated, and transmitted to the gateway. After demodulation, decoding, and decompression, fine adaptive beamforming is applied regenerating the user signals [39].

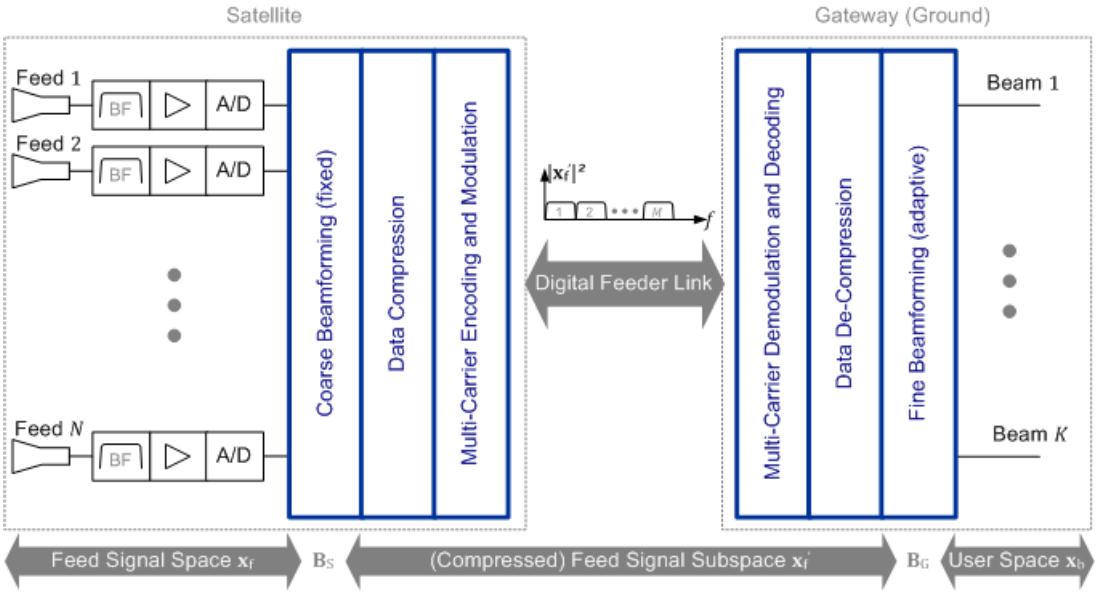

Figure 3.7: DigiSat hybrid space ground processing with wave field digitization

3.2.3 Precoding

The Spatial Division Multiplexing MIMO DigiSat scenario assumes the use of the same frequency band for all 100 cells, thus a user terminal observes 99 interferers on the forward link. This MAI significantly degrades the achievable performance and claims for countermeasures.

Precoding can help to mitigate this detrimental interference. Its basic idea is to tweak the signal at the gateway such that it reconstructs through the MAI on the channel at the receiver end. Knowledge about the channel, often referred to as CSI, is necessary [40, pp. 4-8]. This information must be timely, thus it is intuitive that the time variance of the channel must be low compared to the round-trip time of the signal.

Given an AWGN channel impaired by a random interference sequence $\mathbf{i} \sim \mathcal{N}(0, \sigma_i^2)$, which is perfectly known to the transmitter; it is shown in [41] that by adapting the transmitter signal to $\mathbf{i}$ the Shannon capacity for AWGN channels can be achieved independent of σ_i^2. In literature this framework is known as *Dirty Paper Coding* (DPC). DPC is optimal to be used for Gaussian MIMO *broadcast channels* (BCs) in terms of capacity [42]. Suboptimal methods such as the non-linear Tomlinson-Harashima precoding or linear precoding schemes (*e.g. zero-forcing* or *minimum mean square error* methods) exist, tailored to spatial multiple access MIMO broadcast channels [43][44, pp. 19-22][32, pp. 54-56].

To outline the principles of precoding, the MIMO signal model

$$\mathbf{y} = \mathbf{H}^{FL} \cdot \mathbf{x} + \mathbf{n} \tag{3.4}$$

is exemplified, where $\mathbf{y} = (y_1, y_2, \dots, y_K)^T$ and $\mathbf{x} = (x_1, x_2, \dots, x_N)^T$ are the receive and transmit vectors, respectively, $\mathbf{H}^{FL}$denotes the $K \times N$ channel matrix of the forward link and $\mathbf{n}$ represents zero-mean circular-complex Gaussian noise $\sim\mathcal{N}_c\ (0,\ \sigma_n^2)$. It is to be noticed that the input power constraint $E[\|\mathbf{x}\|^2] \leq P$ applies, $E[\cdot]$ denoting expectation. With

$$\mathbf{x} = \mathbf{F} \cdot \mathbf{s}, \tag{3.5}$$

where $\mathbf{F}$ is the $N \times K$ precoding matrix and $\mathbf{s}$ is the $(K \times 1)$ stack of modulated source symbols, equation (3.4) becomes

$$\mathbf{y} = \mathbf{H}^{FL} \cdot \mathbf{F} \cdot \mathbf{s} + \mathbf{n} = \mathbf{H}_{pc}^{FL} \cdot \mathbf{s} + \mathbf{n}, \tag{3.6}$$

with $\mathbf{H}_{pc}^{FL}$ denoting the precoded channel matrix. Assuming knowledge of $\mathbf{H}^{FL}$ as postulated in [41], $\mathbf{F}$ can be constructed such that

$$\mathbf{H}^{FL} \cdot \mathbf{F} = \gamma_p \cdot \mathbf{I}, \tag{3.7}$$

where γ_p fulfils the input power constraint and $\mathbf{I}$ is the $K \times K$ identity matrix. Equation (3.7) shows that MAI can be cancelled by channel inversion; this approach is known as *zero-forcing precoding* and aims to decouple the multi-user channel into separate sub-channels. Considering per antenna input power constraints or criteria such as maximal fairness or maximal throughput, more sophisticated precoding procedures apply [45] [32, pp. 54-56].

In practise, $\mathbf{H}^{FL}$ is not known and must be estimated, *i.e.* $\widehat{\mathbf{H}}^{FL}$, thus interference cannot be completely removed. Moreover, practical channels often deal with imperfections, such as nonlinearities, which detrimentally affect the achievable gain in system performance [44, p. 22].

3.2.4 Multi-User Detection

On the return link, the central gateway has no knowledge about the data other user terminals transmit, but is aware of the respective CSI. The return link is a MIMO *multiple access channel* (MAC), thus no symbol synchronicity can be assumed. Nevertheless, appropriate MUD at the central gateway can improve the performance and mitigate MAI. Akin to the forward link model represented in (3.4), the return link can be modelled as

$$\mathbf{y} = \mathbf{H}^{RL} \cdot \mathbf{x} + \mathbf{n}, \tag{3.8}$$

where $\mathbf{y} = (y_1, y_2, \dots, y_K)^{\mathrm{T}}$ and $\mathbf{x} = (x_1, x_2, \dots, x_N)^{\mathrm{T}}$ are the receive and transmit signal vectors, respectively, $\mathbf{H}^{RL}$ denotes the $K \times N$ channel matrix on the return link and $\mathbf{n}$ represents zero-mean circular-complex Gaussian noise of σ_n^2. As we are interested in $\mathbf{x}$, its estimate can be computed using linear MUD as $\hat{\mathbf{x}} = \mathbf{W}^{\mathrm{H}} \cdot \mathbf{y}$. With $\mathbf{W}^{\mathrm{H}} = f\left(\widehat{\mathbf{H}}^{RL}\right)$, the equalized channel matrix computes to $\mathbf{H}_{eq}^{RL} = \mathbf{W}^{\mathrm{H}} \cdot \mathbf{H}^{RL}$; thus

$$\hat{\mathbf{x}} = \mathbf{H}_{eq}^{RL} \cdot \mathbf{x} + \mathbf{W}^{\mathrm{H}} \cdot \mathbf{n}, \tag{3.9}$$

where $\mathbf{W}^{\mathrm{H}} \cdot \mathbf{n}$ describes the noise term. It is to be noticed that $E[\mathbf{W}^{\mathrm{H}} \cdot \mathbf{n} \cdot \mathbf{n}^{\mathrm{H}} \cdot \mathbf{W}] = \mathbf{W}^{\mathrm{H}} \cdot \mathbf{W} \cdot \sigma_n^2$, thus the noise power may be amplified [32, pp. 82-85][44, pp. 26-29].

Besides linear methods such as *linear MMSE* (LMMSE) detectors, non-linear methods or iterative methods such as *successive interference cancellation* (SIC) are well known and promising for MIMO-MAC channels [36][46]. The latter exhibit increased performance compared to LMMSE schemes, which suffer from a large number of interferers with respect to their filter length [47, pp. 26-27]. SIC is realized by iteratively detecting and subtracting the already detected/decoded user signal from the sum signal $\mathbf{y}$. Optimistically assuming correct detection and cancellation of the i^{th} user's contribution, a reduction of interference for the remaining user signals in $\mathbf{y}$ is achieved [48, pp. 344-345]. The principle of MMSE-SIC is depicted in Figure 3.8 [36].

It is to be noticed that the MUD performance on a MIMO-MAC increases when implemented in the feed space instead of beam space; nonetheless, adequate channel estimation is required [32, pp. 85-86].

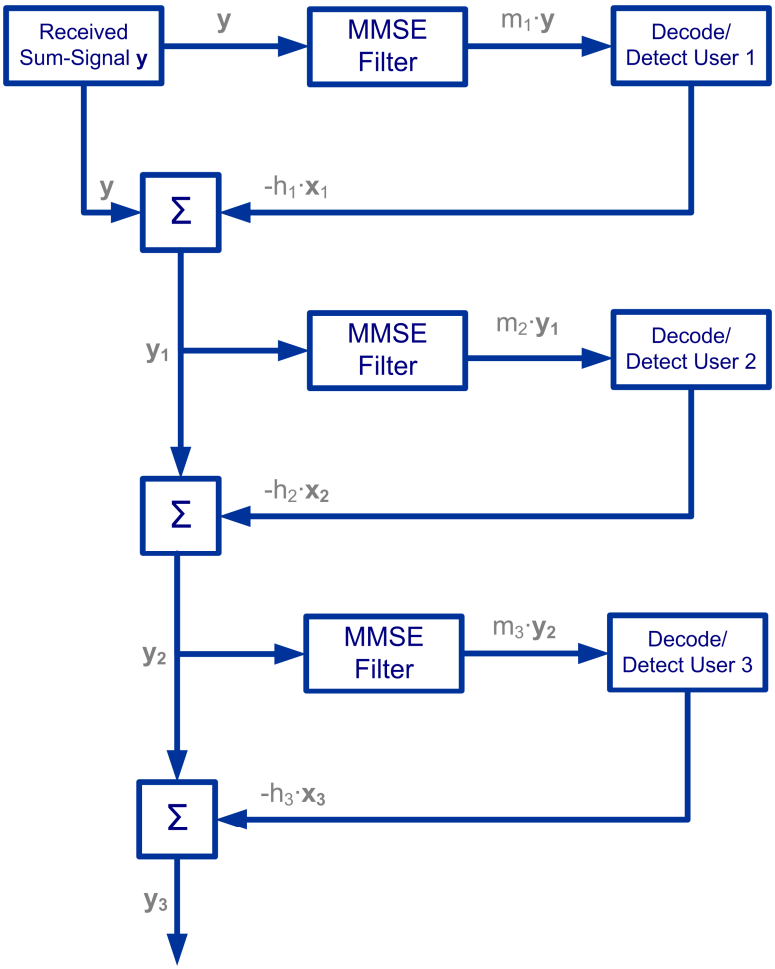

Figure 3.8: Concept of MMSE-SIC

3.3 Channel Estimation on the Forward Link

The forward link is a symbol-synchronous memory-less MIMO-BC and is the link between gateway, satellite, and user terminals, as visualized in Figure 3.9; three user terminals are exemplified on the MIMO-BC hosted by their respective cells which are formed by an AFR antenna with beamforming, as described in 3.2.1 and 3.2.2. To meet next generation throughput requirements, strategies enhancing the system's spectral efficiency – more specifically, aggressive frequency reuse – are necessary but cause tremendous interference; the latter becomes more and more evident the closer a user terminal is located to the border of its cell. As introduced in 3.2.1 and 3.2.3, (joint) beamforming and precoding strategies can mitigate interference effects but require accurate determination of the CSI, thus adequate and accurate channel estimation is pivotal.

The subsequent paragraphs elaborate on means to perform appropriate channel estimation on the forward link, thus in 3.3.1 the signal model is presented, paragraph 3.3.2

explains the choice and construction of identifier sequences, in 3.3.3 and 3.3.4 channel estimation is evaluated using the pseudo-inverse and correlation, respectively, and effects of orthogonal and non-orthogonal identifier sequences are analysed.

It is to be noticed that all forward link simulations *a priori* assume an ideal recovery of symbol timing and carrier frequency.

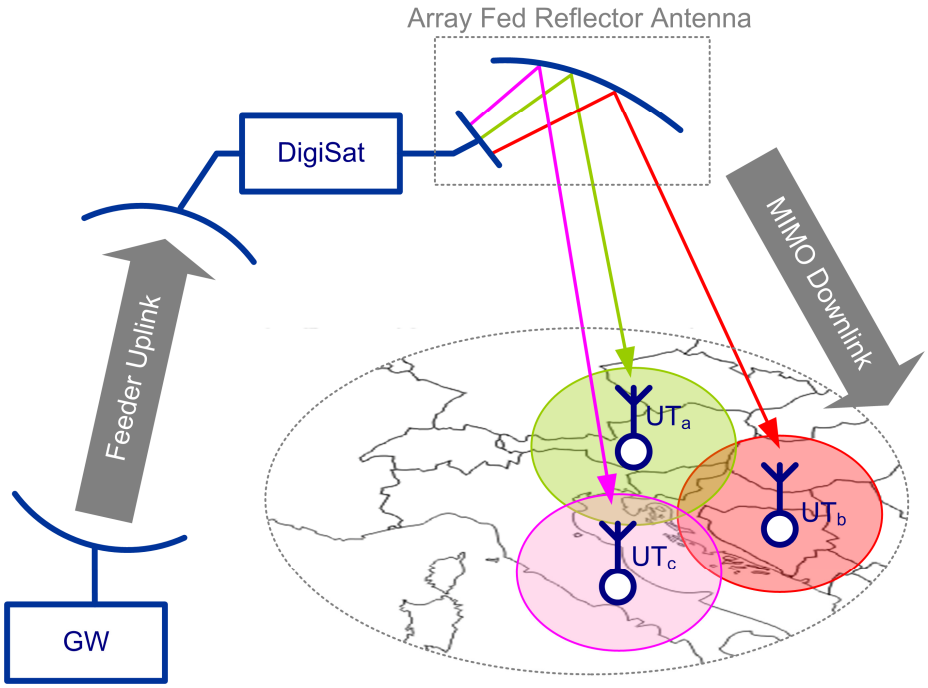

Figure 3.9: DigiSat forward link architecture with three outlined cells[3]

3.3.1 The Signal Model

As already mentioned, DigiSat implements $K = 100$ spot beams which form 100 user cells; each of which is capable to serve one user at a time, thus 100 users can be served simultaneously. These 100 beams (Figure 3.2) are generated by $N = 155$ feeds (Figure 3.3) and are operated on the same frequency. Hence, full frequency reuse boosts the spectral efficiency at the expense of high interference. Joint beamforming and precoding can mitigate interference, but requires accurate and timely CSI in order to perform well. It is to be noticed, the system performance in terms of throughput can be increased by applying beamforming and precoding in the feed space, thus channel estimation must be implemented accordingly [35].

[3] The depicted map in Figure 3.9 is used and modified from source: http://d-maps.com/carte.php?lib=europe_map&num_car=2233&lang=en (2011-09-27).

Without loss of generality, both the superscript indicating the forward link and the subscript indicating the feed signal space are omitted subsequently, so $\mathbf{H}_f^{FL} \Rightarrow \mathbf{H}$ and $\mathbf{x}_f \Rightarrow \mathbf{x}$.

According to the DigiSat concept for hybrid space ground processing, the digital feeder uplink may be regarded as ideal [29, p. 67]; with (3.2) and (3.5), the emitted feed signals are given by

$$\mathbf{x} = \mathbf{B}_S \cdot \mathbf{B}_G \cdot \mathbf{F} \cdot \mathbf{s}, \tag{3.10}$$

where $\mathbf{B}_S$ is the $N \times M$ coarse beamforming matrix on board the satellite, $\mathbf{B}_G \cdot \mathbf{F}$ is a $M \times K$ joint beamforming and precoding matrix at the gateway, and $\mathbf{s}$ is the stack of modulated user symbols.

Adopting (3.4) to the DigiSat feed signal space, then

$$\mathbf{y} = \mathbf{H} \cdot \mathbf{x} + \mathbf{n}, \tag{3.11}$$

where $\mathbf{H}$ is the $K \times N$ channel matrix in the feed signal space, $\mathbf{y} = (y_1, y_2, \dots, y_K)^{\mathrm{T}}$, and $\mathbf{x} = (x_1, x_2, \dots, x_N)^{\mathrm{T}}$. The channel matrix $\mathbf{H} = \mathbf{W}^{FL} \cdot \mathbf{G}^{FL} \cdot \mathbf{D}^{FL}$, where [44, p. 36]

- $\mathbf{W}^{FL}$ is the $K \times K$ diagonal fading matrix on the downlink; the entry (m, m) accounts for the gain of user terminal m,
- $\mathbf{G}^{FL}$ represents the $K \times N$ feeder matrix whose entries (m, n) represent the gain between user signal path m and antenna feed n, and
- $\mathbf{D}^{FL}$ is a $N \times N$ matrix accounting for effects occurring on the feeder link and in the on-board repeater chain; as mentioned above $\mathbf{D}^{FL}$ may be regarded as ideal because of the envisaged hybrid space ground processing concept.

Figure 3.10 sketches the MIMO-BC link to the m^{th} user terminal, *i.e.* the m^{th} row of the channel matrix $\mathbf{H}$; hence, $\mathbf{h}_m = (h_{m,1}, h_{m,2}, \dots, h_{m,N})$, $m = 1,2, \dots, K$, holds $N = 155$ complex values describing the respective channel effects such as feed radiation pattern, atmospheric fading, path loss, and receive antenna gain [35].

In order to estimate $\mathbf{H}$, DA channel estimation requires non-precoded training sequences to be foreseen in the physical layer framing structure [44, pp. 35-37]. These identifier sequences $\mathbf{c}_m = (c_{m,1}, c_{m,2}, \dots c_{m,L})$, $m = 1,2, \dots, N$, of length L must be unique for each feed; their desired properties, like orthogonality and linear independence, are discussed hereafter in 3.3.2. With $\mathbf{C} = (\mathbf{c}_1, \mathbf{c}_2, \dots, \mathbf{c}_N)^{\mathrm{T}}$ and $\mathbf{X} = (\mathbf{x}_1, \mathbf{x}_2, \dots, \mathbf{x}_{L_x})$, where

$\mathbf{x}_i = \mathbf{x}|_{i \cdot T_s}$, $i = 1,2,\dots,L_x$, L_x representing the payload data length, and T_s represents the symbol period, the on the MIMO-BC emitted signal time series is $[\mathbf{C} \quad \mathbf{X}]$, as shown in Figure 3.11, where $L \ll L_x$.

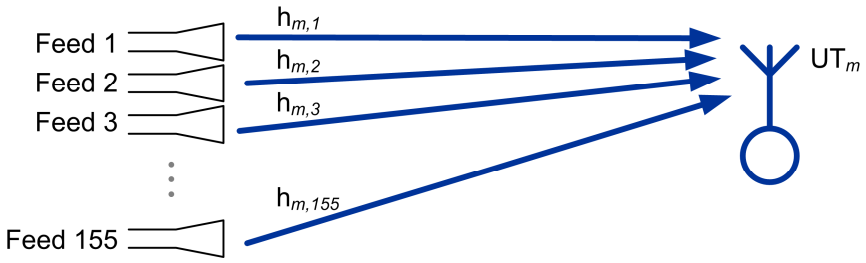

Figure 3.10: Satellite downlink for the m-th user terminal

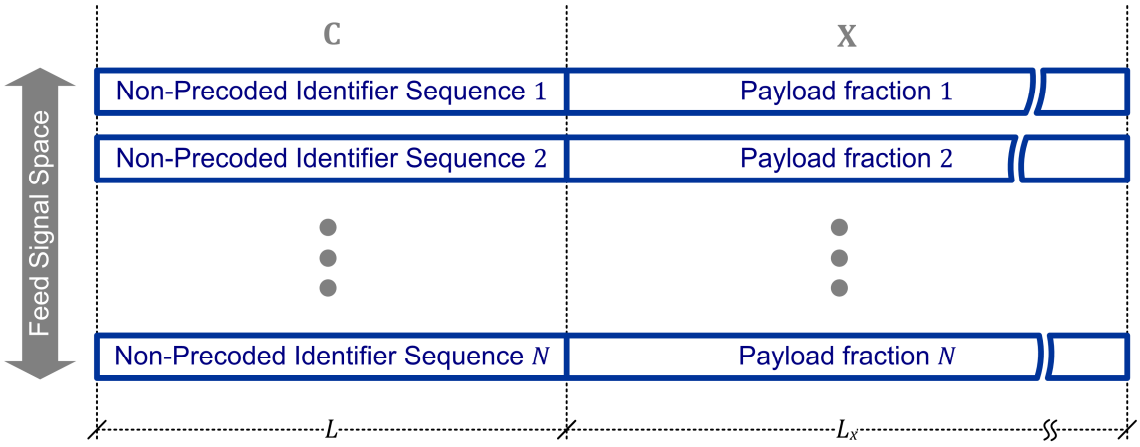

Figure 3.11: Physical layer framing on the DigiSat MIMO-BC[4]

Incorporating the above mentioned steps in the signal model for the MIMO-BC and focusing on the identifier sequences only, as required for channel estimation, then the signal model becomes

$$\mathbf{Y} = \mathbf{H} \cdot \mathbf{C} + \mathbf{N}, \tag{3.12}$$

where $\mathbf{Y} = (\mathbf{y}_1, \mathbf{y}_2, \dots, \mathbf{y}_L)$, $\mathbf{y}_i = \mathbf{y}|_{i \cdot T_s}$ and $i = 1,2,\dots,L$.

[4] It is to be noticed that due to the beamforming concept (3.10), each line in $\mathbf{X}$ hosts fractions of the payload consisting of training sequences and user data, thus Figure 3.11 denotes them as "Payload fraction".

3.3.2 The Choice and Construction of Identifier Sequences

Transmission on the forward link happens in a symbol-synchronous manner, thus identifier sequences, in the sequel also denoted as *unique words* (UWs), for MIMO channel estimation can either be *orthogonal* or *non-orthogonal*. Whereas it is intrinsic for orthogonal sequences to be linearly independent [49, pp. 15] ($L \geq N$ is implied), non-orthogonal sequences require $L \geq N$ to be fulfilled, in order to be able to comprise an independent set of vectors. Complementary, $L < N$ sequences are linearly dependent.

Orthogonal UWs are optimal with respect to mutual interference, *i.e.* $\mathbf{C} \cdot \mathbf{C}^{\mathrm{H}} = \mathbf{I}$. Well known and frequently used orthogonal sequences are *Walsh-Hadamard* (WH) codes; they are often applied in terrestrial mobile spread spectrum communications, such as in the CDMA2000 standard [50]. WH codes are limited to $L = 2^m$, $m \in \mathbb{N}_0$, but are easy to construct using a recursive principle [48, pp. 11-13], *i.e.*

$$\boldsymbol{\mathcal{H}}_{(m)} = \begin{bmatrix} \boldsymbol{\mathcal{H}}_{(m-1)} & \boldsymbol{\mathcal{H}}_{(m-1)} \\ \boldsymbol{\mathcal{H}}_{(m-1)} & -\boldsymbol{\mathcal{H}}_{(m-1)} \end{bmatrix}, \tag{3.13}$$

where $\boldsymbol{\mathcal{H}}_{(0)} = 1$ and $\boldsymbol{\mathcal{H}}_{(m)}$ is of size $L \times L$.

Length limitations also apply to *maximal-length linear feedback shift register sequences*, often denoted as *m-sequences*, as well as Gold and Kasami sequences, which are limited to $L = 2^m - 1$, $m \in \mathbb{N}$. They typically exhibit low cross-correlations with time-shifted copies of themselves or other UWs in the set [51][52][53].

To find identifier sequences of arbitrary length, resorting to *pseudo-random sequences* (PRSs) is necessary; they suffer from mutual interference, *i.e.* $\mathbf{C} \cdot \mathbf{C}^{\mathrm{H}} \neq \mathbf{I}$. To minimize estimation errors, low cross-correlation values amongst the member UWs are indispensable, thus resorting to an appropriate brute force search algorithm is necessary. A brief description of the applied algorithm can be found in Appendix A-(c). However, Figure 3.12 depicts a histogram of the cross-correlation values of a set of linearly independent UWs with $N = 155$ and $L = 156$ binary symbols, *i.e.* $\{-1,1\}$, where $|R_{nm}| = |\mathbf{c}_m^{\mathrm{T}} \cdot \mathbf{c}_n|$, $n = 1,2,\dots,N$, and $m = n+1, n+2, \dots, N$; ρ denotes the normalized frequency density for each value of $|R_{nm}|$.

Figure 3.13 compares histograms of the cross-correlation values of linearly dependent UW sets with $N = 155$ and $L = 63$ binary symbols. The notation is equivalent to Figure 3.12; the magenta, blue and green bars indicate the distribution in cross-correlation

using a large set of Kasami sequences [53], PRSs, and randomly[5] generated binary sequences, respectively.

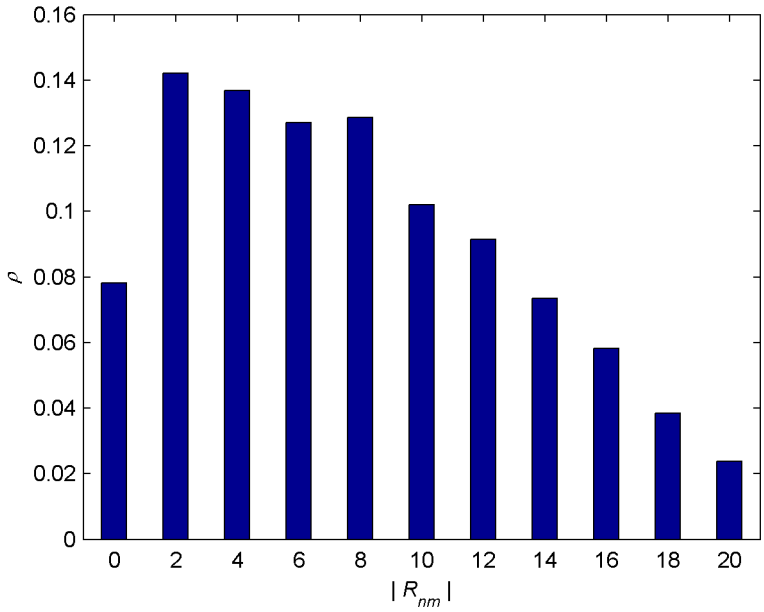

Figure 3.12: Histogram of the cross-correlation of linearly independent PRSs (L = 156)

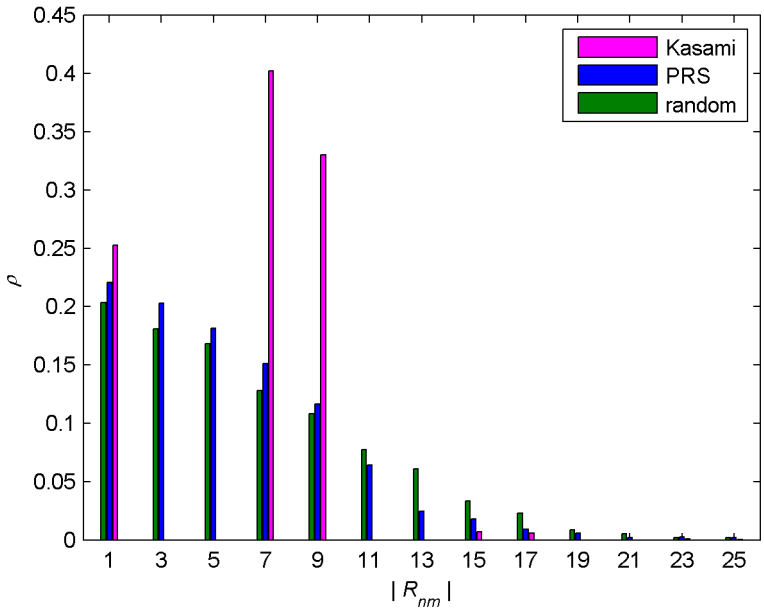

Figure 3.13: Histogram of the cross-correlation of linearly dependent UWs (L = 63)

[5] Randomly generated binary sequences are here understood as sequences generated by a binary random generator (Bernoullian) without optimization criterion as it was applied for PRSs; for the latter it may be assumed that the sequences are quasi orthogonal.

Not surprisingly, randomly generated sequences in Figure 3.13 offer the weakest properties since they encompass higher cross-correlation values more frequently. PRSs and the large set of Kasami sequences appear more promising, whereas the latter frequently exhibit cross-correlation values of seven and nine.

It is to be noticed that binary sequences of even/odd length lead to even/odd cross-correlation values, because for all i

$$c_{n,i} \cdot c_{m,i} = \begin{cases} 1, & c_{n,i} = c_{m,i} \\ -1, & c_{n,i} \neq c_{m,i} \end{cases}, \tag{3.14}$$

thus only inverse pairs cancel out. Comparing Figure 3.12 and Figure 3.13 it is obvious that longer UWs exhibit higher absolute cross-correlation values. However, Figure 3.14 indicates for PRSs of length $L = \{26, 32, 63, 78, 155, 250\}$ the average absolute cross-correlation value $|\bar{R}_{nm}|$ normalized by the autocorrelation value R_{nn}, *i.e.* $|\bar{R}_{nm}|/R_{nn}$, as blue circlets. It is to be noticed that $|\bar{R}_{nm}|/R_{nn}$ decreases with increasing L as outlined by a black-dashed trend-curve; hence, longer identifier sequences exhibit relatively lower cross-correlation values, thus leading to lower interference noise.

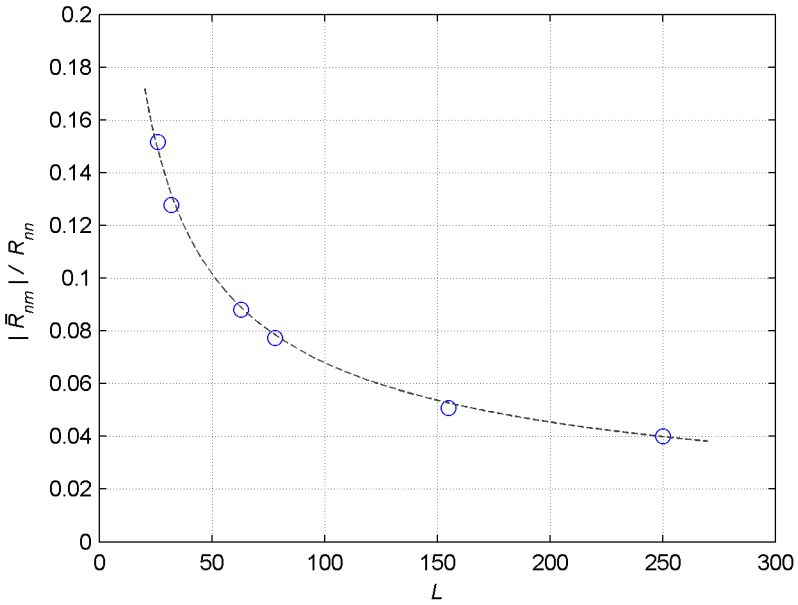

Figure 3.14: Relative average cross-correlation value of PRSs

3.3.3 Channel Estimation using the Pseudo-Inverse

Channel estimation on the forward link happens at the receiver. As outlined above, the non-precoded identifier sequences are used. Straightforwardly from (3.12), the channel matrix can be estimated as

$$\widehat{\mathbf{H}} = \mathbf{Y} \cdot \mathbf{C}^{+}, \tag{3.15}$$

whereas $\mathbf{C}^{+} = \mathbf{C}^{\mathrm{H}} \cdot (\mathbf{C} \cdot \mathbf{C}^{\mathrm{H}})^{-1}$, *i.e.* the Moore-Penrose pseudo-inverse of $\mathbf{C}$ [29, pp. 69-70]. It is to be noticed that the pseudo-inverse of the $N \times L$ matrix $\mathbf{C}$ only exists, if $\mathbf{C}$ consists of linearly independent rows, hence requiring $L \geq N$. A detailed insight on that issue can be found in Appendix A-(b).

To minimize channel estimation errors for contributions from neighbouring as well as distant feeds, a set of orthogonal UWs is desirable. Figure 3.15 visualizes the signal contributions of close and distant feeds: not surprisingly, the two adjacent feeds in the right part of Figure 3.15 mutually interfere more than the distant feed on the left.

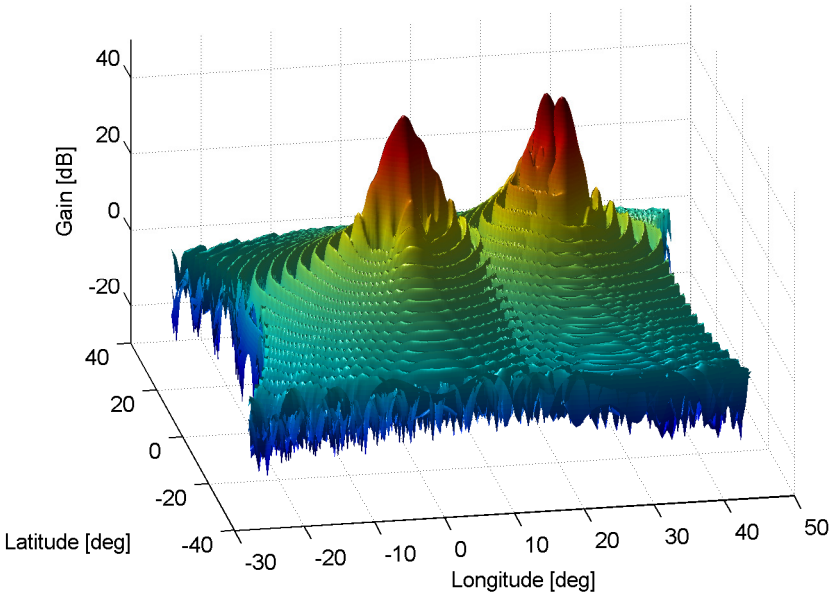

Figure 3.15: Interference pattern for neighbouring and distant feeds

Recalling Figure 3.10, the signal model for user terminal m is

$$\mathbf{y}_m = \mathbf{h}_m \cdot \mathbf{C} + \mathbf{n}_m, \tag{3.16}$$

where $\mathbf{y}_m$ is the received signal vector and $\mathbf{n}_m$ is the complex AWGN vector. While $E[\mathbf{n}_m \cdot \mathbf{n}_m^{\mathrm{H}}] = \sigma_{\mathbf{n}_m}^2$ remains constant, the received signal power of each of the signal components differs, so each component suffers from a different SNR. More specifically, for orthogonal UWs, $\mathbf{C} \cdot \mathbf{C}^{\mathrm{H}} = \mathbf{I}$; assuming equal and normalized emit signal powers, the receive signal powers derive as: $\mathbf{y}_m^{\mathrm{H}} \cdot \mathbf{y}_m = (\mathbf{h}_m \cdot \mathbf{C})^{\mathrm{H}} \cdot (\mathbf{h}_m \cdot \mathbf{C})$. Therefore, $diag(\mathbf{h}_m^{\mathrm{H}} \cdot \mathbf{h}_m) = \left\{|\mathbf{h}_{m,1}|^2, |\mathbf{h}_{m,2}|^2, \dots, |\mathbf{h}_{m,L}|^2\right\}$, so

$$\frac{S_i}{N} = \frac{|\mathbf{h}_{m,i}|^2}{\sigma_{\mathbf{n}_m}^2}. \tag{3.17}$$

For the receive signal vector of user terminal m in (3.16), the channel estimation with pseudo-inverse described in (3.15) becomes

$$\hat{\mathbf{h}}_m = \mathbf{y}_m \cdot \mathbf{C}^{+} = \mathbf{h}_m + \mathbf{e}_m, \tag{3.18}$$

with error vector

$$\mathbf{e}_m = \mathbf{n}_m \cdot \mathbf{C}^{+}. \tag{3.19}$$

3.3.3.1 Orthogonal Identifier Sequences

As introduced above, WH sequences are orthogonal and as such best suited for channel estimation since no interference noise occurs. In this case the Moore-Penrose pseudo-inverse simplifies to $\mathbf{C}^{+} = \mathbf{C}^{\mathrm{H}}$, thus (3.19) becomes $\mathbf{e}_m = \mathbf{n}_m \cdot \mathbf{C}^{\mathrm{H}}$. In more detail, the i-th element of the error vector $\mathbf{e}_m$, *i.e.*

$$e_{m,i} = \sum_{k=1}^{L} n_{m,k} \cdot c_{k,i}^{\mathrm{H}}, \tag{3.20}$$

where $c_{k,i}^{\mathrm{H}}$ denotes the (k,i)-th entry in $\mathbf{C}^{\mathrm{H}}$. Since the elements in $\mathbf{C}$ are given by $c_{k,i} \in \{-1,1\}$, the elements in $\mathbf{C}^{\mathrm{H}}$ are given by $c_{k,i}^{\mathrm{H}} \in \{-1/L, 1/L\}$, so as to satisfy

$\mathbf{C} \cdot \mathbf{C}^{\mathrm{H}} = \mathbf{I}$. Straightforwardly from that and with $E\left[\left|n_{m,k}\right|^2\right] = \sigma_n^2 = N_0/E_s$, the total jitter variance for WH identifier sequences becomes [34]

$$\sigma_{\mathcal{H}}^2 = \sigma_n^2 \cdot \sum_{i=1}^{L} \left|c_{k,i}^{\mathrm{H}}\right|^2 = \frac{1}{L \cdot {}^{E_S}/_{N_0}}. \tag{3.21}$$

In Appendix A-(d) further explanations on (3.21) can be found. The jitter variance in (3.21) refers to the *error vector magnitude* (EVM) of the estimation; resorting to amplitude and phase error instead, the jitter variance for orthogonal identifier sequences can analytically be given as [29, pp. 72-73][22, pp. 189-204]

$$\sigma_o^2 \approx \frac{\sigma_{\mathcal{H}}^2}{2} = \frac{1}{2 \cdot L \cdot {}^{E_S}/_{N_0}}. \tag{3.22}$$

As already mentioned, the DigiSat scenario requires $N = 155$ feed signals to be distinguished; with $L \geq N$, $L = 2^m$, and $m \in \mathbb{N}_0$, the $N \times L$ identifier sequence matrix $\mathbf{C}$ forms as a subset of the $L \times L$ WH matrix, *i.e.*

$$\mathbf{C} = \left[\boldsymbol{\mathcal{H}}_{(ld(L))}\right]_{N \times L}. \tag{3.23}$$

Of course, $L = 256$ is the minimum length that fulfils the DigiSat requirements according to the above mentioned criteria.

Figure 3.16 compares the in (3.22) described analytical relationship with Monte Carlo simulations using the UW set (3.23) with $L = 256$: the red dashed line indicates the theoretical result for both (N)MSE of magnitude and phase, where the former is normalized by $\left|h_{m,k}\right|^2$; the blue circlets and asterisks represent numerical results for the NMSE of the amplitude, denoted as Δ_a, and the MSE of the phase, denoted as Δ_{ph}, of $\hat{h}_{m,k}$, respectively. It is to be observed that for high E_S/N_0, simulation and analytical results match. For low E_S/N_0, *i.e.* < -30 dB, the simulation curve for phase estimates starts to converge to a variance of $\pi^2/3$, since phase estimates become equally distributed between $\pm\pi$.

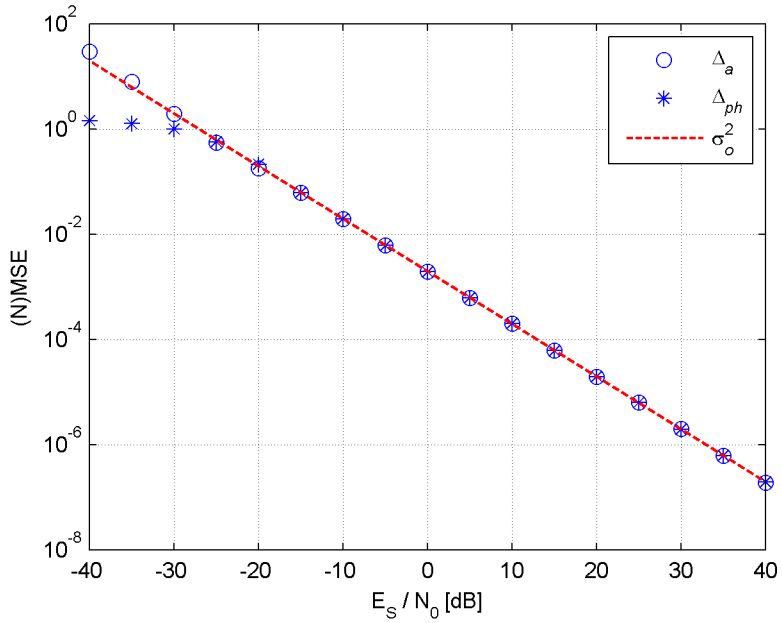

Figure 3.16: Estimation accuracy for orthogonal UWs achieved with the pseudo-inverse

3.3.3.2 Linearly Independent Pseudo-Random Sequences

Linearly independent PRSs of arbitrary length are not bound to length limitations, but $L \geq N$, so they can be sized accordingly to save communication bandwidth. Contrary to orthogonal identifier sequences, linearly independent PRSs introduce interference noise: with $\mathbf{C}^+ = \mathbf{C}^{\mathrm{H}} \cdot (\mathbf{C} \cdot \mathbf{C}^{\mathrm{H}})^{-1}$, $\mathbf{C} \cdot \mathbf{C}^+ = \mathbf{I}$, and (3.19), the estimation error becomes

$$e_{m,i} = \sum_{k=1}^{L} n_{m,k} \cdot c_{k,i}^{+}, \tag{3.24}$$

where $c_{k,i}^{+}$ denotes the (k,i)-th entry in $\mathbf{C}^+$. Again, the noise samples are $\sim \mathcal{N}(0, \sigma_n^2)$ such that the total jitter variance for linearly independent PRSs is expressed by

$$\sigma_{li}^2 = \sigma_n^2 \cdot \sum_{k=1}^{L} \left| c_{k,i}^{+} \right|^2. \tag{3.25}$$

The summation term in (3.25) results in a constant factor, which – in contrast to (3.21) – increases the total jitter variance, hence the noise becomes amplified, caused by the non-orthogonal properties of the PRS. A detailed analysis of (3.25) can be found in Ap-

pendix A-(e); comparing it to Appendix A-(d) explains in detail the difference to orthogonal UWs. Analogous to (3.22) the jitter variance for linearly independent PRSs is half of that for amplitude and phase errors with respect to the EVM.

Figure 3.17 compares the in (3.25) and (3.22) described analytical relationships with Monte Carlo simulations using PRSs of $L = 156$; without loss of generality, the depicted simulations were carried out for a user terminal in cell 48 (see Figure 3.2); the estimation results for the strongest entity in $\mathbf{h}_m$ are illustrated in Figure 3.17. The analytically predicted jitter variance for linear independent sequences σ_{li}^2, plotted as cyan dashed line, matches the simulation results for amplitude (blue circlets) and phase (blue asterisks) in the higher E_S/N_0 range, *i.e.* $E_S/N_0 > -10\,dB$. Below that, analogous to the orthogonal case, the phase estimations become more and more equally distributed between $\pm\pi$ resulting in a flattening of the curve. Additionally, the theoretical performance achieved with orthogonal codes ($L = 156$) is indicated by σ_o^2 as red dashed line. With respect to that, it is clear that PRSs obviously cause a tremendous degradation in the achievable performance denoted as error amplification.

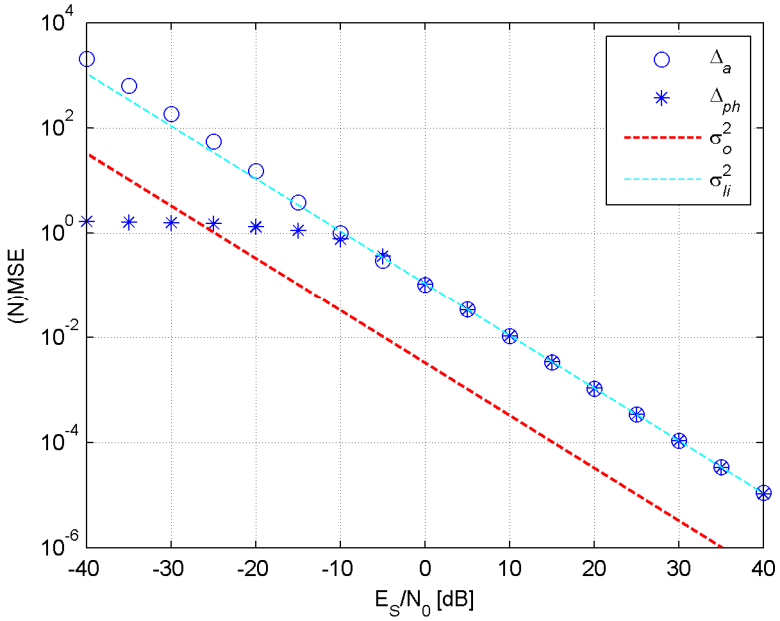

Figure 3.17: Estimation accuracy for PRS achieved with the pseudo-inverse

Figure 3.18 and Figure 3.19 indicate the estimation accuracy achievable with linearly independent PRS in terms of jitter variance (colour coded according to the scheme on the right in Figure 3.18) of the amplitude for the DigiSat scenario. Both plots stem from the same simulation data. The 155 linearly independent UWs ($E_S/N_0 = 40\,dB$, $L = 156$) were assigned to the feeds prior to simulations. It is to be noticed that, regarding to the location, only the strongest component in **H** is plotted. A regular pattern correlat-

ing with feed-footprints provided in Figure 3.3 can be observed in Figure 3.18. According to (3.25) the jitter variance only depends on E_S/N_0 and the PRSs. Figure 3.19 shows that the estimation accuracy in terms of jitter variance varies in the range of approximately two orders of magnitude throughout the scenario. Finally, the green surface in Figure 3.19 indicates the achievable performance with assumed orthogonal codes. Obviously the above identified error amplification highly degrades the performance.

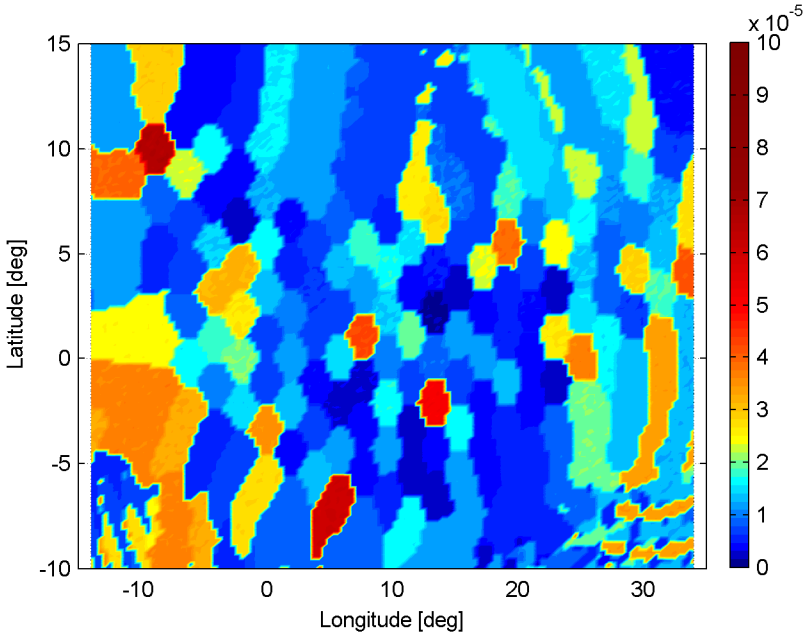

Figure 3.18: Location-related normalized jitter variance using the pseudo-inverse

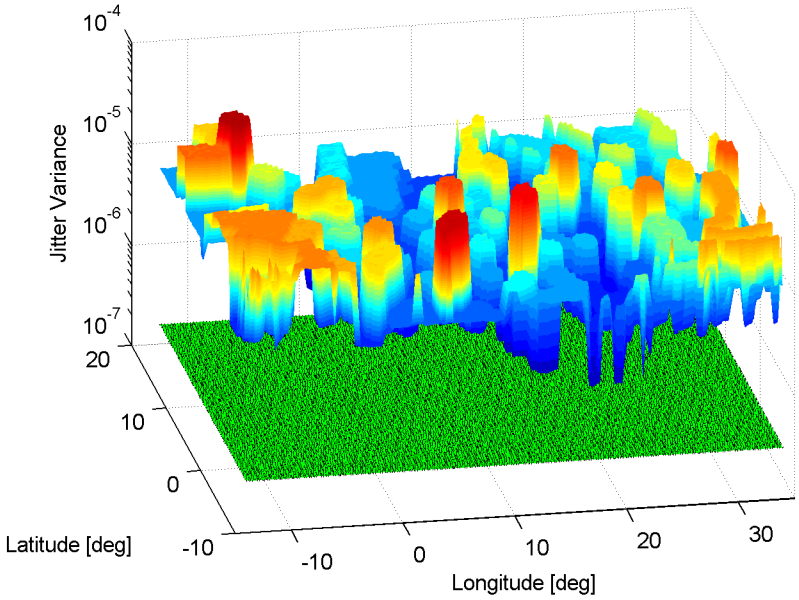

Figure 3.19: 3D normalized jitter variance pattern using the pseudo-inverse

3.3.4 Channel Estimation with Correlation

Analogous to Section 3.3.3, channel estimation with correlation is done on the forward link using the non-precoded UWs at the receiver. The estimations are achieved using

$$\widehat{\mathbf{H}} = \mathbf{Y} \cdot \mathbf{C}^{\mathrm{H}}, \tag{3.26}$$

where $\mathbf{C}^{\mathrm{H}}$ denotes the Hermitian of the identifier sequence matrix. Advantageous with respect to Section 3.3.3 is that UW sequences may be linearly dependent, *i.e.* $L < N$. This potentially helps to reduce the total communications overhead and increases the spectral efficiency.

Of course, the signal model for user terminal m is still given by (3.16); hence each signal component suffers from a different SNR throughout the estimation. For the receive signal vector of user terminal m in (3.16), the channel estimation with correlation, described in (3.26), derives to

$$\hat{\mathbf{h}}_m = \mathbf{y}_m \cdot \mathbf{C}^{\mathrm{H}} = \mathbf{h}_m + \mathbf{e}_m, \tag{3.27}$$

with error vector

$$\mathbf{e}_m = \mathbf{n}_m \cdot \mathbf{C}^{\mathrm{H}}. \tag{3.28}$$

From that the analytical jitter variance is equal to (3.21). Using non-orthogonal UWs for correlation-based estimations exhibits a jitter floor for amplitude estimates which is caused by interference (location-dependent). It can be modelled for the m^{th} user terminal as

$$\sigma_{jf}^2 = \left| \sum_{k \neq m} \sum_{i=1}^{L} h_{m,i} \cdot c_{m,i} \cdot c_{k,i}^* \right|^2, \tag{3.29}$$

where $c_{k,i}^*$ is the conjugate complex of the (k, i)-th entry of matrix $\mathbf{C}$. It is to be noticed that the jitter floor arises for amplitude estimates only. All feeds transmit their uniquely assigned identifier sequences symbol-synchronously on the same physical path. Thus all

emitted signals encounter the same attenuation and time-shifting. Considering that, it is obvious that the correlation process does not affect the phase, thus the phase estimates do not suffer from a jitter floor (see Figure 3.20).

Since correlation procedures are typically applied to recover symbol timing, symbol timing recovery and channel estimation could be jointly implemented in a practical design.

3.3.4.1 Orthogonal Identifier Sequences

As already mentioned in Section 3.3.3, the Moore-Penrose pseudo-inverse leads to $\mathbf{C}^{+} = \mathbf{C}^{\mathrm{H}}$ for orthogonal identifier sequences, since $\mathbf{C} \cdot \mathbf{C}^{\mathrm{H}} = \mathbf{I}$. Hence channel estimations with pseudo-inverse and with correlation are identical. Consequently, results and findings presented in 3.3.3.1 also apply here. Because orthogonal UWs do not produce interference, no jitter floor is observed.

3.3.4.2 Pseudo-Random Sequences

PRSs benefit from their ability to be of any length, but contrary to estimations with pseudo-inverse they do not require to be linearly independent for correlations. Since here $\mathbf{C} \cdot \mathbf{C}^{\mathrm{H}} \neq \mathbf{I}$, it is obvious that interference plays an important role. According to (3.17), all signal components encounter the same noise power at the receiver, but not the same interference power. As outlined before, the achievable accuracy for correlation based estimations is bounded by (3.21) and (3.29), thus according to Figure 3.14, the length of the identifier sequences is a major driver for the achievable performance.

3.3.4.2.1 Linearly Dependent versus Independent Sequences

Figure 3.20 compares analytical results from (3.22) indicated as red ($L = 78$) and black ($L = 156$) dashed lines, with numerical results for both, a linearly independent and a linearly dependent set of UWs at a user terminal in cell 48. The linearly independent PRSs are of length $L = 156$ and are plotted in blue, whereas the linearly dependent PRSs of length $L = 78$ are drawn in magenta: the circlets and asterisks indicate simulation results for amplitude and phase, respectively, whereas the horizontal dashed-dotted line indicates the analytical jitter floor from (3.29). It can be seen, in the low E_S/N_0 region, the jitter variance for phase estimates converges to $\pi^2/3$, because the estimates become more and more equally distributed between $\pm\pi$; in the medium E_S/N_0 region, both amplitude and phase follow the analytically predicted curves, but in the higher E_S/N_0 region the amplitude suffers from a jitter floor.

Surprisingly, the jitter floor in Figure 3.20 is higher for the longer sequences, which on the first sight is in contrast to what can be expected from Figure 3.14. However, it is to

be recalled that the jitter floor (3.29) is location-dependent. Since the identifier sequences are distributed to the feeds on a random basis prior to simulations (and not in an optimized manner), it happens that longer identifier sequences my cause locally more interference than shorter ones.

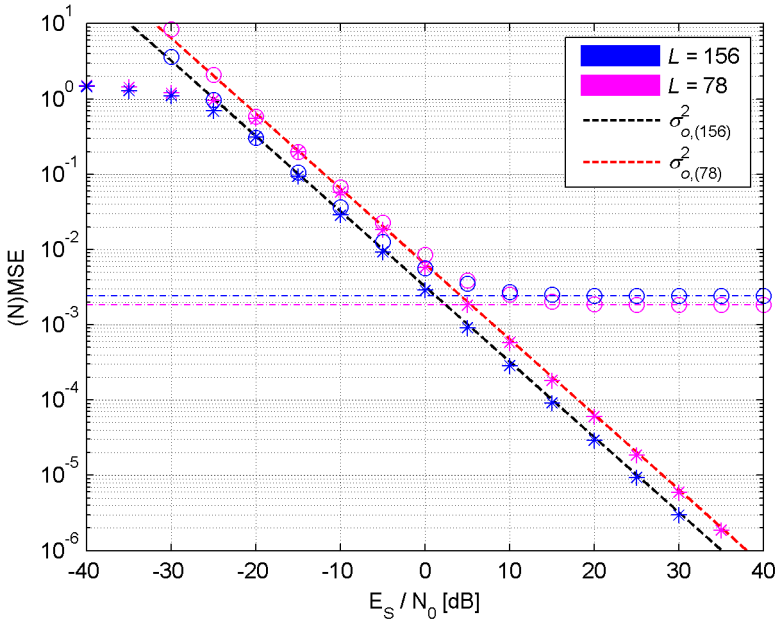

Figure 3.20: Performance comparison for linearly dependent and independent PRSs

Figure 3.21 and Figure 3.22 indicate the achievable accuracy in terms of normalized jitter variance of the amplitude (colour coded according to the scheme on the right in Figure 3.21) for the DigiSat scenario using correlation and a set of linearly independent PRSs. Both plots stem from the same simulation carried out at $E_S/N_0 = 40\ dB$ to investigate the effects of the jitter floor; 155 linearly independent UWs ($L = 156$) were assigned to the feeds prior to simulations. Regarding the location, only the strongest component in **H** is plotted. No regular pattern can be observed. Figure 3.22 furthermore shows that the jitter variance varies over several orders of magnitude throughout the scenario. The green surface indicates the theoretically achievable performance with orthogonal codes. Obviously, the observed error floor highly degrades the performance and additionally varies significantly throughout the scenario.

The observations as seen from Figure 3.21 and Figure 3.22 hold also true for linearly dependent UWs thus encourage omitting further illustrations.

Obviously, the jitter floor defines the achievable estimation accuracy, which in consequence drives the potential throughput gain by precoding. Hence, location-dependent erroneous estimations lead to higher interference on the link which detrimentally affects the achievable net data throughput. Thus appropriate fairness policies need to be applied

mitigating this location-dependent effect. An attempt regarding that issue can be found in Subsection 3.3.4.2.3.

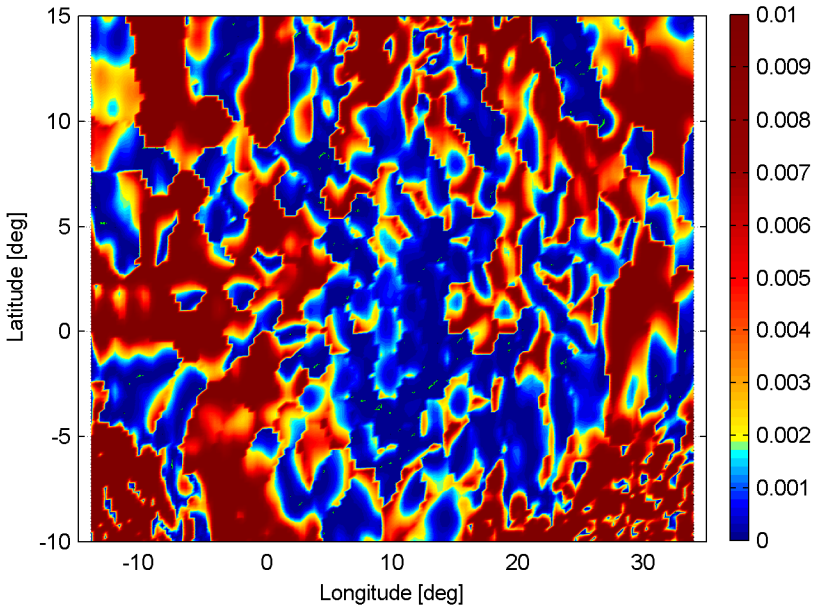

Figure 3.21: Location-related normalized jitter variance using correlation (L = 156)

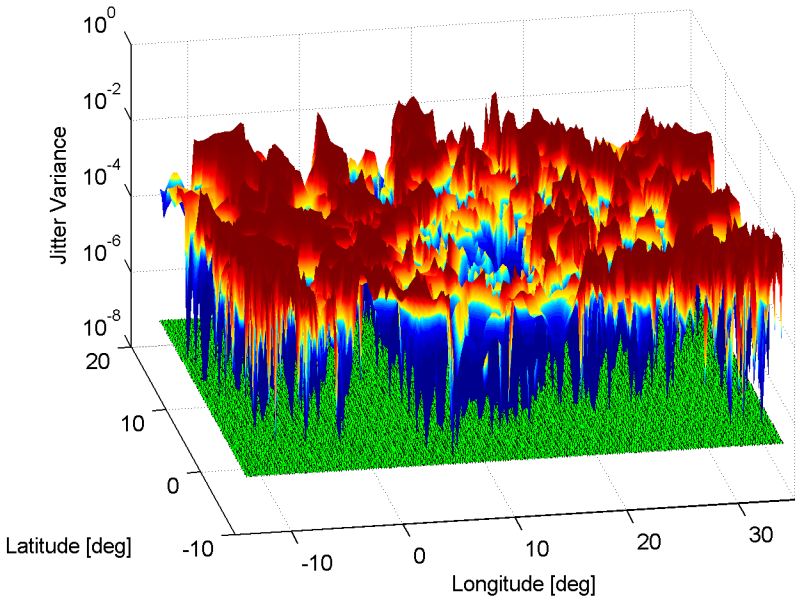

Figure 3.22: 3D normalized jitter variance pattern using correlation (L = 156)

3.3.4.2.2 Pseudo-Random versus Kasami and Random Sequences

In order to assess the potential of differently generated identifier sets, a comparison of PRSs, Kasami and random sequences is detailed in the sequel. Figure 3.23 depicts analytical and simulation results for UWs of $L = 63$. Three different UW sequences are to be distinguished: PRS (blue), a large set of Kasami sequences (magenta) and a set of randomly generated binary sequences (green). The results for NMSE of amplitude and MSE of phase estimates are depicted as accordingly coloured circlets and asterisks. The horizontal dashed lines indicate the respective jitter floors. The red dashed line indicates the jitter variance according to (3.22). Again simulations were carried out for a user terminal in cell 48: The three different sets of identifier sequences exhibit equal performance in the lower E_S/N_0 region, but suffer from different jitter floors in the higher E_S/N_0 region. As already mentioned, the jitter floor is location-dependent, thus the relation between the observed jitter floor levels in Figure 3.23 holds only punctually true.

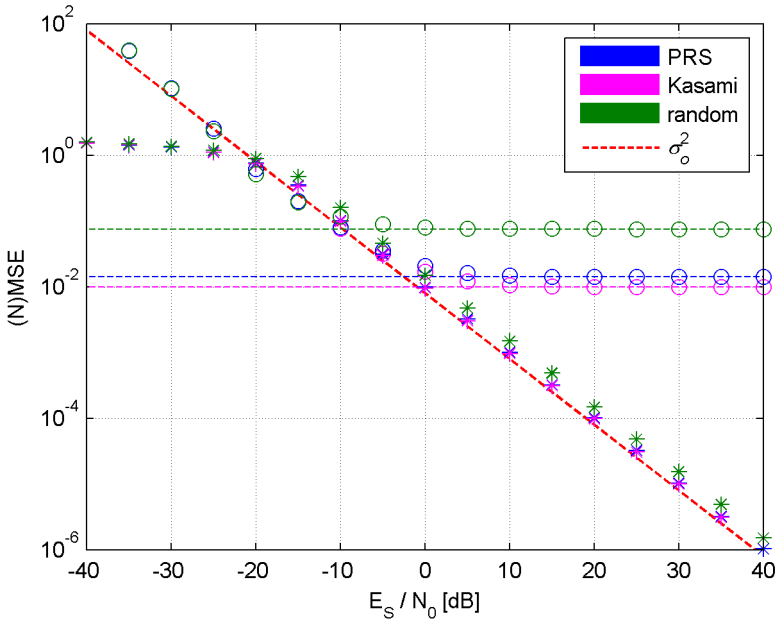

Figure 3.23: Performance comparison of linearly dependent sequences with correlation (L = 63)

Figure 3.24 depicts the best performing identifier sequences ($L = 63$) at an $E_S/N_0 = 40\ dB$ according to the location in the DigiSat scenario, using the same colour coding as Figure 3.23. Obviously, PRSs and Kasami identifier sequences dominate, as could be expected from Figure 3.23 and Figure 3.13. A further prove for that can be found in Figure 3.25. It compares the achievable mean jitter floor of the identifier sequences investigated in the DigiSat framework. The blue, magenta and green circlets indicate simulation results for PRSs, a large set of Kasami sequences, and random sequences, respectively. Not surprisingly, with increasing length of the identifier sequence the mean

jitter floor $\overline{\sigma_{jf}^2}$ decreases, indicated by a grey dashed trend curve. For the sake of completeness, the actual values as depicted in Figure 3.25 are provided in Appendix A-(f) in Table A - 2.

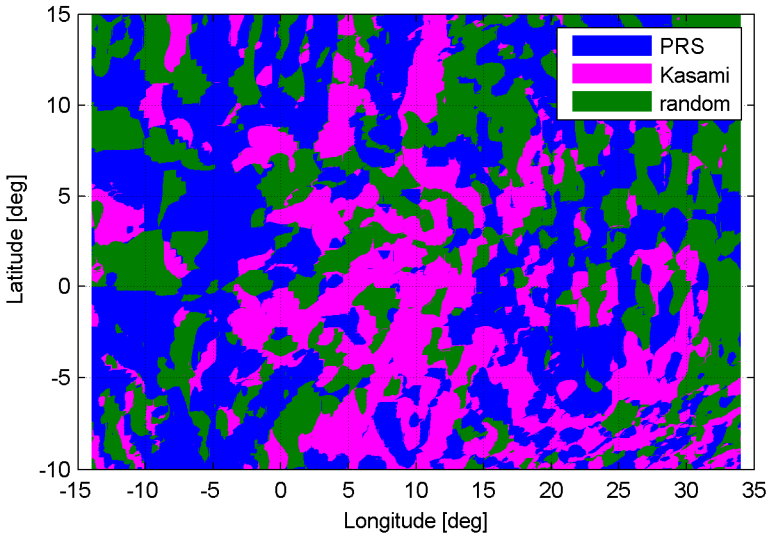

Figure 3.24: Location-dependent performance of linearly dependent identifier sequences (L = 63)

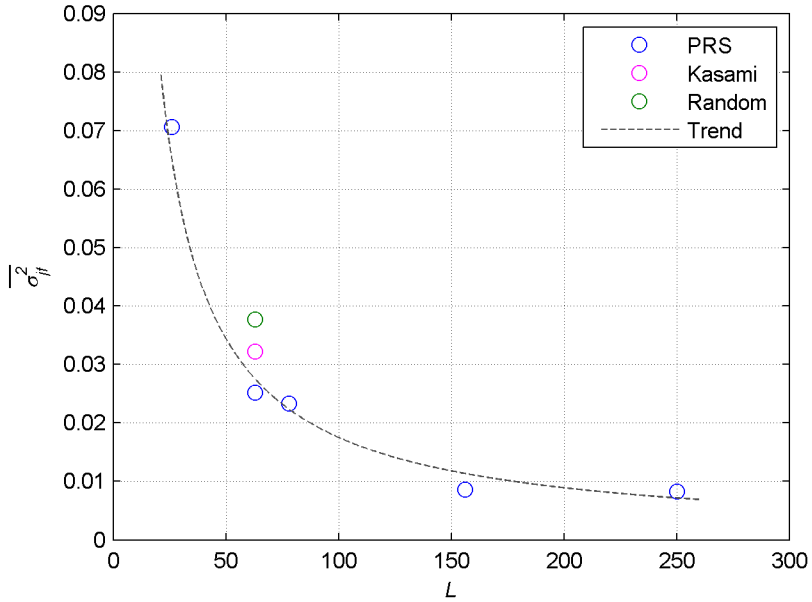

Figure 3.25: Average jitter performance of different identifier sequences versus length

3.3.4.2.3 Identifier Sequence Hopping

As already detailed previously, the achievable estimation accuracy is highly location-dependent. In order to alleviate continuously worse performance on a site, a hopping scheme for identifier sequences could be envisaged, thus each feed swaps its identifier sequence at each frame. Only the gateway must be aware of the applied scheme, thus no additional requirements to the user terminals apply. However, for demonstration purposes a set of linearly independent PRSs ($L = 156$) was used and simulated at $E_S/N_0 = 40\ dB$. In more detail, five mappings, *i.e.* five specific UW-to-feed-mappings on a random basis, were chosen prior to simulations; all five mappings stem from the same UW alphabet, but assign the UW sequences differently to the feeds. Figure 3.26 depicts qualitatively the best performing mapping with respect to the location; each of the five mappings is represented by a distinct colour: blue, magenta, green, orange and grey. Not surprisingly, with regard to the location different mappings are performing best.

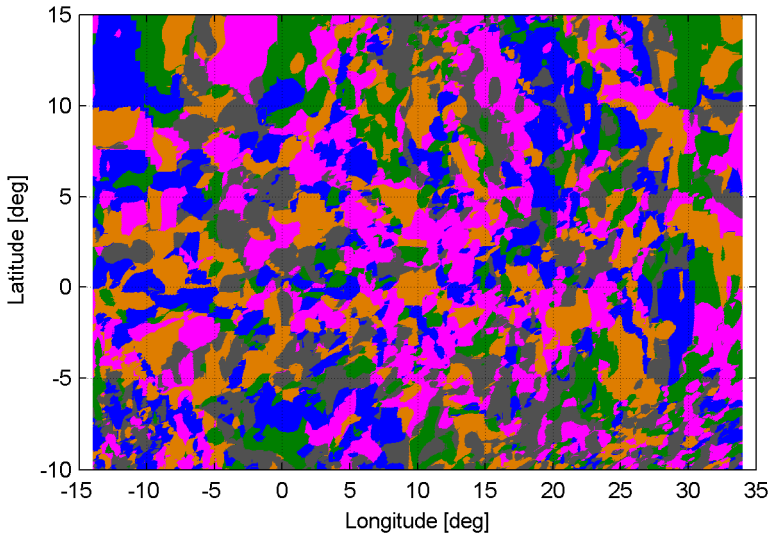

Figure 3.26: Correlation based and location-dependent performance using UW hopping (L = 156)

Additionally, Figure 3.27 depicts the best achievable accuracy in terms of normalized jitter variance using the identifier sequence ($L = 156$) hopping as described above at $E_S/N_0 = 40\ dB$; the jitter variance is colour coded according to the scheme on the right. Comparing Figure 3.27 and Figure 3.21 it becomes obvious that the identifier sequence hopping scheme can significantly improve the achievable performance which as a consequence supports the precoding, hence results in higher system throughputs.

It shall be noticed that a multitude of user terminals in each cell accessed by TDMA and a gateway aware of each user terminal's location could apply specific UW-to-feed-

mappings to mitigate location-dependent jitter floor effects. This would require the gateway to hold a number of optimized UW-to-feed-mappings in stock and to address specific groups of user terminals located advantageous with respect to the mapping scheme.

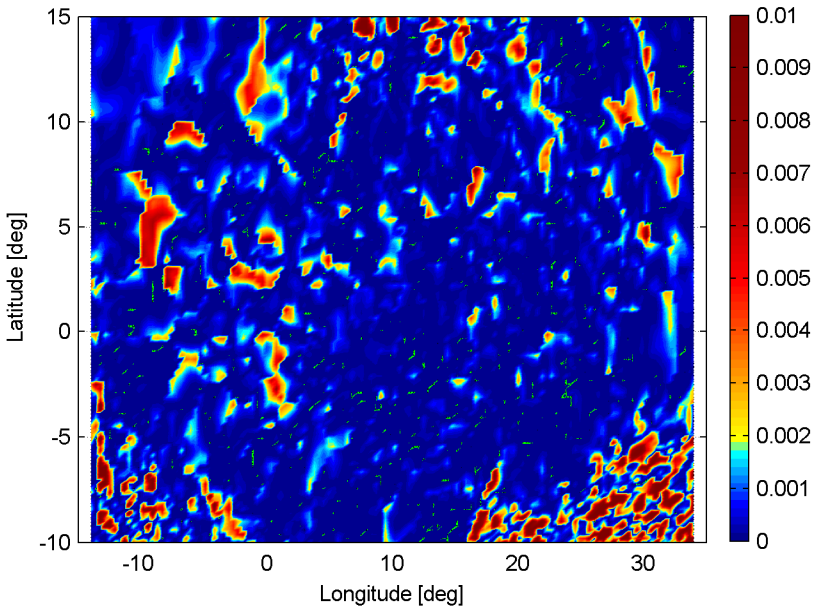

Figure 3.27: Correlation based and location-related performance using UW hopping (L = 156)

3.3.5 Impact of Frequency Reuse on Channel Estimation

As previously outlined and detailed by simulation results, full frequency reuse causes significant amounts of interference, whereas close cells account for more interferer noise than distant ones do (see Figure 3.28). Hence, using different frequencies (bands) in adjacent beams/cells, helps to reduce mutual interference significantly at the expense of system bandwidth. With respect to that, the question to be answered is how much channel estimation benefits from frequency reuse strategies in terms of estimation accuracy.

In Figure 3.1 a scenario with four frequencies indicated by an appropriately selected colour code was depicted. Obviously, only cells of the same colour are affected by mutual interference (neglecting out-of-band transmission). Thus, by investigating Figure 3.28, it is clear that operating close cells on different frequency bands can lower the interference noise significantly. However, beamforming is achieved by sending various copies of the signal differently adjusted in amplitude and phase through a set of antenna elements, which in the DigiSat case are represented by 155 feeds. A detailed analysis of the beam forming concept reveals that typically 20 feeds are used to form a single beam

(see Figure 3.4). Hence all 155 feeds are needed to form the beams belonging to the same frequency band, thus the same amount of estimates needs to be computed as in case of full frequency reuse. In other words, frequency reuse does not relax channel estimation challenges.

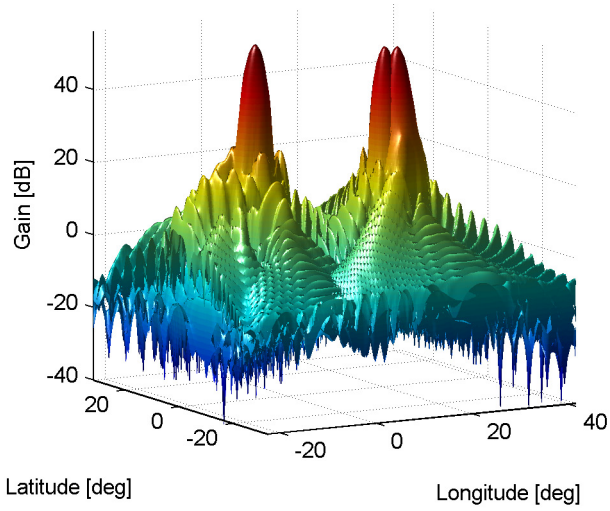

Figure 3.28: Interference pattern for neighbouring and distant beams

3.3.6 Influence of Frequency Errors

Up to this point frequency errors were not considered for the forward link. This does not hold true for practical cases. Hence it is of interest to investigate the influence of residual frequency errors on the performance of the CSI estimation.

The theoretically achievable performance for carrier frequency recovery is limited for AWGN channels by the CRLB [55]. *Normalized* to the symbol period, the latter can be written for frequency estimates as

$$NCRLB(\Delta fT) = \frac{3}{2\pi^2} \cdot \frac{1}{L \cdot (L^2 - 1) \cdot {}^{E_S}/_{N_0}}. \tag{3.30}$$

Inspecting (3.30) shows that the achievable performance of carrier frequency recovery is to a good approximation proportional to $1/L^3$, thus the length of the training sequence is of paramount importance for the achievable performance.

For simulations a normalized frequency error $|\Delta fT| \leq 0.05$ is used; frequency estimation is done using the algorithm proposed by *Rife* and *Boorstyn* (RB) in [56] with a zero padding factor of 4.

Figure 3.29 depicts the frequency estimation performance in terms of NMSE for the RB frequency estimator on the MIMO-BC at three different lengths of UWs, namely $L = \{78, 156, 256\}$ colour coded in green, red, and blue, respectively. Simulation results are depicted as circlets and the pertaining NCRLBs are indicated as dashed lines, appropriately coloured. The results show the strongest signal component in user terminal 48. In the higher SNR region saturation effects can be observed which basically stems from MAI and the finite resolution of the algorithm. In the lower SNR region deviations from the NCRLBs can be observed which are intrinsic to the RB algorithm [56]. Surprisingly the sequence with length $L = 256$ performs worse in the transition region. One explanation for this behaviour is that in case of a frequency error Hadamard sequences lose their orthogonal properties.

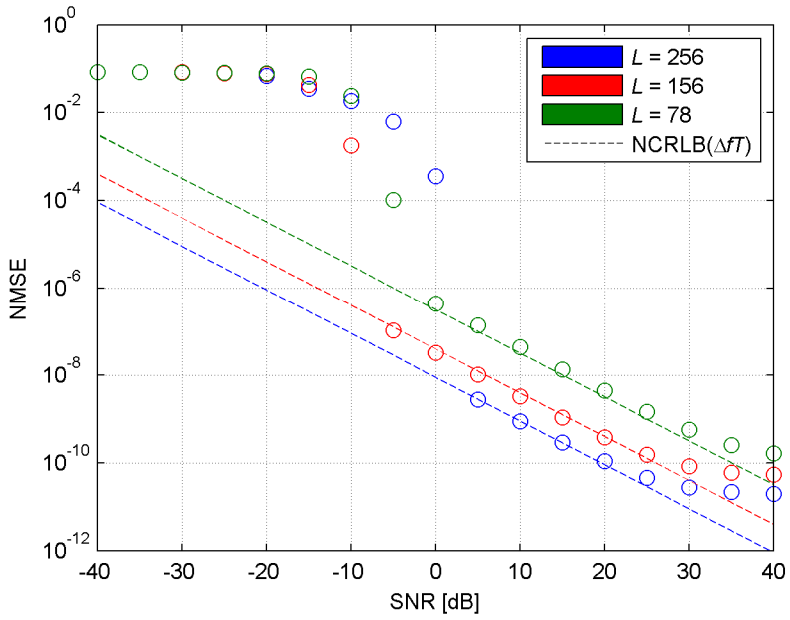

Figure 3.29: Performance of frequency error correction on the forward link

Subsequent figures depict the influence of residual frequency errors on the performance of channel estimation on the forward link. The figure of merit to be investigated is the amplitude of the channel matrix of the strongest impinging feed signal.

Figure 3.30 compares at an $\Delta fT = 0.05$ in a) the analytical relationship described in (3.22) with Monte Carlo simulations using the UW set (3.23) with $L = 256$: the red dashed line indicates the theoretical result for the NMSE of the amplitude and the blue circlets indicate the numerical results for the NMSE of the amplitude, denoted as $\Delta_a^{\sim}$. It

is to be observed for a wide E_S/N_0 range that simulation results and analytical results match. For very low E_S/N_0, *i.e.* < -30 dB, the simulation results deviate from the theoretical bound because orthogonality cannot anymore be maintained due to too large residual frequency errors. In b) the analytical relationships described in (3.22) and (3.25) are compared to Monte Carlo simulations using quasi orthogonal PRS with $L = 156$: the red dashed line represents theoretical results from (3.22) indicating results achievable with orthogonal codes, whereas the cyan dashed line from (3.25) represents the analytical results pertinent to error amplification which are inherent to estimations using the pseudo-inverse. The blue circlets represent the simulation results for the amplitude. By close inspection of the simulation results in b) and in comparison with Figure 3.17 no significant degradations can be observed.

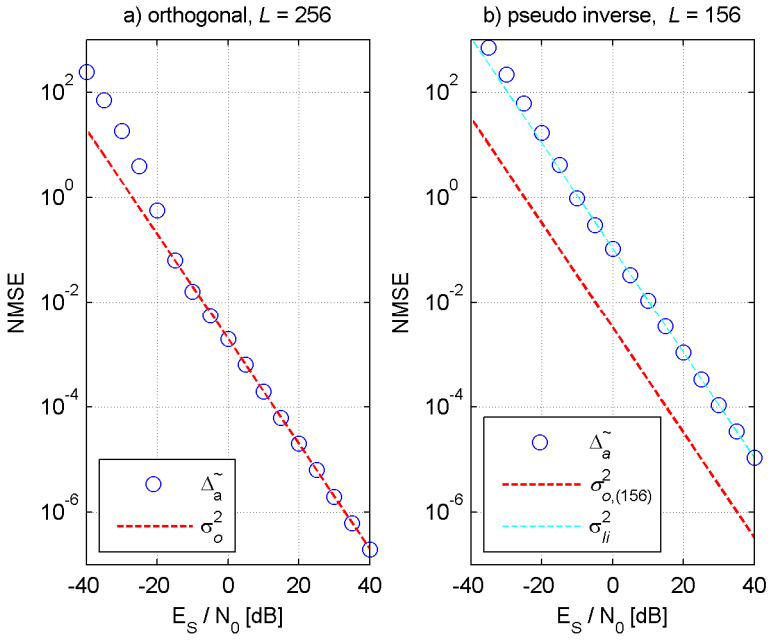

Figure 3.30: Performance of orthogonal and PRS identifier sequences with frequency errors

Figure 3.31 compares the analytical relationships described in (3.22) (red dashed line) and in (3.29) (blue dot-dashed line) with Monte Carlo simulations (blue circlets) using PRSs of $L = 156$. The depicted results were carried out using correlations and represent the NMSE of the amplitude of the strongest signal component in user terminal 48. In the range from $E_S/N_0 > 0\ dB$ a jitter floor is encountered which for negligible frequency errors is described in (3.29). At $E_S/N_0 < -15\ dB$ the simulations deviate from the analytical bound because of large residual frequency errors.

The results, depicted in Figure 3.29, Figure 3.30 and Figure 3.31, could be verified in [57].

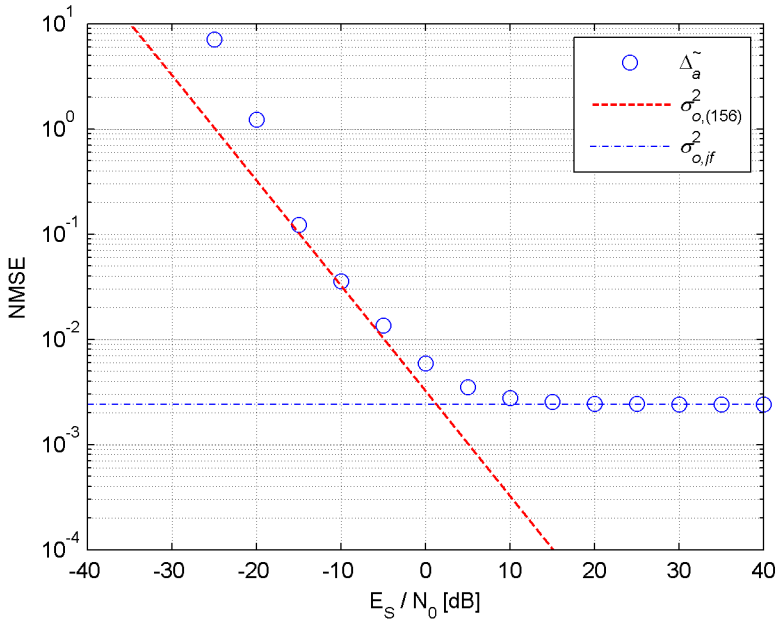

Figure 3.31: Performance of PRS identifier sequences with frequency errors using correlation

3.4 Channel Estimation on the Return Link

In contrast to the forward link, the return link, *i.e.* the link between user terminals, satellite, and gateway, as visualized in Figure 3.32, cannot be regarded as symbol-synchronous mainly because the user terminals are differently located resulting in different propagation conditions. However, it may be assumed that all occurring deviations can be kept small, such that user terminal signals arrive at the satellite within a guard-time of a few symbol periods. Thus the return link is a frame-synchronous memory-less MIMO-MAC.

Three user terminals hosted by their respective cells are exemplified in Figure 3.32. The cells are formed by an AFR antenna with beamforming, as described in Sections 3.2.1 and 3.2.2. Analogously to the forward link, also the return link suffers from significant interference in the DigiSat scenario due to full frequency reuse for all served cells. Hence for 100 simultaneously served users, as outlined for the DigiSat scenario, 99 signals are interferers to a single user signal. As introduced in Sections 3.2.1 and 3.2.4, (joint) beamforming and MUD strategies can mitigate interference effects on the return link but require accurate determination of the CSI and timing. Again, adequate and accurate channel estimation is pivotal.

The subsequent paragraphs elaborate on channel estimation on the return link. In Section 3.4.1 the signal model is presented, Section 3.4.2 explains the choice and construc-

tion of identifier sequences, in Section 3.4.3 channel estimation is outlined based on correlation and SIC, theoretical bounds, simulation results, and analyses are provided as well.

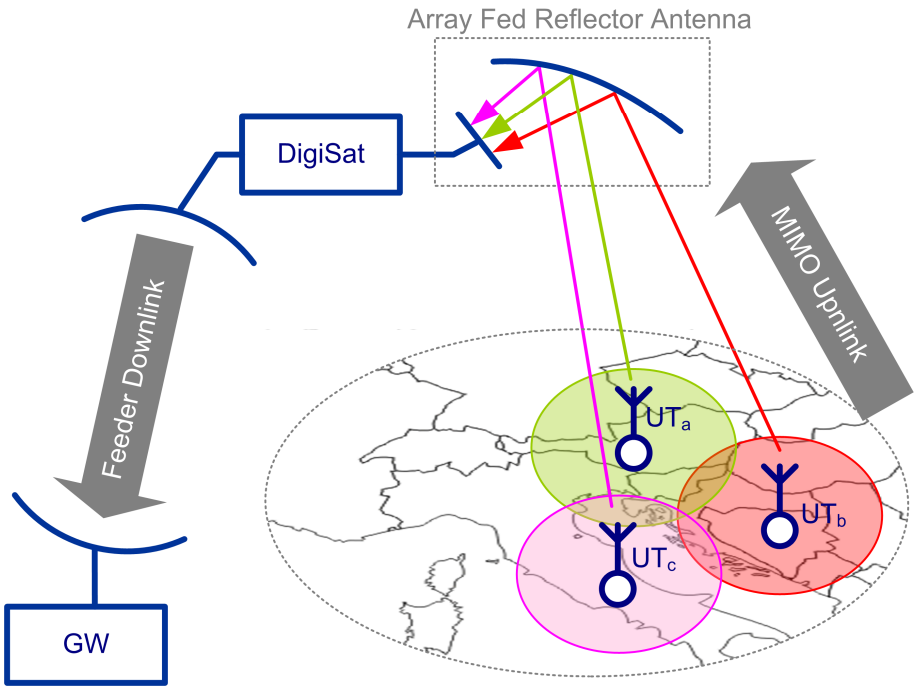

Figure 3.32: DigiSat return link architecture with three outlined cells[6]

It is to be noticed that all return link simulations assume an ideal recovery of the carrier frequency beforehand.

3.4.1 The Signal Model

DigiSat envisages serving $K = 100$ user terminals simultaneously on the return link, *i.e.* one user terminal per beam/cell. Analogous to the forward link, the 100 beams/cells of the return link (see Figure 3.2) are generated by $N = 155$ feeds (Figure 3.3) and apply full frequency reuse. Suitable access schemes are required allowing for more than a single user terminal per cell, which for the specific case is provided by TDMA. Therefore communications on the return link must be synchronized using a frame-synchronous transmission strategy guaranteeing an arrival of the transmitted user packets at the satellite within a predefined guard-time. Figure 3.33 a) exemplifies this approach with three colour-coded user terminals. Figure 3.33 b) depicts the signal components representing

[6] The map depicted in Figure 3.32 is used and modified from source: http://d-maps.com/carte.php?lib=europe_map&num_car=2233&lang=en (2011-09-27).

the contributions of the user signals amplified by the appropriate feed gain which specifically points to the direction of signal arrival. The signal components are furthermore shifted in time and phase according to the signal path between the respective user terminal and the feed.

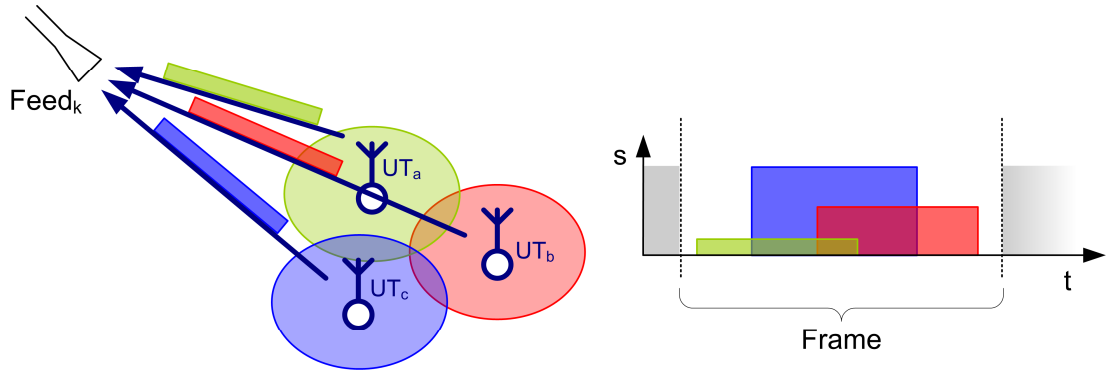

a) b)

Figure 3.33: Frame-synchronous transmission strategy on the return link

The baseband signal related to the i-th user terminal can be modelled as

$$x_i(t) = e^{j(2\pi\Delta f_i t+\theta_i)} \cdot s(t-\tau_i) * h(t), \tag{3.31}$$

where $s(t-\tau_i) * h(t)$ is the convolution of the transmitted and by τ_i delayed sequence, *i.e.* $s(t-\tau_i)$, with the matched filter[7] response; the exponential term accounts for frequency (Δf_i) and phase (θ_i) mismatch between transmitter (user) and receiver (satellite).

It is to be recognized that the channel is assumed to be time-invariant throughout one frame. Furthermore it is assumed that each user terminal controls its emitted signal power such that differences of incident power flux densities at the satellite are negligible, hence equal (or specifically adjustable) power flux densities are obtained obeying a defined *signal-to-interference ratio* (SIR).

With x_i being a time instance of (3.31), the vector for K user terminals is given by $\mathbf{x} = (x_1, x_2, \ldots, x_K)^{\mathrm{T}}$. Disregarding the subscripts and superscripts indicating the feed-space and the return link, the channel matrix is denoted as $\mathbf{H}$ ($\widehat{=}\ \mathbf{H}_f^{RL}$) in the sequel. The signal model can be written similarly to the forward link as

[7] It is to be noticed that the raised-cosine filter is implemented as two RRC filters, equally split between transmitter and receiver.

$$\mathbf{y} = \mathbf{H} \cdot \mathbf{x} + \mathbf{w}, \tag{3.32}$$

with $\mathbf{y} = (y_1, y_2, \dots, y_N)^{\mathrm{T}}$ being the received signal vector, and $\mathbf{w}$ representing the root raised-cosine filtered Gaussian noise vector of zero mean and variance σ_w^2. It is to be noticed, the $(N \times K)$ channel matrix $\mathbf{H}$ represents a memory-less MIMO-MAC. In contrast to the forward link, the channel matrix on the return link is given as $\mathbf{H} = \mathbf{D}^{RL} \cdot \mathbf{G}^{RL} \cdot \mathbf{W}^{RL}$, where [30, p. 11]

- $\mathbf{W}^{RL}$ is the $K \times K$ diagonal fading matrix on the uplink; the entry (m, m) accounts for the gain of user terminal m,
- $\mathbf{G}^{RL}$ represents the $N \times K$ feeder matrix whose entries (m, n) represent the gain between user link m and antenna feed n, and
- $\mathbf{D}^{RL}$ is an $N \times N$ matrix accounting for effects on the feeder downlink and in the on-board repeater chain. As mentioned above $\mathbf{D}^{FL}$ may be regarded as ideal because of the envisaged hybrid space ground processing concept.

Figure 3.34 depicts the framing on the physical layer for the i-th user terminal. A data package consisting of an identifier sequence $\mathbf{c}_i$ of length L followed by L_X payload symbols incorporating user data and properly interspersed pilots[8] is transmitted. Each cell is distinguished by a uniquely assigned identifier sequence, denoted as UW. The data package of duration T_D must arrive at the satellite within a given time frame, *i.e.* T_F, $T_F > T_D$. The transmission must be synchronized such that

$$\tau_i = t_{D0} - t_{F0}, \qquad 0 \leq \tau_i \leq T_F - T_D, \tag{3.33}$$

where t_{F0} and t_{D0} represent the start of frame and the start of the data package arriving at the satellite, respectively. Thus τ_i is the resulting delay in-between.

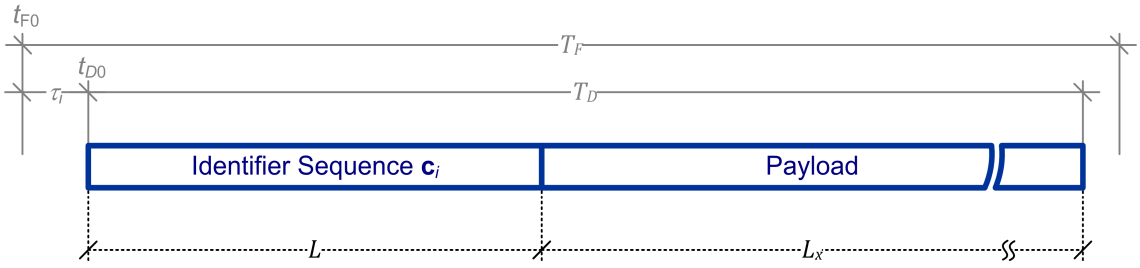

Figure 3.34: Physical layer framing for the DigiSat MIMO-MAC

[8] Pilot symbols are required for tracking the CSI throughout the frame in order to maintain synchronization.

The maximum delay between t_{F0} and t_{D0} is denoted as guard-time, which in subsequent sections is provided normalized by the symbol period in numbers of symbols.

3.4.2 The Choice and Construction of Identifier Sequences

Albeit detailed considerations about the choice and construction of identifier sequences for the forward link were discussed in Section 3.3.2, additional considerations arise for the frame-synchronous, but not symbol-synchronous return link. From Section 3.3 it is known that orthogonal sequences behave ideally with respect to MAI, thus orthogonality is a desired property of UWs, because it directly affects the achievable performance of channel estimation. WH sequences lose their orthogonal properties on the return link, thus resorting to quasi-orthogonal PRSs with good auto-correlation and cross-correlation properties is required. Gold and Kasami sequences are well known in that respect [58], but are limited to sequences of certain length [51][52].

Again, identifier sequences of arbitrary length, which is a desirable property for UWs on the return link, require resorting to PRSs. To approach orthogonality, low cross-correlations amongst UWs and their time-shifted versions are desired. Furthermore, low autocorrelation values are necessary to ease recovery of timing and synchronization. To generate sequences with the outlined properties an appropriate brute-force search algorithm was applied.

3.4.3 Channel Estimation using Correlation and SIC

Since transmission cannot be regarded as symbol-synchronous on the return link, channel estimation cannot be carried out with the pseudo-inverse. Correlations, however, can tackle that issue. Amplitude and phase as well as symbol timing can jointly be established. Two basic principles building on correlations will be explored and compared, namely the correlation method and the SIC method. Additionally, theoretical limits will be introduced, followed by simulation results covering different aspects of channel estimation on the return link.

3.4.3.1 Correlation

Correlation is a relatively simple method able to jointly estimate timing, amplitude, and phase for each signal component independently by using a set of training sequences. As already known from the forward link, magnitude estimations with correlations suffer from a jitter floor at medium-to-high SNR regions. This is caused by the non-orthogonal properties of the training sequences which are of concern on the return link too. On the

forward link the phase did not exhibit a jitter floor due to the symbol synchronicity of the link; this beneficial behaviour cannot be expected on the return link.

After the receiver matched filter of feed n the resulting oversampled signal vector is $\mathbf{y}_n$; the correlation with the k-th oversampled identifier sequence resolves to

$$R_{y_n c_k}[m] = \frac{1}{L} \cdot \sum_{i=0}^{L-1} y_n[M_O \cdot i + m] \cdot c_k^*[i], \tag{3.34}$$

where L denotes the length of the identifier sequence, M_O is the oversampling factor, $M_O \in \mathbb{N}$, and $c_k^*[i]$ is the i-th conjugate complex symbol of the k-th UW. It is to be noticed that with $\varepsilon_{\max}$ being the maximum normalized delay (in symbols), only the first $m \leq M_O \cdot \varepsilon_{\max}$ realizations of $R_{y_n c_k}[m]$ need to be evaluated. It is furthermore to be noticed that (3.34) inherently assumes oversampled identifier sequences according to its implementation. Additional symbols are interspersed by oversampling in the UWs which are zero in amplitude and phase.

A coarse timing estimation for the k-th signal component of the n-th feed signal can be done according to

$$\hat{\varepsilon}_{n,k} = \arg\max_m \left(R_{y_n c_k}[m] \right). \tag{3.35}$$

The resulting coarse estimate for the (n,k)-th entry of the channel matrix is

$$\hat{h}_{n,k} = R_{y_n c_k}(\hat{\varepsilon}_{n,k}). \tag{3.36}$$

The results in (3.35) and consequently in (3.36) can be refined. This is often accomplished by cubic interpolations. Throughout the simulation framework carried out for this work a slightly different approach was chosen by introducing a so-called fine-step factor M_F, *i.e.* the neighbourhood around the correlation peak is resolved with $M_F \cdot M_O$ samples per symbol. Figure 3.35 depicts that approach. The oversampled correlation function is indicated in blue, a zoom window details the refinement in resolution around the correlation peak. Red dots indicate the computed fine-steps. The best of the refined samples, *i.e.* the one succeeding from criterion (3.35) represents the estimation result for timing, amplitude, and phase.

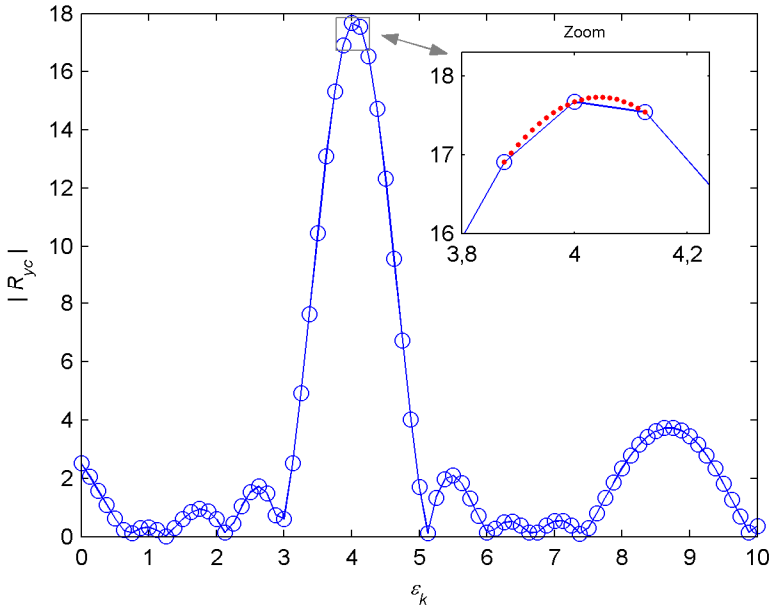

Figure 3.35: Correlation procedure with fine-step to estimate the symbol timing

In a practical sense, independent correlations can easily be processed in parallel and since it is a common digital signal processing method, it is widely supported by standard hardware. In the DigiSat context the channel matrix is of size (155×100), thus parallelizing computations at the gateway helps to reduce the latency.

3.4.3.2 Successive Interference Cancellation

Successive interference cancellation (SIC) is a well-known method and was identified in [36] as a promising implementation of MUD over a MIMO-MAC. In terms of data-aided channel estimation, the application of SIC aims to mitigate MAI as to improve the estimation performance through a better *signal-to-noise-plus-interference ratio* (SNIR). Since the set of identifier sequences is known to the receiver, no additional uncertainties from decoding processes arise; hence SIC can perform to the best of its abilities.

The principle concept of SIC was already depicted in Figure 3.8. But in this approach the filter process followed by the detection process is carried out through correlation as described in Section 3.4.3.1.

The SIC method operates as follows for channel estimation: the most significant contributor is identified and subtracted from the feed signal. Assuming minor errors only in this first step, the remaining portion of interference is reduced, thus the SNIR for the remaining signal components improves. This is repeatedly done until estimations for all signal components are available.

3.4.3.3 Theoretical Limits

Analogous to the forward link, channel estimation on the return link is performed in the feed space applying a DA approach, which can jointly deliver estimates for amplitude, phase and symbol timing. The theoretical lower bounds for amplitude and phase are given under the condition of perfect symbol timing and in absence of interference in (3.22).

To establish symbol timing, (normalized) delay estimates are necessary, which are limited by the MCRB describing the achievable jitter variance [22, pp. 53-69]:

$$MCRB(\varepsilon) = \frac{1}{2 \cdot L \cdot {}^{E_S}/_{N_0} \cdot \left[\frac{1}{3} \cdot \pi^2 \cdot (1 + 3\alpha^2) - 8\alpha^2\right]}. \tag{3.37}$$

In (3.37) L denotes the length of the training sequence, E_S/N_0 is the SNR per symbol, and α represents the roll-off factor of the matched filter.

3.4.3.4 Simulation Results

Within this section, simulation results and their interpretations are presented. If not stated otherwise, the simulations are based on the following settings:

- Guard period $\varepsilon_{\max} = 10$ symbols
- Oversampling factor $M_O = 8$
- Fine-step factor $M_F = 10$
- Matched filter with roll-off factor $\alpha = 0.35$
- BPSK modulation for trainings sequences and user data
- $L = 155$ training symbols
- No frequency error.

Throughout the following, the SIR is defined as the ratio of useful incident signal power flux density at the satellite, received from the observed (strongest) user signal, and that of each of the 99 remaining interfering stations. It is assumed that all user terminals adjust their emitted signals such that they arrive at the satellite at the same power flux density, represented by a SIR = 0 dB. This is done to counteract individual signal fading. However, to investigate effects caused by deviations from this policy an SIR value other than zero adjusts the incident power flux density of the useful signal accordingly. In that respect, a SIR = 10 dB means, that the useful signal incidents at a 10 dB higher power flux density than the interfering signals.

It is to be noticed that results presented in Sections 3.4.3.4.1 and 3.4.3.4.2 were carried out using the correlation method. Nevertheless, they also hold true for the SIC method, because the presented results only refer to the best, *i.e.*, the strongest and most reliable entry of the channel matrix, which as such is the first estimate of the SIC algorithm, which suffers from the same interference as observed with the correlation method.

3.4.3.4.1 Single User Terminal operated without Interferers

According to Section 3.4.3.1, estimations of symbol timing and CSI go together. The accuracy of the CSI is linked to the accuracy of symbol timing recovery, thus proper establishment of symbol timing is indispensable for accurate estimation of the CSI.

Figure 3.36 depicts the mean square error of the normalized delay ε as a function of the SNR, with different oversampling and refinement parameters, *i.e.* M_O and M_F. Only a single user terminal transmits to the satellite, thus no MAI is encountered. The red dashed line indicates the MCRB for training sequences with $L = 155$ symbols. The simulation results, depicted as coloured circlets, show that the estimation performs as theoretically predicted in the low-to-medium SNR regime (disregarding the very low SNR), but it exhibits a floor at higher SNRs. This floor can be explained by the finite resolution (quantization) of the time axis, which depends on parameters M_O and M_F.

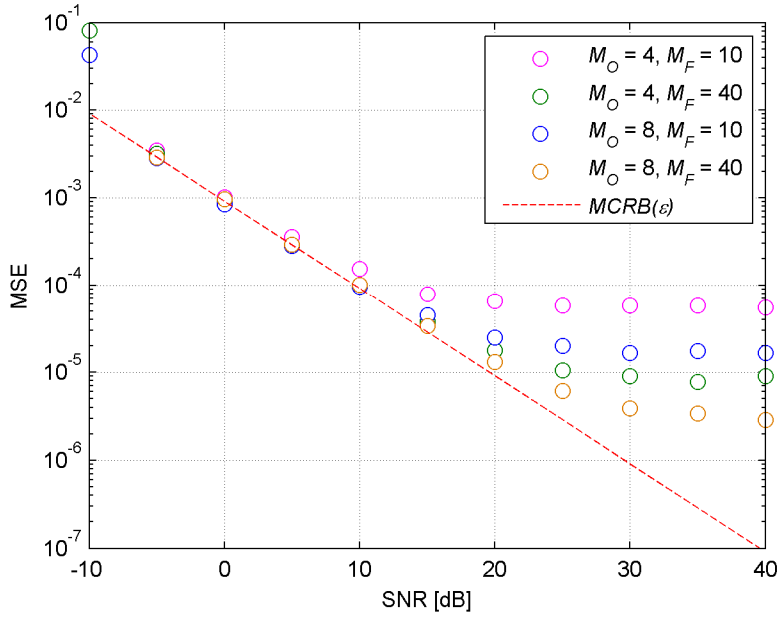

Figure 3.36: Accuracy of delay estimates,
no interferers

In Figure 3.37 the estimation accuracy in terms of (normalized) jitter variance of amplitude and phase of the user terminal is presented. The estimation of timing as well as amplitude and phase is done in a joint approach. The red dashed line indicates the

(N)CRLB for amplitude and phase for training sequences of $L = 155$. The NMSE of the amplitude and the MSE of the phase (in rad^2) are indicated by blue circles and stars, respectively. Simulation results for both are close to the respective (N)CRLB. No significant impact of other than the nominal M_O and M_F parameters could be observed in the depicted SNR regime. Thus, minor inaccuracies in delay estimates account for only negligible impacts on the accuracy of amplitude and phase estimation. They would only affect results in the very high SNR regions. Degradations originating from interference are much more problematic in that respect, as will be shown in the following.

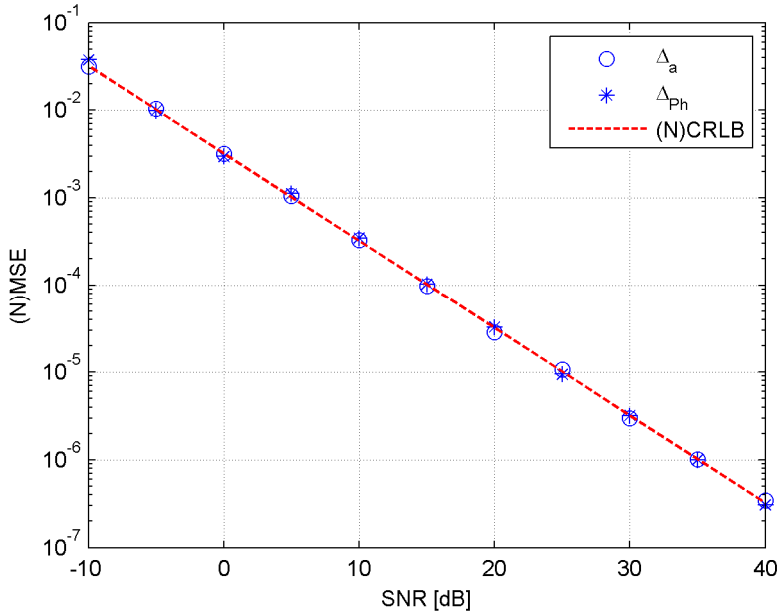

Figure 3.37: Accuracy of amplitude and phase estimates, no interferers

3.4.3.4.2 Single User Terminal operated at different Levels of Interference

In the previous subsection, the achievable performance of channel estimation on the return link was explored by operating just one user terminal, which obviously has not been affected by interference from other user terminals. However, according to the DigiSat scenario, there are 100 user terminals (one per cell) simultaneously in operation, hence each suffers from 99 interferers.

Figure 3.38 indicates the MSE of the delay for different SIR as a function of the SNR. The power flux density of all interfering stations is assumed to be equal, their ratio to the observed signal is indicated by the SIR value. The red dashed line indicates the MCRB for $L = 155$. The simulation results reveal that the interference level, defined by the chosen SIR value, dominates over the jitter floor caused by the finite resolution of the time axis (see Figure 3.36).

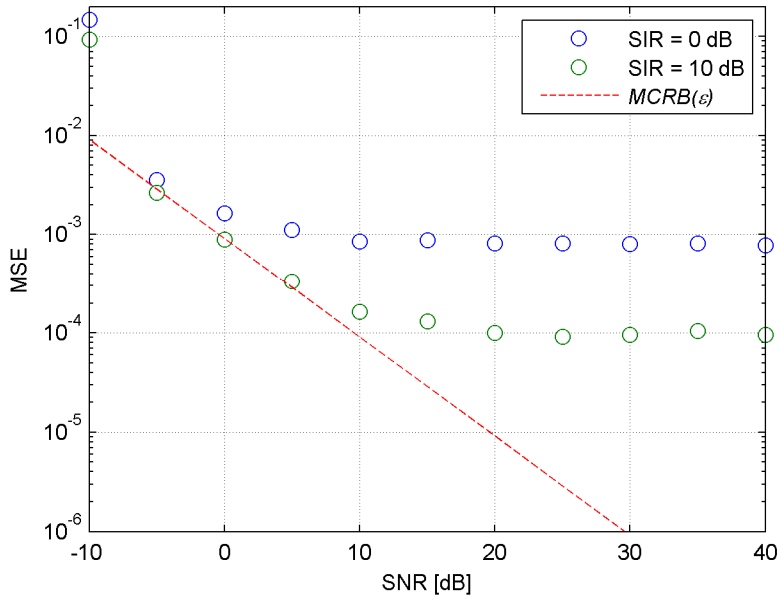

Figure 3.38: Accuracy of delay estimates

Figure 3.39 illustrates the estimation accuracy for amplitude and phase with respect to the strongest component in the channel matrix **H**. The magenta dashed line depicts the (N)CRLB for amplitude and phase ($L = 155$). Not surprisingly, the amplitude (circles) suffers significantly from the level of interference – similar results were obtained on the forward link (see Figure 3.20). But also the phase (in rad^2) is affected by interference, because symbol-synchronous conditions are not given any longer. Hence, both amplitude and phase exhibit a significant jitter floor on the return link.

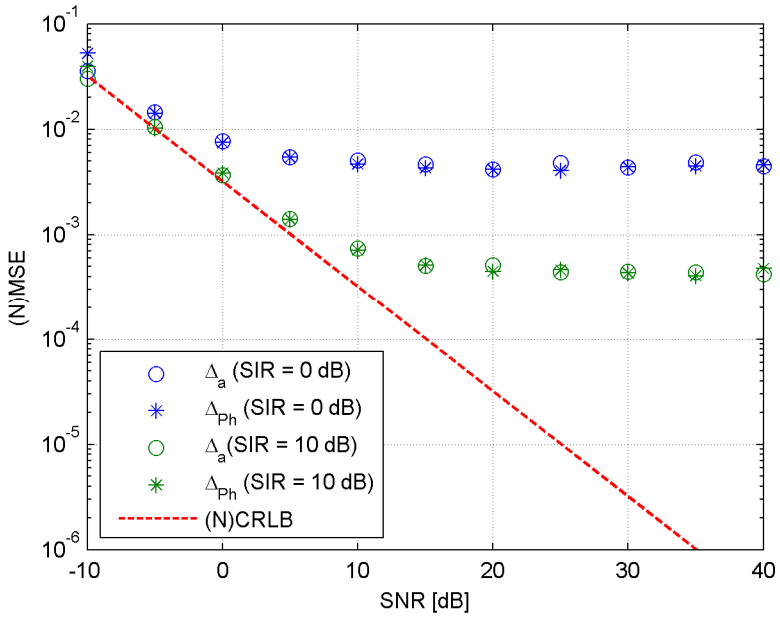

Figure 3.39: Accuracy of amplitude and phase estimates

It could be verified that a more accurate knowledge of the delay does not lead to a significant decrease of the jitter variance, because the error introduced by interference is much larger than the error caused by delay jitter.

3.4.3.4.3 Comparison of Correlation and SIC Method

In the following, not just estimation of the strongest signal component, but also that of the 99 interferers is performed. In this context, both correlation and SIC are compared regarding their performance.

In Figure 3.40 and Figure 3.41 the estimation performance of the correlation method is compared with the SIC method in terms of NMSE of the amplitude and MSE of the phase, respectively. Both figures indicate the estimation accuracies of the entries in $\mathbf{h}_1$, *i.e.* the channel vector gained from feed 1 which represents the first row in **H**. All plotted curves are a function of the SNR referring to the signal component received from the user terminal in cell 48, consequently referred to as SNR_{48} in the sequel. The numbering is aligned with the antenna model delivered by ESA (see Figure 3.2 and Figure 3.3).

Obviously, the SIC method improves the accuracy of the amplitude of weaker signal components significantly, whereas the strongest component is not improved since it is the first one to be estimated (no difference in the method between correlation and SIC).

The SIC method also increases the overall accuracy of the phase as depicted in Figure 3.41.

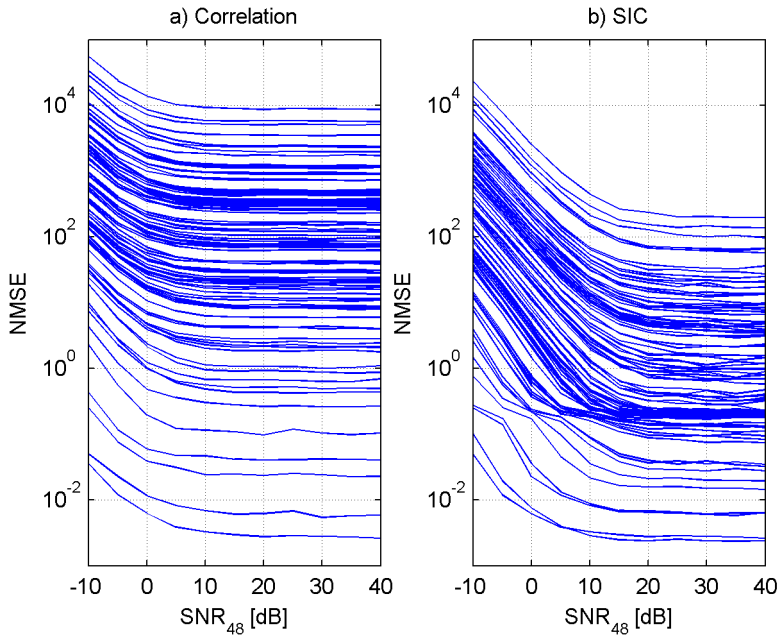

Figure 3.40: Performance comparison of amplitude estimates

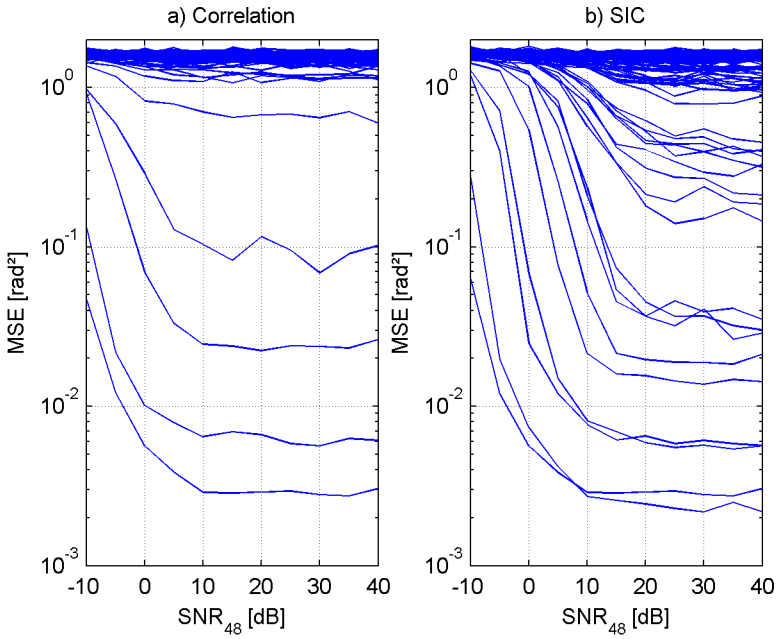

Figure 3.41: Performance comparison of phase estimates

Figure 3.42 illustrates the performance from a different perspective at $SNR_{48} = 40$ dB; the jitter variance of the amplitude for all entries in $\mathbf{h}_1$ ordered by their index is presented. The results achieved with SIC are indicated in red and those achieved with correlation are indicated in blue.

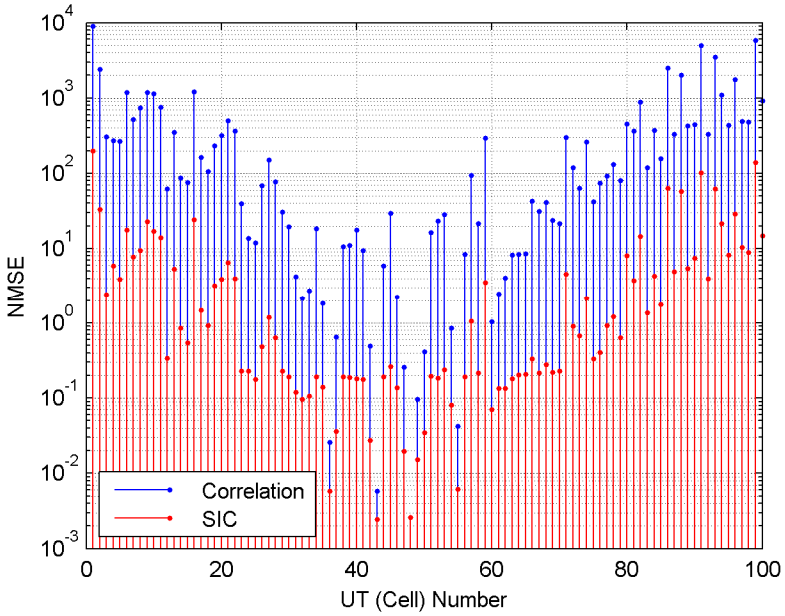

Figure 3.42: Estimation accuracy of amplitude versus cell neighbourhood

Of course, the signal component from cell 48 performs best in Figure 3.42, since it is the strongest one. Not surprisingly, the results reveal that signals sent by user terminals, which are hosted by cells in close neighbourhood, to the cell towards which the observed feed is pointing (best cell), suffer from less jitter than the others do. It can easily be seen that SIC achieves a remarkable performance gain compared to correlation for all, but the signal component of the best cell.

Figure 3.43 visualizes the accuracy of delay estimation, based on the same settings as the previous figures. The red dashed line represents the MCRB, the blue line shows the performance of the strongest signal component and the black lines indicate the remaining signal components. In contrast to the previous plots, all signal components now refer to their true SNR and not to the SNR of the strongest contributing user terminal in cell 48.

By close inspection of Figure 3.43 it becomes clear, that efforts for good performance of CSI estimation are nullified by inaccurate timing recovery. The see-saw behaviour of the signal components in the MSE range between 10^{-1} and 10^{-2} could not be entirely clarified. Systematic simulation errors were examined and excluded. A possible explanation could be up to the cross-correlation properties of the UWs.

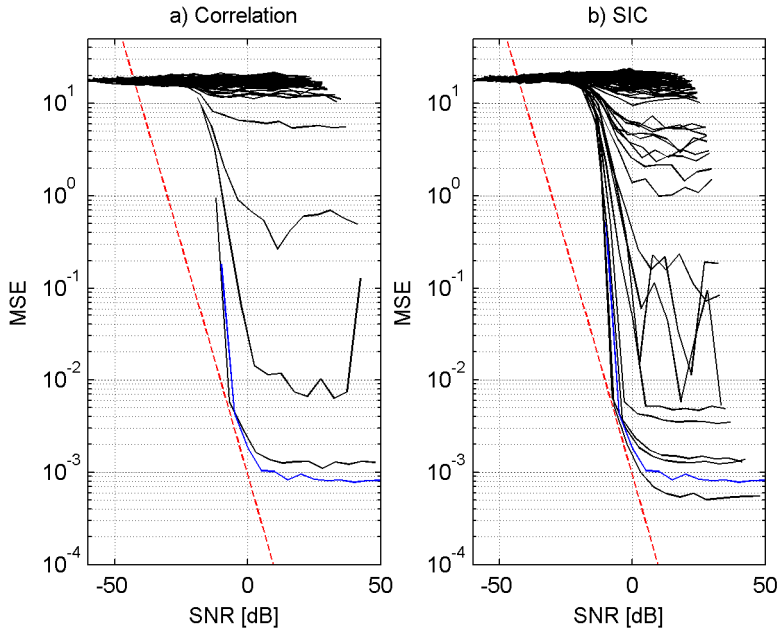

Figure 3.43: Correlation versus SIC performance comparison of delay estimates

Figure 3.44 shows the same results as Figure 3.40 does, but now scaled to the SNR encountered by each of the signal components. The red dashed line is the NCRLB, the blue and black lines indicate the results in terms of NMSE of the amplitude, whereas the blue line represents the strongest signal component (user terminal in cell 48).

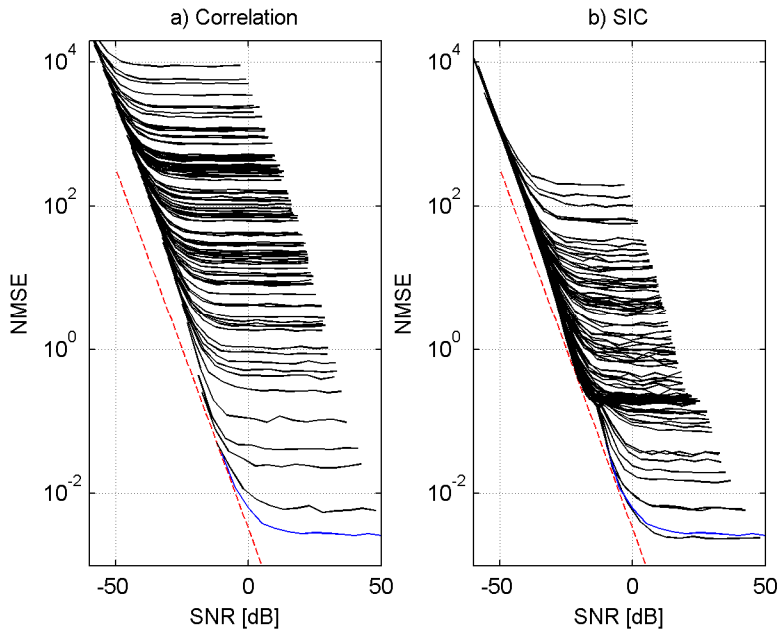

Figure 3.44: Correlation versus SIC performance comparison of amplitude estimates

3.4.3.4.4 Effect of a Silent Period

The results presented so far originate from simulations applying the physical layer framing presented in Figure 3.34, *i.e.* after the UW random data are appended. Due to the frame synchronicity of the return link the user signals arrive at the satellite within a predefined guard time. Thus an overlapping of fractions of UWs of user signals with data of other user signals is intrinsic and causes interference. Since the data are random, interference with the UWs could be quite high. Additionally important in that context is the size of the fractions that can overlap, which of course is at maximum the size of the guard period. However, to eliminate degradations due to the appended data, a silent period of the length of the guard-period is interspersed.

Figure 3.45 and Figure 3.46 compare the estimation accuracy with or without silent period using correlation. In Figure 3.45 results for both scenarios, *i.e.* a) without silent period and b) with silent period are indicated; these results refer to the NMSE of the amplitude, normalized by the true SNR as encountered by each signal component. No significant differences between a) and b) can be observed. This is also backed by Figure 3.46 comparing at $SNR_{48} = 40$ dB the NMSE for amplitude of each signal component, where results with and without silent period are depicted in red and blue, respectively.

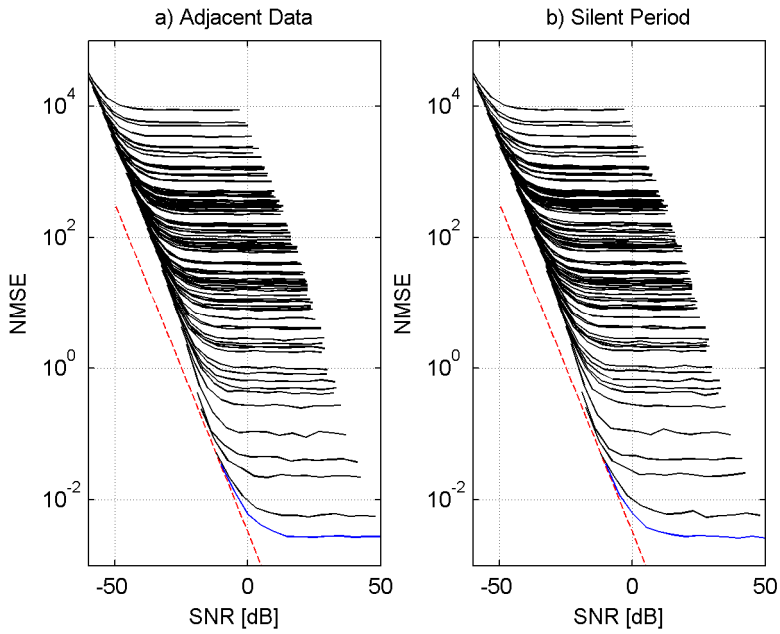

Figure 3.45: Effect of silent period on correlation based estimations

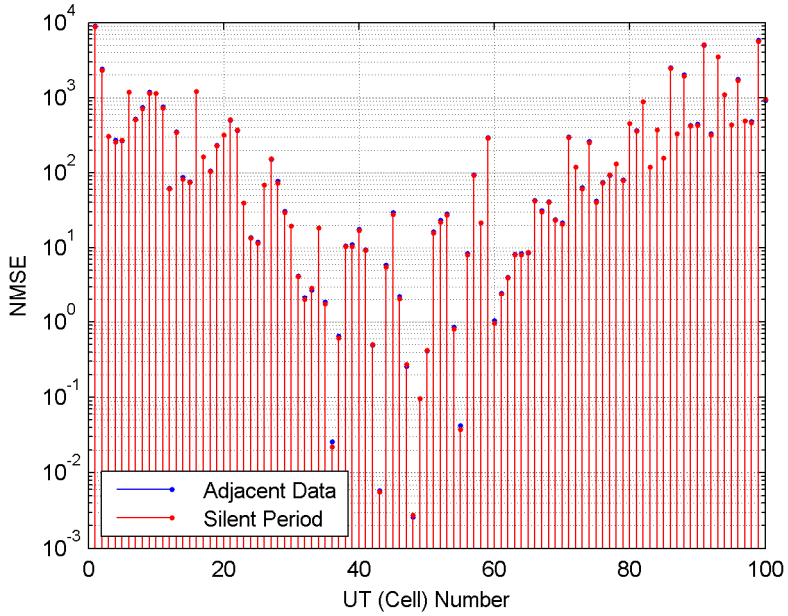

Figure 3.46: Amplitude estimation accuracy improvement using a silent period and correlations

Analogous to the results for the correlation method, results for SIC are plotted in Figure 3.47 and Figure 3.48. In Figure 3.47 results for both scenarios, *i.e.* a) without silent period and b) with silent period are depicted. These results present the NMSE of the amplitude, normalized by the true SNR as encountered by each signal component. Albeit results for correlation did not show remarkable differences before, SIC does. This is

also backed by Figure 3.48 comparing for both scenarios at $SNR_{48} = 40$ dB the NMSE of the amplitude of each signal component, whereas results with and without silent period are depicted in red and blue, respectively.

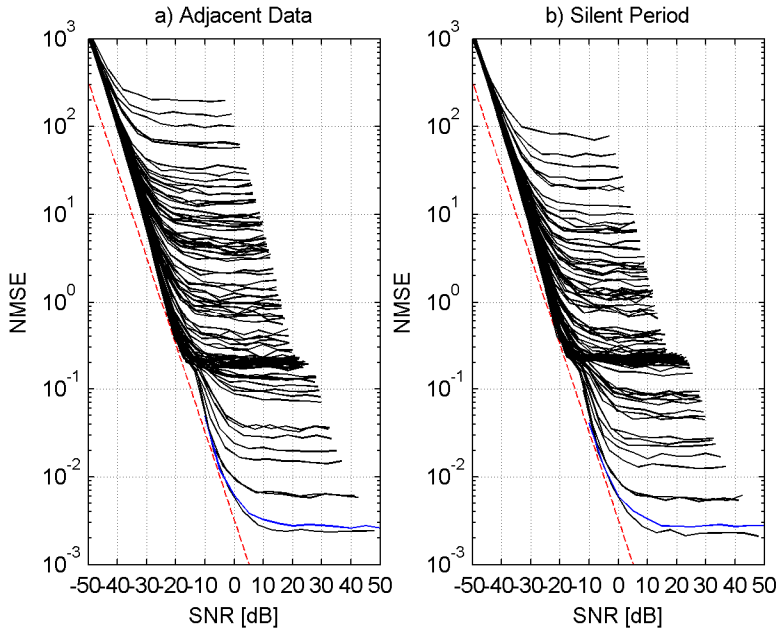

Figure 3.47: Effect of silent period on SIC based estimations

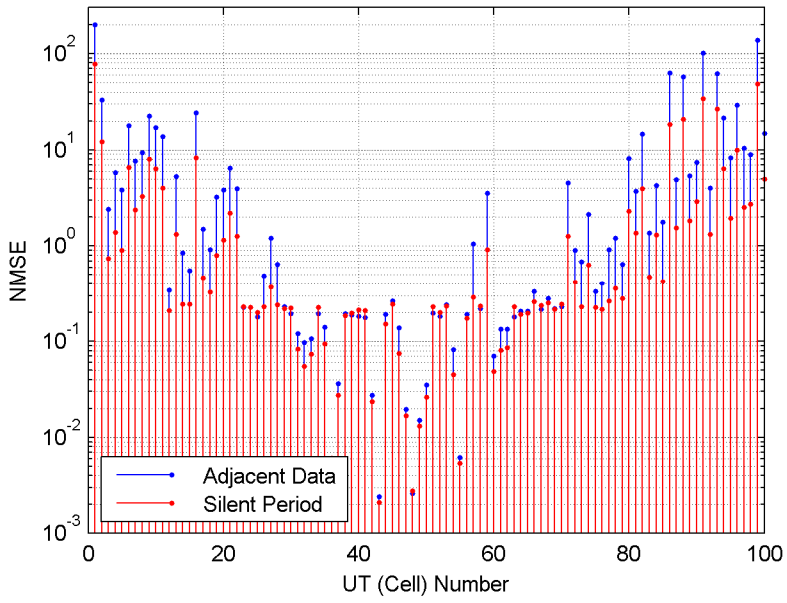

Figure 3.48: SIC estimation accuracy improvement using a silent period

3.4.3.4.5 Effect of different Lengths for Unique Words

Using UWs with different lengths L, Figure 3.49 and Figure 3.50 illustrate the estimation performance in terms of NMSE of the amplitude of correlation and SIC method, respectively. For all plots, the red dashed line indicates the NCRLB, the blue and black lines indicate the strongest and the remaining signal components, respectively.

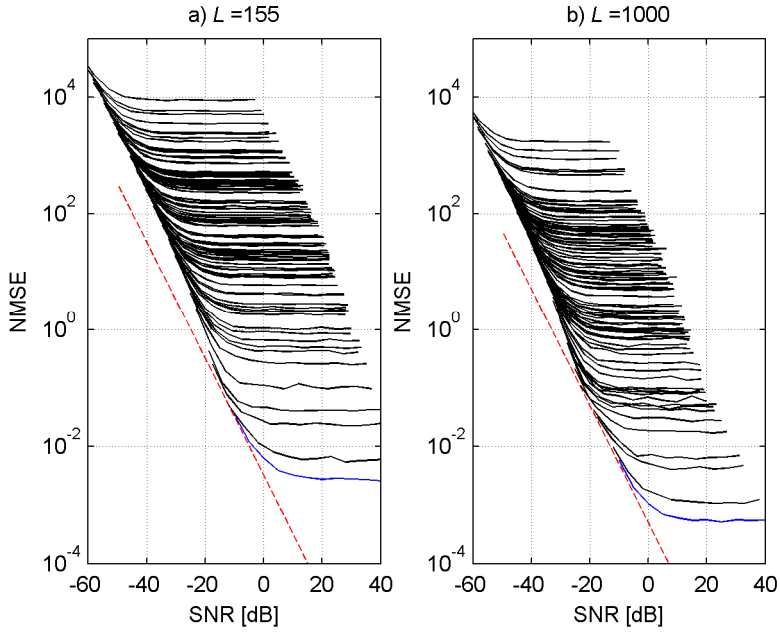

Figure 3.49: UW length performance comparison using correlation

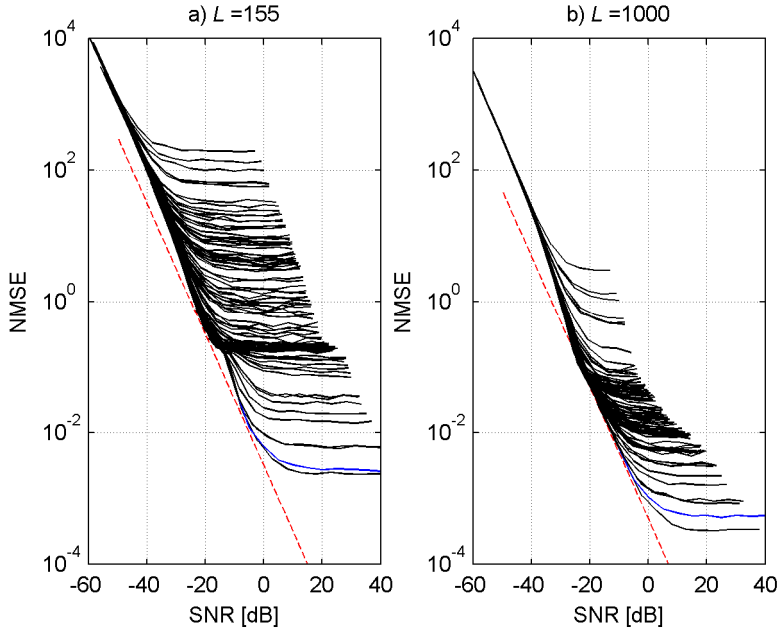

Figure 3.50: UW length performance comparison using SIC

Not surprisingly, for both the correlation and SIC method the estimation accuracy increases for larger values of L. Compared to the correlation method, the SIC method benefits even more from an increase in the UW length. For the sake of completeness, additional results of lengths $L = \{64, 155, 1000\}$ which were simulated using feed 144 heading towards the border region of the coverage area are provided in Appendix A-(g).

3.4.3.4.6 Performance of Iterative SIC Principles

It was previously demonstrated that SIC improves the estimation performance of all but the strongest signal component compared to correlation. It shall be recapped that SIC (as applied) ranks and executes according to signal components estimated power, thus SIC and correlation are equal for the first (strongest) component. Again, $K = 100$ user terminals are present in the DigiSat scenario, thus for both methods the strongest signal component suffers from $K - 1 = 99$ interferers. As to improve the estimation performance of this best component as well, two fairly simple amendments of the classical SIC are investigated in this subsection:

- The *Iterative SIC Method A* (ISIC-A) iteratively processes the SIC method. After executing the classical SIC (0-th iteration), the remaining signal vector denoted as $\mathbf{y}_{rem}$ is exploited. Again following the previously gained ranking of signal components, the algorithm adds the currently considered component to $\mathbf{y}_{rem}$, re-estimates and subtracts it again. This is done for all signal components consecutively, whereas it is optimistically assumed, that the method converges.
- The *Iterative SIC Method B* (ISIC-B) stepwise iteratively processes the SIC method; Methods A and B use the same principle of re-estimating the CSI. Whereby Method A makes full iterations, *i.e.* it processes all K signal components during each iteration, Method B only processes a stepwise increasing number of k components starting with the strongest component. After k re-estimations are established it iterates again, thus suggests that the stronger signal components suffer from less error, which is supposed to positively contribute to the estimates of the weaker components. Again convergence of the method is assumed.

Figure 3.51 compares the for ISIC-A achievable accuracy for timing estimates; Figure 3.51 a) depicts results of the classical SIC method, *i.e.* zero iterations, and Figure 3.51 b) depicts results for ISIC-A after five iterations. The red-dashed line indicates the MCRB, the solid blue line indicates estimation results for the strongest signal component and the solid black lines indicate the results for the remaining components.

Figure 3.52 depicts the achievable performance of ISIC-A in terms of NMSE of the respective amplitudes; all plotted results refer to SNR_{48} = 40 dB. Simulation results based on 0, 1, and 5 iterations are indicated in blue, green and red, respectively. Look-

ing closer at the results, it is obvious that the ISIC-A method does not necessarily converge. Estimations for signal components closely located to the strongest signal component (*i.e.* component 48) typically improve due to the iterations, but all others suffer. This detrimental behaviour is also indicated by Figure 3.51: Timing can properly be established for a few signal components only.

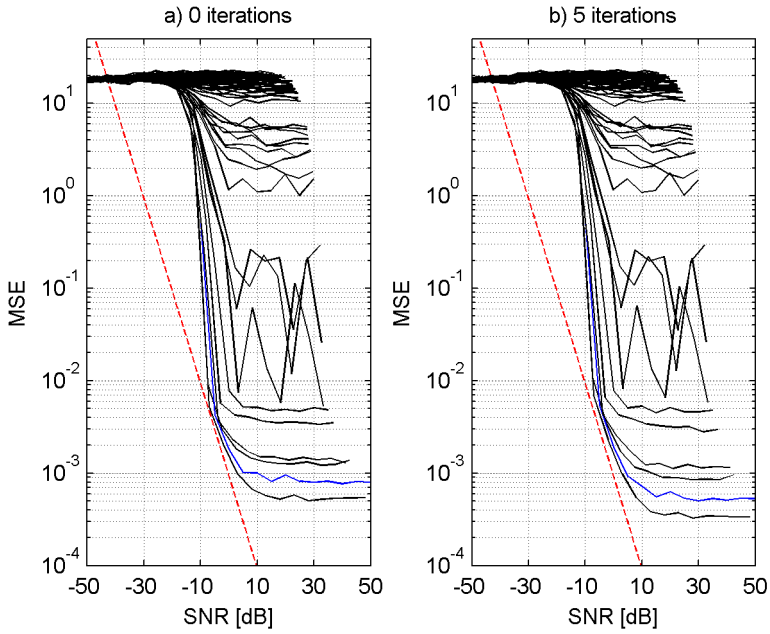

Figure 3.51: Performance comparison of timing estimates using SIC and ISIC-A

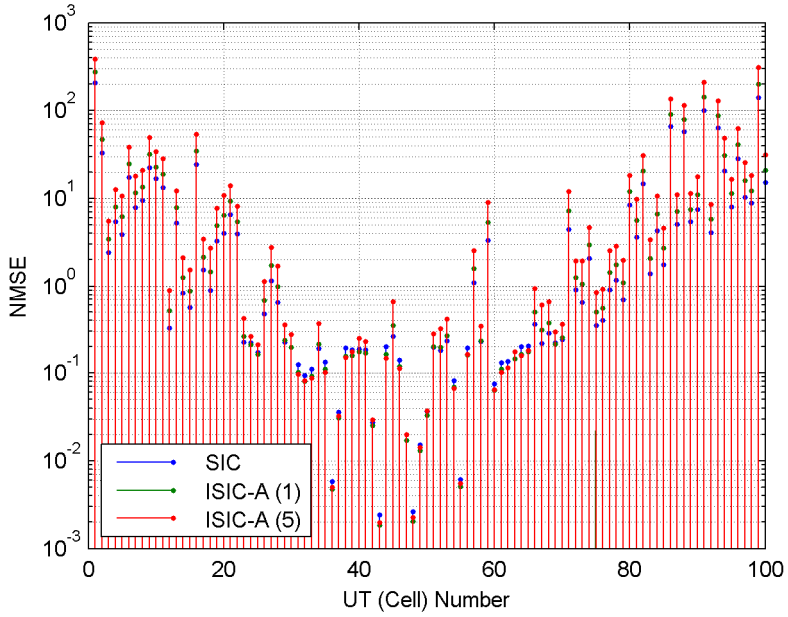

Figure 3.52: Signal amplitude estimation accuracy of ISIC-A

The performance of ISIC-B is benchmarked in Figure 3.53 comparing results of SIC (blue) with ISIC-B (red). A group of 10 with an increment factor of 20 – indicated in the legend as (10/20) – was considered for ISIC-B iterations, which means the first iteration executes the 10 best ranked signal components, the second iteration the best 30 $(= 10 + 1 \cdot 20)$, the third the best 50 $(= 10 + 2 \cdot 20)$, and so forth. Similar results as above are obtained suggesting that only improvements for signal components which are closely located to the observed user terminal can be obtained.

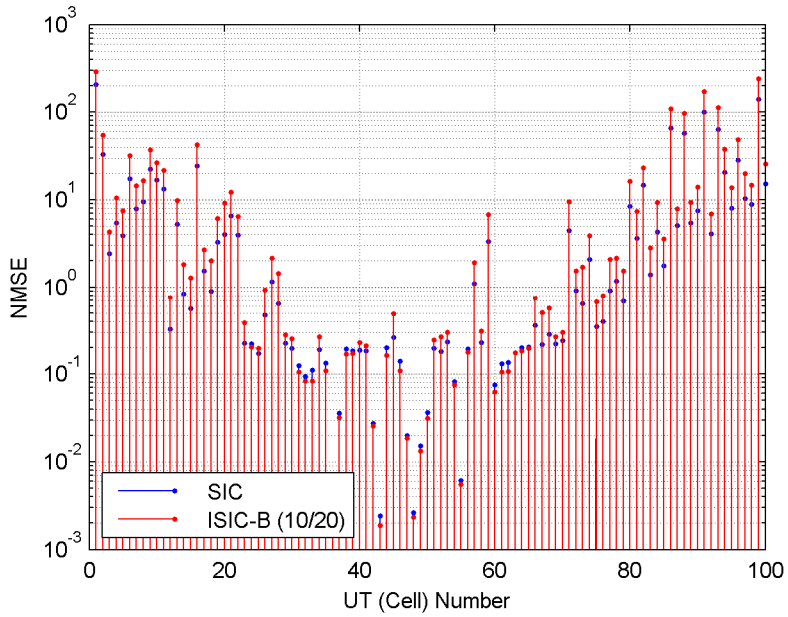

Figure 3.53: Signal amplitude estimation accuracy of ISIC-B

3.4.3.4.7 Influence of Frequency Errors

Frequency errors are intrinsic to asynchronous digital free space transmissions, thus it is of interest to study their impact on the on the DigiSat MIMO return link. Throughout the simulations the frequency estimator of *Mengali* and *Morelli* was applied promising performance close to the CRLB (see (3.30)) at a reasonably large estimation range [59].

For the subsequently presented simulation results the maximum frequency error, normalized by the sampling period, was chosen to be $\Delta fT = 0.05$. Besides that the settings as outlined in Section 3.4.3.4 apply. The simulation results refer to the correlation method, thus for the sake of completeness additional simulation results based on the SIC method are presented in Appendix A-(h).

Figure 3.54 depicts the achievable performance of frequency estimation for feed 1 using the above mentioned settings. The red dashed line indicates the NCRLB, the solid lines represent the performance for the respective user terminal signals, whereas the blue solid line represents the strongest contributing user terminal. Only for a small number of

user terminal signals the performance improves compared to the maximum allowed normalized frequency error.

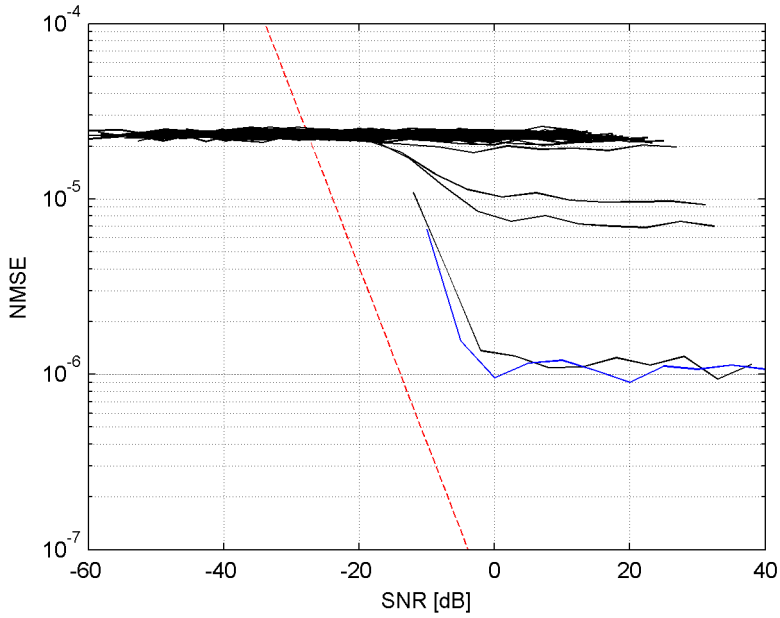

Figure 3.54: Frequency estimation performance on the return link

Figure 3.55, Figure 3.56, and Figure 3.57 compare the performance of timing, phase, and magnitude estimates using the correlation method without residual frequency errors in a) to estimates with residual frequency errors in b) at feed 1. In all figures the red dashed lines indicate the MCRB and NCRLB, respectively, the solid lines represent the (N)MSE of the estimates, whereas the blue one represents the signal component of user terminal 48, *i.e.* the strongest component in feed 1.

In Figure 3.55 degradations of the accuracy of the timing estimates can be observed, which are induced by the residual frequency errors. These additional uncertainties as a consequence detrimentally influence the phase and amplitude estimates as to be observed in Figure 3.56 and Figure 3.57. These effects also take place when applying the SIC method, as can be observed in Appendix A-(h).

Figure 3.58 shows a comparison of amplitude estimates at an SNR_{48} = 40 dB for each of the 100 user terminal signal components. By recalling the results presented in Figure 3.42, it becomes obvious that SIC basically loses its improved performance compared to correlations, so it suffers significantly more from residual frequency errors.

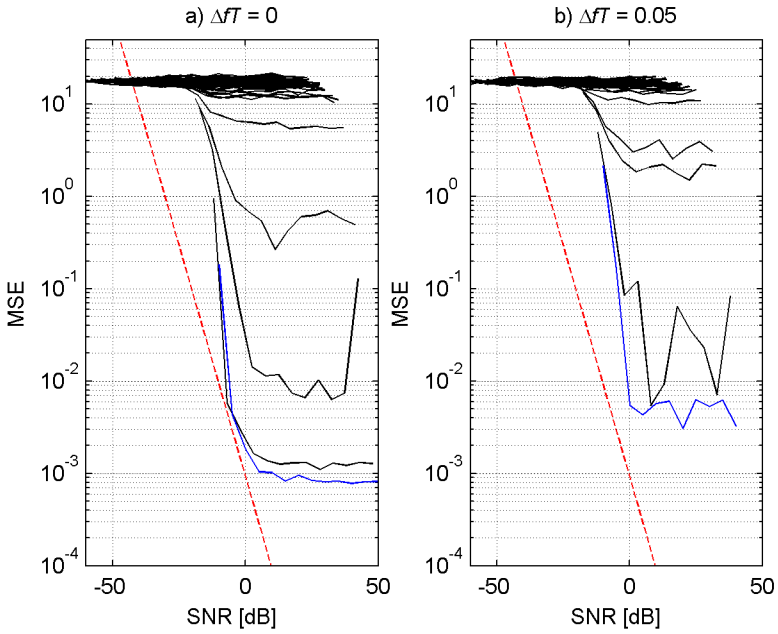

Figure 3.55: Accuracy of timing estimates due to frequency errors using correlations

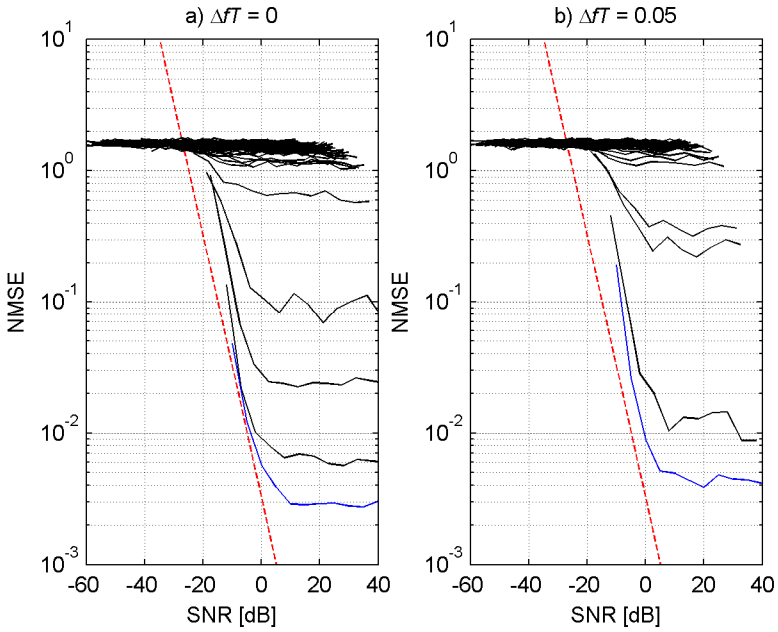

Figure 3.56: Accuracy of phase estimates due to frequency errors using correlations

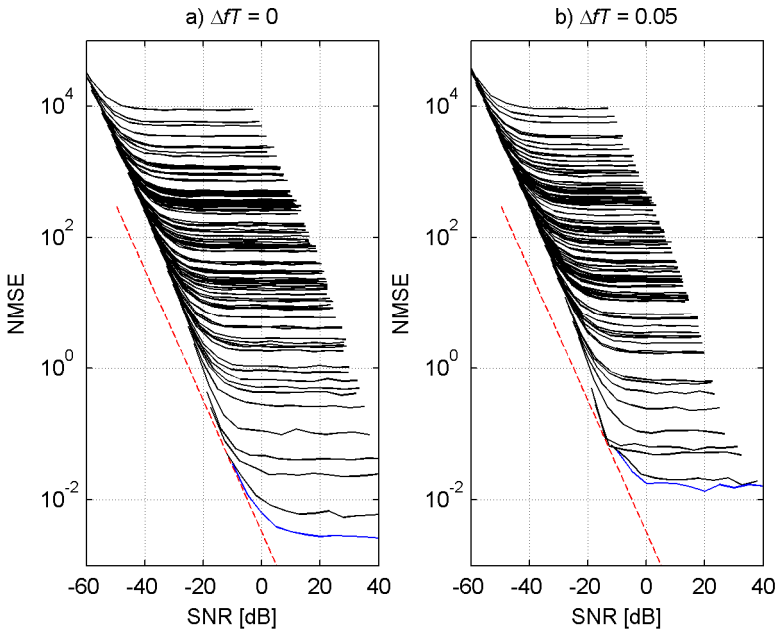

Figure 3.57: Accuracy of amplitude estimates due to frequency errors using correlations

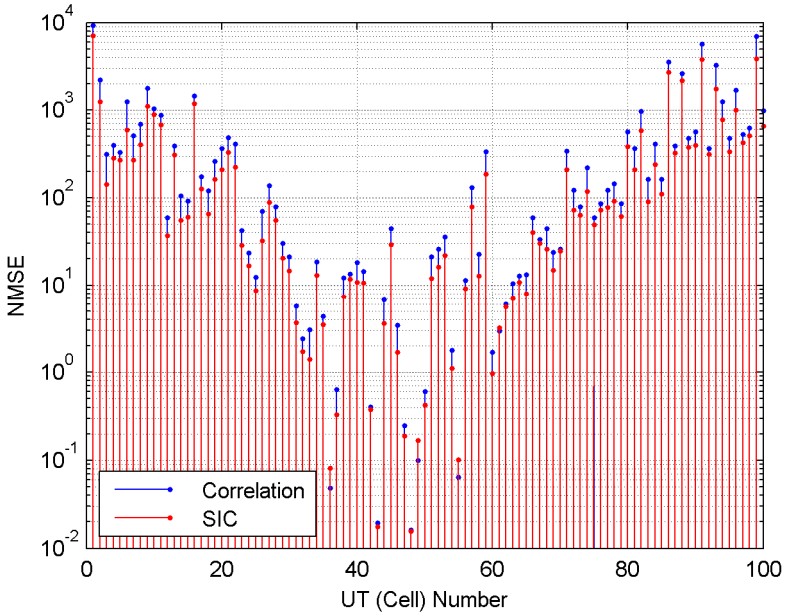

Figure 3.58: Comparison of amplitude estimation accuracy of correlation and SIC method

Investigations on the SIC method revealed that the residual frequency errors hamper the convergence of the SIC method, since in duality with erroneous timing recovery they detrimentally affect the performance by introducing errors which are fed forward by the algorithm. Since the strong signal components, *i.e.* those the feed heads to, exhibit a promising performance in terms of frequency estimation and the frequency error is

equal in each feed signal for a given user, a smart estimation approach is required which *a-priori* establishes the frequency and timing recovery before finally CSI is estimated. Additional thoughts about that may be found in Chapter 4, whereas frequency errors are yet neglected. The required framework would be beyond the scope of this thesis.

3.4.3.5 Analysis of the Jitter Floor

As previously described, a jitter floor of timing, amplitude, and phase is observed on the return link. Analogous to the forward link, this phenomenon is caused by interference and seems intrinsic to estimation methods based on correlation applied to interference-imposed MIMO channels. Within the following, the applicability of (3.29) to the return link is investigated in Subsection 3.4.3.5.1. The version adapted to the return link is presented in Subsection 3.4.3.5.2.

3.4.3.5.1 Applicability of the Forward Link Jitter Floor Bound for the Return Link

For the forward link, the jitter floor could be given in closed form for amplitude and phase in (3.29). Due to the non-symbol-synchronous conditions on the return link, however, (3.29) is no more a general solution. A closed form solution for the jitter floor on the return link is in principle possible as well (see Section 3.4.3.5.2), but the related analytical framework is intricate and results in fairly complex relationships.

Nonetheless, it could be verified that the SIC method provides a lower jitter floor than pure correlation, because the amount of interference is reduced (Figure 3.40 and Figure 3.41). However, in order to qualify the applicability of (3.29), which was derived for the symbol-synchronous forward link, it is compared to simulation results achieved for the return link in Figure 3.59. The strongest signal components in the feeds 48 (blue) and 144 (green) are exemplified in that respect. The red dashed line represents the (N)CRLB, the dashed lines indicate the computed jitter floor, the circlets and stars indicate the simulated NMSE for amplitude and MSE for phase, respectively. It is evident that the results for the strongest signal component in feed 144 are rather close to the analytical ones, whereas those in feed 48 are not.

Evaluations of the rest of the antenna feeds made clear that most simulations are fairly well aligned with analytical predictions from (3.29); the majority of the results exhibit a jitter floor, denoted as $\sigma^2_{jf,RL,sim}$, which is quite close to the analytical one, denoted as $\sigma^2_{jf,FL}$. So Figure 3.60 a) details the distribution of the ratio $\sigma^2_{jf,RL,sim}/\sigma^2_{jf,FL}$, whereas the difference, *i.e.* $\sigma^2_{jf,RL,sim} - \sigma^2_{jf,FL}$, is plotted in b). It can be observed that $\sigma^2_{jf,RL,sim}$ is in the range of $1/3$ to 3 times the value of $\sigma^2_{jf,FL}$. Furthermore it can be seen that for about $1/3$ of the simulation results the analytical prediction is very accurate, whereas for about 94 % of the results (3.29) tends to be an upper bound.

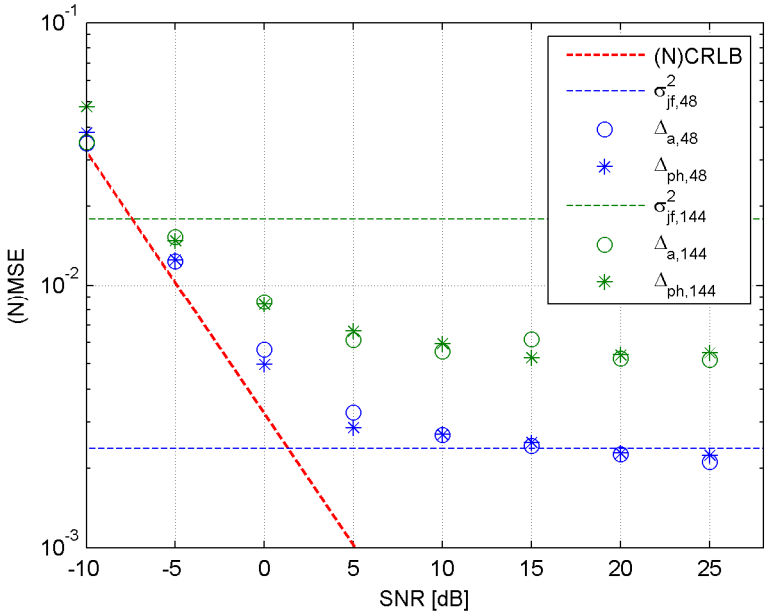

Figure 3.59: Comparison of analytical jitter floor with simulations

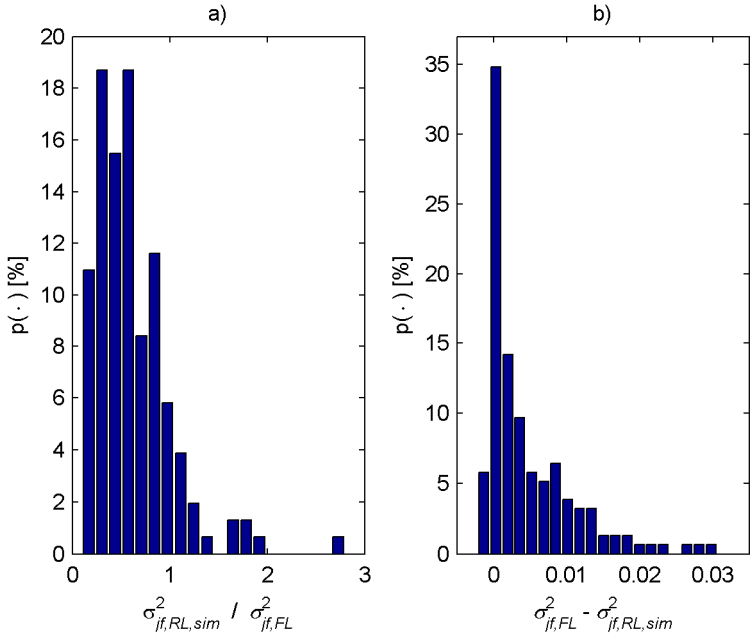

Figure 3.60: Distribution of ratio and difference of analytical and simulated jitter floor

Analogous to the forward link, the jitter floor on the return link is location-dependent. In order to qualify the applicability of (3.29) over various locations, Figure 3.61 and Figure 3.62 compare such analytical results with simulation using the following settings:

- The location of user terminal 48/1 varies in the latitude and longitude range of the coverage zone of feed 1/144 (see Figure 3.3).
- All user terminals, but user terminal 48/1, remain fixed according to Table A - 1 in Appendix A-(a).
- Common settings as described in 3.4.3.4 are valid.

Figure 3.61 depicts analytical results for feed 1 using (3.29), denoted as $\sigma^2_{jf,48}$, and numerical results regarding the NMSE of the amplitude of the CSI, denoted as $\Delta_{a,48}$, as a green and a blue surface respectively – the subscript 48 refers to the user terminal in beam/cell 48; the simulations were performed at an $E_S/N_0 = 40\ dB$.

Figure 3.62 depicts analytical results using (3.29), denoted as $\sigma^2_{jf,1}$, and numerical results regarding the NMSE of the amplitude of the CSI, denoted as $\Delta_{a,1}$, as a green and a blue surface respectively – the subscript 1 refers to the user terminal in beam/cell 1; the simulations were performed at an $E_S/N_0 = 40\ dB$.

Figure 3.61 and Figure 3.62 suggest that predicted and analytical results coincide in shape throughout the coverage zone taking a constant deviation factor into account; this behaviour may be explained by the non-symbol-synchronicity of the return link which leads to different levels of interference depending on the mutual time shift which the particular UWs encounter. The deviations between σ^2_{jf} and Δ_a seem to be deterministic for the respective coverage zone, which is further discussed in Subsection 3.4.3.5.2[9].

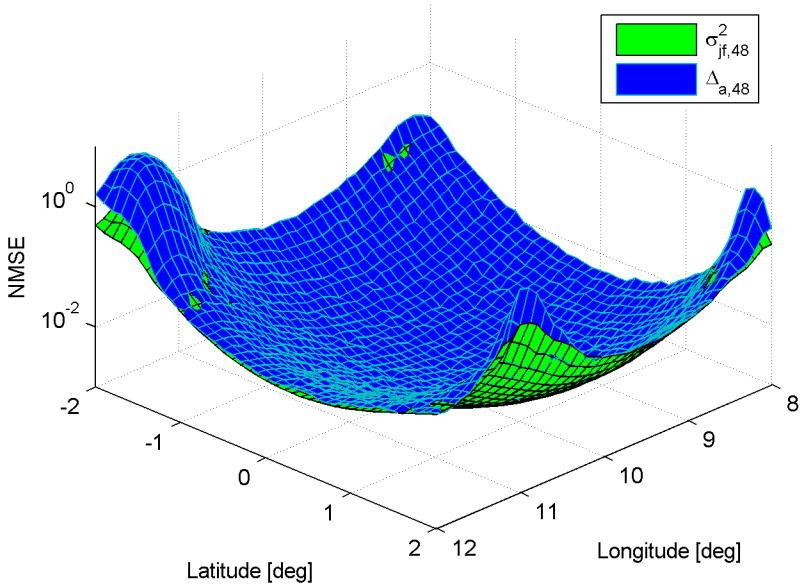

Figure 3.61: Location-related analysis of the jitter floor (feed 1)

[9] It is to be noticed that the simulation results for the phase are similar as described above for the amplitude, thus further illustrations are omitted.

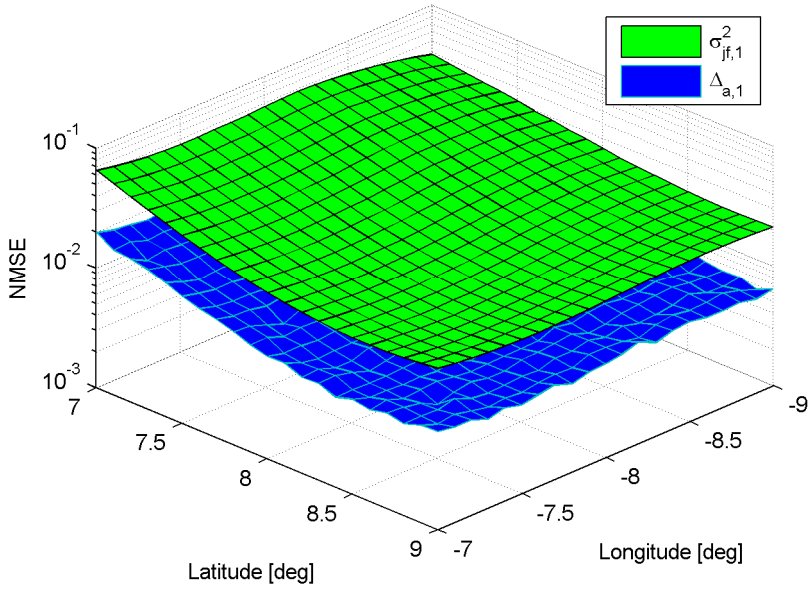

Figure 3.62: Location-related analysis of the jitter floor (feed 144)

Close inspection of Figure 3.61 reveals additional deviations of the predicted performance at boundary regions of the coverage zone, *i.e.* where the performance starts to decrease. These observations coincide with Figure 3.63 depicting the MSE of the normalized delay ε (blue), *i.e.* Δ_ε, compared to the respective MCRB (red) at $E_S/N_0 = 40\ dB$. Figure 3.63 suggests that the additional deviations as observed in the boundary regions in Figure 3.61 originate from inaccurate timing estimations caused by interference.

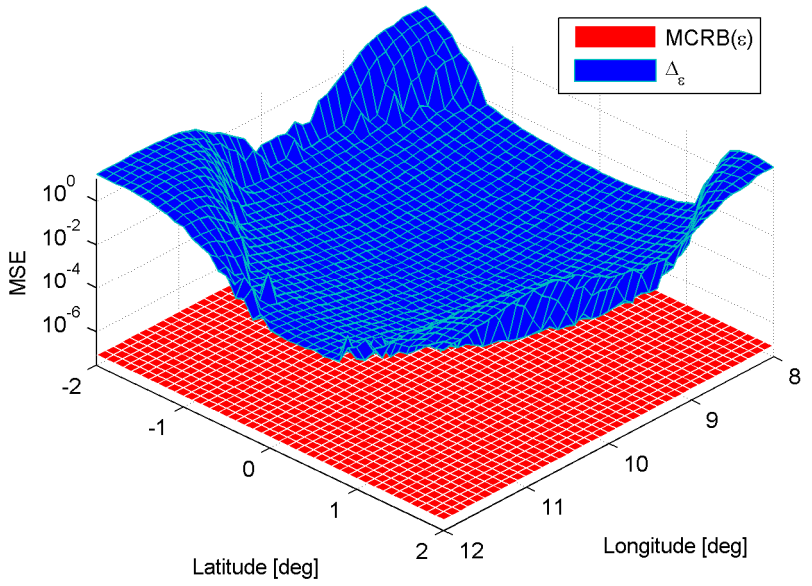

Figure 3.63: Location-related timing jitter (feed 1)

3.4.3.5.2 Accurate Jitter Floor Prediction on the Return Link

It could previously be observed that (3.29) provides a good guess of the expectable jitter floor on the return link too. Furthermore a hypothesis suggesting a deterministic offset between analytical and numerical results was postulated presuming an accurate enough establishment of the timing. So this subsection expands upon this hypothesis in order to find an improved analytical description of the jitter floor for the return link.

Originally the analytical model of the jitter floor on the forward link stems from the observation that it is proportional to the ratio of average interference power in terms of MAI, denoted as $\bar{I}$, and average signal power $\bar{S}$, *i.e.*

$$\sigma_{jf,(n,k)}^2 = \frac{\bar{I}_{n,k}}{\bar{S}_{n,k}}, \tag{3.38}$$

where subscripts n and k indicate the feed and the observed signal component, respectively. Presuming negligible errors in symbol timing, negligible residual frequency errors as well as a normalized guard period with $\varepsilon_{\max} = 0$ (basically symbol-synchronous conditions) the following considerations apply:

$$S_{n,k} = \frac{1}{L^2} \cdot \left| h_{n,k} \cdot \mathbf{c}_k \cdot \mathbf{c}_k^* \right|^2, \tag{3.39}$$

$$I_{n,k} = \frac{1}{L^2} \cdot \sum_{\substack{i=1 \\ i \neq k}}^{K} \left| h_{n,i} \cdot \mathbf{c}_i \cdot \mathbf{c}_k^* \right|^2. \tag{3.40}$$

In (3.39) and (3.40) $\mathbf{c}_k^*$ denotes the complex conjugate of the identifier sequence $\mathbf{c}_k$.

Introducing a guard period of $\varepsilon_{\max} > 0$ representing frame-synchronous conditions, a normalized time shift of the i-th signal component of ε_k occurs, whereas ε_i is an i.i.d. random variable in the range of $0 \leq \varepsilon_i \leq \varepsilon_{\max}$. For (3.39) a quasi-perfect recovery of the symbol timing of the k-th signal component, *i.e.* the observed signal component, may be assumed, so $\bar{S}_{n,k} \cong S_{n,k}$. By inspection of (3.39) and (3.40) and their boundary conditions, it becomes clear that the vector products $\mathbf{c}_k \cdot \mathbf{c}_k^*$ and $\mathbf{c}_i \cdot \mathbf{c}_k^*$ represent special solutions of auto- and cross-correlation functions. In general (non-symbol-synchronous conditions) the received waveforms are to be considered. After sampling, the received waveform for the i-th signal component in the n-th feed with a specific ε_i is given as

$$s_{n,i}^{(\varepsilon_i)}[m] = h_{n,i} \cdot c_i[m] * g[m - \varepsilon_i], \tag{3.41}$$

whereas $g[\cdot]$ represents the raised cosine filter. Hence, the total interference encountered by the k-th signal component becomes for the n-th feed

$$I_{n,k} = \frac{1}{L^2} \cdot \sum_{\substack{i=1 \\ i \neq k}}^{K} \left| \mathbf{s}_{n,i}^{(\Delta\varepsilon_i)} \cdot \mathbf{c}_k^* \right|^2, \tag{3.42}$$

where $\Delta\varepsilon_i = \varepsilon_k - \varepsilon_i$ represents the relative normalized time shift to the observed signal component. To end up with the mean interference power as postulated in (3.38), the joint PDF, given as

$$f(\Delta\varepsilon) = \begin{cases} -\dfrac{|\Delta\varepsilon| + \varepsilon_{\max}}{\varepsilon_{\max}^2}, & |\Delta\varepsilon| \leq \varepsilon_{\max} \\ 0, & |\Delta\varepsilon| > \varepsilon_{\max} \end{cases}, \tag{3.43}$$

needs to be taken into account. It follows that

$$\bar{I}_{n,k} \cong \frac{1}{L^2} \sum_{\substack{i=1 \\ i \neq k}}^{K} \int_{-\varepsilon_{\max}}^{\varepsilon_{\max}} \left| \mathbf{s}_{n,i}^{(\Delta\varepsilon_i)} \cdot \mathbf{c}_k^* \right|^2 \cdot f(\Delta\varepsilon_i) \cdot d\Delta\varepsilon_i. \tag{3.44}$$

By inspection of (3.43) it becomes obvious that the selected set of UWs should provide rather low cross-correlation values for $|\Delta\varepsilon_i| \ll \varepsilon_{\max}$ regions, whereas towards the edges this requirement relaxes. However, UW sets used for simulations throughout this work do not yet encompass that.

Summarizing the above stated and in analogy to (3.29) where $\bar{S}_{n,k} \overset{\text{def}}{=} 1$, the jitter floor on the return link is expressed as

$$\sigma_{jf,(n,k)}^2 \cong \frac{1}{L^2} \sum_{\substack{i=1 \\ i \neq k}}^{K} \int_{-\varepsilon_{\max}}^{\varepsilon_{\max}} \left| \mathbf{s}_{n,i}^{(\Delta\varepsilon_i)} \cdot \mathbf{c}_k^* \right|^2 \cdot f(\Delta\varepsilon_i) \cdot d\Delta\varepsilon_i. \tag{3.45}$$

Figure 3.64 and Figure 3.65 show the performance at $E_S/N_0 = 40\ dB$ of the improved jitter floor in (3.45) compared to numerical results for the NMSE of the strongest signal component in feed 1 and feed 144, respectively. The same settings as for Figure 3.61 and Figure 3.62 apply. The analytical and numerical results for the amplitude are depicted as green and blue surfaces denoted as $\sigma^2_{jf,(n,k)}$ and $\Delta_{a,(n,k)}$, respectively. The variables n and k refer to the n-th feed and k-th user terminal. Both figures indicate that the analytical results are congruent with the numerical ones throughout the coverage zone[10], disregarding statistical jitter.

Equivalently to the results depicted for the amplitude in Figure 3.64 and Figure 3.65, results upon the MSE of the phase match with (3.45).

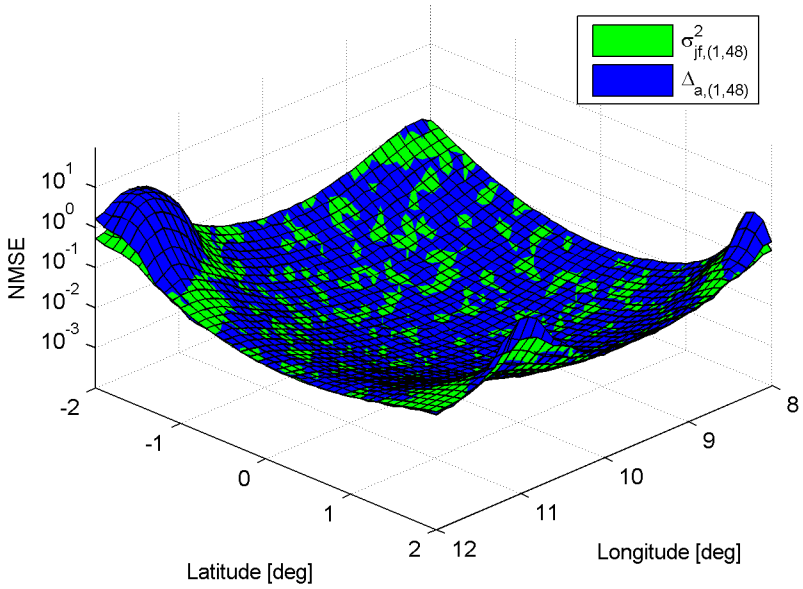

Figure 3.64: Location-related analysis of the improved jitter floor (feed 1)

To gain a more complete picture of the applicability of (3.45), evaluations over several feeds were pursued at an $E_S/N_0 = 40\ dB$, the results are depicted in Figure 3.66: The numerical and analytical results are denoted with some notational abuse as $\sigma^2_{jf,RL,sim}$ and $\sigma^2_{jf,RL}$, respectively. Figure 3.66 a) details the distribution of the ratio $\sigma^2_{jf,RL,sim}/\sigma^2_{jf,RL}$. It can be observed that $\sigma^2_{jf,RL,sim}$ is in the range of 0.9 to 1.2 times the value of $\sigma^2_{jf,RL}$, which is significantly better than the results of the forward link bound in Figure 3.60. The distribution of the estimation error, *i.e.* $\sigma^2_{jf,RL,sim} - \sigma^2_{jf,RL}$, is plotted in Figure 3.66 b. Again, compared to Figure 3.60 the results are very accurate. For both

[10] Coverage zone denotes the area where timing can be established at a certain quality. This can be seen in Figure 3.63.

plots in Figure 3.66 a little bias is observed which obviously originates from the non-perfect timing recovery in the numerical simulations.

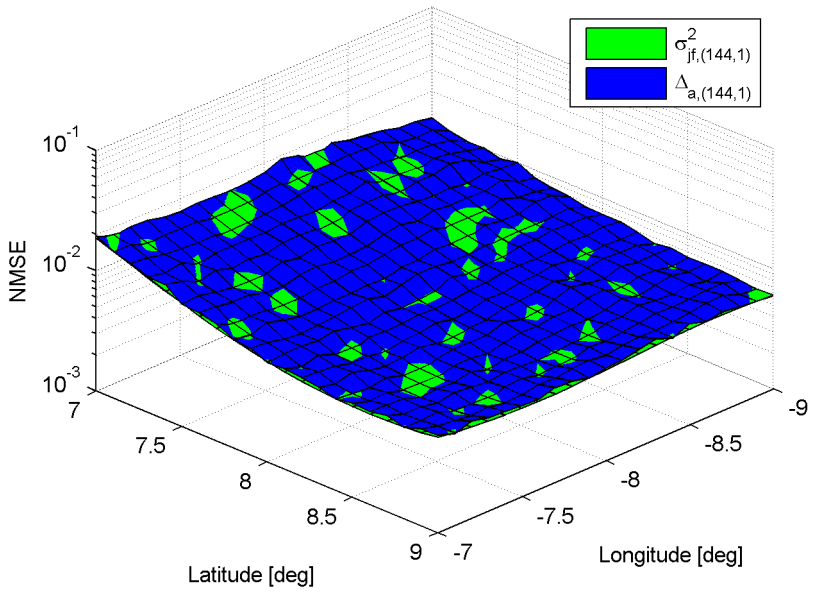

Figure 3.65: Location-related analysis of the improved jitter floor (feed 144)

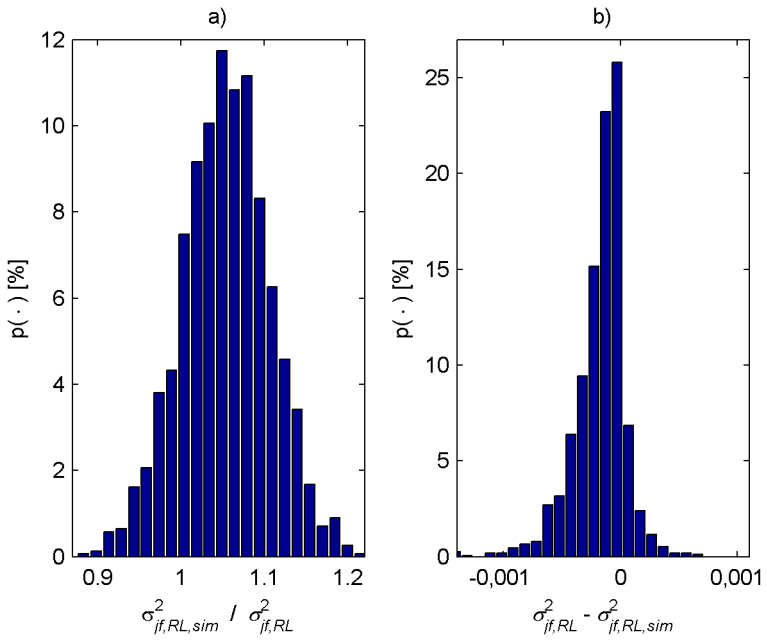

Figure 3.66: Precision of the return link jitter floor bound

3.5 Summary

The work presented in this chapter was mainly carried out in the framework of the *Satellite Communication Network of Experts III Call-off-Order* 1 project supported by the *European Space Agency*. The subtask therein as presented here was to investigate adequate channel estimation methods for the *forward* and *return links* for a generic *multiple-input multiple-output* satellite scenario, called *DigiSat. Full frequency reuse* for the satellite MIMO system is targeted promoting interference to a major issue.

The importance of accurate channel estimation was pointed out given the envisaged countermeasures for interference mitigation achieved by *beamforming*, *precoding*, and *multi-user detection*; all of them require timely and accurate knowledge about the channel state.

Based on the signal model for the symbol-synchronous *forward link*, *i.e.* a memory-less MIMO broadcast channel, a number of candidate methods could be identified:

1) Channel estimation using the *pseudo-inverse*
    a) based on *orthogonal codes*
    b) based on *linearly independent pseudo-random sequences*
2) Channel estimation based on *correlations*

For all listed methods theoretical performance limits could be found, especially for 1b) the exhibited jitter amplification and for 2) the exhibited jitter floor could be analytically described, thus allowing for performance assessments without simulations. It was shown that 1a) provides the best performance in terms of accuracy, because non-orthogonal sequences introduce mutual interference in the estimation process. Contrary to method 1a) all other methods can operate on unique words of arbitrary length. In that respect method 1b) is limited to linearly independent sequences. Location-dependent estimation performance was identified for 2) and an identifier sequence hopping was suggested to counteract that. It was explained that frequency reuse schemes will not positively affect the channel estimation performance in the *DigiSat* context. However, frequency estimation using traditional algorithms also work on the forward link. The impairments on the strongest received signal components are minor due to their beneficial SNIR. Not surprisingly, the Hadamard sequences used in method 1a) lose their orthogonality when non-negligible frequency errors remain.

For the *return link* an appropriate signal model describing a frame-synchronous memory-less MIMO-MAC was introduced. From that basically two candidate techniques were identified for channel estimation:

1) Channel estimation using *correlations*
2) Channel estimation using *successive interference cancellation*

Both methods are fairly straightforward and easy to implement. However, they provide the capability to *jointly* recover *symbol timing* and to estimate the *channel state*. Nonetheless, 2) in general turned out to provide better results than 1), which is important especially for the weaker signal components. It was found that introducing a silent period between the unique word and the typically adjacent data additionally improves the performance of 2). Changes to the iteration principle of 2) did not lead to improvements due to the non-negligible timing jitter of the weaker signal components. Frequency errors turned out to really deteriorate channel estimations when considering them as independent for each feed. Both methods exhibited a similar performance, thus 2) is heavily affected by frequency errors. However, for a few signal components per feed, frequency estimation performs well, so more sophisticated approaches incorporating estimations from other feeds are promising. The jitter floor derived for the correlation method on the forward link turned out to provide well approximated results for the return link too, but due to the different signal model a more sophisticated analytical formulation was developed. The latter definitely marks a milestone within this work and accurately models the performance within its boundary conditions.

(This page is intentionally left blank)

4 Location-Aware Channel Estimation on MIMO Satellite Links

In Chapter 3 channel estimation on MIMO satellite links was treated for each signal component as an independent process. This perception, however, does not fully reflect the actual conditions and interdependencies of such links. Therefore the current chapter builds upon deterministic relationships in MIMO satellite channels to exploit this additional information in order to increase the overall estimation performance.

The work presented throughout this chapter was motivated by findings in the work carried out in the context of the *Satellite Communication Network of Experts III* (SatNEx III) project as previously presented in Chapter 3 and comprises additional ideas which could not be covered in the frame of this contractual activity. Throughout this research, a student bachelor thesis in [57] was supervised by the author aiming at supporting the analytical considerations with simulation work. The achieved results feed into this chapter and are acknowledged. Moreover, appropriate quotations indicate plots which originate from the simulation framework carried out in [57]. Findings and results created by the author are not explicitly quoted in the sequel to avoid confusion and to support the readability of this thesis.

In the following, benefits from deterministic timing recovery and location aware channel estimation are discussed. Comprehensive simulation results back the analytical considerations.

4.1 Preface

On MIMO satellite links certain interdependencies between the signal components can be identified. Exploiting this additional knowledge enables the adaptation of estimation algorithms. On the one hand a reduction of the computational load can be reached relaxing hardware requirements, on the other hand more precise estimation results at the same complexity may be achieved which is of significant importance since these results directly feed into precoding and MUD algorithms (see 3.2.2 and 3.2.3) defining the achievable system throughput. The latter are detrimentally affected by residual estimation errors [33, pp. 21-23][60].

Within this chapter two evolutionary steps from pure independent estimations towards an encapsulating location-aware approach will be discussed: First, estimation errors

induced by incorrect timing recovery as outlined in Subsection 3.4.3.4.3 will be reduced by exploiting deterministic relationships amongst feeds. From that the second step incorporates *a priori* knowledge of the user terminal positions, denoted as location awareness. Achievable improvements to the overall estimation performance will be presented and discussed.

4.2 Deterministic Timing Recovery

Issues with correct timing recovery primarily arise on the return link since no symbol synchronicity is given, thus each signal component arrives within a specified guard period. A correlative approach is envisaged here (analogously to Chapter 3), since it represents the optimal ML implementation for symbol timing recovery [61] and it can jointly deliver the CSI.

By detailed inspection of Figure 3.43 it becomes obvious that timing results stemming from user terminals to which the receiving feed points to exhibit a good precision. In other words, only the strongest signal components in a feed signal lead to sufficiently good timing estimates whilst considering training sequences of reasonable length. Assuming the geometric properties of the space-borne AFR antenna to be such that $T_S \gg \tau$, where T_S represents the symbol period and τ is the delay of the signal between its arrival at the closest and at the most distant feed (with respect to the signals origin, *i.e.* the user terminal position); a phase shift of the received waveform can be used to model the effect of this delay in narrowband scenarios [61]. This motivates to assess the signal timing of the strongest signal component(s) from a feed signal and use those results to ease channel estimation in feed signals where these components are weak. This principle is denoted as *deterministic timing recovery* (DTR) in the sequel.

Figure 4.1 and Figure 4.2 illustrate performance comparisons for channel estimation with and without perfect timing recovery to demonstrate the potential of DTR. Both figures respect the settings as defined in Section 3.4.3.4 and plot the results for CSI estimations based on the signal of feed 1 (see Figure 3.3). The respective NCRLBs are depicted as red dashed lines, the solid lines represent the NMSE of the magnitude of the 100 user terminal signals, which according to the DigiSat signal model, are weighted by the directional feed gain and summed up to the feed signal. The blue line in the ensemble of 100 represents the signal of the strongest contributing user terminal. It is the one the feed points at. Figure 4.1 compares the NMSE of the amplitude using correlation based on conventional timing recovery (treating all feed signals as independent) in a) with DTR in b) (here emulated with perfect timing knowledge, thus denoted as *genie*).

Figure 4.2 depicts the same comparison for the SIC method. Throughout the subsequent analysis an explanation supporting the validity of the genie modelling will be provided.

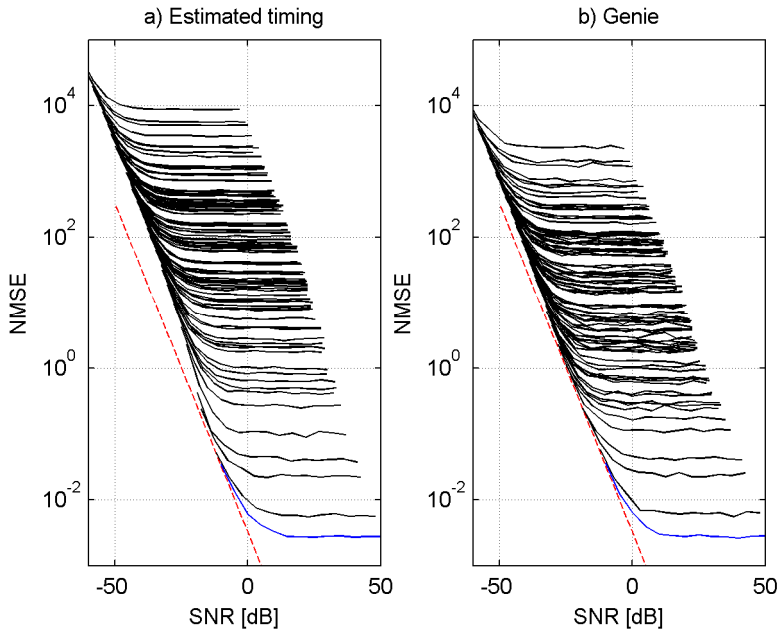

Figure 4.1: Performance comparison of non-ideal and ideal timing recovery using correlation

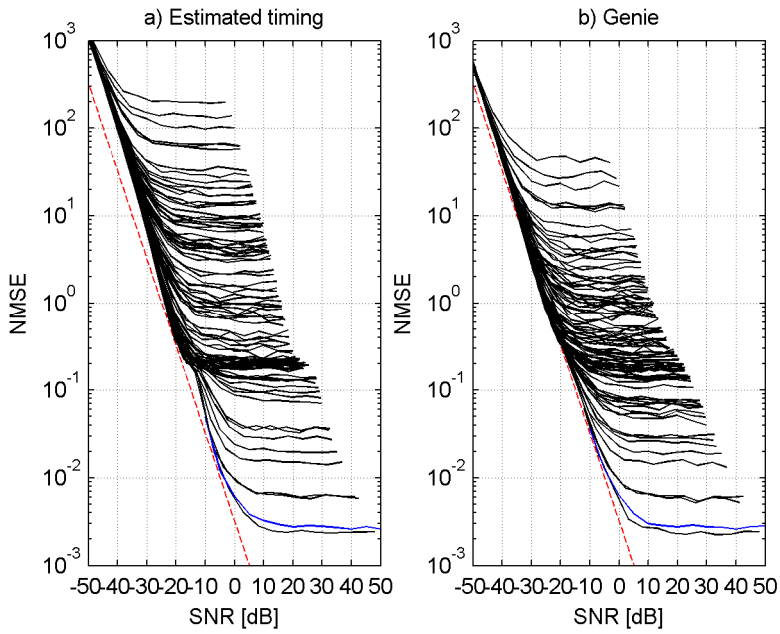

Figure 4.2: Performance comparison of non-ideal and ideal timing recovery using SIC

Both, Figure 4.1 and Figure 4.2 reveal significant improvements of the performance: Whilst a lower jitter floor for the weaker signal components is the most obvious im-

provement at the first glance, a closer look makes obvious that the curves with perfect timing recovery now better approach the NCRLB. The latter allow for an analytic error floor determination using (3.45) since the requirement of sufficiently good timing recovery is definitely fulfilled. Using perfect knowledge of symbol timing to simulate the performance of DTR can be assumed to be valid. This assumption is supported by comparison of the curves of the strongest signal components (blue solid lines) in Figure 4.1 and Figure 4.2: For both figures the blue curves in a) and b) basically match, thus suggesting that a small residual timing error has no significant effect on the CSI estimation performance. This finding agrees with results in Section 3.4.

The analysis is also confirmed through simulation results for phase estimates, which for simplicity are not provided here.

Since SIC already performs significantly better for DTR than pure correlations, Figure 4.3 compares the performance in terms of NMSE of amplitude for SIC and ISIC-A, introduced in Section 3.4.3.4.6 at SNR_{48} = 40 dB. The simulation settings outlined in Section 3.4.3.4 apply. It can be seen that ISIC-A improves the estimates of the stronger signal components with respect to SIC significantly, even though it degrades the weaker ones. This behaviour, however, could still be of interest for *location-aware* channel estimations, as will be demonstrated in Section 4.3, since its performance depends on the accuracy of the strongest signal component(s).

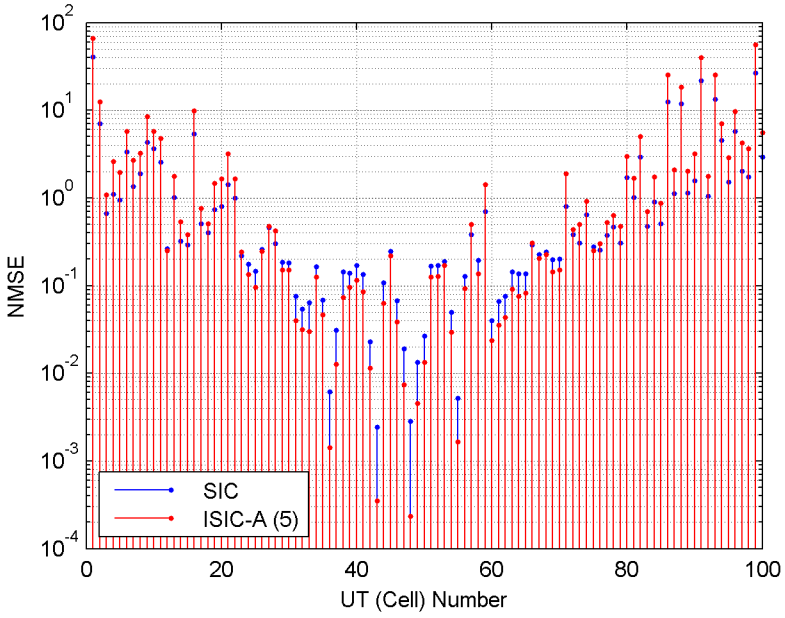

Figure 4.3: Amplitude estimation performance comparison of SIC and ISIC-A for DTR

4.3 Exploitation of the User Terminal Location for Channel Estimation

Throughout Chapter 3 it became clear that weaker signal components suffer from significant estimation errors due to their poor SNIR. Classical approaches like the SIC method (including its variants) can only partially tackle that problem and resorting to significantly longer preambles (UWs) is unwanted for bandwidth efficiency reasons. Knowledge about the user terminal location can help and support the CSI estimation.

Fortunately, both links – the forward link and the return link – can benefit from knowledge about the user terminal's location, whilst only the gateway is required to have that knowledge[11]. A multitude of candidate techniques for gathering the user terminal's position is available today. A brief review is outlined in Section 4.3.1. Subsequently Sections 4.3.3 and 4.3.4 deal with the position exploitation on the forward and return link respectively. The presented simulation results comply with the in Section 3.4.3.4 outlined settings unless otherwise stated.

4.3.1 Position Determination Technique Review

Today a multitude of positioning techniques is available (or being made available) able to meet the needs for *location-aware channel estimation* (LACE). Most prominent in that respect are *Global Navigation Satellite Systems* (GNSSs) such as the US' NAVSTAR *Global Positioning System* (GPS), the *Russian Global Orbiting Navigation Satellite System* (GLONASS), the EU's *Galileo*, the Chinese *Compass/BeiDou* and the Japanese *Quasi-Zenith Satellite System* (QZSS) to name the most prominent ones. Modern civil GNSS systems reach typical accuracies of 5-50 m, whereas current (2012) receivers in smartphones such as the one in the iPhone 4™ reach GNSS-based mobile positioning accuracies of $< 10\,m$ with a confidence level of $\sim 95\%$ and $< 30\,m$ with a confidence level of $\sim 99.5\%$ [62, pp. 9-45][63]. Recent developments targeting the smartphone markets provide the industry with chipsets implementing several GNSS standards at once. For instance, the *Broadcom BCM4752* chip processes GPS, GLONASS, QZSS as well as augmentation data simultaneously allowing for accuracies far beyond receivers implementing a single standard only [64].

Besides satellite-based position determination also terrestrial positioning systems could be envisaged. One technology might be of special interest, *i.e.* the positioning using

[11] Throughout this thesis only technical implications concerning the benefits and challenges of user location determination and utilization are considered. Eventually arising legal obligations as for example data privacy protection are beyond the scope of this work.

cellular networks. This technique uses radio communication parameters to locate the user terminal within the cellular network requiring at least three base stations in range. Its positioning precision is modest at typically $50 - 500\ m$ [62, pp. 9-17][65].

Both above mentioned technologies might be of interest in the MIMO context as well, especially when considering mobile users, because miniaturized and integrated solutions are available on the market for fairly cheap prices. Even recently presented mobile satellite user terminals as the satellite smartphone *TerreStar Genus* which combines the terrestrial cellular networks and the *TerreStar-1* satellite network (spot beam technology), allow for GPS and cellular-based position gathering [66]. The disadvantages of GNSS and cellular positioning systems are their additional hardware, software, and energy requirements increasing the *bill off material* (BOM) of the user terminals. Furthermore, the transmission of the user terminal position to the gateway in time is required which consequently increases the network overhead. Disadvantageous as well is the fact that the MIMO satellite communication system has to rely on third party systems.

A position gathering solution based on the MIMO satellite network itself might be able to tackle the mentioned drawbacks and better meet the system requirements. Whilst for mobile user terminals additional interference may arise due to fading, multipath, and non-line-of-sight effects degrading the performance, fixed user terminal scenarios might be rather easy to approach. The latter require the position estimation algorithms to be bias free and ergodic, thus observations over several time instances provide the same expectation values allowing for averaging to enhance accuracy. However, positioning algorithms for MIMO satellite networks can use the same basic technologies as their terrestrial counterparts, *i.e. received signal strength* (RSS), *time of arrival*, *time difference of arrival* (TDOA), *angle of arrival* (AOA), as well as *geometric*, *fingerprinting*, and *statistical methods* [62, pp.75-90][67][12].

4.3.2 The Scenario

In order to keep the user terminal requirements low, extensive signal processing is preferably done at the gateway. When considering the forward link, a two-step estimation approach as such is favoured, *i.e.* a suboptimal approach which first extracts appropriate signal parameters from the received waveforms (*e.g.* CSI estimated at the user terminal) followed by a separate position estimation process [67][68]. In [69] an algorithm is proposed explicitly for satellite networks using multi-beam antennas. It is able to estimate

[12] CRLBs describing the theoretically achievable performance of the different positioning techniques may be found in [67] and references therein.

the user terminal position (at the user terminal) based on RSS and AOA. Unfortunately this geometric algorithm is susceptible to weather conditions and requires the user terminal to be aware of a stack of system parameters such as the *elevation of the Earth-space link*, the *receive antenna gain*, the *satellite's antenna pattern*, etc., which significantly limits its applicability, since *plug and play* systems are todays standard and expected by users.

In the DigiSat scenario both links, the forward link (memory-less MIMO-BC) and the return link (memory-less MIMO-MAC) can be used to establish location estimates; more precisely, the estimated channel matrix $\widehat{\mathbf{H}}$ can be exploited at the gateway (for forward and return link) to determine the user terminal location. Not surprisingly, errors given by $\mathbf{H} - \widehat{\mathbf{H}}$ will dilute the precision of the position estimation. Neglecting errors, exploiting $\mathbf{H}$ would favour a combined RSS/TDOA estimation approach on the forward link and a combined RSS/AOA approach on the return link. The little difference in distance (a few centimetres) of the user terminal and the closest and the most distant feed translates for narrow band signals [61]

- on the forward link into a deterministic phase difference of the impinging identifier sequences at the user terminal (single antenna),
- and on the return link into a deterministic phase difference according to the direction of signal arrival at the satellite.

Additionally, power (or equivalently amplitude) differences occur due to the antenna pattern with respect to the user terminal position, as mathematically demonstrated below. In other words, the user terminal location influences the received signal power (or amplitude) and phase angle. Hence estimates of those figures are a baseline for position estimation.

Being $\mathbf{h}_k = \{\mathrm{h}_{k,1}, \mathrm{h}_{k,2}, \dots, \mathrm{h}_{k,N}\}$ the channel matrix (vector) between the multi-beam antenna (with N feeds) of the satellite and the k-th user terminal, each entry in $\mathbf{h}_k$ is a complex value composed as follows:

$$\mathrm{h}_{k,n}\big|_{n\in\{1,2,\dots,N\}} = a_{k,n} \cdot e^{j\cdot\theta_{k,n}} \cdot a_{k,0} \cdot e^{j\cdot\theta_{k,0}}, \tag{4.1}$$

where

- $a_{k,n}$ and $\theta_{k,n}$ account for the n-th feed gain and phase shift, respectively, induced by the multi-beam antenna with respect to the position of the k-th user.
- $a_{k,0}$ and $\theta_{k,0}$ account for the gain (inverse attenuation) and phase shift induced by the physical link between the satellite and user terminal k.

By inspection of (4.1) it becomes obvious that all narrowband signals emitted by the satellite towards user terminal k travel on the same physical path, thus encounter the same impairments, so the term $a_{k,0} \cdot e^{j \cdot \theta_{k,0}}$ equals for all signal components. By forming the ratio

$$\beta_{k,n_1,n_2}\big|_{n_1,n_2 \in \{1,\dots,N\}} = \frac{\mathrm{h}_{k,n_1}}{\mathrm{h}_{k,n_2}} = \frac{a_{k,n_1} \cdot e^{j \cdot \theta_{k,n_1}}}{a_{k,n_2} \cdot e^{j \cdot \theta_{k,n_2}}} \tag{4.2}$$

the physical path cancels out, so β_{k,n_1,n_2} only depends on the user terminal position with respect to the properties given in the antenna model. The above considerations likewise apply for forward and return link.

Say $\widehat{\mathbf{B}}_k$ be the $N \times N$ ratio matrix generated with channel estimates for the k-th user terminal, a representative subset of $\widehat{\mathbf{B}}_k$ can be used to be mapped to ratios generated from the antenna model. The position with the best match then represents the position estimate. This task, however, could lead to high computational loads, thus some *a priori* knowledge would help. A fairly simple approach could be to initialize to positions within the coverage area of the best accessed feed and/or to track with previously generated position estimations. Kalman filters as well as grid-based approaches or particle filters are suggested in the literature with respect to the latter [67][70].

4.3.3 LACE on the Forward Link

Accurate channel estimation on the forward link is of high importance for the precoding procedure which strongly influences the achievable overall throughput. In Section 3.3 these estimations are independently obtained for each entry in $\widehat{\mathbf{H}}$, the $(K \times N)$ channel matrix on the forward link, disregarding interrelationships. Knowledge of the user position at the gateway is game changing in that respect, so deterministic interrelations become usable. The signal model and the estimation framework remain the same as introduced in Section 3.3. For a single user terminal, LACE on the forward link necessitates knowledge of the its position, the antenna model and one entity in $\widehat{\mathbf{H}}$ – expediently the one exhibiting the best SNIR. For the k-th user only the strongest entity in the respective channel vector in $\widehat{\mathbf{H}} = \left(\hat{\mathbf{h}}_1, \hat{\mathbf{h}}_2, \dots, \hat{\mathbf{h}}_k, \dots \hat{\mathbf{h}}_K\right)^T$ is required, *i.e.* $\hat{\mathrm{h}}_{k,n_x}$, where $n_x = \arg\max_n \left|\hat{\mathbf{h}}_k\right|^2$, $\hat{\mathbf{h}}_k = \left(\hat{\mathrm{h}}_{k,1}, \hat{\mathrm{h}}_{k,2}, \dots, \hat{\mathrm{h}}_{k,n}, \dots \hat{\mathrm{h}}_{k,N}\right)$. The signalling overhead on the return link may relax, since the user terminal is only required to deliver a single channel value to the gateway (assuming that not all CSIs have to be transmitted for other purposes, *e.g.* position estimation).

Given the user terminal position, the ratios in (4.2) can be obtained from the antenna model. With that and with $\hat{\mathrm{h}}_{k,n_x}$, the estimated channel matrix (vector) for the k-th user terminal can be calculated as

$$\hat{\mathbf{h}}_k^{LA} = \boldsymbol{\beta}_{k,n_x} \cdot \hat{\mathrm{h}}_{k,n_x}, \tag{4.3}$$

where $\hat{\mathbf{h}}_k^{LA} = \left(\hat{h}_{k,1}^{LA}, \hat{h}_{k,2}^{LA}, \dots, \hat{h}_{k,N}^{LA}\right)$, the superscript LA indicates the location-aware estimation, and $\boldsymbol{\beta}_{k,n_x} = \left(\beta_{k,1,n_x}, \beta_{k,2,n_x}, \dots, \beta_{k,N,n_x}\right)$.

The goal when introducing LACE is to reduce the total error in the system. Not surprisingly, the estimation error, which is furnished by $\mathbf{h}_k - \hat{\mathbf{h}}_k$, statistically increases with decreasing SNIR. Estimations of weaker signal components suffer from a relatively higher noise and a relatively higher interference, so their SNIR is much weaker than the one of the strongest signal component. When applying (4.3) all estimated values in $\hat{\mathbf{h}}_k^{LA}$ encounter the best possible SNIR, so the total estimation error reduces due to the exploitation of location knowledge.

Throughout the consecutive paragraphs simulation results are presented, reflecting the impact of different UWs on the estimation performance of LACE. Appropriate methods, as already described in Section 3.3, are applied, namely LACE based on the (pseudo-) inverse and LACE based on correlations. It is to be noticed that the presented results stem from simulations performed throughout a supervised student project [57] and are reprinted with permission. The presented results indicate the estimation accuracy with respect to channel amplitude, since the same conclusions are retrieved from the phase.

4.3.3.1 Ideal LACE

Given perfect knowledge of the user's position and the antenna model, Figure 4.4, Figure 4.5, and Figure 4.6 [57] compare the performance in terms of NMSE of the channel amplitude over the SNR of the strongest received feed; the latter is denoted as SNR with a subscript indicating the best feed's number. Each of the figures depicts in a) results of conventional-type estimations (presented in Section 3.3) and in b) results of LACE-type estimations. The blue solid line indicates the performance curve of the best received feed, whereas the black ones indicate the remaining feed signals. The red dashed line indicates the NCRLB for orthogonal codes, *i.e.* (3.22), whereas the cyan dashed line and the blue dashed line indicate (3.25) and (3.29), , if applicable to the respective figure. All refer to the strongest received feed's signal.

It can be observed that by using LACE the performance for all signal components can achieve the one of the strongest component; this holds true for all introduced estimation

methods on the forward link. When considering the results for Hadamard sequences or PRSs with pseudo-inverse, instead of exploiting information about the antenna model and the user location, channel sounding could be performed; hence, by applying unique words with lengths much larger than currently considered, highly accurate channel estimations could be obtained, from which $\boldsymbol{\beta}_{k,n_x}$ might be retrieved.

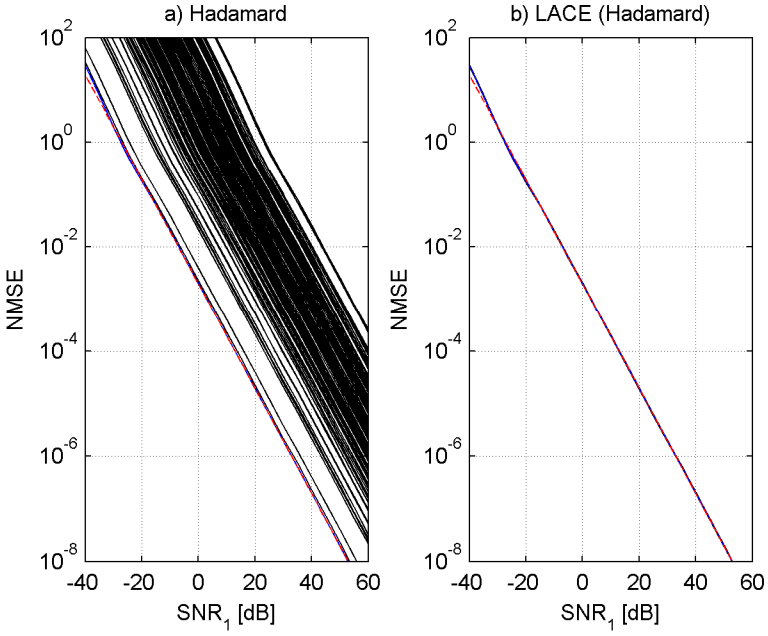

Figure 4.4: LACE with Hadamard identifier sequences

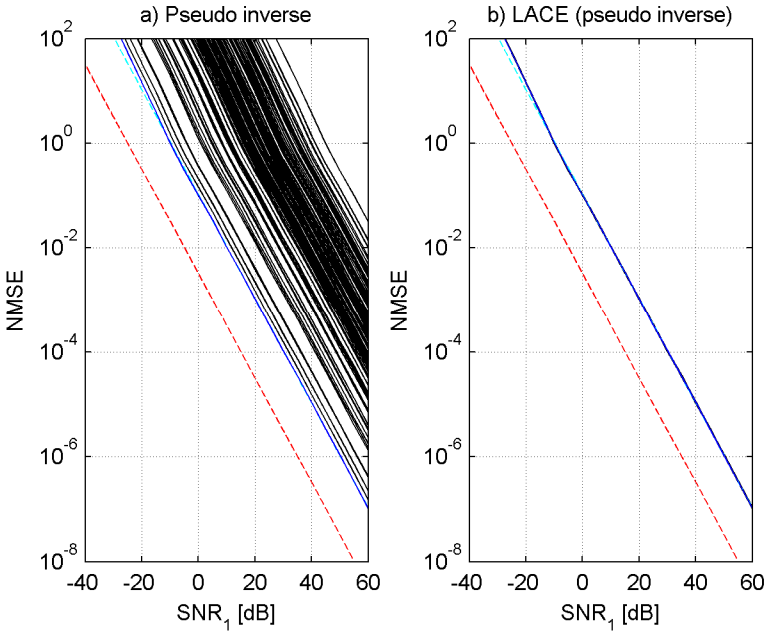

Figure 4.5: LACE with PRSs and pseudo-inverse

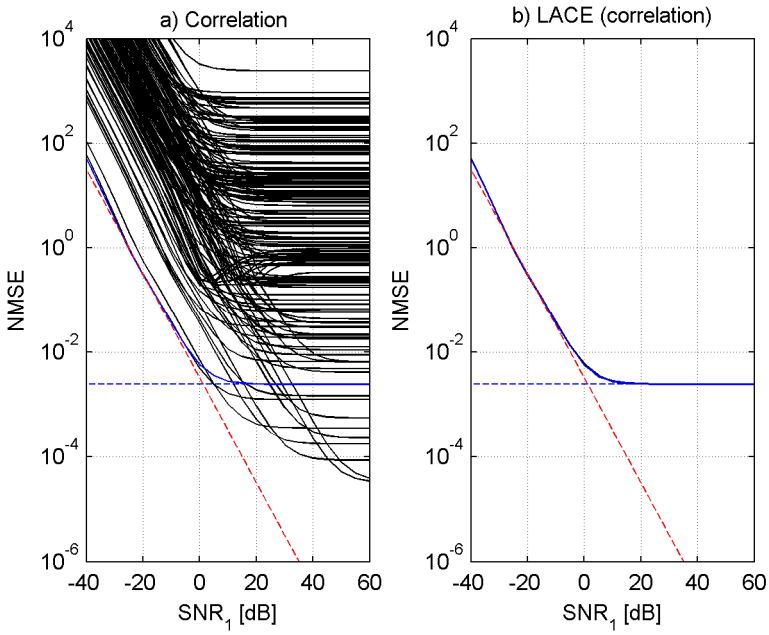

Figure 4.6: LACE with PRS and correlation

4.3.3.2 LACE with Dilution of Position Precision

Assuming perfect knowledge about the antenna model only and a *dilution of position precision* (DOPP) of < 100 m, Figure 4.7, Figure 4.8, and Figure 4.9 [57] indicate the performance in terms of NMSE of the channel amplitude over the SNR of the strongest received feed. The latter is denoted as SNR including a subscript indicating the best feed's number. The blue solid line indicates the performance curve of the best received feed, whereas the black ones indicate the remaining feed signals. The red dashed line indicates the NCRLB for orthogonal codes, *i.e.* (3.22), whereas the cyan dashed line and the blue dashed line indicate (3.25) and (3.29), if applicable to the respective figure. All refer to the strongest received feed's signal.

Not surprisingly, the performance degrades slightly, resulting in jitter floors for Hadamard sequences and PRSs with pseudo-inverse at around 10^{-5}. Since the resulting additional jitter lies below the jitter floor caused by the correlation method, it does not appear in Figure 4.9. Results for DOPP < 10 km in [57] exhibit jitter floors below 10^{-2}.

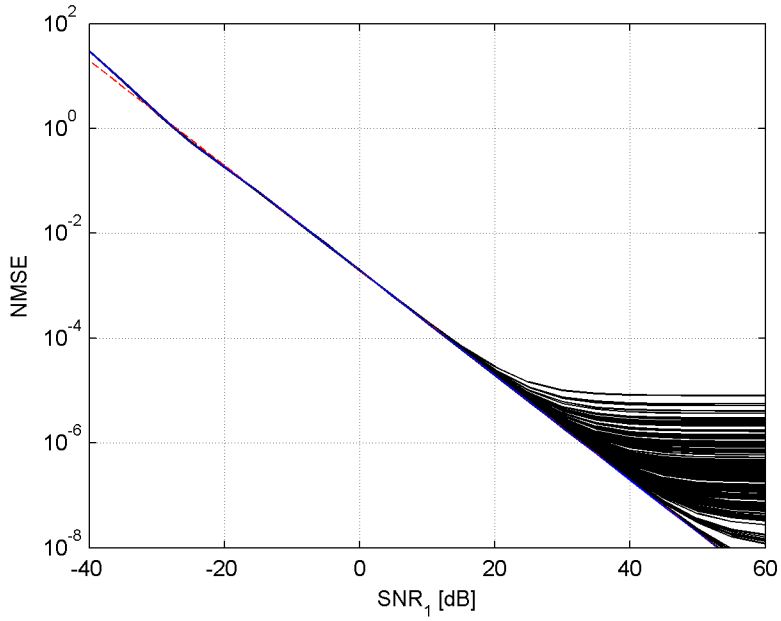

Figure 4.7: LACE performance using Hadamard sequences with DOPP

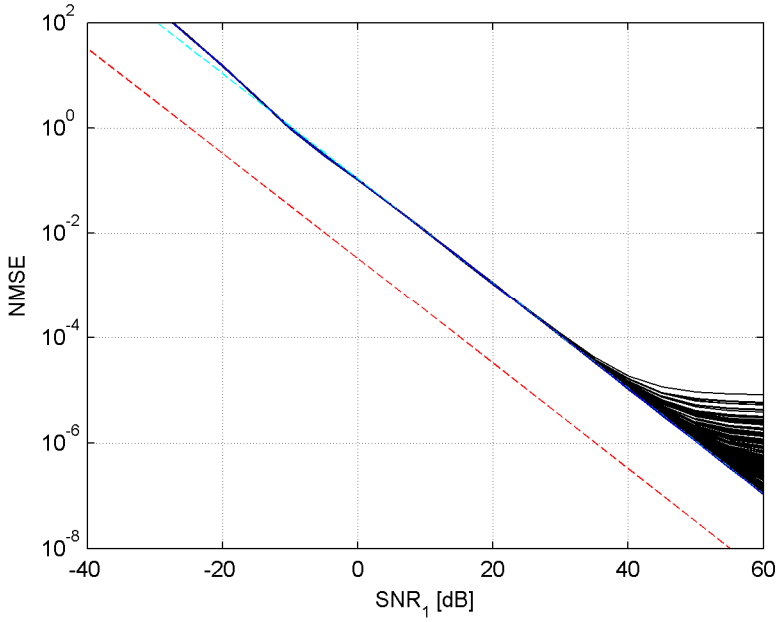

Figure 4.8: LACE performance using the pseudo-inverse with DOPP

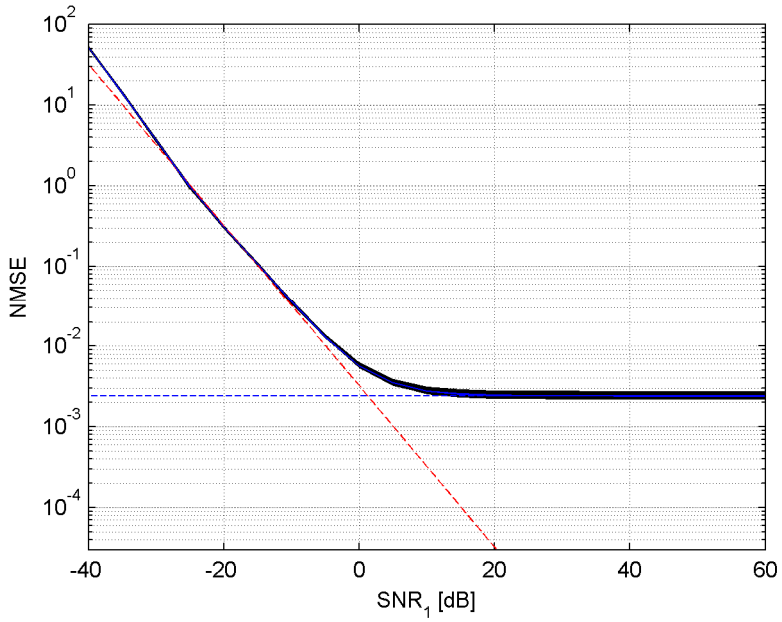

Figure 4.9: LACE performance using correlations with DOPP

4.3.4 LACE on the Return Link

Also on the return link accurate channel estimation is of high importance, not at least to support MUD which is applied to reduce the detrimental interference (*i.e.* MAI) from data. In Section 3.4, channel estimation on the return link was regarded as independent, exhibiting a low performance for weak signal components, but already in Section 4.2 remarkable performance improvements could be obtained through DTR. Similarly to the forward link, LACE is also applicable on the return link based on the signal model described in Section 3.3.1. LACE also incorporates the channel estimates, so the same estimation methods as detailed in Section 3.4 can be used.

Similar to the forward link, the ratios for the return link can be computed using (4.2) given the estimated $(N \times K)$ channel matrix $\widehat{\mathbf{H}} = \left(\hat{\mathbf{h}}_1, \hat{\mathbf{h}}_2, \dots, \hat{\mathbf{h}}_k, \dots \hat{\mathbf{h}}_K\right)$ of the return link, where $\hat{\mathbf{h}}_k = \left(\hat{\mathrm{h}}_{1,k}, \hat{\mathrm{h}}_{2,k}, \dots, \hat{\mathrm{h}}_{3,k}, \dots \hat{\mathrm{h}}_{N,k}\right)^T$, thus the strongest component in $\hat{\mathbf{h}}_k$ is $\hat{\mathrm{h}}_{n_x,k}$, $n_x = \arg\max_n \left|\hat{\mathbf{h}}_k\right|^2$; the entities for the channel vector of the n-th feed, *i.e.* $\hat{\mathbf{h}}_n^{LA} = \left(\hat{\mathrm{h}}_{n,1}^{LA}, \hat{\mathrm{h}}_{n,2}^{LA}, \dots \hat{\mathrm{h}}_{n,k}^{LA}, \dots, \hat{\mathrm{h}}_{n,K}^{LA}\right)$, are then obtained as

$$\hat{\mathrm{h}}_{n,k}^{LA} = \beta_{k,n,n_x} \cdot \hat{\mathrm{h}}_{n_x,k}. \tag{4.4}$$

Subsequent sections investigate the achievable performance of LACE in comparison to the methods introduced in Section 3.4.

4.3.4.1 Performance of Correlation-based LACE

In this paragraph a performance comparison of channel estimation using correlations (as introduced for the return link in Section 3.4) and LACE based on correlations is provided. The latter means that prior to the LACE step $\widehat{\mathbf{H}}$ is estimated using correlations.

For feed 1, Figure 4.10 compares the achievable timing performance of a) channel estimation with correlation (as in Section 3.4) and b) LACE based on correlations. The depicted results refer to the SNR of user terminal 48 for feed 1 labelled at the abscissa as SNR_{48}. The red dashed line in a) indicates the MCRB for the signal of user terminal 48 in both plots[13]. The solid lines represent the MSE of the normalized timing ε; the blue line indicates the signal component of user terminal 48 which is the strongest signal component in feed 1. Close investigations revealed that in b) the signal of user terminal 48 (blue line) was established from a neighbouring feed, since LACE identified a higher incident power there. In total the accuracy of LACE outperforms traditional correlations; moreover, LACE inherently implements the DTR principles as described in Section 4.2.

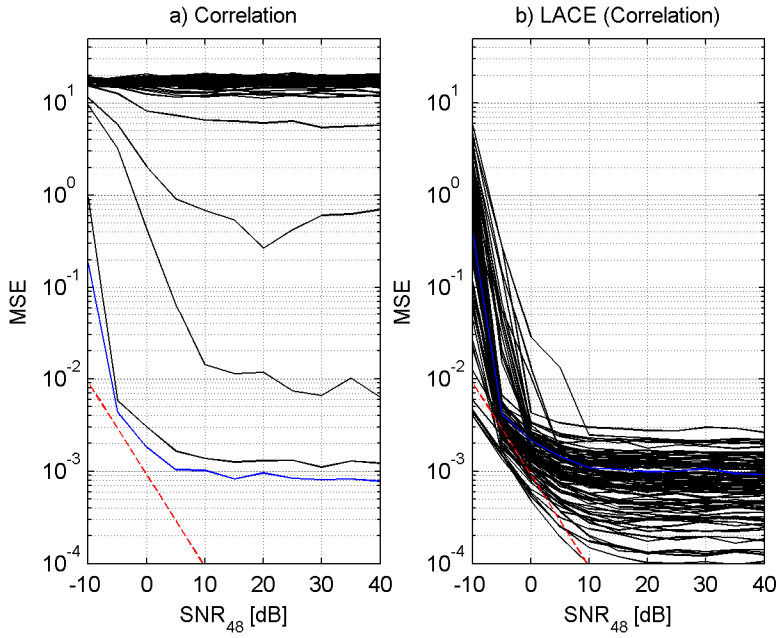

Figure 4.10: Timing estimation performance using LACE based on correlation

[13] The MCRB in b) is in the strict sense not compliant with any of the depicted results of the signal components, because all of them stem from signals of feeds different to feed 1; in other words they were translated with LACE. However, the MCRB matches for the signal of user terminal 48

Figure 4.11 depicts a performance comparison of a) correlations and b) of LACE based on correlations in terms of NMSE of the amplitude. Again the red dashed lines indicate the NCRLB[14] for sub-signals of user terminal 48 (blue solid lines) and the solid lines represent the simulation results for the remaining sub-signals in feed 1. It can be seen that at an SNR_{48} of about 0 dB almost all components exhibit an NMSE of less than 10^{-2}; all signal components in b) achieve estimation accuracies of what in a) only the very best do. These observations also apply to phase estimates; hence it was refrained from providing separate illustrations.

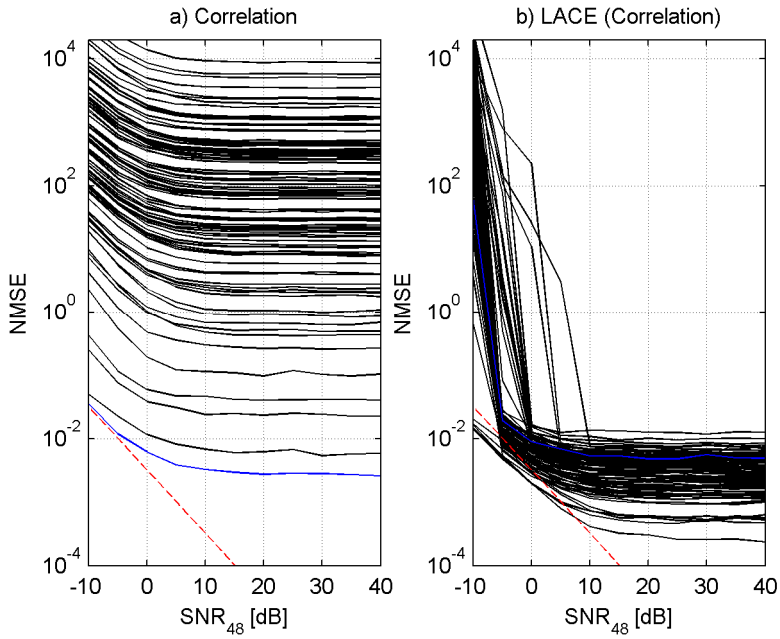

Figure 4.11: Amplitude estimation performance using LACE based on correlations

It could be observed that, by implementing ideal timing recovery results for LACE based on correlations similar to Figure 4.11 b) can be achieved, so no significant degradations from little timing recovery errors occur (details are given in Appendix B).

[14] The NCRLB in b) is not strictly compliant with the depicted results, because all of them stem from signals of feeds different to feed 1; in other words, they were translated with LACE. However, the NCRLB depicts the achievable performance for user terminal 48 in feed 1, thus is supposed to agree with the respective results (blue solid line).

4.3.4.2 Performance of SIC-based LACE

In this paragraph a performance comparison of channel estimation using ISIC-A, as discussed for the return link in Section 3.4.3.4.6, and LACE based on ISIC-A is provided. For all presented simulations, 5 iterations are made for ISIC-A.

Figure 4.12 and Figure 4.13 compare the performance of a) ISIC-A and b) LACE based on ISIC-A in terms of MSE of the normalized timing and NMSE of the amplitude, respectively. Both figures show the performance of feed 1 and use the following colour coding: the red dashed lines indicate the MCRB for the normalized timing and the NCRLB for the amplitude, the solid lines indicate the simulation results for the signal components, whereas the blue solid lines represent the results for user terminal 48 and the black ones the rest.

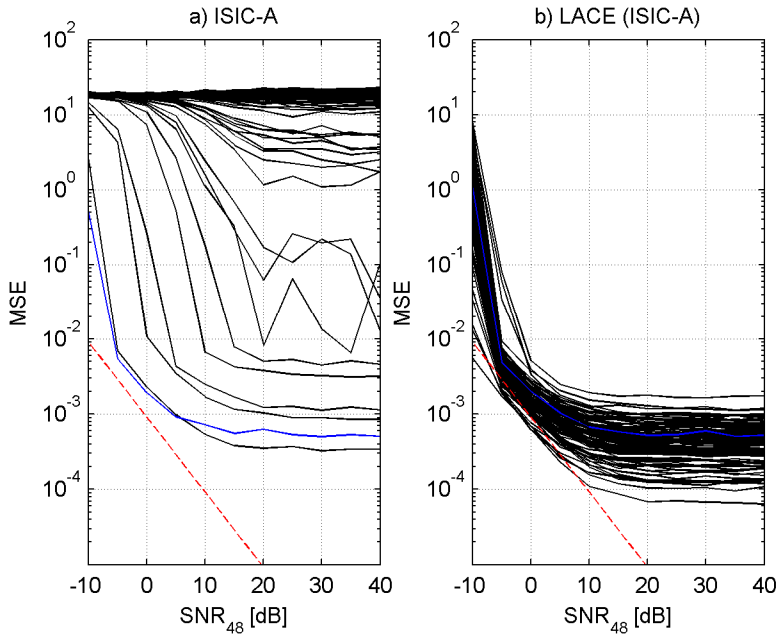

Figure 4.12: Timing estimation performance of LACE based on ISIC-A

Applying LACE significantly improves the overall performance in terms of accuracy especially for the weaker signal components. Furthermore it could be observed that by implementing ideal timing recovery, results for LACE based on ISIC-A increase in accuracy of approximately one order of magnitude. Respective results are detailed in Appendix B.

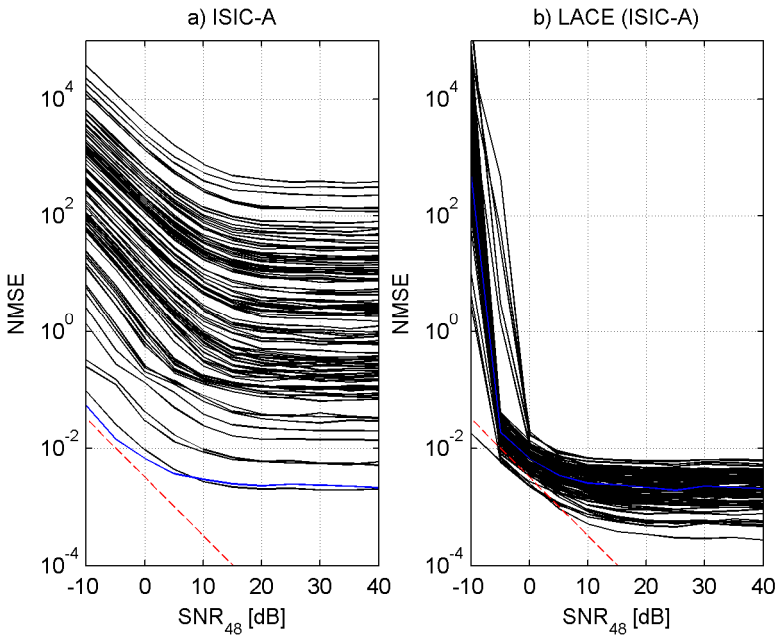

Figure 4.13: Amplitude estimation performance of LACE based on ISIC-A

4.3.4.3 Performance Comparison of Correlation and SIC-based LACE

Within this subsection a performance comparison of LACE based on correlation and on ISIC-A (with 5 iterations) is presented.

Figure 4.14, Figure 4.15, and Figure 4.16 compare the performance in terms of MSE of the normalized timing, NMSE of the amplitude and NMSE of the phase for above mentioned algorithms, respectively. In all before mentioned figures, results for LACE based on correlations are depicted in blue and those for LACE based on ISIC-A are depicted in red. All results refer to an SNR_{48} = 40 dB and the simulation settings outlined in Section 3.4.3.4 apply. It can be seen that LACE based on ISIC-A improves the estimates over practically the whole range of signal components compared to LACE based on correlations. With respect to channel estimation as performed throughout Section 3.4, no huge variations in estimation accuracy for the different signal components are observed, so LACE achieves a similarly good performance for all the components ranging from weak to strong in the investigated feed 1.

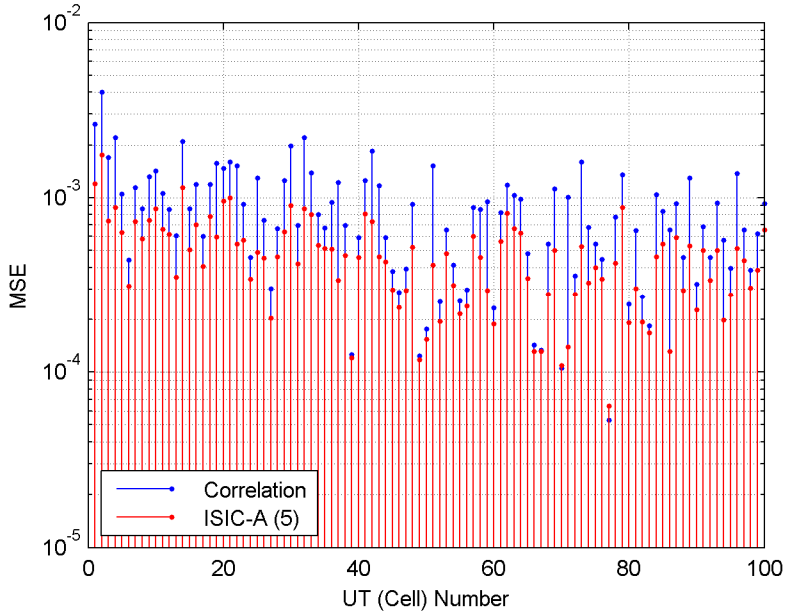

Figure 4.14: Timing estimation comparison of LACE based on correlations and ISIC-A

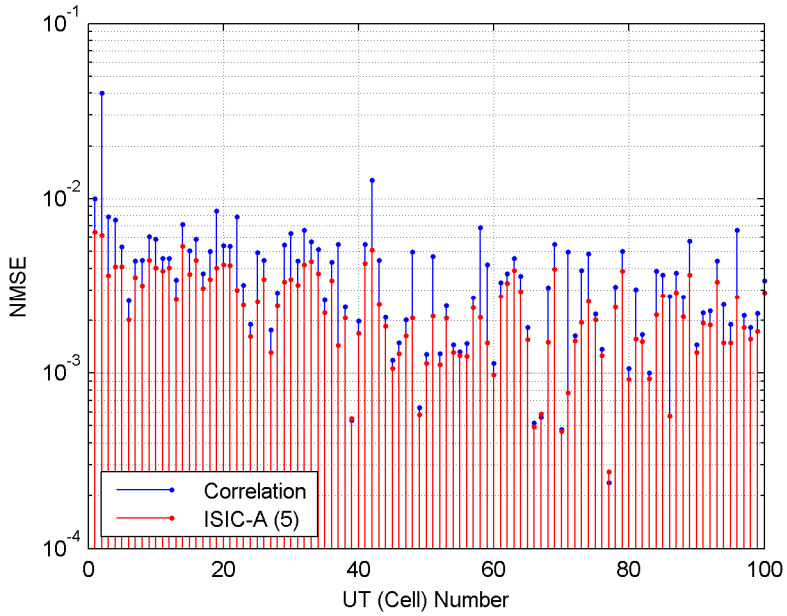

Figure 4.15: Amplitude estimation comparison of LACE based on correlations and ISIC-A

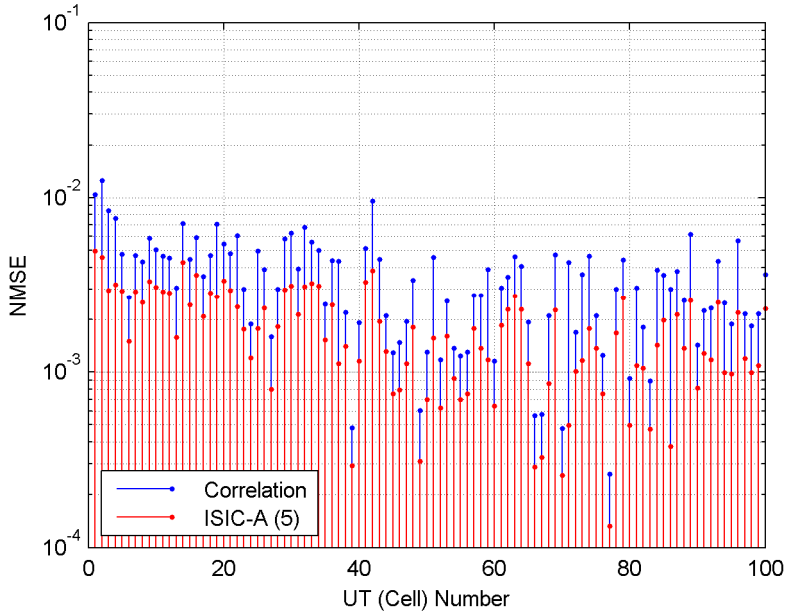

Figure 4.16: Phase estimation comparison of LACE based on correlations and ISIC-A

4.4 Summary

MIMO satellite links exhibit certain deterministic relationships which can be exploited for parameter estimation in order to increase the performance and to reduce the complexity. The presented work was motivated by findings from Chapter 3 approaching MIMO estimations as if they were fully independent. Two evolutionary steps were presented:

The *first* one is *deterministic timing recovery*, which was motivated by the observation that accurate channel estimation requires accurate timing recovery first. Since the latter is inherently given for the forward link, only the return link was considered. A maximum likelihood approach was applied, whereas the time shift was modelled as suggested from the literature for narrowband signals as a deterministic phase shift. It was shown that significant improvements in terms of jitter performance of the channel estimates are possible.

The *second* one is *location-aware* channel estimation, which was motivated by the observation that the signal components of the arriving signal on both the forward and the return link have deterministic interdependencies which can be leveraged by knowledge of the user terminal's position and the antenna model. Important was the observation that the physical path of the MIMO model cancels out. An additionally interesting as-

pect of location-aware channel estimation is that all processing can be done at the gateway, so the hardware requirements of the user terminals do not increase.

It was outlined that a multitude of technologies is available for determining the user terminal's position. After introducing the scenario, investigations for the applicability and performance evaluations on the forward and the return link were presented:

It could be shown for the *forward link* that by using the location-aware principle, the achievable jitter performance of the weaker signal components can be brought up to the one of the strongest component. Modest dilutions of positioning precision resulted in a moderate estimation jitter floor. It was pointed out that Hadamard sequences of a significant length, interspersed in the physical layer framing, could replace the position determination and provide to the cost of extra signalling bandwidth the necessary information instead.

Similar to the forward link, the *return link* exhibited significant performance gains by applying the location-aware principle. It was demonstrated that both correlations and an iterative successive interference cancellation method drastically increase the estimation performance, where the latter achieves the best results.

5 Parameter Estimation on Rician Fading Channels

The work presented in this chapter was mainly carried out within the framework of the *Satellite Communication Network of Experts III Call-off-Order* 2 project supported by the *European Space Agency*. The task executed focused on channel estimation in land-mobile satellite channels tailored to flexible and high performance modulation and coding techniques [71].

Findings and results, created by the author throughout the SatNEx III CoO 2 study, were already integrated in technical notes and reports [72 – 75] and partially published in [76]. However, they are not explicitly quoted in the following to avoid confusion and to support the readability of this thesis. Quotations on the listed documents refer to results and findings not or not only created by the author himself.

5.1 Preface

User mobility is a challenging task for communication systems, especially for satellite based systems due to the relatively long *round-trip time* (RTT). Dynamic methods such as adaptive transmission power or *adaptive coding and modulation* (ACM) are well known in the realm of satellite communications in order to compensate for slow fading effects to exploit the available bandwidth efficiently [77][78]. These two methods are capable, when employed, to achieve the capacity limit of a fading channel, but require accurate, yet timely information about the channel [79]. Adaptively changing the transmission power, however, might be problematic because of non-linearities of amplifiers in the transmission chain. Resorting to ACM schemes is the logic consequence demanding accurate and timely CSI at the transmitters' end. Hence, its estimation is of paramount importance on time-variant links [80, pp. 37-39].

The work presented within this chapter is preparatory for Chapter 6 and motivated by the assumption that a *land-mobile satellite* (LMS) link may be approximated with some restrictions by a *frequency-flat* and *time-selective correlated Rician fading channel* [76]. Hence, the latter is here understood as a test bench for algorithms to be adopted for the LMS channel at a later stage of research.

In accordance with the project partners, parameter estimations should also be performed by periodograms evaluated at the receiver. A set of parameters were identified as necessary figures of merit for the envisaged ACM strategy which are [76][72, pp. 37-38]:

- The SNR
- The SIR or in that context the Rice factor K_R
- The Doppler spread of the mobile link

Subsequently the scenario will be outlined, the periodogram of a Rician channel will be introduced, estimations of carrier parameters, of Doppler spread and power parameters will be discussed and finally their joint performance evaluated.

5.2 The Rician Scenario

As already mentioned, the investigated Rician fading scenario is selected as a test-bed for algorithms opted for LMS channels (see Chapter 6). Throughout the following paragraphs a concise description of the applied Rice channel model will be provided and analytically elucidated.

A typical mobile satellite scenario, as envisaged in SatNEx III CoO2 [80, p. 28], is sketched in Figure 5.1: a geostationary communication satellite serves the mobile user, it receives a direct *line-of-sight* (LOS) signal (blue arrow) and a combination of many constructively and destructively interfering multipath signals (green arrows), which are randomly delayed, affected by *Doppler* shift, scattered, reflected, and diffracted. The combination of the LOS signal and the random (Rayleigh-distributed) multipath signals is described by the Rician (*Nakagami-n*) model [81, pp. 18-22][82, pp. 334-337][83].

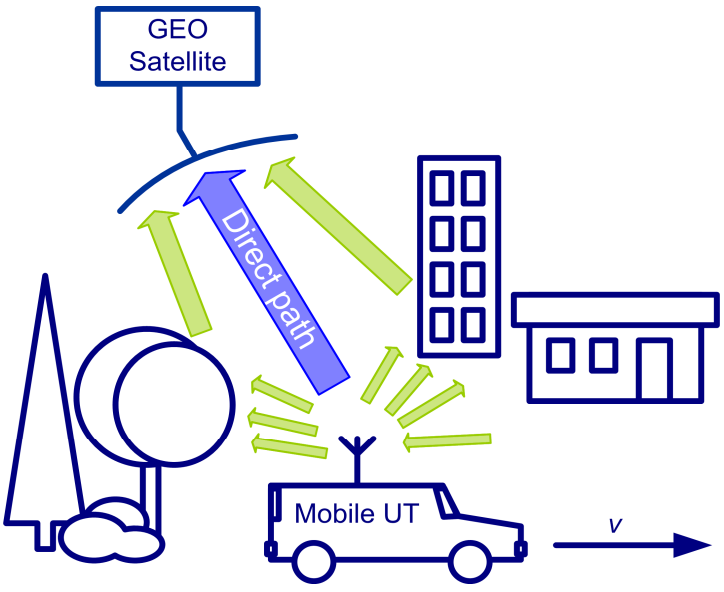

Figure 5.1: Mobile satellite scenario

5.2.1 Rician Signal Model

As already mentioned above, the Rice channel consists of a LOS and a multipath component. Frequency selectivity, which is typical for multipath propagation is considered to be negligible [76].

Figure 5.2 depicts the signal model of the Rician channel including frequency and phase error, ν and θ. The time-selective fading component μ_k is a circular-complex zero-mean Gaussian process with unit variance generated by two mutually independent Gaussian processes (denoted as $u_{k,i}$ and $u_{k,q}$) and a *low pass filter* (LPF) with normalized power, *i.e.* $\sum_k |h_k|^2 = 1$, where h_k represents the k-th filter tap; the properties and shape of the LPF are discussed in Section 5.2.2. The AWGN is represented by w_k, an independent circular-complex zero-mean Gaussian random variable of unit variance. Furthermore, the following nomenclature and assumptions are used [76]:

- c_k … pilot symbol of an *M*-ary PSK alphabet normalized such that $|c_k| = 1$
- S … power of the LOS component
- I … power of the fading process
- N … noise power induced by the complex Gaussian noise process.

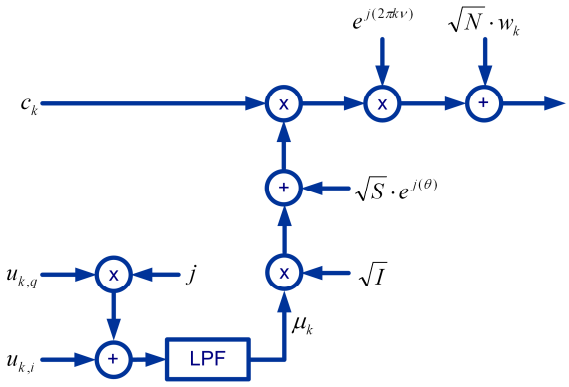

Figure 5.2: Rician channel signal model

Under the assumption of perfect symbol timing, the samples at the output of the receiver matched filter resort to [84][76]

$$r_k = \left(\sqrt{S}\cdot e^{j\theta} + \sqrt{I}\cdot \mu_k\right)\cdot e^{j2\pi k\nu}\cdot c_k + \sqrt{N}\cdot w_k. \tag{5.1}$$

The characteristic channel figures of merit are straightforwardly assessed from (5.1) as the true SNR, *i.e.*

$$SNR = \varrho = \frac{S}{N}, \tag{5.2}$$

and as the SIR or in that context prominently denoted as *Rice factor* K_R, *i.e.*

$$SIR = K_R = \frac{S}{I}. \tag{5.3}$$

By detailed inspection of (5.1) it becomes obvious that the Rician channel can vary from an AWGN channel, *i.e.* no fading ($I = 0$, $K_R = \infty$), to a Rayleigh channel without LOS component ($S = 0$, $K_R = 0$) [84].

5.2.2 Coherence Time and Doppler Spread

Not yet discussed, the *coherence time* T_c and the *Doppler spread* f_D of the fading components are important characteristics of the Rician channel; the latter derives from the vehicle's velocity $\dot{s}$ such that [85][86]

$$f_D = \frac{\dot{s}}{\lambda_c}, \tag{5.4}$$

where λ_c denotes the carrier wavelength.

The coherence time T_c measures the time the fading components are mutually correlated. It relates to the Doppler spread as [81, pp. 16-17]

$$T_c \cong \frac{1}{f_D}. \tag{5.5}$$

5.2.3 Spectrum of the Fading Component

Depending on the scattering model applied, different spectral shapes to model the correlation of the fading components of the Rician channel exist. Prominent in that respect is

the frequently used Jakes filter model, which is used for isotropic scattering [85][86]. Its related PSD is given by [86]

$$S_\mu(f) = \frac{1}{\pi \cdot f_D \cdot \sqrt{1 - f^2/f_D^2}}, |f| < f_D. \tag{5.6}$$

It is to be noticed that $S_\mu(f) = 0$, when $f > f_D$, and that $S_\mu(f_D) = \infty$. A realization of of (5.6) for a Doppler spread of 10% with respect to the symbol rate can be seen in Figure 5.3, where f_D represents the cut-off frequency. A *finite impulse response* (FIR) filter implementation restricted to 201 taps was used therefore (black dashed line). The blue signal represents the simulated power spectrum, indicated as PSD on the ordinate. The peak at $fT_S = 0$ represents the signal power, whereas the remainder is the interference power shaped according to the Jakes PSD.

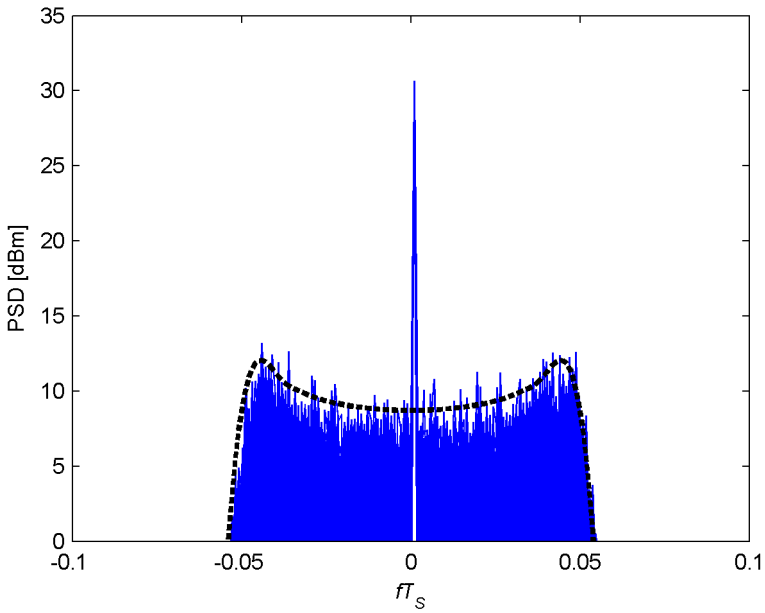

Figure 5.3: Spectrum of the Rician channel
(Jakes filter, 201 tap FIR implementation)

For satellite mobile channels simple Doppler spectra such as the Butterworth filter model for the LPF is suggested in literature. Its related PSD is furnished by

$$S_\mu(f) = \frac{1}{1 + (f/f_D)^{2p}}, \tag{5.7}$$

where p denotes the number of poles [22, p. 247]. A realization of (5.7) for a Doppler spread of 10% with respect to the symbol rate can be seen in Figure 5.4. A 10^{th} order Butterworth filter was implemented therefore (black dashed line). The blue signal, as in Figure 5.3, represents the simulated power spectrum, indicated as PSD on the ordinate. The peak at $fT_S = 0$ represents the signal power, whereas the remainder is the interference power shaped according to the Butterworth LPF.

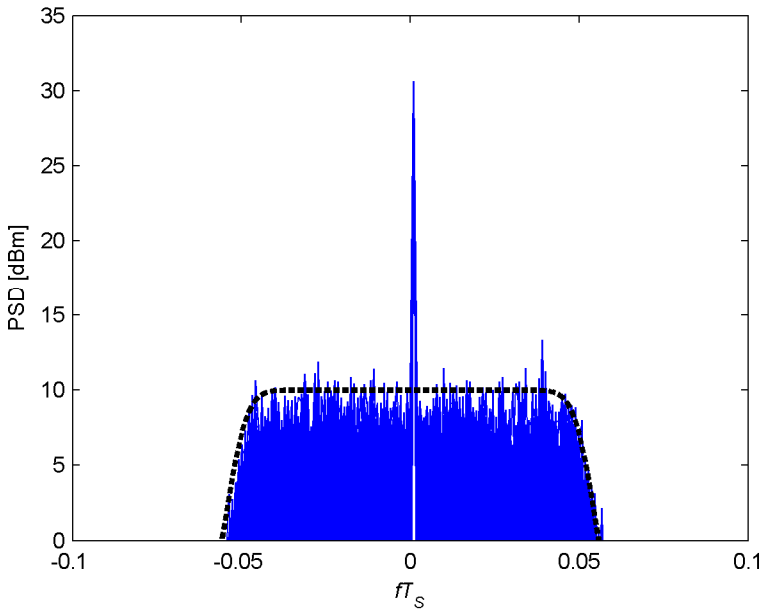

Figure 5.4: Spectrum of the Rician channel
(10^{th} order Butterworth filter)

In the open literature the exact knowledge of the PSD shape characterizing the fading process is regarded to be of minor importance. The relevant parameter is the *Doppler spread* [84][72, p. 38].

5.2.4 Simulation Setup

In the context of the correlated Rician channel, it turned out that both time and frequency domain should be used for parameter estimation.

If not stated otherwise, the following setup for simulations apply [72, pp. 39-40]:

- Ideal symbol timing is presumed.
- $L = 1024$ QPSK training symbols.
- Carrier parameters:
  - Phase error: $\theta \in [-\pi,\ \pi)$.
  - Frequency error: $\nu = \Delta f T_S \in [-0.1, 0.1]$.

- Channel parameters:
  - LPF to shape the scattering component:
    - Jakes filter (RICE_J), implemented as FIR structure with 201 taps.
    - 10^{th} order Butterworth filter (RICE_BW).
  - Maximum Doppler spread: $f_D = 0.05/T_S$ (or equivalently $B_D = 2 \cdot f_D = 0.1/T_S$).
  - Rice factor (SIR): $K_R \in [0, 10]$ dB.
- A guard band of $k_G = 30$ DFT bins as to improve the power estimates applies.

The *cut-off frequency* f_{co} of the LPF relates to the Doppler spread such that

$$f_{co} = f_D. \tag{5.8}$$

5.3 Periodogram of the Rician Channel

As already mentioned, within the project consortium it was agreed to use also periodograms to establish the estimation framework. Thus, obtaining the spectrum of the Rician channel is necessary. Given the available training sequences, resorting to DA estimations is envisaged, which is implemented by removing the data modulations from (5.1) first. Presuming accurate estimates for carrier frequency and phase, *i.e.* $\hat{\nu}$ and $\hat{\theta}$, this resolves to [76]

$$\begin{aligned} z_k &= c_k^* \cdot r_k \cdot e^{-j(2\pi k\hat{\nu}+\hat{\theta})} \\ &= \sqrt{S} \cdot |c_k|^2 \cdot e^{j[2\pi k(\nu-\hat{\nu})+(\theta-\hat{\theta})]} \\ &\quad +\sqrt{I} \cdot |c_k|^2 \cdot \mu_k \cdot e^{j[2\pi k(\nu-\hat{\nu})-\hat{\theta}]} \\ &\quad +\sqrt{N} \cdot c_k^* \cdot w_k \cdot e^{j(2\pi k\hat{\nu}+\hat{\theta})}. \end{aligned} \tag{5.9}$$

From Section 5.2.1 it follows:

$$\begin{aligned} E\{|c_k|^2\} &= 1 \\ E\{\mu_k\} &= 0 \\ E\{c_k^* \cdot w_k\} &= 0 \end{aligned} \tag{5.10}$$

By taking (5.10) into account, further assuming that $|\nu - \hat{\nu}| \ll 1$ and $\left|\theta - \hat{\theta}\right| \ll 1$, (5.9) reduces to

$$z_k = \sqrt{S} + \sqrt{I} \cdot \eta_k + \sqrt{N} \cdot n_k, \tag{5.11}$$

where η_k and n_k are still circular-complex zero-mean Gaussian variables with unit variance; a vector representation of the Rician channel can be seen in Figure 5.5:

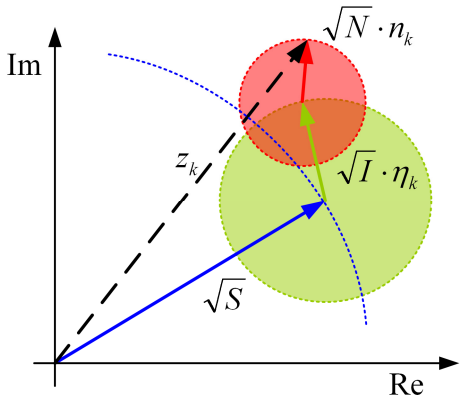

Figure 5.5: Vector diagram of the correlated Rician channel

From (5.11) the L-point periodogram, *i.e.* the *discrete Fourier transform* (DFT), can be calculated as

$$Z_k = \frac{1}{L} \cdot \sum_{i=0}^{L-1} z_i \cdot e^{j \cdot 2\pi \cdot i \cdot \frac{k}{L}}. \tag{5.12}$$

Of course, $\mathbf{Z} = (Z_0, Z_1, \ldots, Z_{L-1})$ comprises the same information as the time series $\mathbf{z} = (z_0, z_1, \ldots, z_{L-1})$. The power spectrum is thus achieved by computing $|Z_k|^2$ [76]. Figure 5.6 sketches the evolution of $|Z_k|^2$, where the signal power S, the interference power I, and the noise power N are indicated separately. The Doppler spread and the symbol rate are represented by the DFT indices k_D and k_S.

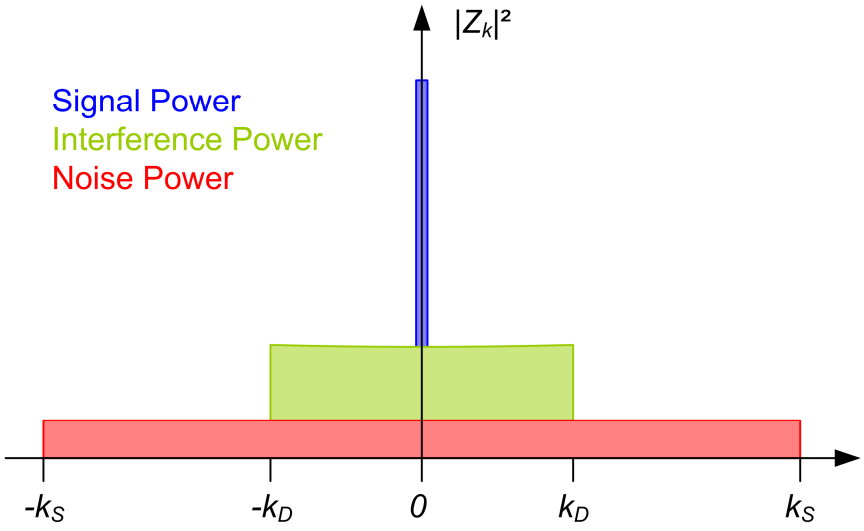

Figure 5.6: Components of the power spectrum
for a correlated Rician channel

Figure 5.7 depicts a realization of the two-sided power spectrum of a RICE_{BW} channel ($S = 0$ dBW, $K_R = 3$ dB, $SNR = 10$ dB, and $B_D T_S = 0.3$) with the zero-frequency component at $k = 0$.

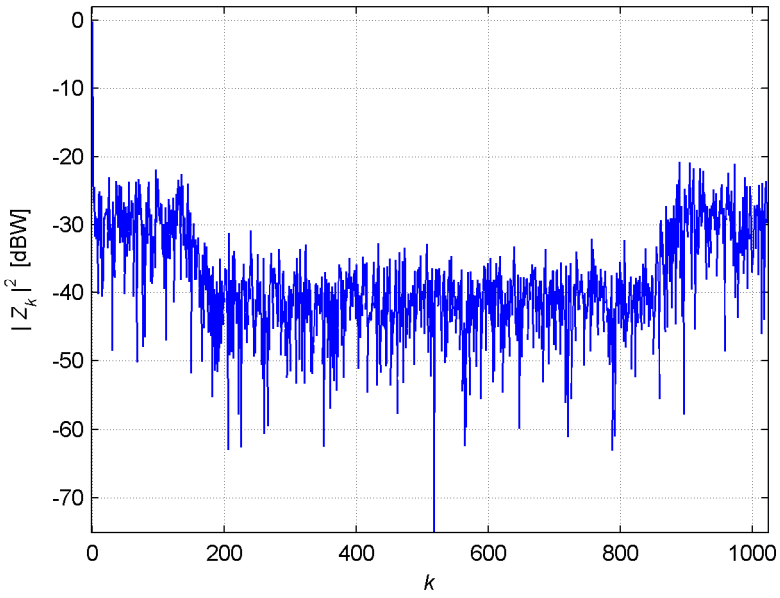

Figure 5.7: Power spectrum of the correlated
Rician channel (Butterworth)

In order to estimate the power figures, *i.e.* S, I, N, and their ratios (see 5.6) from the periodogram, the carrier frequency and phase must be recovered as well as knowledge about the Doppler spread must be available.

5.4 Estimation of the Carrier Parameters

Before estimating the Doppler spread and the power parameters, the carrier frequency and phase need to be recovered, thus estimated and corrected. Throughout the subsequent sections the applicable performance bounds are stated, appropriate estimation algorithms are introduced and their performance for Rician channels is investigated, discussed, as well as benchmarked.

5.4.1 Analytical Performance Bounds

Considering (5.1) and introducing

$$\Phi = 1 + K_R + \varrho \cdot \left(1 + \frac{1}{K_R}\right) \cdot S_\mu(0), \tag{5.13}$$

the analytical performance bound for carrier frequency estimation in correlated Rician channels is given as [84][76]

$$CRLB(\nu) = \frac{3 \cdot \Phi}{2\pi^2 \cdot \varrho \cdot (1 + K_R) \cdot L^3}, \tag{5.14}$$

where it is presumed that $L \gg L_c$, the latter denoting the coherency length of the Rician channel, *i.e.* $L_c = T_c/T_S$. It is to be noticed that $\varrho = S/N$ and that (5.14) depends only on the spectral component at $f = 0$ expressed by $S_\mu(0)$.

The jitter variance of the carrier phase is limited by [76]

$$CRLB(\theta) = \frac{\Phi}{2 \cdot \varrho \cdot (1 + K_R) \cdot L}. \tag{5.15}$$

5.4.2 Carrier Frequency Estimation

Having a training sequence available, resorting to DA frequency estimation algorithms is preferred, since performances close to the theoretical limit can be achieved. In the

context of periodogram-based estimations the RB algorithm [56] is the preferred choice [22, pp. 79-143].

Figure 5.8 depicts the jitter performance of the normalized frequency estimates using the RB estimator at a Doppler spread of $B_D T_S = 0.1$. Simulation results for isotropic scattering (RICE_J) and non-isotropic scattering (RICE_BW) are indicated as diamonds and circlets, respectively, whereas the appropriate NCRLBs are plotted as dashed lines. For the AWGN case (red) the simulation results deviate from the respective NCRLB in the higher SNR region, because of the finite resolution of the frequency domain in the RB estimator. It can further be observed that results from the RICE_BW channel better match with the predicted NCRLBs than the RICE_J ones do. This behaviour can be explained by the fact that $S_\mu(0)$ in (5.14) is achieved assuming an ideal LPF with rectangular shape. Hence, the resulting mismatch is evident for the RICE_J channel rather than for the RICE_BW channel.

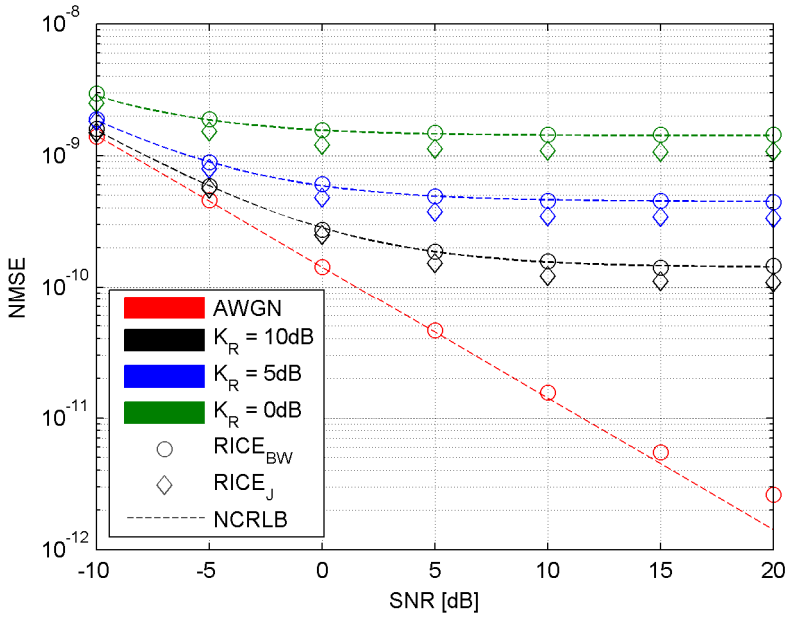

Figure 5.8: Jitter performance of the normalized frequency estimates ($B_D T_S = 0.1$)

For a RICE_BW channel with Rician factor $K_R = 5$ dB, Figure 5.9 depicts the achievable jitter performance in terms of normalized frequency. Besides the AWGN case (red), results for three different Doppler spreads, *i.e.* $B_D T_S = \{0.02, 0.07, 0.1\}$, in green, black, and blue, respectively, are plotted. Again, adequate NCRLBs are indicated as appropriately colour-coded dashed lines; not surprisingly, the NCRLBs perfectly match with the simulation results.

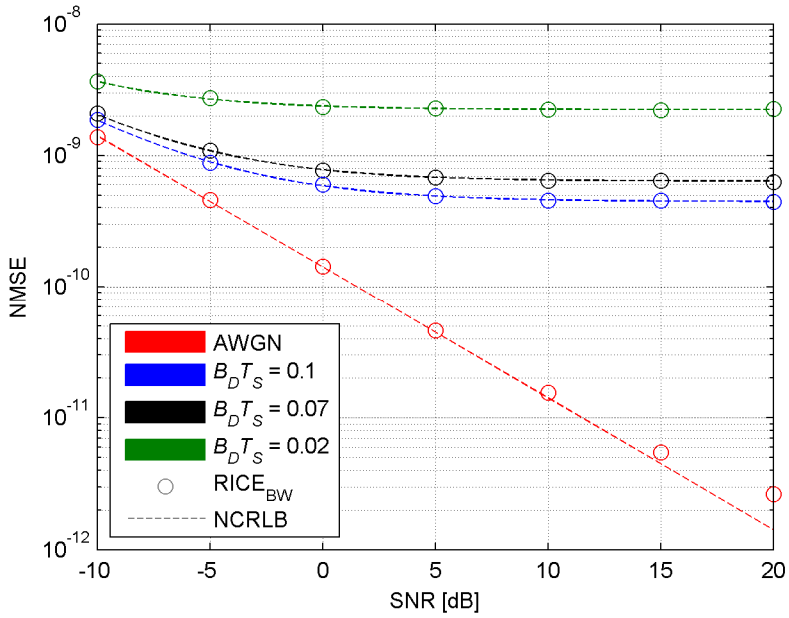

Figure 5.9: Jitter performance of the normalized frequency estimates (K_R = 5 dB)

5.4.3 Carrier Phase Estimation

After having achieved the frequency estimates, the carrier phase offset can be tackled with [76][75, p. 101]

$$\hat{\theta} = \arg\left(\sum_{k=0}^{L-1} c_k^* \cdot r_k \cdot e^{-j2\pi k\hat{\nu}}\right), \tag{5.16}$$

where $\arg(\cdot)$ delivers the argument of the complex sum.

Figure 5.10 depicts the jitter performance of the carrier phase estimates using (5.16) at a Doppler spread of $B_DT_S = 0.1$. Simulation results for the RICE$_{BW}$ and RICE$_J$ channels are indicated as circlets and diamonds, respectively, whereas the appropriate CRLBs are plotted as dashed lines. The results for the AWGN channel are indicated in red, whereas those for the Rice channel are illustrated in black, blue, and red with respect to $K_R = \{10, 5, 0\}$ dB. Akin to carrier frequency estimation, it is observed that results from the RICE$_{BW}$ channel better match with the predicted NCRLBs than the RICE$_J$ ones do for obvious reasons.

Given $K_R = 5$ dB and a RICE$_{BW}$ channel, Figure 5.11 depicts the achievable performance in terms of MSE of the carrier phase. Besides the AWGN case (red), results for

three different Doppler spreads, *i.e.* $B_D T_S = \{0.02, 0.07, 0.1\}$, in green, black, and blue, respectively, are plotted. Again, adequate NCRLBs are indicated as dashed lines, appropriately colour coded; again, the NCRLBs perfectly match with the RICE_{BW} scatter model's simulation results.

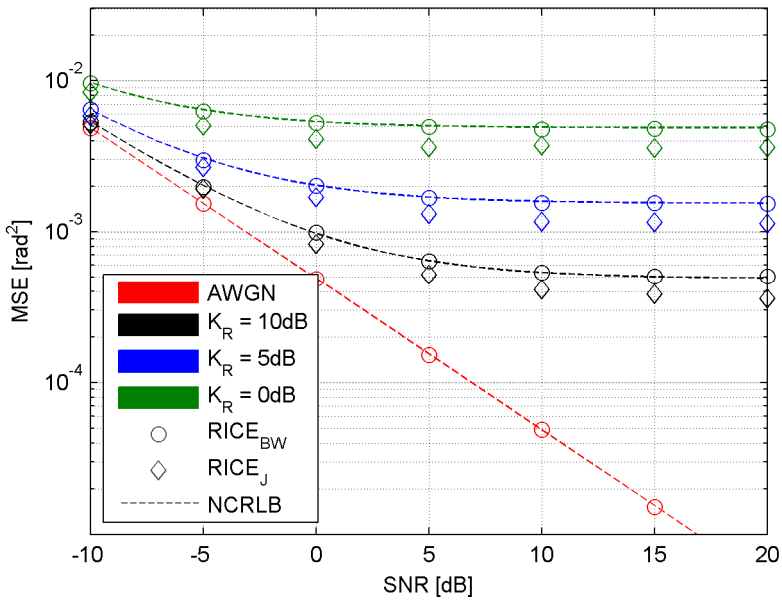

Figure 5.10: Jitter performance of the carrier phase estimates ($B_D T_S = 0.1$)

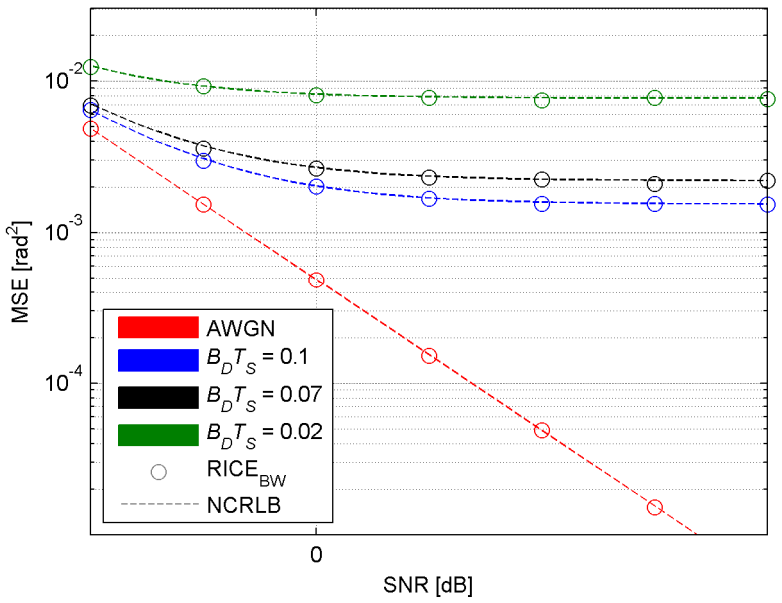

Figure 5.11: Jitter performance of the carrier phase estimates ($K_R = 5$ dB)

5.5 Doppler Spread Estimation

The Doppler spread estimation is supposed to estimate the highest Doppler spread frequency f_D or equivalently its discrete representation k_D (see Figure 5.6). This estimation is obligatory and feeds in to the power parameter estimations explained in Section 5.6; thus any applied Doppler spread estimator is required to operate accurately along a wide SNR and K_R range. The Doppler spread estimation furthermore delivers a measure for the variability of the Rician channel which can be exploited in the context of an ACM scheme or can be translated into the mobile speed in order to improve the performance of the communication system [87].

In [24, pp. 514-533] *level-crossing schemes* are proposed in order to estimate the Doppler spread, but for short observation periods they turn out to be less efficient than spectrum-based or correlation-based algorithms. Thus the periodogram-based algorithm proposed in [87], here denoted as *nonparametric Doppler spread* (NDS) estimation algorithm, was envisaged, because it was claimed to perform better than the schemes proposed in [88-92] [76].

The NDS algorithm implicitly estimates the discrete Doppler spread k_D by monitoring the following inequality:

$$\frac{|Z_o|^{2\beta} + \sum_{k=1}^{k_D}\left(|Z_k|^{2\beta} + |Z_{-k}|^{2\beta}\right)}{\sum_{k=-k_S}^{k_S}|Z_k|^{2\beta}} > \zeta. \tag{5.17}$$

The form factors β and ζ shape the performance of (5.17), values suggested for specific applications can be found in [87]. Figure 5.12 depicts the NDS performance in terms of NMSE of f_D for two selected form factor sets: the blue and green curves were simulated using $\beta = 1.75,\ \zeta = 0.97$ and $\beta = 1,\ \zeta = 0.94$, respectively; a RICE_J channel with $B_D T_S = 0.1$ without frequency error was applied.

Both form factor sets in Figure 5.12 exhibit a limited region of "*good performance*" (assumed to exhibit an NMSE of about 10^{-2} or less). In that respect the blue curve performs well for a wide SNR range, but limited to a very low K_R (< -10 dB), whereas for the green curve it behaves *vice versa*. However, vast trials of different form factor sets could not solve that issue, the SNR/K_R application area for the NDS estimator remained limited. It could be revealed that the NDS approach is in part very susceptible to the LOS component, which in the end limits its applicability. The latter discovery motivated to tweak the NDS algorithm in order to produce an improved version.

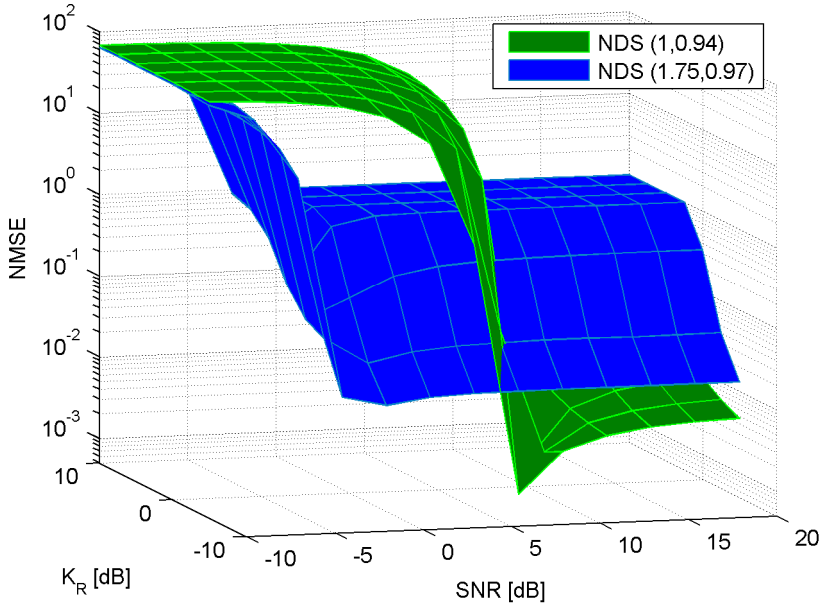

Figure 5.12: Jitter performance of the NDS algorithm for different form factors

5.5.1 Modified Nonparametric Doppler Spread Estimator

As mentioned before, shortcomings in the applicability of the NDS estimator motivated modifications in the algorithm so as to tackle its LOS susceptibility. Since the position of the LOS component in the discrete spectrum is known (presuming successful carrier frequency recovery), it can be blanked out by modifying (5.17) to

$$\frac{\sum_{k=m+1}^{k_D}\left(|Z_k|^{2\beta}+|Z_{-k}|^{2\beta}\right)}{\sum_{k=m+1}^{k_S}\left(|Z_k|^{2\beta}+|Z_{-k}|^{2\beta}\right)} > \zeta. \tag{5.18}$$

The estimator formulated in (5.18) is referred to as *modified NDS* (mNDS). As mentioned, it supresses the LOS component via a pre-specified guard band, which describes specific DFT indices to be left out. An additional form factor m identifies these indices as $k = \{1,2,\ldots,m\}$.

Performance curves and comparisons of the mNDS algorithm can be found in Section 5.5.3.

5.5.2 Novel Heuristic Doppler Spread Estimator

The novel *Heuristic Doppler Spread* (HDS) estimator delivers accurate Doppler spread estimates based on the power spectrum[15] of a Rician (or Rayleigh) fading channel. The basic idea underlying this estimation principle is to compare a function $\boldsymbol{\psi}$, derived from the periodogram, to a set of test functions $\widetilde{\boldsymbol{\psi}}_m$; the index m which provides the closest match between $\boldsymbol{\psi}$ and the respective test function $\widetilde{\boldsymbol{\psi}}_m$ is then translated into a Doppler estimate.

Continuing from (5.12) and with $m = \{0,1,\dots,L/2-1\}$ the values $\psi_m^{(1)}$ and $\psi_m^{(2)}$ are computed as:

$$\psi_m^{(1)} = \sum_{k=0}^{m} |Z_k|^{2\cdot\beta}, \tag{5.19}$$

$$\psi_m^{(2)} = \sum_{k=0}^{m} |Z_{L-1-k}|^{2\cdot\beta}. \tag{5.20}$$

The form factor β is a scalar tuning parameter which is determined heuristically. By extensive simulation work $\beta = 2$ could be identified to perform well allowing the channel to vary in a broad range referring to K_R and SNR.

The m-th entry of $\boldsymbol{\psi}$ computes with (5.19) and (5.20) to

$$\psi_m = \psi_m^{(1)} \cdot \psi_m^{(2)} - \psi_0^{(1)} \cdot \psi_0^{(2)}. \tag{5.21}$$

The test functions $\widetilde{\boldsymbol{\psi}}_m$, $m = \{0,1,\dots,L/2-1\}$, are composed of two straight lines (line fragments) connected to ψ_m. These originate at ψ_0, end at $\psi_{L/2-1}$ and are indicated in the consecutive by the superscripts (a) and (b). Since ψ_m is normalized in (5.21), *i.e.* $\psi_0 = 0$, the test functions are constructed as follows:

[15] It is to be noticed that pilot sequences of length $L = 2^m$, $m \in \mathbb{N}$, should be used in case of establishing the periodogram with a *fast Fourier transform* as to avoid windowing effects through zero padding.

$$\gamma_m^{(a)} = \begin{cases} 0, & m = 0 \\ \dfrac{\psi_m}{m}, & m > 0 \end{cases}, \tag{5.22}$$

$$\gamma_m^{(b)} = \begin{cases} 0\,, & m = {}^{L}\!/_{2} - 1 \\ \dfrac{\psi_{L/2-1} - \psi_m}{{}^{L}\!/_{2} - 1 - m}\,, & m < {}^{L}\!/_{2} - 1 \end{cases}, \tag{5.23}$$

$$\delta_m^{(b)} = \psi_{L/2-1} - \left({}^{L}\!/_{2} - 1\right) \cdot \gamma_m^{(b)}. \tag{5.24}$$

With $\mathbf{a}_m = \{0,1, \dots, m\}$ and $\mathbf{b}_m = \{m+1, m+2, \dots, L/2-1\}$ the respective test function becomes

$$\widetilde{\boldsymbol{\psi}}_m = \left\{\gamma_m^{(a)} \cdot \mathbf{a}_m\,, \quad \gamma_m^{(b)} \cdot \mathbf{b}_m + \delta_m^{(b)}\right\}. \tag{5.25}$$

Finally, by calculating

$$m_{min} = \arg\min_m \sum \left(\boldsymbol{\psi} - \widetilde{\boldsymbol{\psi}}_m\right), \tag{5.26}$$

where $\boldsymbol{\psi} - \widetilde{\boldsymbol{\psi}}_m$ represents the *mean error* (ME), the estimated Doppler spread is established as

$$\hat{f}_D = \frac{m_{min}}{L \cdot T_S}. \tag{5.27}$$

When replacing the term $\boldsymbol{\psi} - \widetilde{\boldsymbol{\psi}}_m$ in (5.26) with $\left(\boldsymbol{\psi} - \widetilde{\boldsymbol{\psi}}_m\right)^2$, *i.e.* the MSE, the performance degrades for Rician fading channels (see Figure 5.14).

Figure 5.13 depicts the estimation principle of the HDS algorithm. The blue curve illustrates $\boldsymbol{\psi}$, whose entries are calculated according to (5.21). The grey dotted and red solid curve(s) as well as the appropriately coloured dots indicate a subset of the test functions from (5.25) and the associated intersection points ψ_m of their line fragments, respective-

ly. In addition, the red curve outlines the test function in (5.26) with its corresponding index m_{min}.

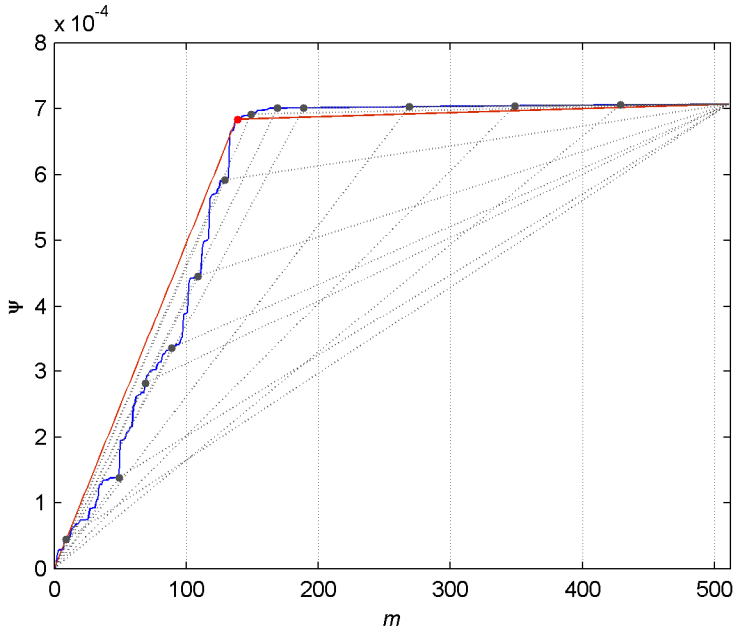

Figure 5.13: HDS estimation principle

Figure 5.14 compares the performance in terms of NMSE of f_D of the two mentioned estimation principles, *i.e.* $\boldsymbol{\psi} - \widetilde{\boldsymbol{\psi}}_m$ representing the ME, and $\left(\boldsymbol{\psi} - \widetilde{\boldsymbol{\psi}}_m\right)^2$ representing the MSE. The simulation is based on the RICE$_J$ channel, a form factor of $\beta = 2$ is applied. As mentioned, the ME approach generally outperforms the MSE approach.

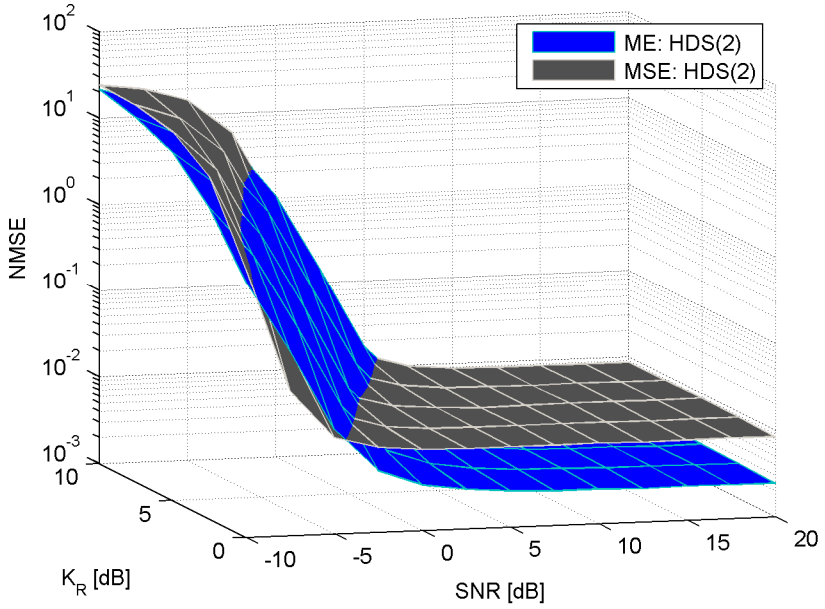

Figure 5.14: HDS performance comparing ME and MSE

It is to be recalled that the NDS and mNDS estimators require two and three form factors, respectively, whereas the HDS estimator requires just a single one.

5.5.3 Doppler Spread Estimator Performance Comparison

Within this section the performance of the three introduced Doppler spread estimators is investigated and compared. Therefore the most promising, heuristically discovered form factor sets are applied as follows:

- NDS: $\beta = 1;\ \zeta = 0.94$
- mNDS: $\beta = 3;\ \zeta = 0.97;\ m = 0$
- HDS: $\beta = 2$.

In the subsequent paragraphs various figures of merit for these three estimators will be tested and compared: sensitivity to Doppler spread, different scattering models, their bias behaviour, and the success rate.

Nevertheless, it will be shown that the HDS estimator possesses favourable properties which make it most attractive for power estimations.

5.5.3.1 Sensitivity to Doppler Spread

Figure 5.15 and Figure 5.16 compare the performance in terms of NMSE of f_D for the introduced estimators on a RICE_{BW} channel. It can be seen, that in both figures the HDS estimator outperforms the others, whereas obviously the higher Doppler spread in Figure 5.16 can be estimated more accurately compared to Figure 5.15.

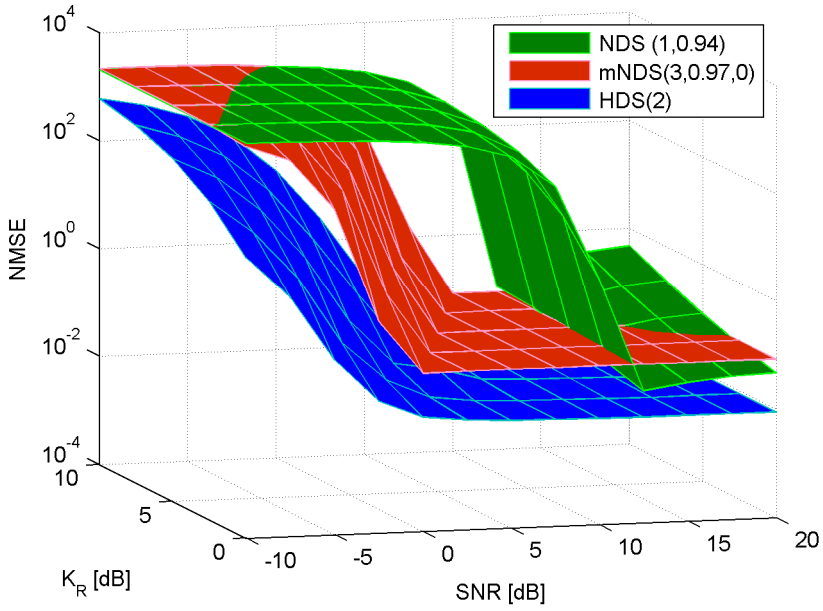

Figure 5.15: Jitter performance of the Doppler spread estimators ($B_D T_S = 0.02$)

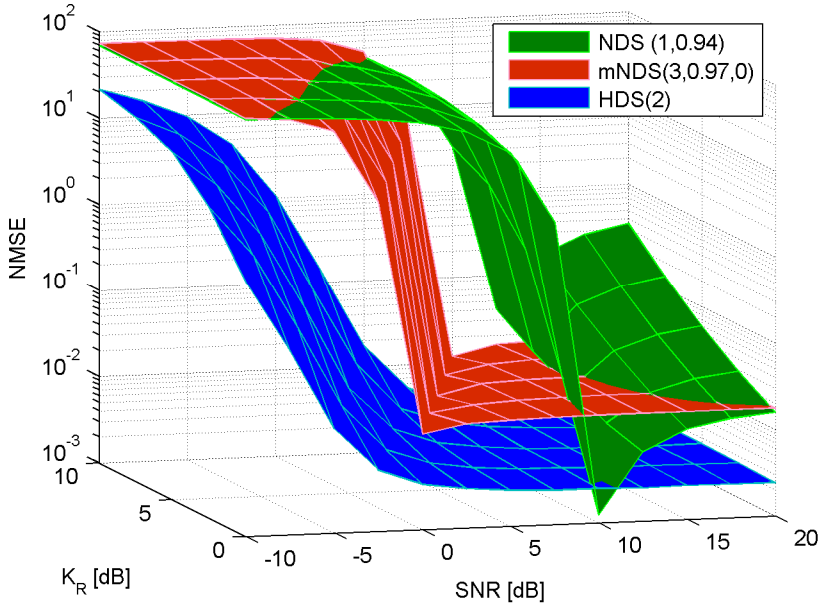

Figure 5.16: Jitter performance of the Doppler spread estimators ($B_D T_S = 0.1$)

5.5.3.2 Isotropic and Non-Isotropic Scattering

The jitter performances of the Doppler spread estimators on isotropic and non-isotropic scattering Rician channels ($K_R = 5\text{dB},\ B_D T_S = 0.1$) are depicted in Figure 5.17 a) and b), respectively. Results for the NDS estimator are plotted in green, those for the mNDS and HDS estimators in red and blue.

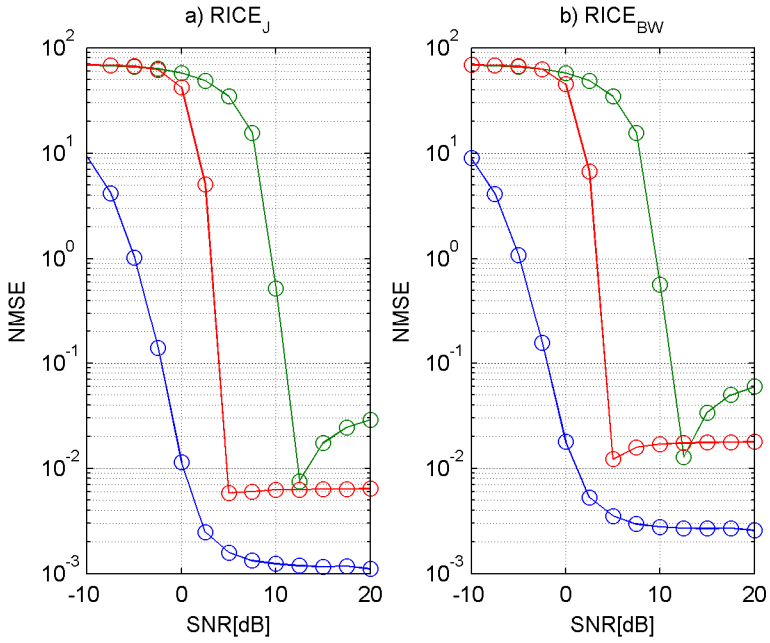

Figure 5.17: Doppler spread estimators at different scattering ($K_R = 5$ dB, $B_D T_S = 0.01$)

Interestingly, the jitter performance in Figure 5.17 is better for the RICE_{J} channel than for the RICE_{BW} channel, which obviously follows from the fact that the isotropic scatter model possesses relatively more interference energy close to $|f_D|$. Henceforth, the transition in the periodogram between the $f \leq f_D$ region and the $f > f_D$ region is easier to detect (see Figure 5.6). An additional comparison supporting this statement can be found in Appendix C-(a).

5.5.3.3 Estimation Bias

Results comparing the *normalized mean estimator value* (NMEV) on the RICE_{BW} channel are presented in Figure 5.18 in order to point out the bias which the different estimation principles suffer from. A NMEV of 1 means *"bias-free"*. For each estimator (NDS/green, mNDS/red, HDS/blue) results are plotted for different Doppler spreads, *i.e.* $B_D T_S = \{0.02, 0.07, 0.1\}$. For all Doppler spreads it is obvious that the HDS estimator exhibits the best performance with respect to bias. By close inspection of the presented results the HDS estimator tends to slightly overestimate the Doppler spread then to underestimate it as the NDS and the mNDS estimators tend to do. Of course underestimating the Doppler spread has negative consequences for the accuracy of the power estimates.

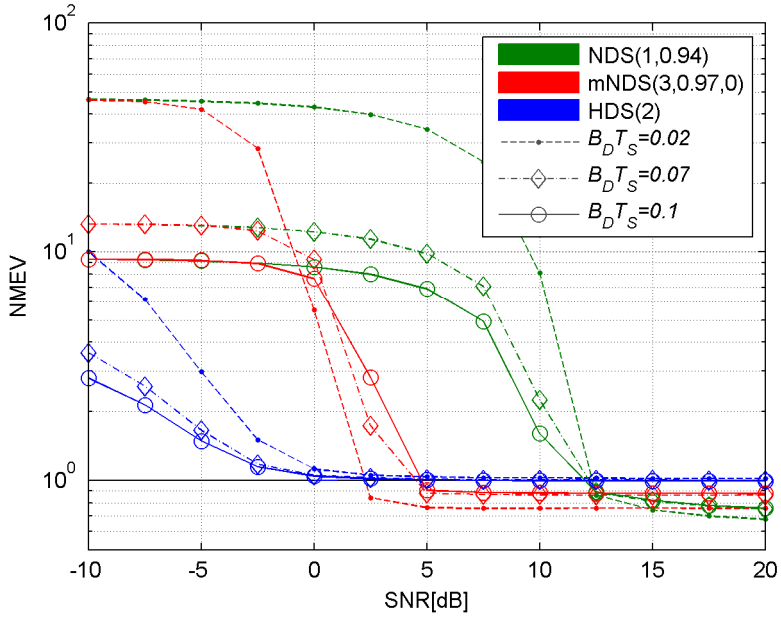

Figure 5.18: Doppler spread estimator bias comparison (K_R = 5 dB)

Figure 5.19 depicts for a RICE_{J} channel with $B_D T_S = 0.1$ and $K_R = \{0, 5, 10\}$ dB the achievable NMEV. Using the same colour coding as for the previous figure, the previ-

ously drawn conclusion attesting the HDS estimator the most favourable bias behaviour is supported.

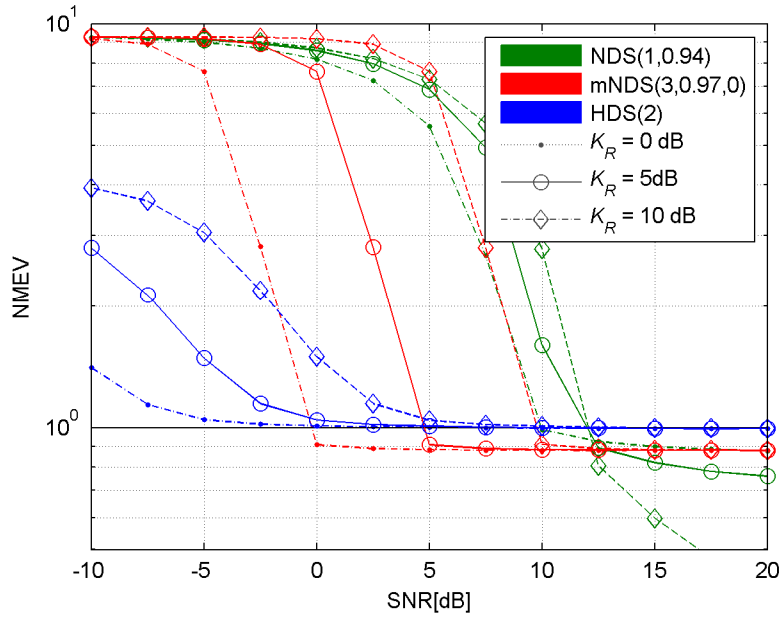

Figure 5.19: Doppler spread estimator bias comparison at ($B_D T_S = 0.1$)

Results outlining the beneficial behaviour of the HDS estimator with respect to the achievable success rate of the consecutive power estimations can be found in Appendix C-(b).

5.6 Estimation of the Power Parameters

As the carrier frequency and phase error is corrected and the Doppler spread on the Rician channel is known, the power estimates can be performed. The parameters so obtained, *i.e.* S, I, N, and more importantly their ratios SNR and SIR are relevant figures of merit so as to adopt an ACM scheme accordingly [72, pp. 41-43].

In the following, the analytical lower bounds are stated and the power parameter estimation is introduced. Within the context of the latter, two estimators are proposed – named without creative effort as estimator A and estimator B – and their performance is evaluated.

5.6.1 Analytical Performance Bounds

The CRLBs applicable to the power parameter estimates and their ratios were derived in [93] and [76] based on the work in [84] and [26, pp. 27-81]. As far as used in simulations the bounds are stated below; they were derived conditioned that $L \gg L_c$ and that the PSD of the fading component is flat, *i.e.* $S_\mu(0) = S_\mu(f)$, $f \leq f_D$, and $S_\mu(f) = 0$, $f > f_D$.

With $\varrho = S/N$ and $K_R = S/I$ the diagonal elements of the FIM are given as [76]:

$$J_{33} = \frac{2 \cdot L \cdot (1 + K_R)}{\mathrm{N} \cdot \Phi}, \tag{5.28}$$

$$J_{44} = \frac{L}{N^2} \cdot \left\{ (1 - B_D T_S) + B_D T_S \cdot \left[\frac{1 + K_R}{\Phi} \right]^2 \right\}, \tag{5.29}$$

$$J_{45} = \frac{L \cdot B_D T_S}{N^2} \cdot \frac{\varrho \cdot (1 + K_R)^2 \cdot S_\mu(0)}{K_R \cdot \Phi^2}, \tag{5.30}$$

$$J_{55} = \frac{L \cdot B_D T_S}{N^2} \cdot \left(\frac{\varrho \cdot \left(1 + \frac{1}{K_R}\right) \cdot S_\mu(0)}{\Phi} \right)^2. \tag{5.31}$$

From above the NCRLBs for the power estimates are given as [93]:

$$NCRLB(S) = \frac{CRLB(S)}{S^2} = \frac{2\Phi}{\varrho \cdot (1 + K_R) \cdot L}, \tag{5.32}$$

$$NCRLB(I) = \frac{CRLB(I)}{I^2} = \frac{1}{I^2} \cdot \frac{J_{44}}{J_{44} \cdot J_{55} - J_{45}^2}, \tag{5.33}$$

$$NCRLB(N) = \frac{CRLB(N)}{N^2} = \frac{1}{N^2} \cdot \frac{J_{55}}{J_{44} \cdot J_{55} - J_{45}^2}. \tag{5.34}$$

In the high SNR regime (5.32), (5.33), and (5.34) simplify to [93]:

$$NCRLB(S)|_{\varrho \to \infty} = \frac{2 \cdot S_\mu(0)}{L \cdot K_R}, \tag{5.35}$$

$$NCRLB(I)|_{\varrho \to \infty} = 0, \tag{5.36}$$

$$NCRLB(N)|_{\varrho\to\infty} = \frac{1}{L \cdot (1 - B_D T_S)}. \tag{5.37}$$

Estimations of S and N naturally suffer from a jitter floor given in (5.35) and (5.37), whereas actually no jitter floor imposes the estimations of I according to (5.36). Furthermore interesting is the fact that (5.32) depends on the zero frequency component of the scatter model only and not on the spectrum itself – a property which can also be observed below [76].

For the power ratios the NCRLBs are obtained as [76][93]:

$$NCRLB(\varrho) = \frac{CRLB(\varrho)}{\varrho^2} = \frac{4}{J_{33} \cdot \varrho} + \frac{J_{55}}{J_{44} \cdot J_{55} - J_{45}^2}, \tag{5.38}$$

$$\begin{aligned} NCRLB(K_R) &= \frac{CRLB(K_R)}{K_R^2} \\ &= \frac{4}{J_{33} \cdot \varrho} + \frac{K_R^2}{\varrho^2} \cdot \frac{J_{44}}{J_{44} \cdot J_{55} - J_{45}^2}. \end{aligned} \tag{5.39}$$

In the high SNR regime (5.38) and (5.39) simplify to [76][93]:

$$NCRLB(\varrho)|_{\varrho\to\infty} = \frac{1}{L \cdot (1 - B_D T_S)} + \frac{2 \cdot S_\mu(0)}{L \cdot K_R}, \tag{5.40}$$

$$NCRLB(K_R)|_{\varrho\to\infty} = \frac{2 \cdot S_\mu(0)}{L \cdot K_R}. \tag{5.41}$$

5.6.2 Power Parameter Estimation

Power parameter estimation should be done in the frequency domain. The equations (5.11) and (5.12), as well as the schematic periodogram in Figure 5.6 mark the baseline for that.

Two power parameter estimators – estimator *A* and estimator *B* – are implemented based on the below presented analysis, whereas estimator *A* follows a fully heuristic principle and estimator *B* incorporates a partially heuristic principle.

Recapping that in (5.11) n_k and η_k are mutually independent circular-complex zero mean Gaussian variables with unit variance, that $|\nu - \hat{\nu}| \ll 1$ and $\left|\theta - \hat{\theta}\right| \ll 1$ (negligible residual carrier frequency and phase error) and that $|c_k| = 1$, the zero- and second-order moments straightforwardly yield

$$E\{z_k\} = \sqrt{S} \tag{5.42}$$

and

$$E\{|z_k|^2\} = S + I + N. \tag{5.43}$$

Another independent equation is required in order to extract S, I, and N. Unfortunately the fourth order moment, which is frequently used in that context, represents a combination of (5.42) and (5.43) and is yet not independent. That issue, however, is tackled in the frequency domain: by detailed analysis of (5.12) it becomes clear, that the signal power is concentrated at the zero-frequency bin[16], *i.e.* $k = 0$ (see Figure 5.7), stipulating successful carrier frequency correction. Hence, it is

$$|Z_0|^2 = S + I_0 + \bar{N}, \tag{5.44}$$

whereas on the one hand I_0 depends on the interference power I, the scattering model $S_\mu(f)$ and the normalized Doppler spread $B_D T_S$, the average noise power $\bar{N}$ on the other hand depends on N only (given a fixed observation bandwidth), since n_k has a flat spectrum in the range of $\pm k_S$; considering that and the fact that the interference power is band-limited to $\pm k_D$, where $|k_D| \ll |k_S|$ (see Figure 5.6) the noise power is estimated as [75, pp. 101-103][76]

$$\widehat{N} = \frac{L}{2 \cdot (k_S - k_D)} \cdot \sum_{|k| > k_S - k_D} |Z_0|^2. \tag{5.45}$$

[16] Resorting to FFT instead of DFT for obtaining the periodogram requires some attention: zero padding will cause a windowing effect thus blurring the spectrum, which in turn dilutes the accuracy of the estimations. In order to avoid that employing training sequences with $L = 2^m$, $m \in \mathbb{N}$, is suggested.

Considering the Doppler spread to be estimated and a guard band interspersed, the latter represented by k_G, (5.45) can be rewritten as

$$\widehat{N} = \frac{L}{2 \cdot (k_S - \lceil \hat{k}_D + k_G \rceil)} \cdot \sum_{|k| > k_S - \lceil \hat{k}_D + k_G \rceil} |Z_0|^2, \tag{5.46}$$

where $k_S \gg E\{\hat{k}_D\} + k_G$[17]. The guard band interspersion bolsters the confidentiality to estimate N based on DFT bins located outside of $\pm k_S$ only. The filters implemented in the Rice simulation model are not strictly band-limited, so little portions of interference power spill into the noise estimations, but these unwanted influences decrease quickly in strength at $|k| \gg |k_D|$.

5.6.2.1 Estimator *A*

The estimator *A*, based on a fully heuristic approach, exploits the periodogram in order to estimate $\hat{S}$, $\hat{I}$, and $\widehat{N}$ as well as their ratios. Therefore it first establishes the noise power estimate using (5.46). Secondly, $\hat{I}'$ is estimated presuming $k_D + k_G \gg 1$ with

$$\hat{I}' = \sum_{\substack{k=-\lceil k_D + k_G \rceil \\ k \neq 0}}^{\lceil k_D + k_G \rceil} \left(|Z_k|^2 - \frac{\widehat{N}}{L} \right). \tag{5.47}$$

To obtain the total interference power, *i.e.* $\hat{I} = \hat{I}_0 + \hat{I}'$, the interference portion $\hat{I}_0$ adhesive to the zero frequency component must be found. Hence, to estimate it, *a priori* knowledge of the Doppler spread, its shape and the average interference power is required. Whereas the first and third may be regarded as already established, accurate knowledge of the second is fairly theoretical. Anyway, given $\widehat{N}$, $\hat{I}_0$ may be assessed under the assumption of a flat Doppler spread spectrum as

$$\hat{I}_0 = \bar{I} = \frac{\hat{I}'}{2 \cdot k_D}, \tag{5.48}$$

whereas for the Jakes model it deduces to (see Appendix C-(c))

---

[17] The notation using the expectation value of $\hat{k}_D$, i.e. $E[\hat{k}_D]$, was chosen in order to constitute the possibility that the inequality does not hold true in cases of erroneous Doppler spread estimations.

$$\hat{I}_0 = \frac{2 \cdot \bar{I}}{\pi}. \tag{5.49}$$

From that the signal power can be obtained by reshaping (5.44) accordingly, *i.e.*

$$\hat{S} = |Z_0|^2 - \hat{I}_0 - \bar{N}. \tag{5.50}$$

5.6.2.2 Estimator *B*

Contrary to estimator *A*, estimator *B* adheres to a partially heuristic approach only. It implements the noise power estimation as stipulated in (5.46) and exploits the analytical relationships in (5.42) and (5.43). When processing the latter in a practical system, only a limited number of observations of z_k, $k = 0,1, \ldots, \mathrm{L} - 1$, is available resulting in an averaging process [75, pp. 101-102][76]; solving (5.42) provides the signal power estimate as

$$\sqrt{\hat{S}} = \frac{1}{L} \cdot \sum_{k=0}^{L-1} z_k \tag{5.51}$$

and (5.43) is implemented using the L-point periodogram, hence it is $\mathbf{Z} = \mathrm{DFT}(\mathbf{z})$, so

$$\sum_{k=0}^{L-1} |Z_k|^2 = \hat{S} + \hat{I} + \widehat{N}. \tag{5.52}$$

By simply rearranging (5.52) the interference power estimate can straightforwardly be achieved as

$$\hat{I} = \sum_{k=0}^{L-1} |Z_k|^2 - \hat{S} - \bar{N}. \tag{5.53}$$

5.6.2.3 Performance Comparison of the Power Estimators

In the following both previously described estimators are compared. Notwithstanding the general simulation settings as outlined in 5.2.4, the following settings differ for Figure 5.20 and Figure 5.21:

- No frequency error.
- Doppler spread: $B_D T_S = 0.1$, ideally known.
- Guard band: $k_G = 30$ DFT bins.
- $K_R = 5$ dB.

Figure 5.20 and Figure 5.21 compare the performance in terms of NMSE of the SNR and K_R estimates of the introduced estimators *A* and *B* indicated in blue and green, respectively; each of which are further distinguished according to the applied scatter model: RICE_{BW} and RICE_{J} results are marked as circlets and diamonds. Dashed black lines indicate the appropriate NCRLB for the Rice channel (see 5.6.1) and the red dashed line in Figure 5.20 indicates the NCRLB for AWGN conditions.

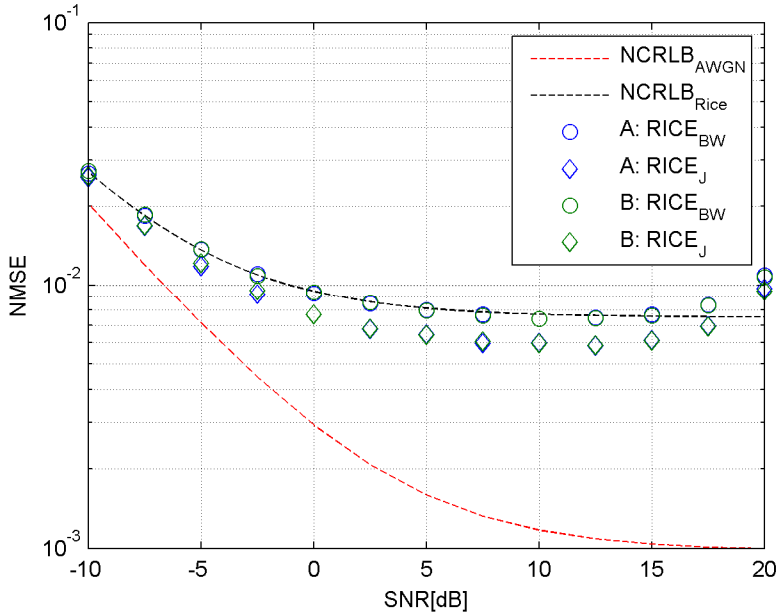

Figure 5.20: NMSE comparison for estimators *A* and *B* of the SNR estimation

It can be seen in Figure 5.20 that both estimators perform as predicted by the NCRLB for the RICE_{BW} fading model, since it better approaches a flat fading spectrum presumed for the NCRLB derivation. In Figure 5.21 the simulated results deviate from the predicted bound which finally is caused by a bias effect. However, no significant differences between both estimators can be observed. Further results supporting this observa-

tion and closely investigating the power estimates rather than their ratios can be found in Appendix C-(d).

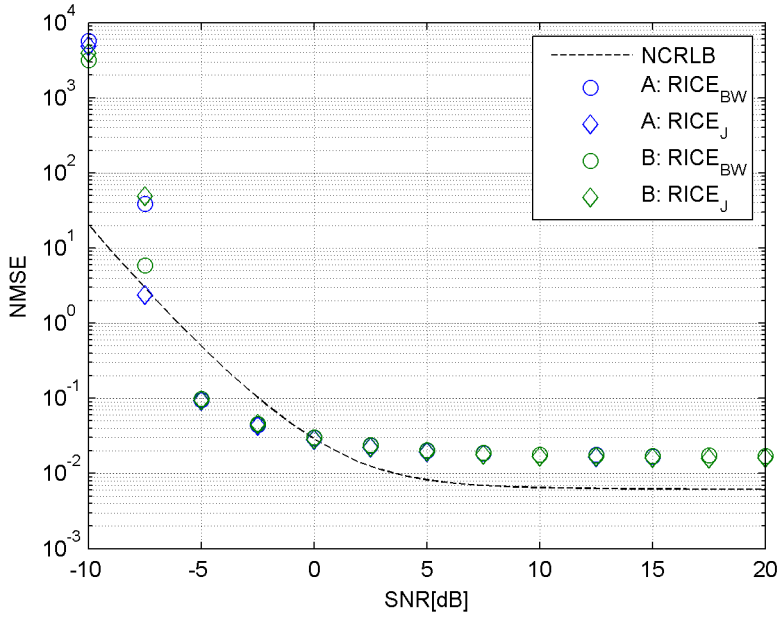

Figure 5.21: NMSE comparison for estimators A and B of the K_R estimation

For further investigations the estimator B will be applied if not stated otherwise.

5.7 Joint Doppler Spread and Power Ratio Estimation Performance

The performance of the power ratio estimation was depicted for ideal conditions in Section 5.6.2.3. Throughout this section the performance of the joint estimation of Doppler spread and power ratios after carrier frequency and phase recovery is investigated. The performance of the latter was depicted for Rician channels in Sections 5.4.2 and 5.4.3. In the following, the influence of guard bands, Doppler spread estimators, and Doppler spreads is investigated with respect to power ratios. Unless otherwise stated, the simulation settings outlined in Section 5.2.4 apply.

5.7.1 Influence of a Guard Band

Figure 5.22 and Figure 5.23 depict the SNR estimation performance and the K_R estimation performance in terms of NMSE for different guard bands, *i.e.* $k_G = \{0, 5, 30, 200\}$

plotted as dotted lines with different markers and different Doppler spreads $B_D T_S = \{0.02, 0.1\}$ in green and blue, respectively. The latter are assumed to be ideally known to the receiver, the RICE_{BW} fading model at $K_R = 5$ dB was applied. The NCRLBs for the Rice channel are indicated as appropriately coloured dashed lines, whereas the red dashed line in Figure 5.22 depicts the NCRLB for the AWGN case.

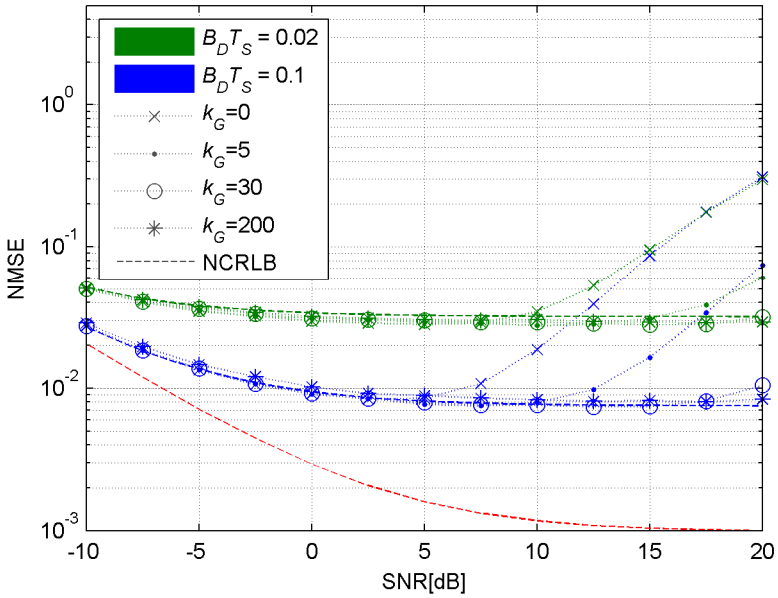

Figure 5.22: SNR evolution at different guard bands

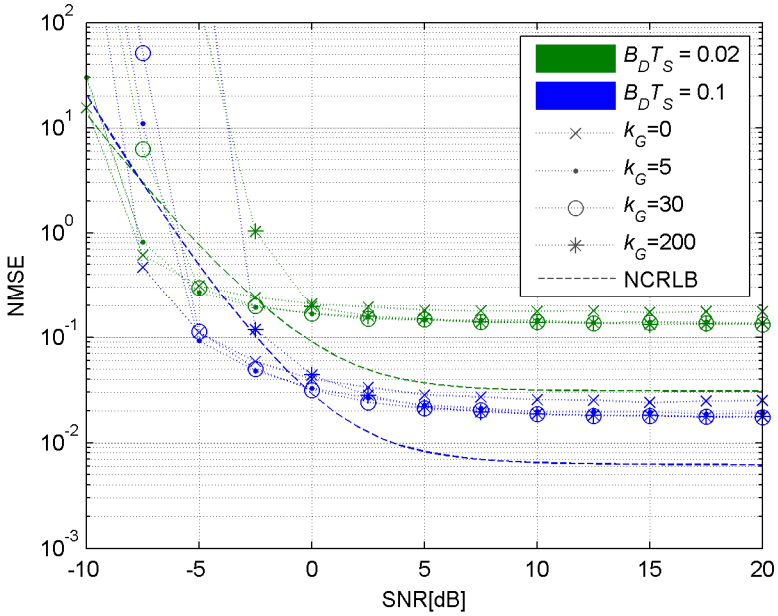

Figure 5.23: K_R evolution at different guard bands

It is to be observed that on the one hand no or only small guard bands cause the SNR estimates to deviate in the medium-to-high SNR regions, but on the other hand they improve the K_R factor estimation accuracy in the low SNR region. The deviations in the high SNR regions in Figure 5.22 can be explained by the out-of-band emissions of the Doppler spread shaping filters in the Rice simulation model. The performance loss in the low SNR region of Figure 5.23 for large guard bands can be explained by an additional estimation jitter introduced, since the noise portion in the interference estimation is higher. In order to bridge the gap between these two effects, resorting to a guard band of 30 DFT bins, *i.e.* $k_G = 30$, was found to be a good compromise.

5.7.2 Influence of the Doppler Spread Estimators

Figure 5.24 and Figure 5.25 compare the SNR estimation performance and the K_R estimation performance in terms of NMSE for different Doppler spread estimators; the results for NDS, mNDS, and HDS are indicated in green, red, and blue, respectively. The simulation was performed using a Doppler spread of $B_D T_S = 0.1$ on a RICE_{BW} channel.

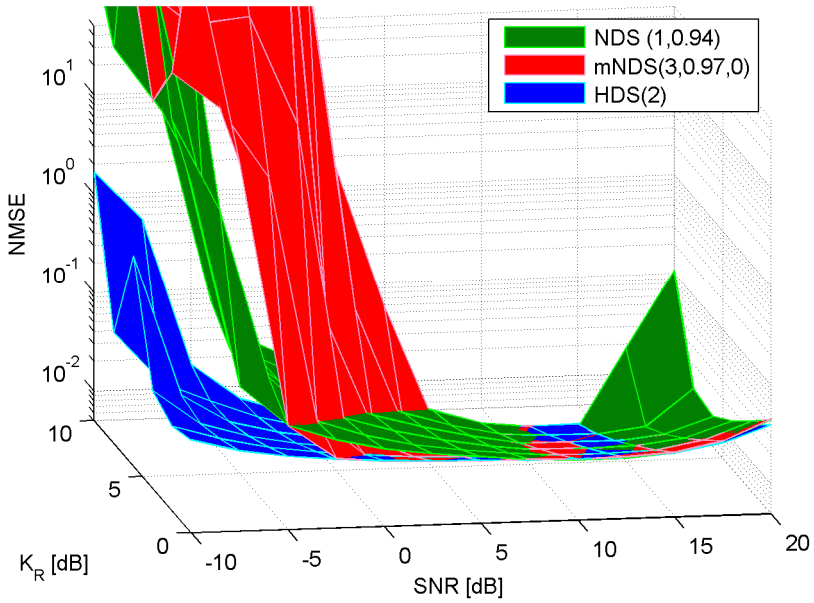

Figure 5.24: Normalized jitter performance of SNR estimation

Figure 5.26 compares the performance in terms of NMSE of the power estimates for the three Doppler spread estimators, where the results in a) represent the NMSE of the signal power, in b) the NMSE of the interference power, and in c) the NMSE of the noise power. Furthermore, results achieved by employing the NDS, mNDS and HDS estima-

tor are plotted in green, red, and blue, respectively. The black dashed line indicates the applicable NCRLB.

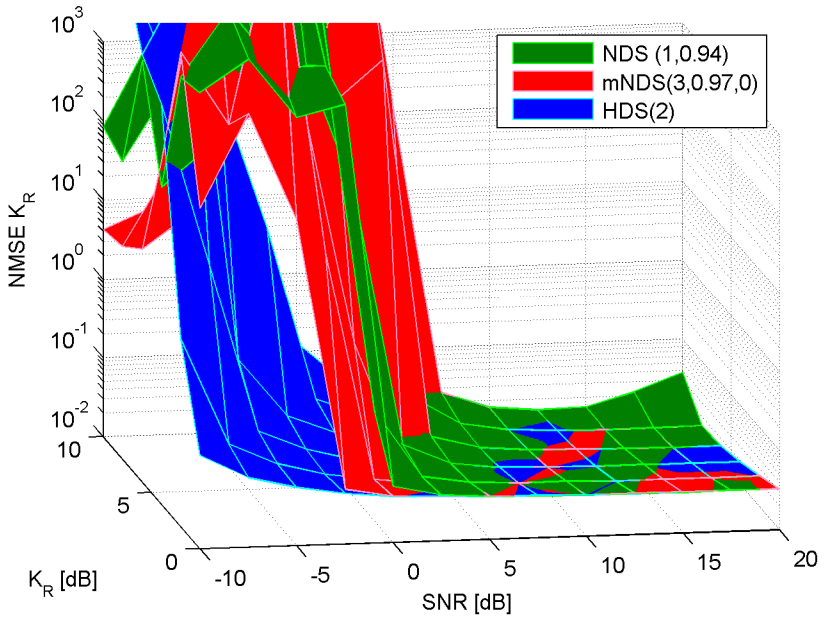

Figure 5.25: Normalized jitter performance of K_R estimation

It can be observed in Figure 5.24, Figure 5.25, and Figure 5.26 that power estimations relying on the estimates of the HDS estimator by far outperform the other principles considered. This conclusion is also backed by the fact that the power parameter estimation performance relying on HDS quasi equals the one with known Doppler spread (see Appendix C-(e) and Section 5.7.3). Not surprisingly, no difference in the signal power estimates is observed in Figure 5.26, but results on interference and noise power are significantly more accurate when resorting to the HDS algorithm. It is further to be noticed that the violation of the NCRLB in Figure 5.26 b) obviously is caused by a bias effect.

If there is no statement to the contrary, the HDS estimator is used for joint estimations in the following.

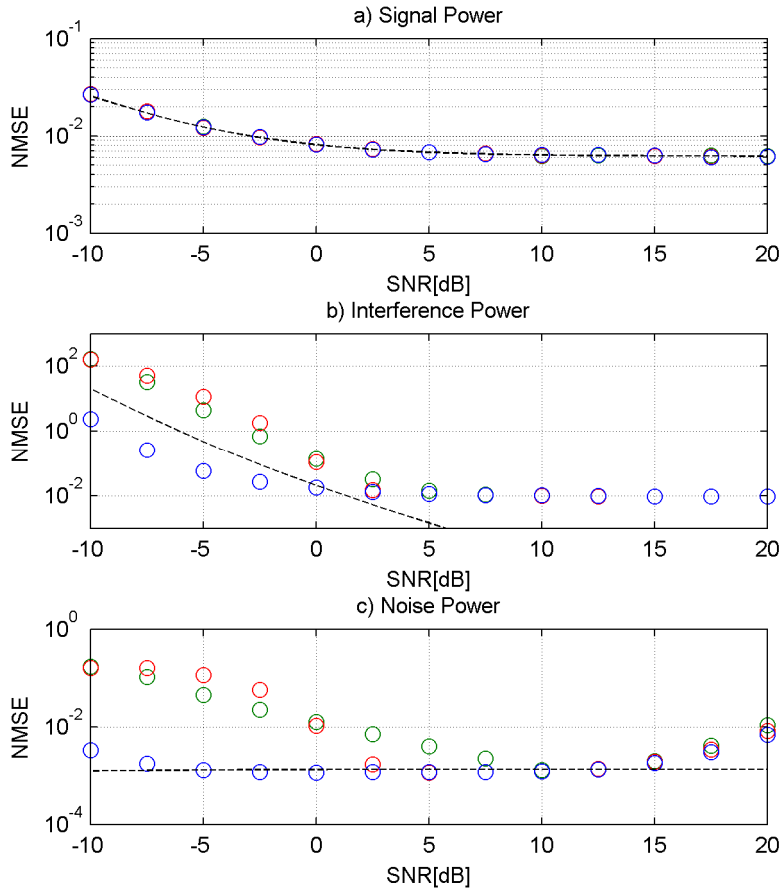

Figure 5.26: Normalized jitter performance
of the power estimates

5.7.3 Performance with Respect to Doppler Spread

In order to assess the performance for different Doppler spreads, Figure 5.27 and Figure 5.28 benchmark the NMSE of SNR and K_R estimation at different Doppler spreads $B_D T_S = \{0.02, 0.1\}$ illustrated in green and blue, respectively. A RICE_{BW} channel model at $K_R = 5$ dB was therefore simulated. Results gathered from simulations employing the HDS estimator (circlets) are compared to results using ideal Doppler spread knowledge (genie case indicated by dots) as well. For all simulations the respective NCRLBs are shown by appropriately coloured dashed lines; the red dashed line in Figure 5.27 indicates the NCRLB for AWGN conditions.

It is clear from Figure 5.27 that all simulation results match well with the indicated bounds, because the RICE_{BW} channel model is in wide consensus with the presumptions of the NCRLBs. In the higher SNR region the simulation results begin to deviate from the bound as a consequence of out-of-band emissions caused by the not strictly band-

limited Butterworth filter applied in the fading model; this behaviour could already be identified in previous sections (*e.g.* see Figure 5.26 c). The matching of results produced with genie and HDS promote the good performance of the latter.

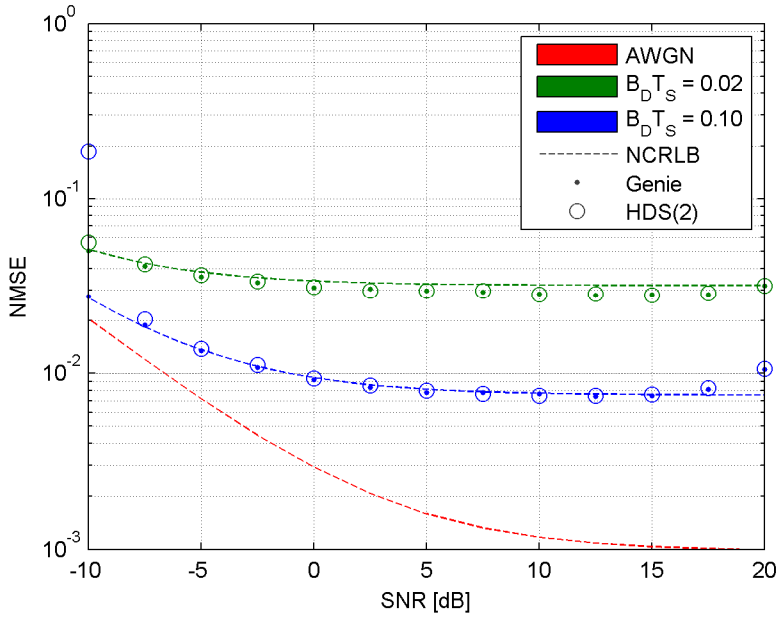

Figure 5.27: Evolution of the jitter performance for normalized SNR estimates

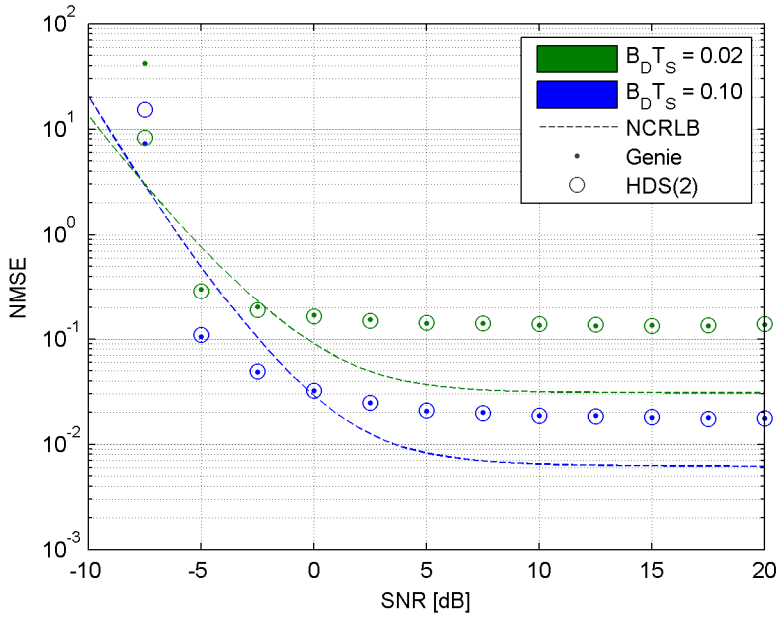

Figure 5.28: Evolution of the jitter performance for normalized K_R estimates

The simulation results for the Rice factor estimation performance in Figure 5.28 unfortunately do not agree with the NCRLBs due to a bias in the interference power estimations. However, again a match between results gathered from estimations applying genie and HDS can be observed.

5.8 Summary

The work presented in this chapter was carried out throughout the framework of the *Satellite Communication Network of Experts III Call-off-Order* 2 project supported by the *European Space Agency*. As presented here it is preparatory to the actual subtask of channel estimation on land-mobile satellite channels (see Chapter 6).

The importance of timely and accurate channel estimation was pointed out for mobile channel models so as to obtain figures of merit (signal-to-noise-ratio, signal-to-interference-ratio, and Doppler spread) feeding in to appropriate adaptive coding and modulation schemes in order to exploit the available bandwidth efficiently. In that context it was stated that a land-mobile satellite channel with some restrictions can be approximated by a frequency-flat time-selective correlated Rician channel, the latter acting as a test bench for estimation algorithms.

The correlated Rician channel was introduced as model for a mobile satellite scenario with a direct line-of-sight component and Rayleigh distributed multipath components; AWGN conditions and carrier frequency and phase error were included as well. Isotropic (Jakes) and non-isotropic (Butterworth) scattering models representing the multipath components were introduced; in this context the Doppler spread was identified from literature to be more important than the actual shape.

Channel estimations were mainly performed exploiting the periodogram, thus after sketching the latter's properties for Rice channels appropriate data-aided algorithms were proposed for

1 carrier frequency and phase estimations,
2 Doppler spread estimations,
3 and power parameter estimations.

For 1) and 3) Cramer-Rao lower bounds were stated tailored to the Rician channel presuming a flat spectrum of the multipath components, thus, not surprisingly, simulation results embracing the Butterworth scatter model fairly well match with the bounds.

The Rife-Boorstyn algorithm was employed to tackle carrier frequency estimations and a maximum likelihood method estimating the carrier phase. Both exhibited performances close to the theoretical limit.

For 2) a heuristic non-parametric Doppler spread estimation algorithm, which was attested in literature to perform better than other algorithms for Rician channels, was investigated. It turned out that, with appropriately chosen form factors, good performance can be achieved, but only in narrow SNR/SIR regions. Pertinent work on that issue first led to an improved version – the modified non-parametric Doppler spread estimator – and finally to a novel approach – the heuristic Doppler spread estimator. Whilst being a simple principle the latter exhibited superior performance in a multitude of thoroughly and fairly compared disciplines as overall performance, sensitivity to Doppler spread, different scattering models, estimation bias, and success rate. Together with power estimates it performed quasi as well as if the Doppler spread was known.

Two estimation algorithms were introduced for 3), one being a fully heuristic approach and the other being a partially heuristic approach. After comparison, featuring an equal performance, it was chosen to go with the partially heuristic estimator.

Joining all the estimation algorithms for 1)-3), accurate estimations for the Doppler spread as well as SNR and SIR were obtained, although in the lower SNR regime the latter tends to violate the respective theoretical bound, which to the best of the author's knowledge, results from a bias effect.

6 Parameter Estimation on Land-Mobile Satellite Channels

The work presented in this chapter elaborates on the results and findings presented in Chapter 5. It was mainly carried out in the framework of the *Satellite Communication Network of Experts III Call-off-Order* 2 project supported by the *European Space Agency*.

Findings and results, created by the author throughout the SatNEx III CoO 2 study, were already integrated in technical notes and reports [72 – 75] and partially published in [76]. However, they are not explicitly quoted in the following to avoid confusion and to support the readability of this thesis. Quotations on the listed documents refer to results and findings not or not only created by the author himself.

The author hereby acknowledges the work of *G. Vazquez-Vilar* (University of Vigo), author of the Loo-Fontan-MATLAB®-simulation model which was used as baseline for the CoO 2 activity; this simulation model was further adapted, tested and qualified by *J. Arnau Yanez* (University of Vigo) and the author of this thesis.

6.1 Preface

User mobility is a challenging task for communication systems, especially for satellite-based systems due to the relatively long *round-trip time* (RTT). Dynamic methods such as adaptive transmission power or *adaptive coding and modulations* (ACM) are well known in the realm of satellite communications in order to compensate for slow fading effects as to exploit the available bandwidth efficiently [77][78]. These two methods are capable, when employed, to achieve the capacity limit of a fading channel, but require accurate yet timely information about the channel [79]. Adaptively changing the transmission power, however, might be problematic because of non-linearities of amplifiers in the transmission chain. Resorting to ACM schemes is the logical consequence demanding accurate and timely CSI at the transmitters' end. Hence, its estimation is of paramount importance on time-variant links [80, pp. 37-39].

The work presented within this chapter elaborates on the preparatory work in Chapter 5 examining periodogram-based estimation algorithms for Rician channels and adapts them for *land-mobile satellite* (LMS) links which are implemented in the context of this

activity according to the statistical model presented in [94][95], denoted as Loo-Fontan (LF) model.

A set of parameters were identified as necessary figures of merit for the envisaged ACM strategy which are [76][72, pp. 37-38]:

- The SNR
- The SIR
- The Doppler spread of the LMS link

In the sequel, the simulation scenario is introduced detailing on the LF-channel model and its mathematical description. The estimation framework as postulated in Chapter 5 is adapted and evaluated. Finally, state classification as to aid ACM schemes is outlined and a heuristic approach is discussed.

6.2 The Scenario

Based on the observations gathered for the Rice channel in Chapter 5 the algorithms are applied to the LF channel. In the following paragraphs a concise description of the LF model will be provided and analytically elucidated.

A typical LMS scenario, as envisaged in SatNEx III CoO2 [80, p. 28], is sketched in Figure 6.1. A geostationary communication satellite serves the mobile user, the link either embodies *line-of-sight* (LOS) conditions or shadowed conditions on the direct path (blue arrow) and a combination of many constructively and destructively interfering multipath signals (green arrows), which are randomly delayed, affected by *Doppler* shifts, scattered, reflected, and diffracted. The combination of the direct LOS signal and the random (Rayleigh-distributed) multipath signals was already introduced in Chapter 5 as the Rician model [81, pp. 18-22][82, pp. 334-337][83]. However, mainly due to the shadowed or non-shadowed direct path, the LMS channel can no longer be described by a single distribution, thus the LF model implements different distributions embraced by a first-order Markov chain [94].

For CoO 2 S-band frequencies for the forward and return link were considered, the latter require compatibility with the ETSI standards DVB-S2 [17] and DVB-RCS2 [18][75, p. 72].

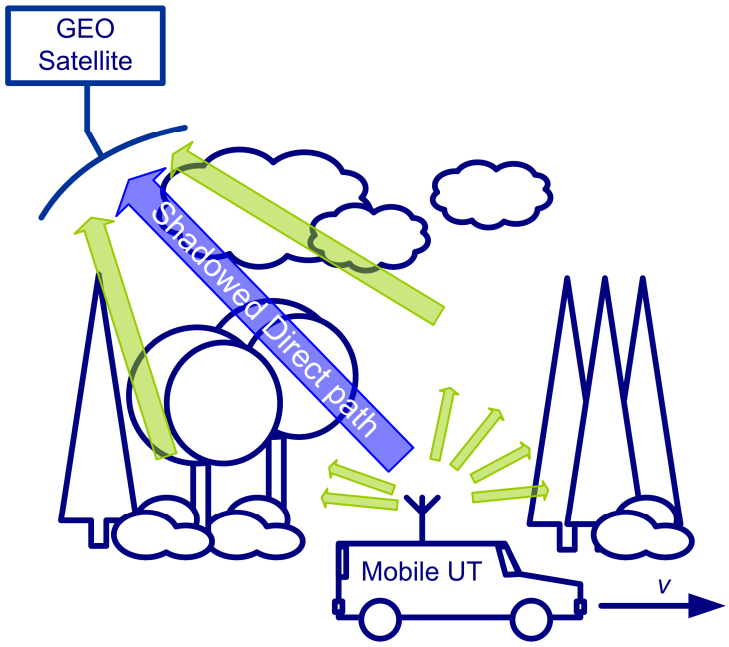

Figure 6.1: Land-mobile satellite scenario
sketching intermediate tree shadowing

6.2.1 The Loo-Fontan Signal Model

The LF channel model represents a statistical channel model for LMS links. It incorporates shadowing of different kind of the direct signal and multipath (scatter) components inherent to mobile channels.

The *direct path* is modelled by means of a three-state first-order Markov[18] chain whose states describe the *very slow signal variations*, whereas by means of a log-normal distribution *slow signal variations* are described. The states of the Markov process describe three conditions [94][96]:

- State 1: LOS conditions
- State 2: Moderate shadowing conditions
- State 3: Deep shadowing conditions

Figure 6.2 [94] depicts the Markov state model for the LF channel, where the circles represent the states and the arrows indicate transitions. The state probability is indicated by W_i, i marking the current state number, and the transition probabilities are indicated by P_{ij}, where j marks the future state; $\sum_i W_i = 1$ and $\sum_j P_{ij} = 1, i = \{1, 2, 3\}$, are im-

[18] A Markov chain is a stochastic process with different states; transitions between states are characterized by probabilities. A Markov process of first order means that the probability of entering a state only depends on the previous state [97][94].

perative. A minimum length in metres, denoted as s_F, defines with respect to the mobile terminals' speed how long the Markov chain at minimum resides in one state.

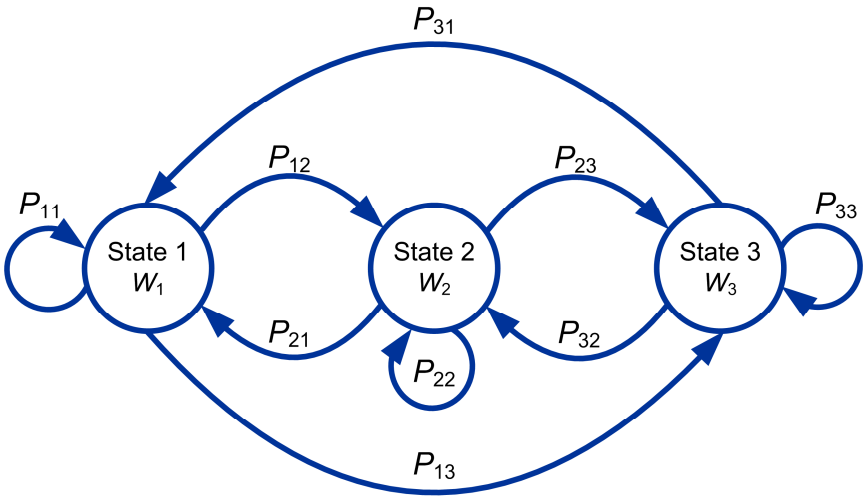

Figure 6.2: Markov states of the LF model

Equal to the Rice channel model, investigated in Chapter 5, the *multipath component* is known to follow a Rayleigh distribution [96]; by adding that to the log-normally distributed direct signal, a Loo distribution is obtained [95][94].

Figure 6.3 depicts the signal model of the LF-channel. Compared to Figure 5.2 it is clear that the LOS component has changed from a constant factor (Rice channel) to a log-normal distribution. Since the log-normally shadowed direct component varies slowly, the realizations ω_m are resampled and interpolated in the *rate conversion and interpolation* (RCI) block resulting in ω_k. The ω_k samples come at a symbol rate of $1/T_S$, so the rate conversion must be flexible because the rate of ω_m depends on the mobile terminal's speed and the respective correlation distance s_c [80, pp. 18-19][94].

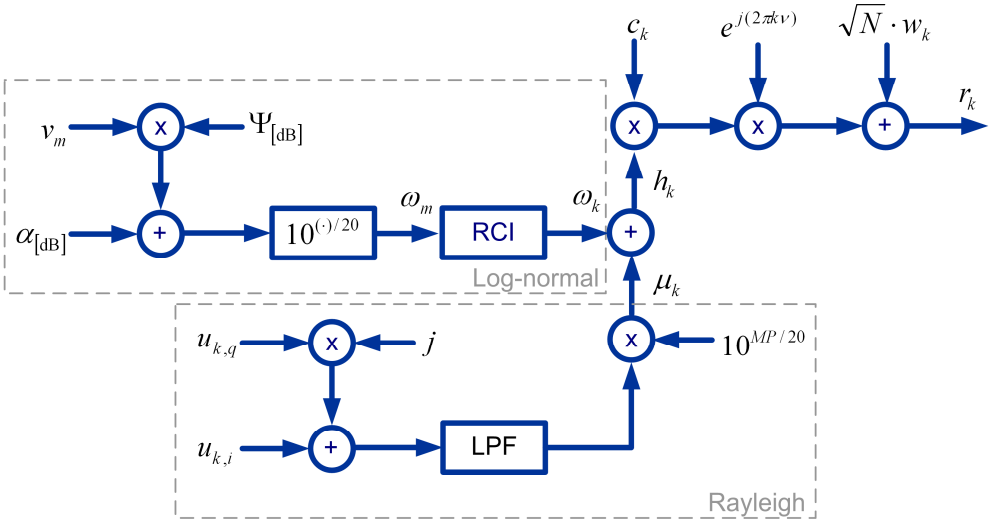

Figure 6.3: Signal Model of the Loo channel

In accordance with Figure 6.3 the received signal furnishes to

$$r_k = h_k \cdot c_k \cdot e^{j2\pi\nu} + \sqrt{N} \cdot w_k, \tag{6.1}$$

where h_k represents the complex envelope of the LF-channel, c_k represents the k-th training symbol (M-PSK modulated), $|c_k| = 1$, ν accounts for the normalized carrier frequency error, and $w_k \sim \mathcal{N}_c(0,1)$. The complex envelope of the LF channel is given by

$$h_k = \omega_k \cdot e^{j\theta} + \mu_k, \tag{6.2}$$

with ω_k representing an up-sampled log-normally distributed random variable with mean α (in dB relative to LOS conditions) and standard deviation Ψ (in dB), θ being an i.i.d. random phase offset in the range of $(-\pi, \pi]$ and μ_k representing a Rayleigh-distributed random variable [95]. The latter is generated by appropriately filtered circular-complex zero-mean Gaussian random variables ($u_{k,i}$ and $u_{k,q}$) and weighted by a power factor MP (in dB) [94]. For the sake of completeness, ω_k forms an independent random process driven by $v_m \sim \mathcal{N}(0,1)$. Since ω_k and μ_k stem from mutually independent random processes, it is clear that

$$E[|h_k|^2] = E[|\omega_k|^2] + E[|\mu_k|^2], \tag{6.3}$$

where

$$E[|\omega_k|^2] = e^{2\xi(\alpha+\xi\Psi^2)} \;\Big|\; \xi = \frac{\ln 10}{20} \tag{6.4}$$

and

$$E[|\mu_k|^2] = 10^{MP/10}. \tag{6.5}$$

An extensive set of parameters, *i.e.* α, Ψ, and MP, shaping the Loo distribution, as well as state probabilities W_i and state transition probabilities P_{ij} are provided for different elevations, environments and frequencies in [94][96].

Figure 6.4 depicts for an intermediate tree shadowing environment at an elevation of 40° [94] and at a mobile terminal speed of $\dot{s} = 30$ m/s the evolution of the channel magnitude $|h(t)|$ in dB (top plot, blue curve) and the respective Markov state (bottom plot, red dashed curve) evolution over time.

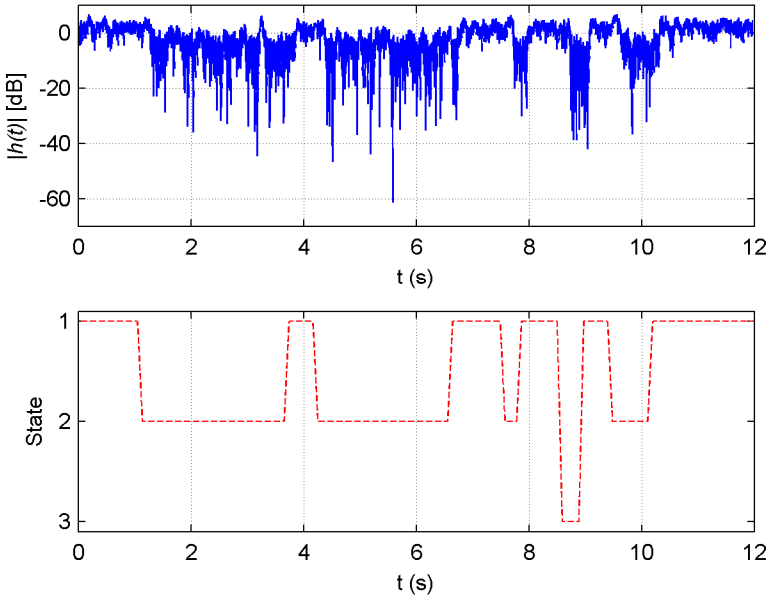

Figure 6.4: Evolution of the LF channel magnitude and state over time

6.2.2 Periodogram of the LF-Channel

In order to investigate the periodogram of the channel, the data modulation must be removed from the received signal in (6.1). Assuming proper recovery of the carrier frequency and phase error, *i.e.* $|\nu - \hat{\nu}| \ll 1$ and $|\theta - \hat{\theta}| \ll 1$, this furnishes to

$$\begin{aligned} z_k &= c_k^* \cdot r_k \cdot e^{-j(2\pi k\hat{\nu}+\hat{\theta})} \\ &= |c_k|^2 \cdot \omega_k \cdot e^{j[2\pi k(\nu-\hat{\nu})+(\theta-\hat{\theta})]} \\ &\quad +|c_k|^2 \cdot \mu_k \cdot e^{j[2\pi k(\nu-\hat{\nu})-\hat{\theta}]} \\ &\quad +\sqrt{N} \cdot c_k^* \cdot w_k \cdot e^{-j(2\pi k\hat{\nu}+\hat{\theta})}. \end{aligned} \tag{6.6}$$

By considering [75, pp. 100-110]

- that the residual carrier frequency errors and phase errors are negligible,
- that the shadowing process consists of a mean signal amplitude $\sqrt{S}$ impaired by a log-normally distributed variable λ_k,
- and that μ_k and w_k are independent zero-mean Gaussian variables,

the relationship in (6.6) simplifies to

$$z_k = \left(\sqrt{S} + \lambda_k\right) + \sqrt{I_\mu} \cdot \eta_k + \sqrt{N} \cdot n_k. \tag{6.7}$$

Analogous to the pure Rician channel, η_k and n_k are still circular-complex Gaussian variables with unit variance and zero mean; a vector representation of (6.7) can be seen in Figure 6.5. With $Z_k = \mathrm{DFT}(z_k)$, the PSD of the LF channel is sketched in Figure 6.6. Both figures have the same colour coding indicating the signal component in blue, AWGN noise in red, multipath fading induced interference in green and shadowing induced interference with grey lines and green surface.

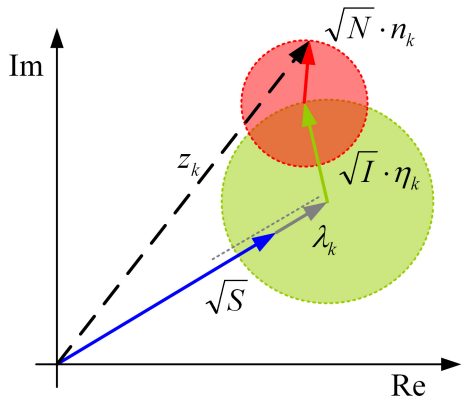

Figure 6.5: Vector diagram of the LF-channel

A spectrum of the considered LF channel can be seen in Figure 6.7 at a mobile terminal speed of $\dot{s} = 30$ m/s (intermediate tree shadowing, elevation 40°). By inspection the signal component can be identified at $f - f_c = 0$, the shadowing-induced interference is observed in the range of $|f - f_c| < 15$ Hz and the remainder indicates the multipath induced interference (Butterworth shape). The latter occurs at a maximum Doppler spread of $B_D = 2 \cdot f_D = f_c \cdot \dot{s}/c \approx 2 \cdot 220$ Hz, whereas c denotes the speed of light.

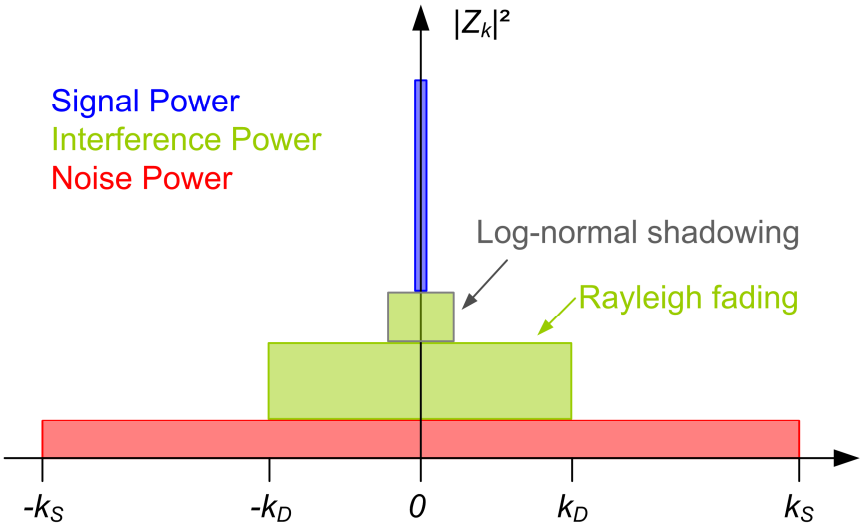

Figure 6.6: Components of the discrete power spectrum of a LF-channel

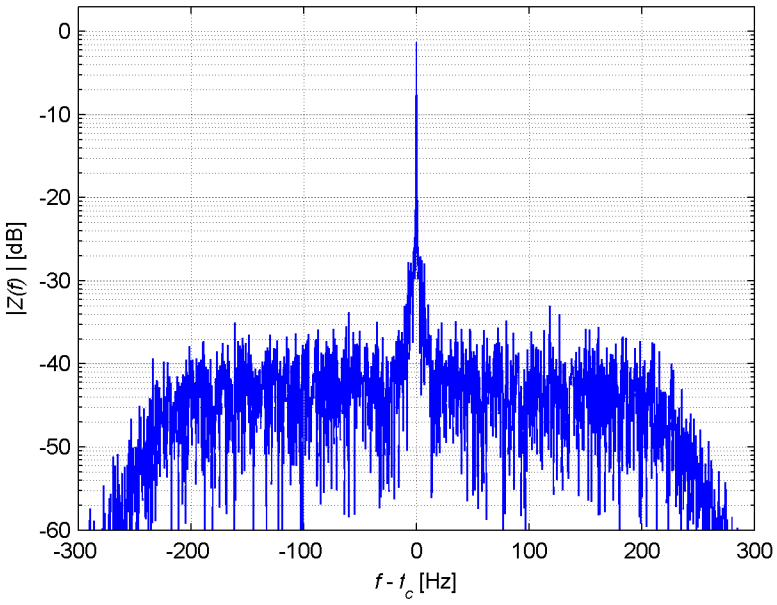

Figure 6.7: Spectrum of the LF channel

6.2.3 Power Factors in the LF-Channel

Considering appropriate carrier frequency and phase recovery the received samples with data modulation wiped out in z_k are derived in (6.7); considering the random processes λ_k (log-normal distributed), η_k (Rayleigh distributed), and n_k (Gauss distributed), all of which are mutually independent and have zero-mean, it is

$$E[z_k] = \sqrt{S} \tag{6.8}$$

and

$$E[|z_k|^2] = S + I_\lambda + I_\mu + N, \tag{6.9}$$

where I_λ represents the interference power induced by λ_k. From that the total interference power is $I = I_\lambda + I_\mu$, thus the total SIR can be rewritten as

$$SIR = \frac{S}{I_\lambda + I_\mu}. \tag{6.10}$$

Furthermore, it is introduced

$$\mu_\lambda = \frac{\log 10}{20} \cdot \alpha, \tag{6.11}$$

$$\sigma_\lambda = \frac{\log 10}{20} \cdot \Psi. \tag{6.12}$$

With (6.11) and (6.12), the powers S, I_λ, and I_μ relate to the parameters shaping the Loo distribution according to [75, pp. 109-111]:

$$S = e^{2\mu_\lambda + \sigma_\lambda^2}, \tag{6.13}$$

$$S + I_\lambda = e^{2\mu_\lambda + 2\sigma_\lambda^2}, \tag{6.14}$$

$$I_\mu = 10^{MP/10}. \tag{6.15}$$

The above discussed power figures represent average measures of the time-variant LF channel, thus in the context of parameter estimations instantaneous power figures are relevant for benchmarking.

6.3 The Estimation Framework and Performance

As already discussed, parameter estimations are supposed to employ the algorithms identified in Chapter 5, which have been identified to be the most promising candidates for the LF channel.

In subsequent sections, important details of the framework as developed for the Rician channel are discussed to adopt them to the needs of the envisaged LF channel, given the DVB-S2 physical layer framing. In that regard, the simulation setup is introduced as a baseline for the presented simulation results. Carrier frequency and phase recovery as well as channel parameter estimations are discussed further on. Finally periodogram-based estimations on the LF channel, more specifically estimations of the Doppler spread and of the power parameters are conveyed.

6.3.1 Simulation Setup

Unless stated otherwise, the following standard settings for simulation results presented throughout this chapter apply:

- The link settings:
  - Carrier frequency: $f_c = 2.2$ GHz.
  - Symbol rate: $1/T_S = 3.7$ MBaud.
  - Physical layer framing: DVB-S2 alike, *i.e.* 36 pilot symbols (QPSK) alternating with 90×16 data symbols [17, pp. 28-31]; no headers.
  - Normalized carrier frequency error: $|\nu| \leq 0.1$.
  - Carrier phase error: $\theta \in (-\pi, \pi]$.
- The LF-channel:
  - Environment: *intermediate tree shadowing* (ITS) at an elevation of 40°.
  - Parameters for the Loo model: Table 2 [94].
  - Correlative distance $s_c = 1.5$ m.
  - State and transition probabilities for the Markov chain: Table 3 [94].
  - Minimum travel distance residing in a state: $s_F = \{6.3, 6.3, 4.5\}$ m for states $\{1, 2, 3\}$, respectively.
  - Transition distance between two states: $s_T = 2.6$ m.

- Rayleigh fading shaped with 10th order Butterworth filter (see 5.2.3).

- Channel Estimation
  - A training sequence of length $L_M = 1024$ is extracted from 1024 DVB-S2 pilots each of length $L = 36$ symbols.
  - Carrier frequency and phase recovery with RB algorithm [56] and (5.16).
  - Doppler spread estimation with HDS estimator (see 5.5.2).
  - Power parameter estimation with estimator B (see 5.6.2.2).

Intermediate tree shadowing, elevation 40° (all values in dB)								
State 1			State 2			State 3		
α	Ψ	MP	α	Ψ	MP	α	Ψ	MP
-0.4	1.5	-13.2	-8.2	3.9	-12.7	-17.0	3.14	-10.0

Table 2: Parameters for the Loo model

Intermediate tree shadowing, elevation 40°						
State 1:	W_i	0.3929	P_{ij}	0.7193	0.1865	0.0942
State 2:		0.3571		0.1848	0.7269	0.0883
State 3:		0.2500		0.1771	0.0971	0.7258

Table 3: State and transition probabilities of the ITS scenario

The simulation results presented in the following use the same plot style. Thus if not otherwise stated the performance plots use the styles as accumulated in Table 4.

Plot styles			
State:	1	2	3
Colour:	Black	Blue	Green
Velocity [m/s]:	1	15	30
Line style:	Dotted	Dash-dotted	Solid
Marker:	Dot	Diamond	Circlet

Table 4: Performance plots style

To ease interpretation of the figures applying the plot styles described in Table 4, the following line is added where considered helpful: [State {1,2,3}→{black, blue, green}; $\dot{s}$ = {1,15,30} m/s → Line/Marker = {dotted/dot, dash-dotted/diamond, solid/circlet}]

6.3.2 Carrier Frequency and Phase Estimation

Carrier frequency estimation performance is investigated based on an *instantaneous SNR* (ISNR)[19] utilizing the RB algorithm under the assumption of a preamble sequence of 1024 symbols in Figure 6.8. Speeds of 1 m/s and 30 m/s at different states were simulated and plotted according to the styles introduced in Table 4. Additional results applying the full Markov-LF model for ITS conditions are plotted in ochre. It can be observed that the estimation performance is geared at the NCRLB, but there exists a jitter floor depending on both the state and the velocity of the mobile terminal.

Akin to the results for carrier frequency estimation, the carrier phase estimation performance employing the algorithm in (5.16) is depicted in Figure 6.9 over ISNR. The same preamble sequence of $L = 1024$ at equal colour coding was used therefore. Only results for mobile terminal speeds of 30 m/s are indicated, because those for speeds of 1 m/s followed the CRLB for the depicted ISNR region. This in turn supports the statement from above, *i.e.* the LF channel can be regarded as AWGN-like for short time periods with respect to the mobile speed. Again, the observable jitter floor depends on the state and the mobile speed.

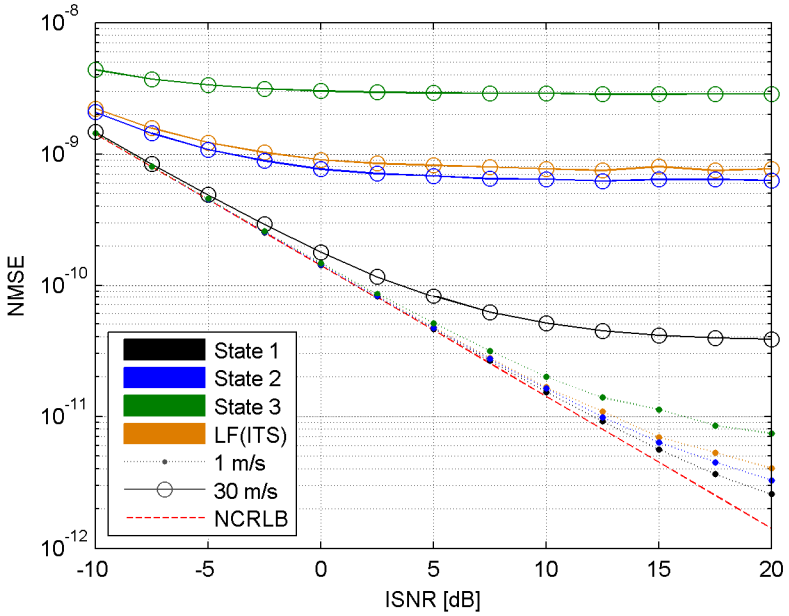

Figure 6.8: Evolution of the jitter performance
for normalized frequency estimates

[19] The ISNR describes a during the time interval of the preamble/pilot sequence occurring mean SNR, thus denoted as instantaneous.

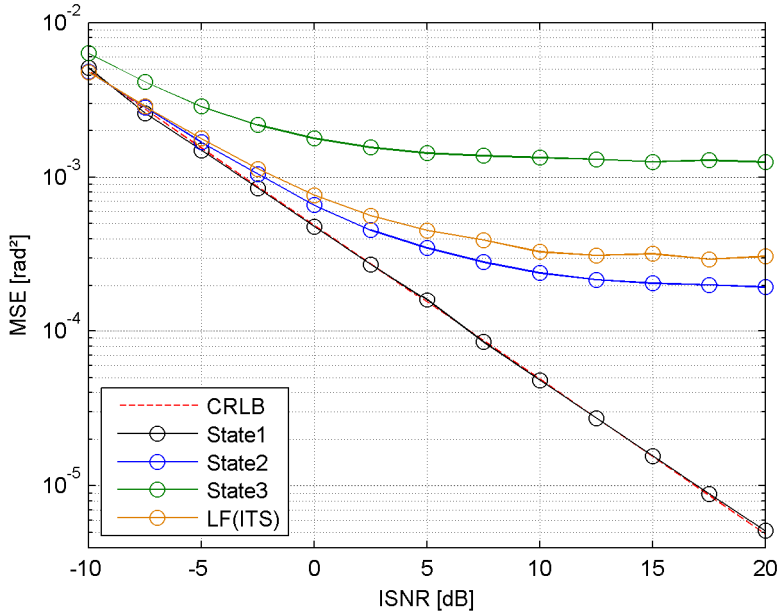

Figure 6.9: Evolution of the jitter performance
for phase estimates

It is furthermore to be noticed that a preamble sequence of $L = 1024$ is not foreseen in the DVB-S2 signalling. However, it was chosen to detail the influence of shadowing and fading effects on the carrier frequency estimation, because for shorter training sequences, say $L = 36$ symbols, no difference in performance for the different states or velocities could be observed within a reasonable ISNR regime. This is explained by the fact that during the time period of a training sequence the channel variations resulting from shadowing and fading are typically low necessitating observations over larger time periods to properly observe them.

To support the above statements, simulation results for carrier frequency and phase estimates on the LF channel with ITS conditions are depicted in Figure 6.10 a) and b), respectively, utilizing training sequences of $L = 36$ symbols. As mentioned above, the results behave as predicted by the appropriate (N)CRLBs for AWGN conditions. This also supports the hypothesis that for short time intervals AWGN-like conditions are predominant on the LF channel.

In order to improve the accuracy of carrier synchronization without requiring additional signalling bandwidth a resorting to *code-aware* (CA) techniques, which in recent years received quite some attention in the scientific community, could be considered. With CA algorithms performances close to the theoretical bounds are possible. Based on intrinsic information in decoding schemes of modern FEC codes, as LDPC codes and Turbo codes, the carrier parameters can be estimated more accurately without becoming more and more inefficient by increasing the signalling bandwidth [19][20].

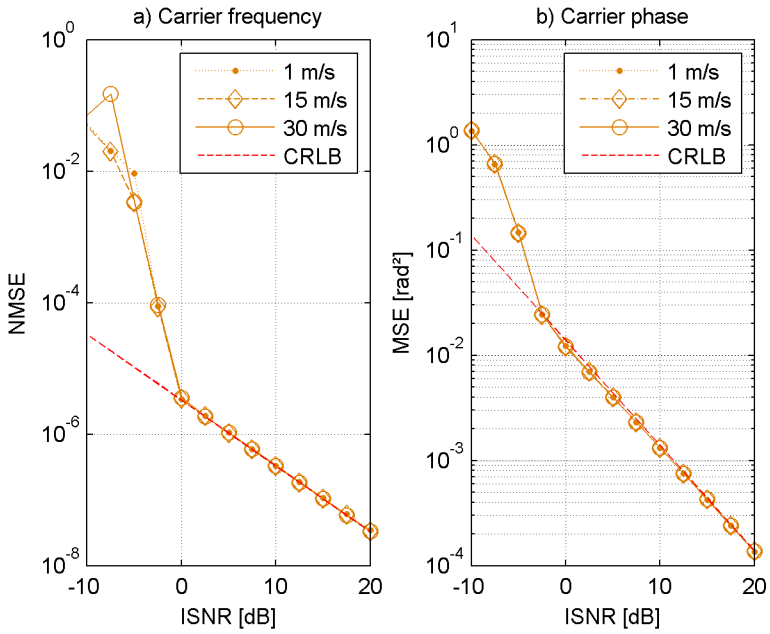

Figure 6.10: Carrier parameters estimation performance utilizing on the LF channel

6.3.3 Channel Parameter Estimation and Interpolation

Knowledge of the current channel state information (not to be confused with the Markov state of the LF channel) is important at the receiver to improve the decoding process, for instance by changing the metric of FEC decoding schemes. Hence, knowledge of the CSI is not just important at the time instances of the training sequences. Moreover it is important within the data block. CSI at any time instance can be assessed with respect to some uncertainty through interpolation (here cubic interpolations were used) of CSI information gained from the interspersed training sequences. The latter are obtained for the m-th training sequence given the carrier frequency and phase as

$$h_m = \sum_{k=0}^{L-1} c_k^* \cdot r_k \cdot e^{-j(2\pi k\nu-\theta)}, \tag{6.16}$$

whilst disregarding inherent amendments in the notation for application as estimator.

Figure 6.11 depicts a time series of CSI estimations (black squares) and interpolations (red x) based on the true channel (blue solid line) at a mobile speed of 30 m/s. By comparison of the top and bottom plots in Figure 6.11, it is clear that noise degrades the accuracy, but since most of the time the variability of the channel is quite low accurate approximations are preserved.

Figure 6.12 provides the quantitative statement of what is qualitatively discussed in Figure 6.11. A plot detailing the jitter performance of the normalized amplitude of h, denoted as Δ_a, is depicted; a suffix in the subscripts explains the method applied for estimations, thus

- m stands for results estimated directly from the training sequences using (6.16),
- i stands for results gained from cubic interpolations between the training sequences,
- and i, [1,1,1] indicates results gained from cubic interpolations, but using a moving average filter with three filter taps, *i.e.* [1,1,1], to previously average $\hat{h}_m$.

Furthermore, the respective NCRLB is illustrated as red dashed line. It only applies to $\Delta_{a,m}$, since the other results are subject to averaging which contrasts the inherent claim for statistical independence of the samples. It can be seen that results applying a moving average filter before interpolation exhibit improved performance in the low SNR regime, whereas a jitter floor occurs in the higher SNR regime.

Using interpolated results for parameter estimations does not provide any benefit for accuracy, since they do not hold any new information with respect to the original samples. Even worse, a small additional portion of noise is introduced due to the interpolation process.

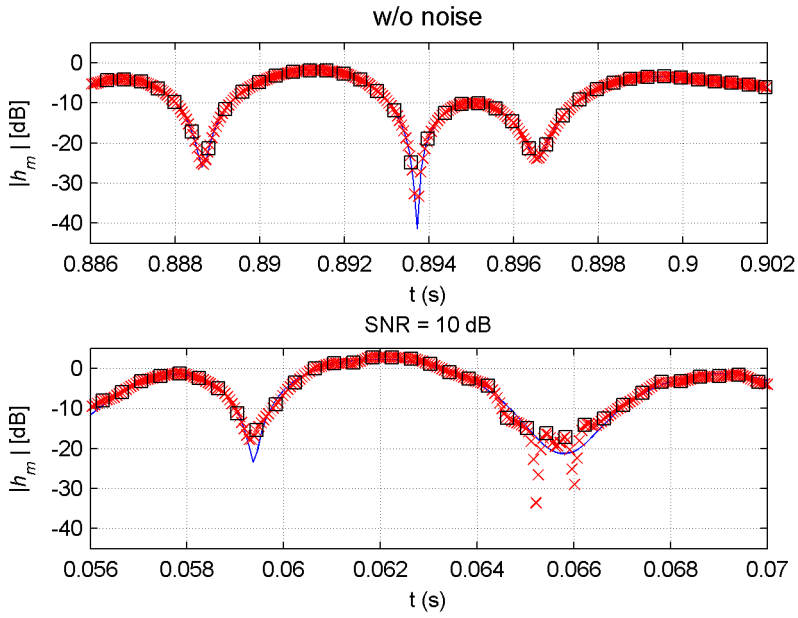

Figure 6.11: Realization of CSI interpolation

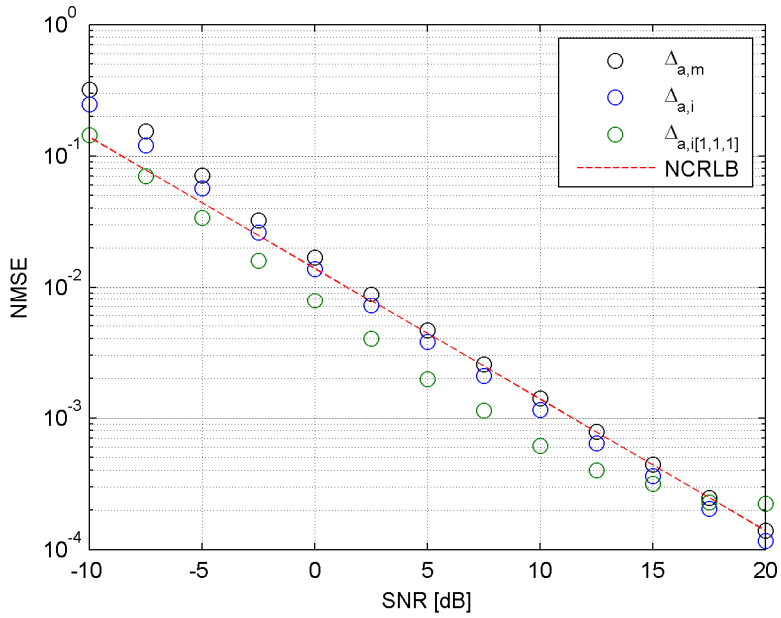

Figure 6.12: Jitter performance of the normalized channel amplitude

6.3.4 Periodogram-based Estimations

As follows from the essence of the previous subsections, the channel must be observed over a period significantly longer than its coherence time T_c. Reconsidering the channel model and also considering two adjacent samples from (6.7), it is clear that only the noise term is statistically independent between the two instances. Moreover given the DVB-S2 training sequences it is clear that $L \ll L_c$, $L_c = T_c/T_S$. Hence, within the period of a training sequence the signal vector incorporating the signal and interference powers essentially remains constant as depicted in Figure 6.13. By using the notations of Figure 6.13, it is clear that $z_k = z'_k + \sqrt{N} \cdot n_k$; furthermore considering $z'_k \approx const.$, $k = \{0, 1, \dots, L-1\}$, it can be put down for the m-th training sequence

$$\bar{z}_m = \frac{1}{L} \cdot \sum_{k=0}^{L-1} z_k, \tag{6.17}$$

whereas the instantaneous signal power S_i is embodied in z'_k, so $\bar{z}'_k = \sqrt{S_i}$, $k = 0, 1, \dots, L-1$. Moreover, since $n_k \sim \mathcal{N}_c(0,1)$, it is easy to see that

$$E[\bar{z}_m] = \sqrt{S} \tag{6.18}$$

and

$$E[|\bar{z}_m|^2] = S + I_\lambda + I_\mu + N/L, \tag{6.19}$$

thus resulting in a noise power suppression due to the averaging. From there the L_m-point periodogram can be calculated as $\bar{Z}_m = \mathrm{DFT}(\bar{z}_m)$, but keeping in mind that the noise term will be estimated to N/L.

Advantageous for a practical implementation is that only a single complex value, *i.e.* $\bar{z}_m$, has to be stored in a memory. In the realm of simulations, when calculating $\widehat{N}$ from the estimated ratio $\widehat{N}/L$, an unwanted side-effect originating from the non-ideal simulation model of the channel occurs: due to the previously described out-of-band emissions of the LPF, modelling the Rayleigh fading, the noise estimations are corrupted. Since here the resulting noise estimate has to be multiplied by L, also the systematic error introduced by the filter is L times higher. To provide results not suffering from that detrimental and in practice non-occurring effect, it was decided to resort to the following procedure for estimating the parameters from a single $\bar{z}_m$ training sequence of length L_m:

- calculate L times the periodogram, *i.e.* $Z_{m,k} = \mathrm{DFT}(z_{m,k})$, $m = 0, 1, \ldots, L_m - 1$, $k = 0, 1, \ldots, L - 1$,
- Perform L times the relevant estimations,
- and finally average the L obtained results.

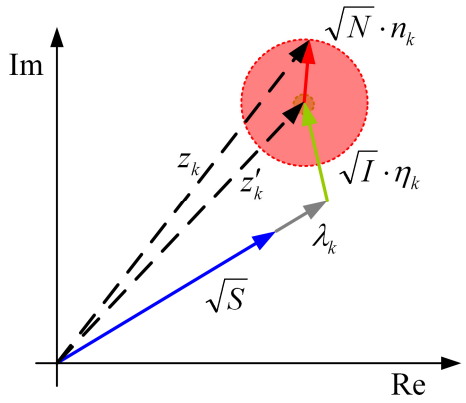

Figure 6.13: Vector diagram of the LF channel in a short time interval

Within the following subsections, simulation results discussing the performance of the HDS estimator on the LF channel as well as subsequent power parameter estimations are discussed.

6.3.4.1 Doppler Spread Estimation

Since the HDS algorithm turned out to provide superior performance for Rician channels, it is employed for the LF channel as well.

For the Loo model, Figure 6.14 depicts achievable jitter performance of the Doppler spread using a training sequence derived from 1024 DVB pilots over a time period of 0.41 s. The colour coding as introduced in Table 4 is used. It can be seen that state 1 (blue) in general exhibits the weakest performance, which correlates to the fact that it possesses the lowest interference power. Furthermore it can be observed that low speeds (dotted lines) are hard to estimate since the variability of the channel is bound to the distance covered by the mobile user terminal.

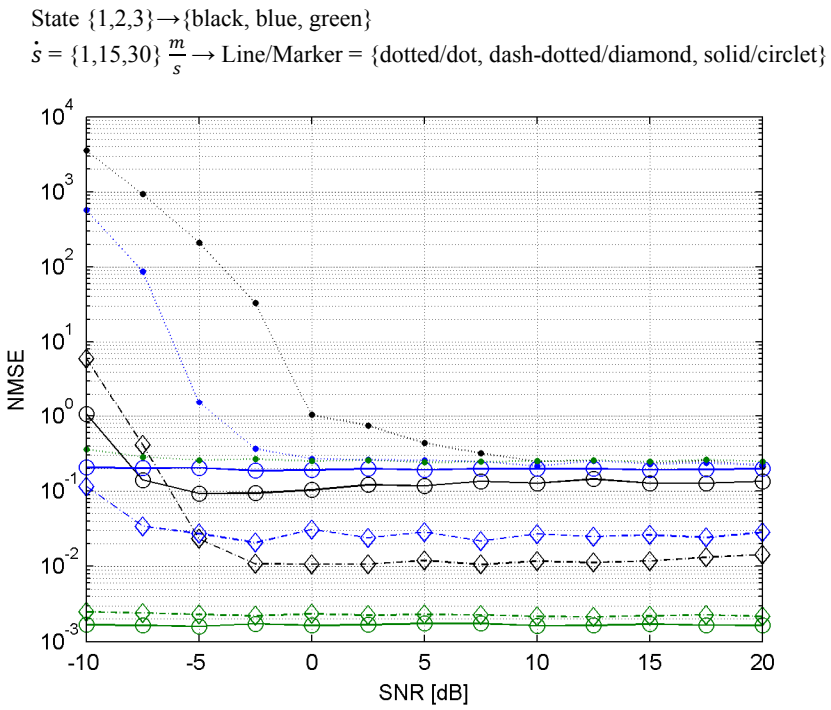

Figure 6.14: Jitter performance over SNR
of the Doppler spread estimation

For the same training sequence Figure 6.15 depicts the achievable Doppler spread jitter performance at variable speeds. The Markov states $\{1, 2, 3\}$ are indicated in black, blue, and green, respectively, using SNR = 10 dB. Obviously, the states 1 and 2 exhibit a poor performance towards higher velocities; detailed investigations revealed that the shadowing component becomes the predominant interference source for states 1 and 2

which at higher speeds leads to an underestimation of the actual Doppler spread. Hence, for practical systems it is suggested to implement an adaptive concept with either variable training lengths and/or a masking of the shadowing in the spectrum – which can be obtained from the correlative distance s_c as is typically $1 - 3$ m [94][98].

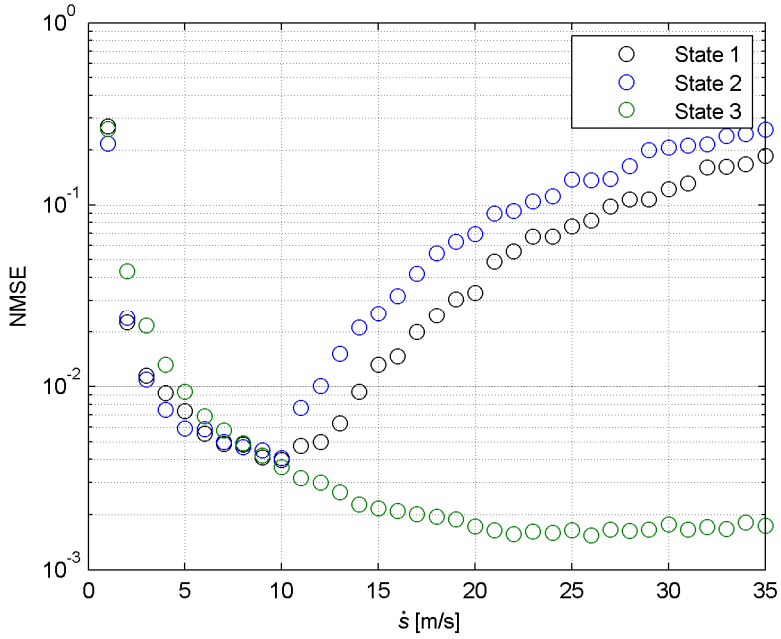

Figure 6.15: Jitter performance over velocity
of the Doppler spread estimation

It is to be noticed that a maximum user terminal speed of 42 m/s ($\cong$ 150 km/h) was assumed for simulations; an adequate assumption will also make sense for practical implementations in order to catch unsuccessful Doppler spread estimations.

6.3.4.2 Power Parameter Estimation

As previously mentioned, a sequence of 1024 samples derived from interspersed DVB-S2 pilots (see Section 6.3.1) is used for power estimations, in order to ensure enough variability throughout the observation period to receive significant results.

Considering ideal frequency and phase error recovery as well as Doppler spread estimation, Figure 6.16 and Figure 6.17 depict the achievable performance in terms of NMSE of SNR and SIR, respectively. Both implement the settings as outlined in Section 6.3.1; the plot style follows Table 4. SNR estimates turn out to be practically useless at low speeds (1 m/s – dotted lines with dots) for medium and heavy fading conditions. This observation also applies to the SIR estimates indicated in Figure 6.19, which for low speeds degrades significantly, but for any Markov state.

State {1,2,3}→{black, blue, green}
$\dot{s}$ = {1,15,30} $\frac{m}{s}$ → Line/Marker = {dotted/dot, dash-dotted/diamond, solid/circlet}

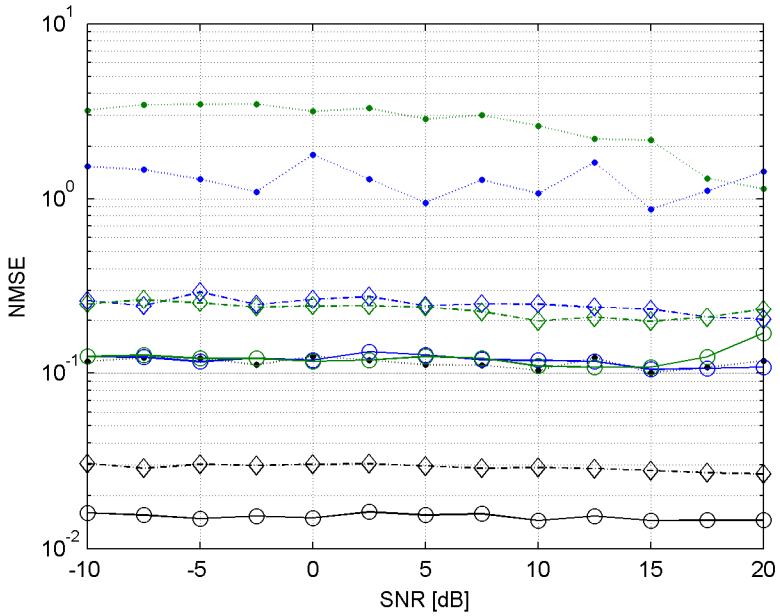

Figure 6.16: NMSE performance of SNR estimation (no frequency error)

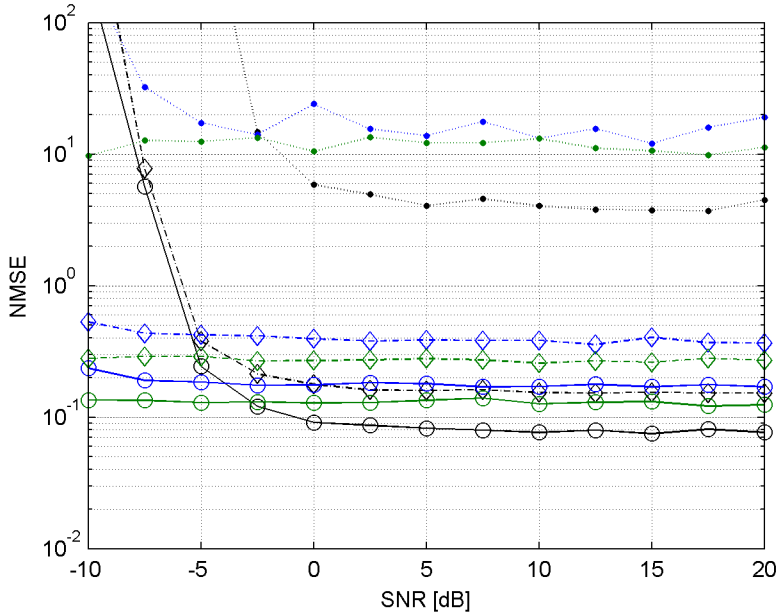

Figure 6.17: NMSE performance of SIR estimation (no frequency error)

Including a frequency error and Doppler spread estimations as described before, Figure 6.18 and Figure 6.19 indicate the achievable performance in terms of NMSE of SNR and SIR estimations, respectively. Both implement the settings as outlined in Section

6.3.1. The plot styles follow Table 4. The SNR estimates at higher speeds (30 m/s – solid lines with circlets) suffer towards the higher SNR regime from a decreasing performance. This basically occurs due to corrupted Doppler spread estimations because of the shadowing, as explained in Section 6.3.4.1. Not surprisingly, the estimations for low speeds perform at least as bad as described before.

State {1,2,3}→{black, blue, green}
$\dot{s}$ = {1,15,30} $\frac{m}{s}$ → Line/Marker = {dotted/dot, dash-dotted/diamond, solid/circlet}

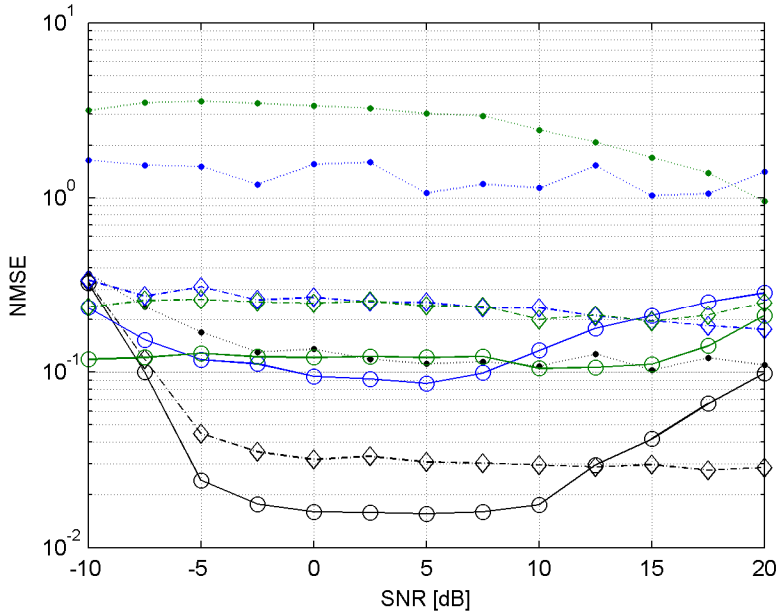

Figure 6.18: NMSE performance of SNR estimation (frequency error)

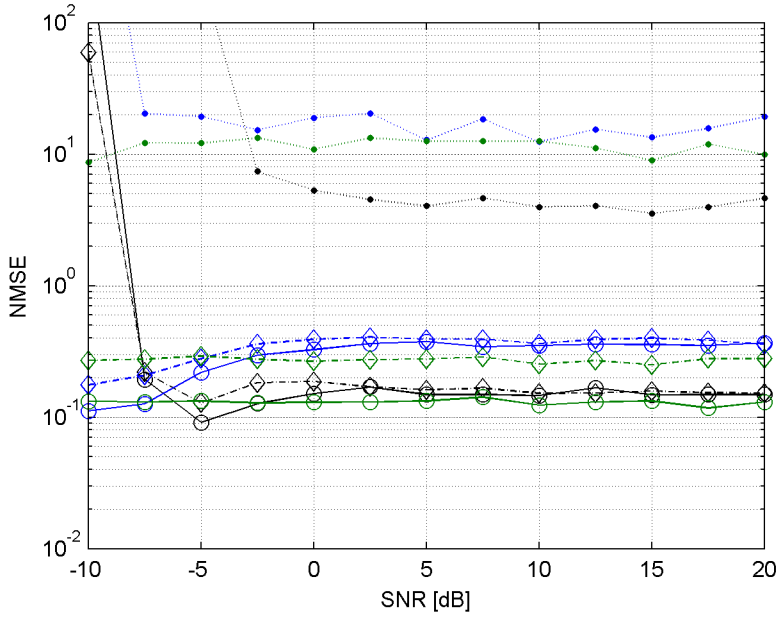

Figure 6.19: NMSE performance of SNR estimation (frequency error)

For the sake of completeness, additional results using a two-step Doppler spread estimation method – two consecutively applied HDS estimators, one estimating the shadowing bandwidth and the second one the Doppler spread – are depicted in Appendix D-(a) and (b).

From the presented results, it is clear that the power parameters can be appropriately estimated on the LF-channel, even when considering estimations at low speeds, which did not perform well at first glance. For the latter the estimation length or alternatively the observation period could adaptively be adjusted according to the mobile terminal speed, which can successfully be derived from the Doppler spread estimations.

6.4 State Classification

As stated in the preface of this chapter, the power parameters as well as the Doppler spread finally are supposed to feed into a tailor-made ACM scheme for LF-channels. In order to support these efforts, it was considered investigating simple means for classifying the current state by using estimation results for the SIR. Within the following subsections a simple heuristic classification algorithm is exemplified and benchmarked by simulation results.

6.4.1 Heuristic Classification Algorithm

Without the claim of novelty, a simple heuristic classification algorithm estimating the current Markov state is presented. It originates from the observation that the simulation results for SIR apparently follow Gaussian distributions, whose mean and variance are unique for each Markov state. Given the general Gaussian PDF, *i.e.*

$$f_{\Upsilon}(x) = \frac{1}{\sqrt{2\pi}\cdot\sigma_{\Upsilon}} \cdot e^{-\frac{1}{2}\cdot\left(\frac{x-\mu_{\Upsilon}}{\sigma_{\Upsilon}}\right)^2}, \tag{6.20}$$

where Υ represents the Υ-th Markov state, the thresholds for the classification algorithm are obtained as:

$$\begin{aligned} \zeta_{12} &= \arg_{\mu_1<x<\mu_2}[f_1(x) = f_2(x)] \\ \zeta_{23} &= \arg_{\mu_2<x<\mu_3}[f_2(x) = f_3(x)]. \end{aligned} \tag{6.21}$$

From there the estimated results can easily be classified with $\Upsilon \in \{1, 2, 3\}$ representing the respective Markov state and K_{LF} representing the for the LF channel estimated SIR by

$$\hat{\Upsilon} = \begin{cases} 1, & K_{LF} < \zeta_{12} \\ 2, & \zeta_{12} < K_{LF} < \zeta_{23} \\ 3, & K_{LF} > \zeta_{23} \end{cases}. \tag{6.22}$$

The appropriate parameters for mean, *i.e.* μ_Υ, and variance, *i.e.* σ_Υ^2, can be extracted from simulation results comprehending the NMSE and the MEV.

6.4.2 Classification Performance

During extensive simulation work it turned out that the classification performanc neither exhibits a dependency on the speed nor on the SNR which were applied to determine the thresholds. Mechanisms adapting the latter to the current channel conditions are not necessary.

Figure 6.20 depicts the achievable total success rate over all three states for fixed and optimized classification thresholds at variable SNR of $\{0, 10, 20\}$ dB indicated in black, red, and blue, respectively. Solid lines indicate results for thresholds which were *a priori* extracted for speeds of 15 m/s (fixed), whereas the dotted lines indicate results for thresholds optimized for the current speed. No significant difference in the success rate can be observed for fixed or optimized thresholds at higher speeds. This also holds true for different SNRs. Interestingly, at low mobile terminal speeds the fixed thresholds exhibit a better performance than the optimized ones.

Figure 6.21 indicates the capability of the proposed classification method explicitly for the Markov states. In the upper plot the channel state was fixed during the simulations to either state 1 (solid blue line), 2 (dashed blue line) or 3 (dotted blue line). At high speeds all results converge towards 100% success rate, thus suggesting the chosen algorithm performs well. At low speeds the success rates for the states 2 and 3 decreases, because of the weak performance of the power parameter estimations. However, employing the full LF model as can be seen in the bottom plot, the results for the states 1 (solid black line), 2 (dashed back line) and 3 (dotted back line) do not approach a success rate of 100 %, but approximately 77% are achieved; this drop can be explained by the state transitions occurring within the observation periods leading to somehow averaged results which become erroneously classified. The total success rate is indicated as red solid line.

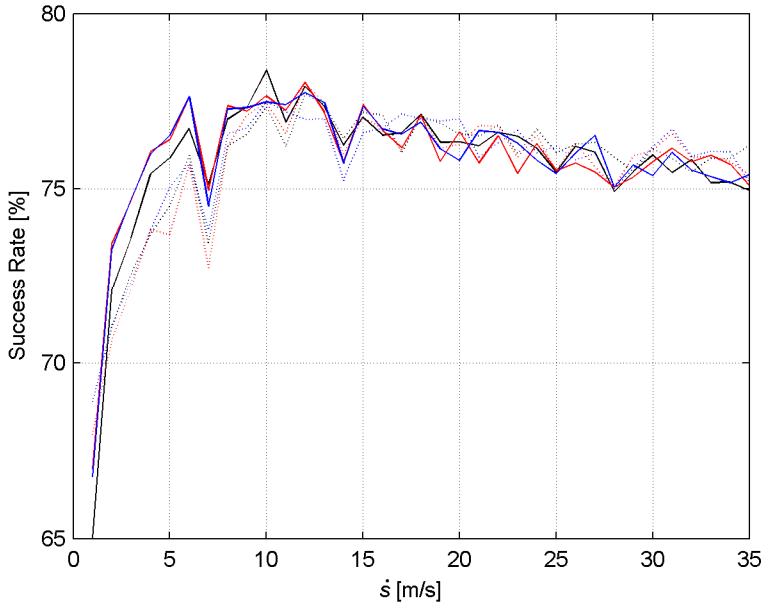

Figure 6.20: Total success rate for differently configured classification thresholds

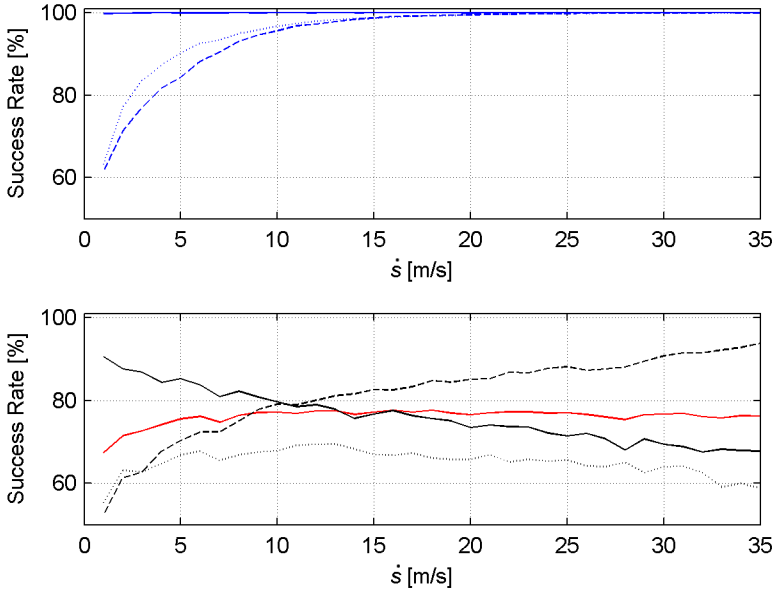

Figure 6.21: Partial success rates for fixed classification thresholds

The bottom plot in Figure 6.22 indicates the performance of the channel state classification as a time sequence over several seconds for a mobile terminal speed of 30 m/s. The top plot in Figure 6.22 indicates the respective channel magnitude (blue). The evolution of the channel states is provided in red, the black line indicates the classified channel state at the time which it refers to, whereas the black dots indicate the actual time when

the classification result is available. Without further investigations it can be seen that from the channel state classification an appropriate ACM scheme can hardly be derived; neither for low speeds because of the inconvenient power parameter estimation accuracy, nor for high speeds because the channel state might already be outdated until the results arrive at the transmitters' end.

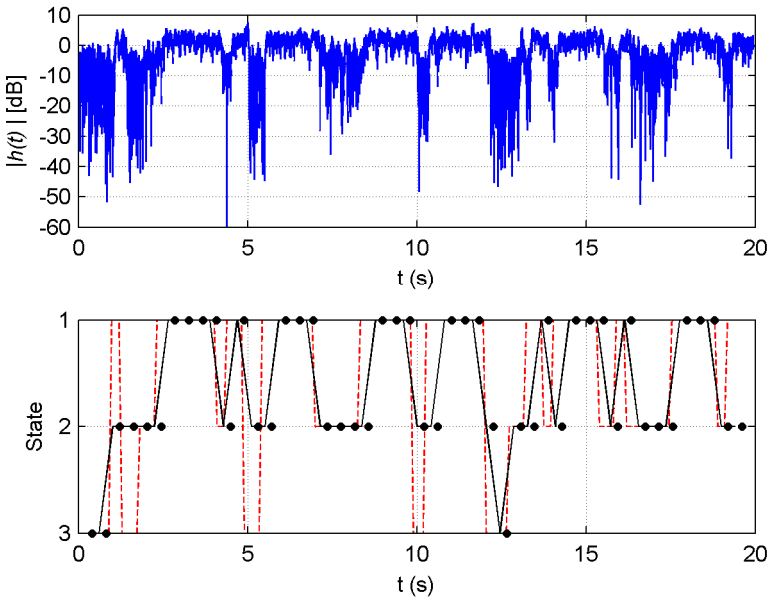

Figure 6.22: Classification of the LF-channel state over time

6.5 Summary

The presented work focused on channel estimation in land-mobile satellite channels aiming at providing accurate and timely figures of merit revealing the current channel state. The latter seeks to serve as input for an adaptive coding and modulation scheme, which is a well-known approach in the realm of satellite communications to compensate for slow fading effects, and comprises the signal-to-noise-ratio, the signal-to-interference-ratio and the Doppler spread. Based on the candidate techniques already identified in Chapter 5 for this purpose, a framework was built up as follows:

The Loo-Fontan channel was closely analysed and its affinity to the Rice channel was pointed out. In comparison to the Rice channel the direct signal component can no more be assumed to be just line-of-sight, moreover it is perturbed by a log-normal random process accounting for shadowing. The latter is known as the Loo-model. To fulfil the stochastic requirements of a land-mobile satellite channel the Loo-Fontan model implements a first-order Markov chain whose states and transitions control the statistical

properties of the underlying Loo model. From that a signal model was formulated and its components were detailed as well as their relations to the Doppler spread and power factors were drawn. The properties of periodograms were pointed out to use them in the context of parameter estimation.

It could be shown that carrier frequency and phase recovery exhibit a performance close to the theoretical bound. Even more, when exploiting the DVB-S2-based training sequences, a performance approaching the theoretical bound for AWGN channels could be observed. Concluding that, for very short time frames with respect to the mobile terminals' speed, the Loo-Fontan channel may be regarded as a AWGN channel, an observation which was backed by several results throughout the study.

Also channel parameter estimations, as independently performed on the training sequences, exhibited a performance approaching the theoretical bounds for AWGN conditions. It was shown that interpolations can be used to provide a good estimate of the current channel conditions throughout the data block, which for instance is required for modern decoding schemes.

Doppler spread estimations perform reasonably well on the Loo-Fontan channel, whereas it could be observed that in cases where the shadowing component becomes the predominant part of the interference the performance vanishes. This problem can be tackled by an adaptive algorithm incorporating some tracking capability, a brief instruction amending the applied heuristic Doppler spread estimation algorithm was provided in that context.

Power parameter estimations turned out to perform quite well, as expected from the results for the Rice channel. Unfortunately, low mobile speeds cause problems and exhibit weak performance. Resorting to adaptively changing the length of the observation period was suggested in that regard; this could be furnished by speed estimations directly derived from the Doppler spread.

Finally a simple classifier was introduced estimating the current Markov state of the Loo-Fontan channel. Based on the estimation results for signal-to-interference ratios, a simple classifier was formulated based on a Gaussian power spectral density approach. This simple approach turned out to asymptotically perform ideally for relatively high mobile speeds, however, in total only a success rate of about 77% can be achieved, which is a significant gain compared to 33% average chance. For the sake of correctness, it is to be noticed that this information would have to be delivered timely to the transmitter, which is not a simple feat, often impossible, considering a round-trip time of approximately 250 ms.

7 Overall Summary

At the first glance satellite communications differ primarily from their terrestrial counterparts by long transmission distances leading to long round-trip times and path losses. By considering a classical communication model it was shown that synchronization is of paramount importance for efficient satellite communications, especially for burst mode transmissions.

Ambitious full frequency reuse was considered for investigations on the MIMO satellite links, where interference is a major hurdle. It was explained that mitigation strategies such as beamforming, precoding, and multi-user detection require accurate channel estimation.

Based on the respective signal models for the forward and return links, appropriate estimation procedures could be identified:

1) Forward link:
    a) Channel estimation using the pseudo-inverse
        i. Based on orthogonal codes
        ii. Based on linearly independent pseudo-random sequences
    b) Channel estimation based on correlations
2) Return link:
    a) Channel estimation using correlations
    b) Channel estimation using successive interference cancellation

For all listed methods theoretical performance limits were provided. Moreover, for 1a) the exhibited jitter amplification and for 1b) and 2a) the exhibited jitter floor could be analytically described, thus allowing for performance assessments without simulations. These results represent an important contribution to the understanding of the limits of parameter estimation on MIMO satellite links. For all methods performance curves were provided and compared, thus allowing system designers to employ one or the other method according to its advantages or disadvantages. Location-dependent estimation performance was identified for 1b) suggesting an identifier sequence hopping to counteract that. The methods for the return link provide the capability to jointly recover symbol timing and to estimate the sought channel state information. Nonetheless, 2b) turned out to provide the best results in that respect. The influence of residual carrier frequency errors was discussed as well and found to be minor when correctly tackled.

Concepts were introduced exploiting certain deterministic dependencies inherent to the MIMO model. Compared to classical approaches, significant performance improvements are possible. First, deterministic timing recovery so as to provide the basis for

successful channel estimation was discussed. Secondly, location-aware channel estimation, requiring knowledge of the user terminal's position and the antenna model was introduced, which to the best of the author's knowledge is a novel idea. For the latter an important observation was that the physical path in the model cancels out when providing the abovementioned knowledge. Having a good channel estimate for a signal component with a good signal-to-noise plus interference ratio obtained, the other signal components can be assessed deterministically.

Based on a simplified model, periodogram-based candidate estimation schemes for land-mobile satellite channels were investigated. The importance of timely and accurate channel estimation delivering the relevant figures of merit (signal-to-noise-ratio, signal-to-interference-ratio, and Doppler spread) was pointed out. Data-aided estimation algorithms were proposed for

1) carrier frequency and phase estimations,
2) Doppler spread estimations,
3) and power parameter estimations.

For carrier and power parameters Cramer-Rao lower bounds tailored to the Rician channel were stated. They were closely met by the applied synchronization algorithms. For the Doppler spread a novel heuristic Doppler spread estimator was developed. It achieved results which were in all investigated disciplines superior with respect to the most promising algorithms in the open literature.

Two estimation algorithms were introduced for power parameters. One is a fully heuristic approach and the other one is a partially heuristic approach, whereas they performed equally well.

Joining the most promising candidate algorithms for 1)-3), accurate estimations for the Doppler spread as well as for the signal-to-noise-ratio and for the signal-to-interference-ratio were obtained, whereas the latter tends to violate the respective theoretical bound in the presence of higher noise, which to the best of the author's knowledge is due to a bias effect.

The estimation framework established for the Rician channel model was applied to the Loo-Fontan land-mobile satellite channel model. After comprehensive discussions of the Loo-Fontan model, detailed simulation results indicated the applicability of the adopted estimation framework. In that context it could be shown that carrier frequency and phase recovery exhibit a performance close to the theoretical bounds. Also channel parameter estimations exploiting a single training sequence exhibited a performance approaching the theoretical bounds for AWGN conditions.

Doppler spread estimations perform reasonably well on the Loo-Fontan channel, whereas it was observed that in cases, where the shadowing component becomes the predom-

inant part of the interference, the performance decreases. This problem could be tackled with an appropriate tracking algorithm. Periodogram-based power parameter estimations turned out to perform well in cases when enough variability of the channel is observed. Finally, a simple classifier was introduced estimating the current Markov state of the Loo-Fontan channel. This approach turned out to asymptotically perform ideally for relatively high mobile speeds. However, in total a success rate of about 77% can be achieved. Compared to a 33% average chance this is a significant gain. For the sake of correctness, this information would have to be delivered timely with respect to the channel variability to the transmitter, which in fact is bounded by obvious physical reasons.

(This page is intentionally left blank)

8 Future Outlook

Throughout this thesis many interesting and valuable answers for current problem statements were found and presented. However, as it typically is with research work, often more questions are identified than answers, especially when considering such a vast topic as the discussed. In that respect this chapter brings up interesting ideas and impulses which could not be covered in this work, but definitely deserve attention in future work.

Estimations on MIMO satellite links were discussed in Chapters 3 and 4; with respect to this, the following points could be considered as an extensive agenda for future activities:

- Incorporating the estimation framework in a full channel simulator including precoding, beamforming, MUD, as well as real data transmission so as to retrieve real figures of how much the achievable estimation accuracy actually influences the data throughput.
- Introducing more sophisticated channel models considering other real world effects, such as phase noise, non-linear effects (*e.g.* from amplifiers), fading, etc.
- Examining the applicability of LACE with respect to non-ideal satellite behaviour, such as inaccuracies in heading and relative movement.

Channel estimations on mobile satellite links were considered in Chapters 5 and 6, for which the following remarks could draw a roadmap for future work:

- Building a simulator which, based on the parameter estimation framework, includes data transport controlled by an ACM scheme which consequently extracts its decisions on the channel estimates.
- Based on the last bullet, appropriate tracking algorithms should be devised which enhance the estimation framework, such that the observation period is adjusted according to the current mobile speed (or the channel variability). This would increase the estimation precision for conditions at slow channel variations and could further enhance the ACM concept.

(This page is intentionally left blank)

APPENDIX

A Ad Chapter 3: Channel Estimation on MIMO Satellite Links

(a) Details of the MIMO Model

Throughout this paragraph, a concise listing of the model parameters used for simulations is provided.

Table A - 1 provides a listing of all 100 user terminals and their respective locations in the scenario as used for simulations.

Nr.	Latitude [deg.]	Longitude [deg.]	Nr.	Latitude [deg.]	Longitude [deg.]
1	8.7272370	-7.4746551	51	6.1526162	10.7713241
2	10.7807427	-9.1588751	52	-6.2530984	11.8955783
3	0.5655775	-4.9213439	53	-3.0207847	12.4289253
4	7.7148323	-6.4275782	54	-1.6214432	12.0563981
5	8.9748082	-6.4576207	55	1.0039262	11.5744176
6	-1.6970040	-3.6398768	56	4.1504503	11.3186005
7	0.6896240	-3.9633545	57	5.6042318	12.2760323
8	2.9875433	-3.1146247	58	-4.1424863	14.3679363
9	4.9539351	-4.6058129	59	-3.0072611	14.6311448
10	8.3788689	-3.5364503	60	-0.1310606	14.3259612
11	10.4010287	-4.7317594	61	3.1881460	13.3195700
12	-3.0869883	-0.6705339	62	3.5454110	13.1805556
13	0.1099898	-1.5640510	63	-3.4400731	15.6171189
14	2.5009284	-2.6606957	64	-1.6169445	16.2417667
15	4.6748983	-1.8595664	65	0.5959737	16.0435425
16	5.7996399	-2.3478064	66	3.1618737	14.8181165
17	9.3076599	-1.7289323	67	5.2889913	16.2977018
18	-2.0174150	0.5171370	68	-3.2731216	17.2633199
19	2.2040269	0.4711045	69	0.3885336	18.2666526
20	2.4388408	0.1828158	70	1.7979551	16.7883997
21	6.3586896	-0.3217894	71	4.1699413	18.5458077
22	7.5586257	1.1608587	72	7.2458342	16.7819490
23	-5.1078440	2.5955715	73	-1.7472074	20.4566434
24	-1.9972965	1.4519978	74	0.2281787	19.6994040
25	-0.2190915	3.3704944	75	3.9139174	19.3203705
26	1.6726340	2.4109374	76	5.8032770	18.5864480
27	4.2537250	1.2932448	77	7.6268499	19.7470782
28	6.4275439	1.6875973	78	-2.1941599	21.6002215
29	-4.7540532	4.7187263	79	0.4463173	22.0658531

30	-3.0647064	5.0627878	80	1.4176682	21.0359916
31	-0.1595079	4.1876304	81	3.9950182	22.1302500
32	1.5715544	4.9397768	82	7.1489263	23.0039691
33	2.8547011	5.2153953	83	-1.8522886	24.0237570
34	-3.8163302	6.5364122	84	1.6451211	24.4935215
35	-2.0852424	6.2653924	85	4.0812292	23.6534992
36	0.3224479	7.2757465	86	6.7883093	23.4071484
37	2.4529022	7.1096437	87	2.5872507	25.3984869
38	4.8578226	5.1777390	88	4.5682544	24.5904731
39	5.9855955	5.3772368	89	7.1200055	26.2694946
40	-4.8389939	7.7784588	90	1.2126411	26.5187846
41	-3.7066817	7.3436687	91	2.5851546	26.7546075
42	-2.1274302	7.8305789	92	5.9029080	27.1643226
43	0.2741363	8.1396764	93	8.7237609	27.3034687
44	3.9082313	7.9996212	94	10.4638946	29.0987655
45	-7.0046837	8.8027576	95	1.8983107	29.9943119
46	-4.0629344	8.9982275	96	5.3996057	30.0228433
47	-2.3155015	10.3770752	97	6.6178201	29.3703008
48	0.1425968	10.7446499	98	7.9039459	30.7286013
49	2.2599892	9.3913390	99	11.4690882	30.1256537
50	4.8516718	9.6495773	100	4.2026722	31.4705865

Table A - 1: User terminal locations for the investigated MIMO model

(b) Limits of the Moore-Penrose Pseudo-Inverse

In this paragraph, a brief analysis details why channel estimation using the Moore-Penrose pseudo-inverse fails for linearly dependent UWs:

The well-known Moore-Penrose pseudo-inverse $\mathbf{A}^{+}$ of the $m \times n$ matrix $\mathbf{A}$ is characterized by the following properties [54]:

(1) $\mathbf{A} \cdot \mathbf{A}^{+} \cdot \mathbf{A} = \mathbf{A}$
(2) $\mathbf{A}^{+} \cdot \mathbf{A} \cdot \mathbf{A}^{+} = \mathbf{A}^{+}$
(3) $(\mathbf{A} \cdot \mathbf{A}^{+})^{\mathrm{T}} = \mathbf{A} \cdot \mathbf{A}^{+}$
(4) $(\mathbf{A}^{+} \cdot \mathbf{A})^{\mathrm{T}} = \mathbf{A}^{+} \cdot \mathbf{A}$

The pseudo-inverse, as used throughout this work, is given by

(5) $\mathbf{A}^{+} = \mathbf{A}^{\mathrm{H}} \cdot (\mathbf{A} \cdot \mathbf{A}^{\mathrm{H}})^{-1}$,

where $\mathbf{A}^{\mathrm{H}}$ denotes the Hermitian. It is to be noticed that $\mathbf{A} \cdot \mathbf{A}^{\mathrm{H}}$ must be invertible, thus $\mathbf{A} \cdot \mathbf{A}^{\mathrm{H}}$ has to be a non-singular $m \times m$ matrix requiring full $rank\ m$. In case of linear dependent rows in $\mathbf{A}$, evidently when $n < m$ (*i.e.* $rank(\mathbf{A}) \leq min\{m, n\}$), the row $rank(\mathbf{A}) \leq n \Rightarrow rank(\mathbf{A} \cdot \mathbf{A}^{\mathrm{H}}) = rank(\mathbf{A}) < m$. Hence, inversion of the term $\mathbf{A} \cdot \mathbf{A}^{\mathrm{H}}$ and furthermore the calculation of the Moore-Penrose pseudo-inverse fails resulting in a

violation of properties (1)-(4). Henceforth, the pseudo-inverse requires $rank(\mathbf{A}) = m$, *i.e.* m linear independent rows in $\mathbf{A}$ [49, pp. 12-14].

To guarantee a set of linearly independent UWs $\mathbf{c}_m = \left(c_{m,1}, c_{m,2}, \dots c_{m,L}\right)\big|_{m=1,2\dots,K}$ in $\mathbf{C} = (\mathbf{c}_1, \mathbf{c}_2, \dots, \mathbf{c}_K)^{\mathrm{T}}$ besides $\mathbf{c}_m$ may not be the zero vector, either one of the following conditions must be fulfilled [49, pp. 3]:

- $L > K$,
- or when $L = K$: a proper linear independent subset of vectors must be chosen, *i.e.* no vector may consist of a linear combination of other vectors.

(c) Generation of Pseudo-Random Sequences for the MIMO-BC

The symbol synchronicity of the MIMO-BC relaxes the search conditions for PRSs. Hence cross-correlations at symbol time granularity are sufficient to be computed for evaluation. However, starting with an initial PRS and threshold ζ, k trials are performed to find a PRS for which $\max_{n=1,2\dots,m-1}|R_{nm}| \leq \zeta$, where $|R_{nm}|$ denotes the magnitude of the cross-correlation value of already found sequences n and the current PRS m under test. If a PRS successfully passed the test within k trials, it is stored and the counter is reset. If no PRS was found within k trials, the threshold is relaxed and the search continues until all N PRSs are found. Figure A - 1 below depicts the described procedure as a flow chart.

Figure A - 2 exemplifies the cross-correlation properties of a linearly dependent set of $N = 155$ PRSs with $L = 26$ binary symbols; a stepwise increase in the cross-correlation from left to right can be observed which stems from the threshold policy of the algorithm: it successively relaxes the acceptance criterion for PRSs after a number of vain trials.

It is to be noticed that the in Figure A - 2 illustrated UWs are not linearly independent because $L < N$. It can as such only be used for channel estimation with correlation. However, the search principle remains the same for linearly independent UWs, *i.e.* $L \geq N$.

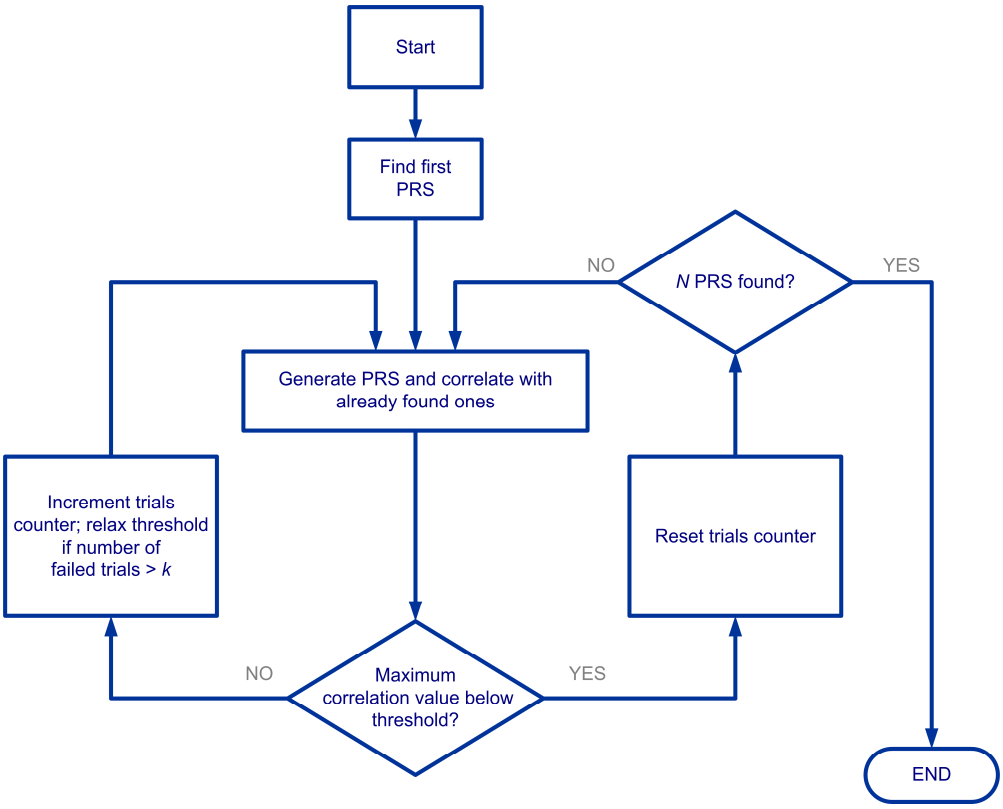

Figure A - 1: Scheme of the PRS generation algorithm

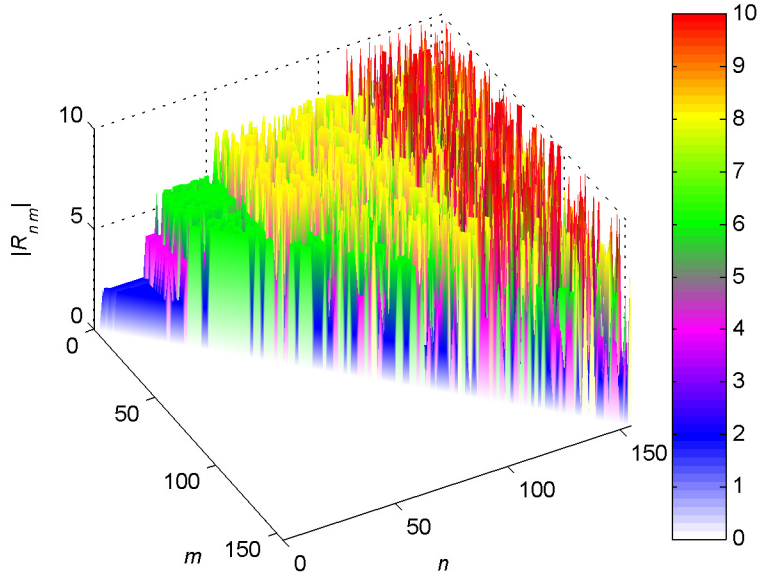

Figure A - 2: Cross-correlation of quasi-orthogonal random sequences ($L = 26$, $N = 155$)

(d) Jitter Variance of Orthogonal Identifier Sequences

To better understand the properties of the jitter variance for orthogonal identifier sequences, *i.e.*

$$\sigma_{\mathcal{H}}^2 = \sigma_n^2 \cdot \sum_{i=1}^{L} \left| c_{k,i}^{\mathrm{H}} \right|^2,$$

an example is carried out in the sequel. A set of eight orthogonal Walsh-Hadamard sequences with $L = 8$ is examined therefore. A number of $N = 8$ MIMO channels is assumed. It will become obvious that for orthogonal sequences no interference noise (as can be seen in Appendix 0-(e) occurs.

The binary WH identifier sequences are

$$\mathbf{C} = \boldsymbol{\mathcal{H}}_{(3)} = \begin{vmatrix} +1 & +1 & +1 & +1 & +1 & +1 & +1 & +1 \\ +1 & -1 & +1 & -1 & +1 & -1 & +1 & -1 \\ +1 & +1 & -1 & -1 & +1 & +1 & -1 & -1 \\ +1 & -1 & -1 & +1 & +1 & -1 & -1 & +1 \\ +1 & +1 & +1 & +1 & -1 & -1 & -1 & -1 \\ +1 & -1 & +1 & -1 & -1 & +1 & -1 & +1 \\ +1 & +1 & -1 & -1 & -1 & -1 & +1 & +1 \\ +1 & -1 & -1 & +1 & -1 & +1 & +1 & -1 \end{vmatrix}.$$

The pseudo-inverse is furnished by

$$\mathbf{C}^{+} = \frac{1}{L} \cdot \mathbf{C}^{\mathrm{T}} = \\ = \begin{vmatrix} +0.125 & +0.125 & +0.125 & +0.125 & +0.125 & +0.125 & +0.125 & +0.125 \\ +0.125 & -0.125 & +0.125 & -0.125 & +0.125 & -0.125 & +0.125 & -0.125 \\ +0.125 & +0.125 & -0.125 & -0.125 & +0.125 & +0.125 & -0.125 & -0.125 \\ +0.125 & -0.125 & -0.125 & +0.125 & +0.125 & -0.125 & -0.125 & +0.125 \\ +0.125 & +0.125 & +0.125 & +0.125 & -0.125 & -0.125 & -0.125 & -0.125 \\ +0.125 & -0.125 & +0.125 & -0.125 & -0.125 & +0.125 & -0.125 & +0.125 \\ +0.125 & +0.125 & -0.125 & -0.125 & -0.125 & -0.125 & +0.125 & +0.125 \\ +0.125 & -0.125 & -0.125 & +0.125 & -0.125 & +0.125 & +0.125 & -0.125 \end{vmatrix}.$$

The summation term then results in

$$\sum_{i=1}^{L}\left|c_{k,i}^{\mathrm{H}}\right|^2 = \begin{vmatrix} 0.125_{i=1} \\ 0.125_{i=2} \\ 0.125_{i=3} \\ 0.125_{i=4} \\ 0.125_{i=5} \\ 0.125_{i=6} \\ 0.125_{i=7} \\ 0.125_{i=8} \end{vmatrix}$$

which exactly equals $1/L$ for each element in the vector given above, thus no error amplification occurs.

(e) Jitter Variance of Linearly Independent PRS

To better understand the properties of the jitter variance for linearly independent PRS, *i.e.*

$$\sigma_{li}^2 = \sigma_n^2 \cdot \sum_{k=1}^{L}\left|c_{k,i}^{+}\right|^2,$$

an example is carried out in the following. A set of seven quasi-PRSs with $L = 8$ is therefore examined. A number of $N = 7$ MIMO channels is assumed. It will become obvious that for linearly independent PRSs interference noise in terms of noise amplification occurs.

The binary PRSs are

$$\mathbf{C} = \begin{vmatrix} -1 & -1 & -1 & -1 & -1 & -1 & -1 & -1 \\ +1 & +1 & -1 & -1 & +1 & -1 & -1 & +1 \\ +1 & -1 & -1 & +1 & -1 & +1 & +1 & -1 \\ +1 & +1 & +1 & +1 & -1 & -1 & +1 & +1 \\ -1 & -1 & +1 & +1 & +1 & +1 & -1 & -1 \\ +1 & -1 & +1 & -1 & +1 & +1 & +1 & +1 \\ +1 & -1 & -1 & -1 & -1 & +1 & +1 & +1 \end{vmatrix}.$$

The pseudo-inverse is given as

$$\mathbf{C}^{+} = \mathbf{C}^{\mathrm{T}} \cdot (\mathbf{C} \cdot \mathbf{C}^{\mathrm{T}})^{-1} =$$

$$= \begin{vmatrix} +0.125 & +0.375 & +0.375 & +0.250 & +0.125 & +0.250 & -0.125 \\ -0.375 & -0.125 & -0.125 & -0.250 & -0.375 & -0.250 & -0.125 \\ +0.125 & -0.125 & -0.125 & +0.250 & +0.125 & +0.250 & -0.125 \\ -0.125 & +0.125 & +0.125 & +0.250 & +0.375 & -0.250 & +0.125 \\ -0.125 & +0.125 & +0.125 & -0.250 & -0.125 & +0.250 & -0.375 \\ +0.375 & -0.125 & -0.125 & -0.250 & +0.125 & -0.250 & +0.375 \\ -0.125 & -0.375 & +0.125 & -0.250 & -0.625 & +0.250 & -0.375 \\ -0.125 & +0.125 & -0.375 & +0.250 & +0.375 & -0.250 & +0.625 \end{vmatrix}.$$

The summation term then results in

$$\sum_{i=1}^{L} \left| c_{k,i}^{+} \right|^2 = \begin{vmatrix} 0.453_{i=1} \\ 0.453_{i=2} \\ 0.203_{i=3} \\ 0.328_{i=4} \\ 0.328_{i=5} \\ 0.453_{i=6} \\ 0.828_{i=7} \\ 0.828_{i=8} \end{vmatrix},$$

where each entity is larger than $1/L = 0.125$; that explains the noise amplification for linearly independent PRSs.

(f) Mean Jitter Variance of different Identifier Sequences

Table A - 2 compares for the identifier sequences investigated within the DigiSat framework the achievable mean jitter floor using correlation-based channel estimations. The values are depicted in Figure 3.25 and interpreted in Paragraph 3.3.4.2.2.

Type	PRS	PRS	Kasami	random	PRS	PRS	PRS
Length	26	63	63	63	78	156	250
$\overline{\sigma_{jf}^2}$	0.0707	0.0252	0.0322	0.0377	0.0233	0.0086	0.0083

Table A - 2: Mean jitter variance of different identifier sequences

(g) Length Variation of Identifier Sequences on the Return Link at Feed 144

Since channel estimation on the return link is based on correlations, no length restrictions for UWs apply, thus both linearly dependent and linearly independent UWs are possible. Figure A - 3 and Figure A - 4 detail the achievable estimation performance in terms of NMSE of amplitude using UWs of length a) $L = 64$, b) $L = 155$, and c)

$L = 1000$ for correlation and SIC, respectively. The presented results were simulated using feed 144 heading towards the border region of the coverage area. For all plots, the red dashed line indicates the NCRLB, the blue and black lines indicate the strongest and the remaining signal components, respectively. Not surprisingly, longer UWs outperform shorter ones to the cost of a higher overhead.

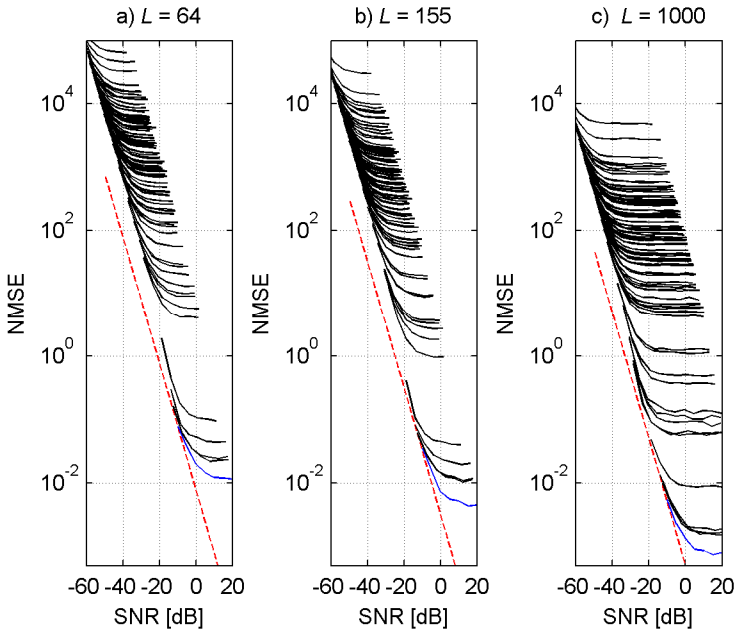

Figure A - 3: Performance comparison of UWs of different length using correlation

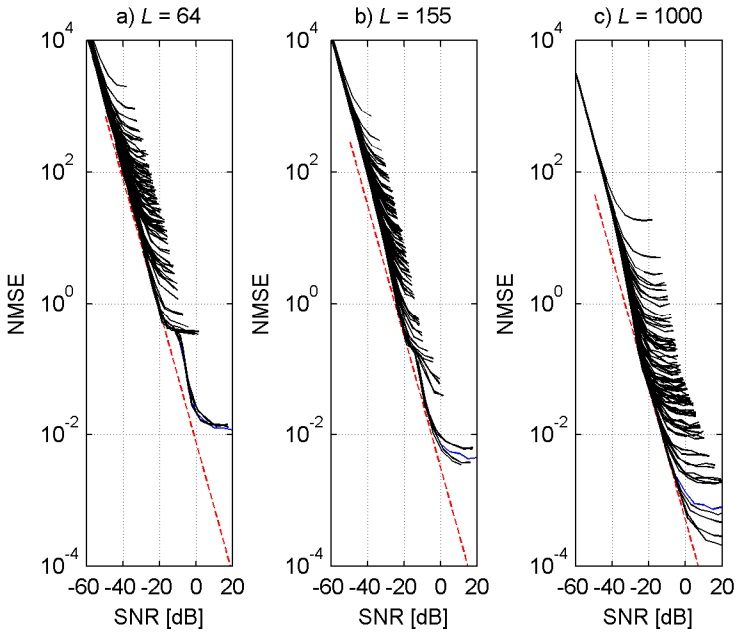

Figure A - 4: Comparison of performance achieved with UWs of different length using SIC

(h) Additional Results on the Influence of Residual Frequency Errors

The simulation results presented in this paragraph depict the influence of residual frequency errors on the estimation performance of the SIC method.

For all results the frequency error normalized by the symbol timing was chosen to be $|\Delta fT| \leq 0.05$; besides that the settings as outlined in Section 3.4.3.4 apply. Frequency estimation and correction was done according to the method proposed by *Mengali* and *Morelli* in [59].

Figure A - 5, Figure A - 6, and Figure A - 7 compare the performance of timing, phase and amplitude estimates for the SIC method without residual frequency errors in a) to estimates with residual frequency errors in b) at feed 1. The red dashed lines indicate the MCRBs and NCRLBs, respectively, the solid lines represent the (N)MSE of the estimates, whereas the blue lines represent the signal component of user terminal 48, *i.e.* the strongest component in feed 1. Analogous to the presented results for the correlation method in Section 3.4.3.4.7 remarkable degradations for amplitude and phase can be observed, because of the additional uncertainties induced by the residual frequency errors and the consequently higher timing jitter.

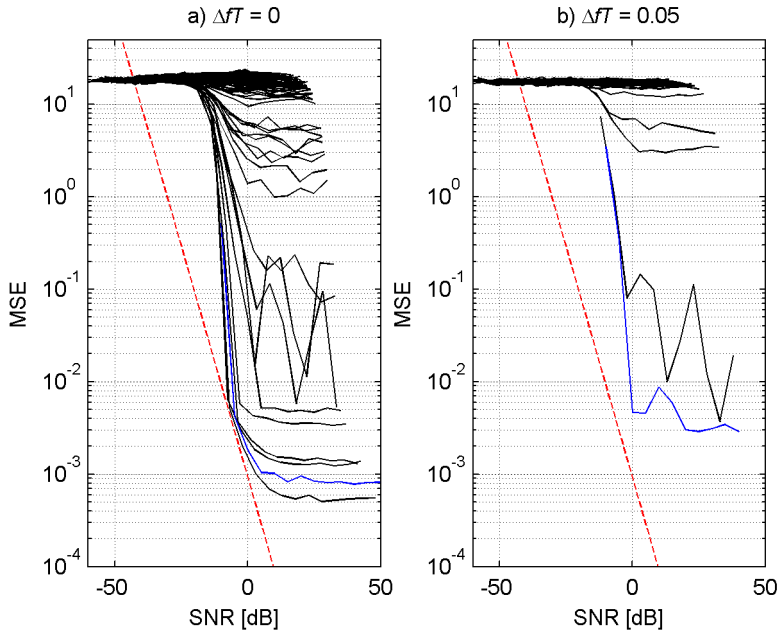

Figure A - 5: Accuracy of timing estimates
due to frequency errors using SIC

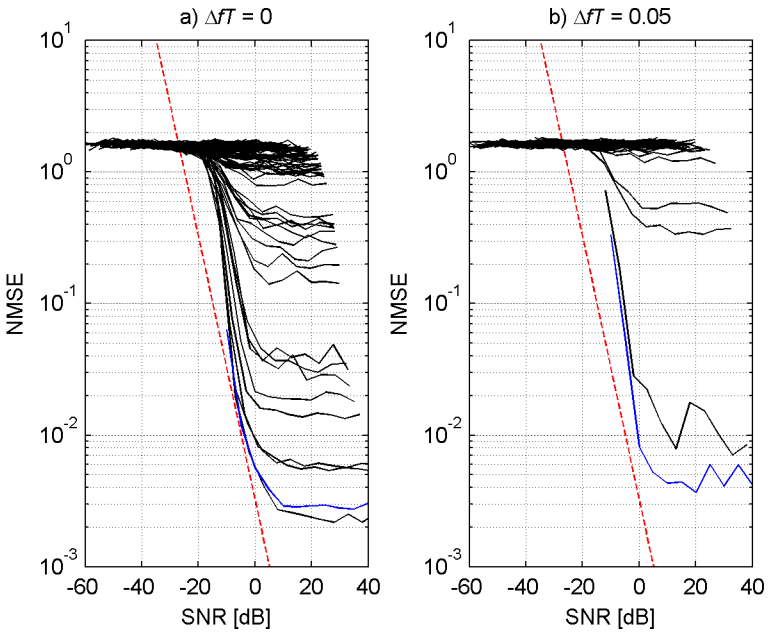

Figure A - 6: Accuracy of phase estimates due to frequency errors using SIC

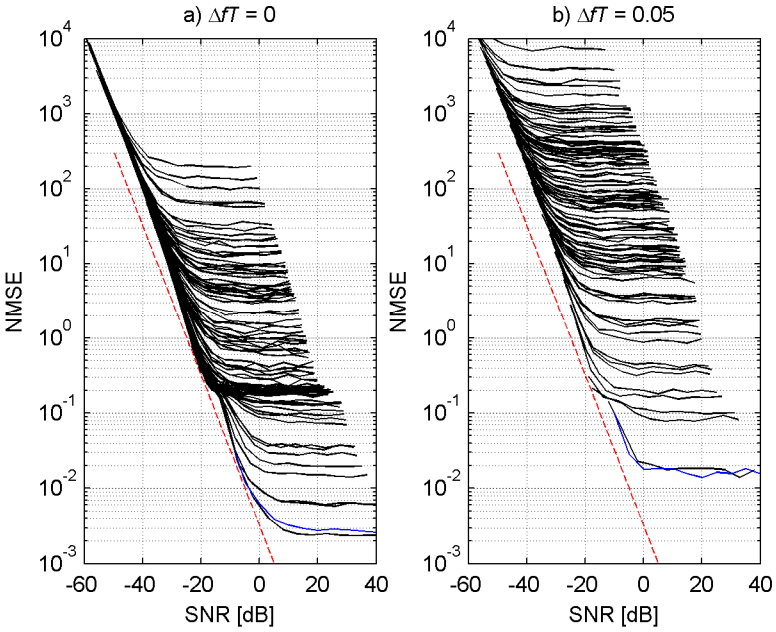

Figure A - 7: Accuracy of amplitude estimates due to frequency errors using SIC

B Ad Chapter 4: Comparison of Ideal and Estimated Timing Recovery using LACE

Figure A - 8 compares the NMSE of amplitude estimates of a) simulations using ideal timing recovery (genie) and b) timing recovery using correlations-based LACE. The simulation setup chosen is detailed in Section 3.4.3.4. Correlations prior to the LACE algorithm estimate the channel matrix. The estimates are done for feed 1, where user terminal 48 is the strongest contributor, thus depicted as blue solid line; the black solid lines indicate the remaining signal amplitude estimates. The red-dashed lines indicate the NCRLB. It can be seen that no significant degradations arise as long as the timing is re-established accurately.

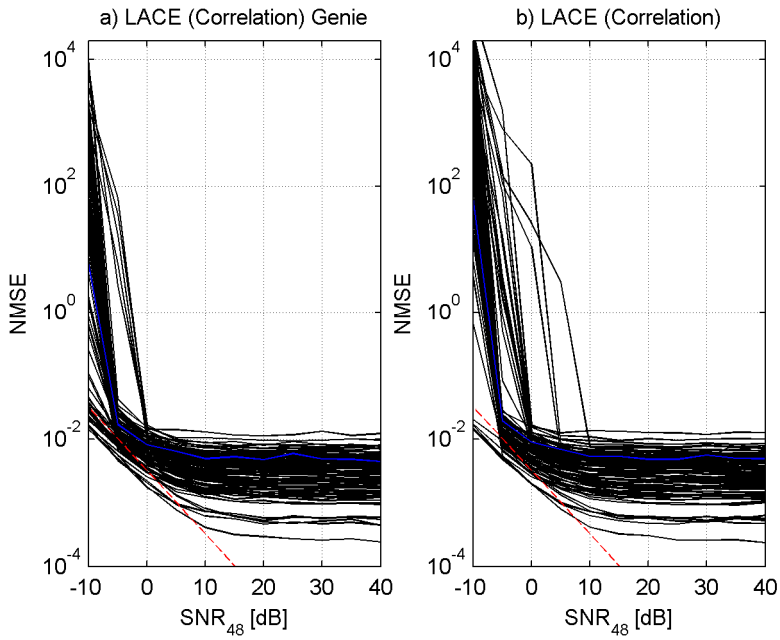

Figure A - 8: Accuracy of LACE (correlation) amplitude estimation due to timing errors

Figure A - 9 compares the NMSE of amplitude estimates of a) simulations using ideal timing recovery (genie) and b) timing recovery using ISIC-A-based LACE (see 3.4.3.4.6). The simulation setup chosen is detailed in 3.4.3.4. ISIC-A prior to the LACE algorithm estimates the channel matrix. All simulations used a number of 5 iterations for ISIC-A. The estimates are done for feed 1, where user terminal 48 is the strongest contributor, thus plotted as blue solid lines; the black solid lines indicate the remaining signal amplitude estimates. The red-dashed lines indicate the NCRLB. Compared to Figure A - 8, LACE based on ISIC-A turns out to be much more sensitive to timing errors, whereas an improved timing accuracy yields to significant performance improvements.

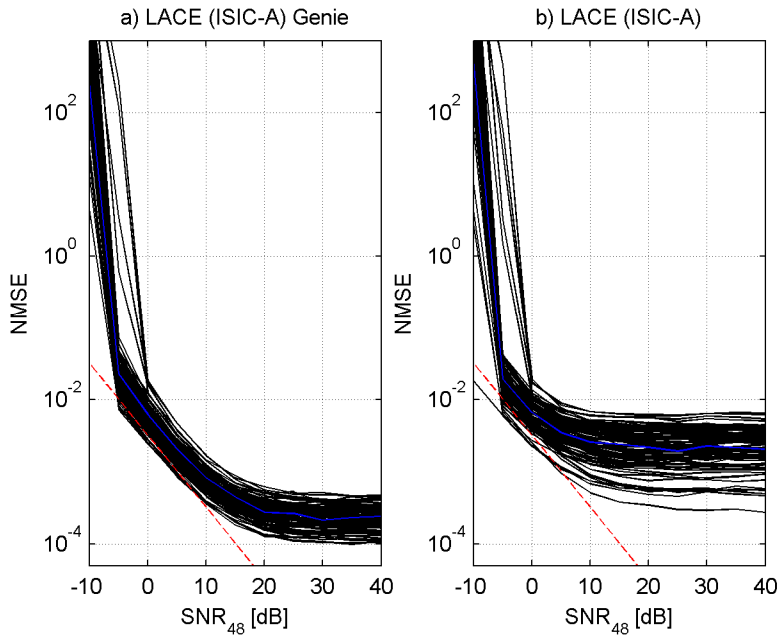

Figure A - 9: Accuracy of LACE (ISIC-A) amplitude estimation due to timing errors

C Ad Chapter 5: Parameter Estimation on Rician Fading Channels

(a) Doppler Spread Estimation Performance at Isotropic and Non-Isotropic Scattering

The jitter performance of the Doppler spread estimators on isotropic and non-isotropic scattering in Rician channels ($K_R = 5dB, B_D T_S = 0.02$) is indicated in Figure A - 10 a) and b), respectively. Results for the NDS estimator are plotted in green, those for the mNDS and HDS estimators in red and blue.

(b) Success Rates achieved with the Doppler Spread Estimators

The success rate provides a measure for the quality of the Doppler spread estimator. It states as a percentage how likely the consecutive power parameter estimations based on the results of the Doppler spread estimations can succeed. The success rate does neither directly relate to the precision of the power parameter estimations nor to the precision of the Doppler spread estimation.

Figure A - 11 compares with respect to the three investigated Doppler spread estimators their achievable success rate. A RICE_{BW} channel with $B_D T_S = 0.1$ was used for simulation. The success rate is plotted in reverse order to better differentiate amongst the curves. Obviously the HDS estimator (blue) again beats the NDS (green) and the mNDS

(red) estimators; simulations with other channel parameters support this observation, but it was refrained from depicting them to preserve clarity and space.

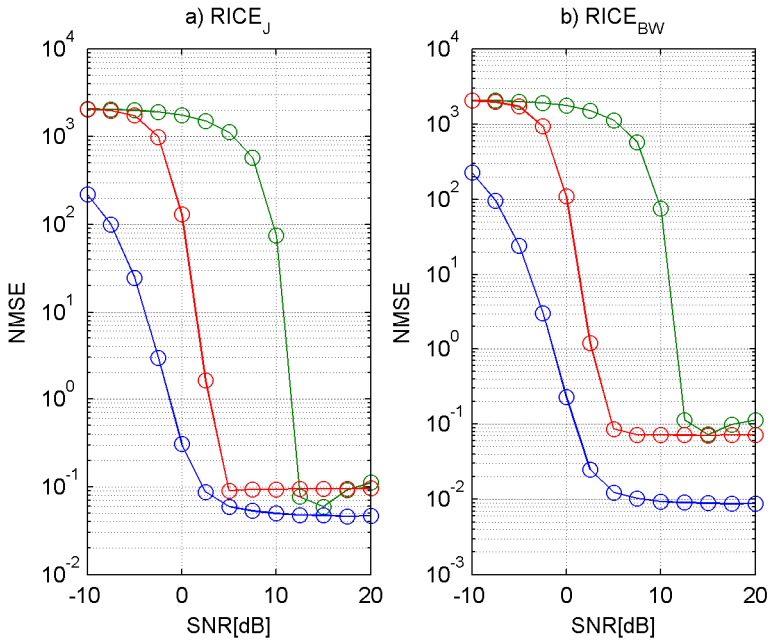

Figure A - 10: Jitter performance of Doppler spread estimators comparing different scattering

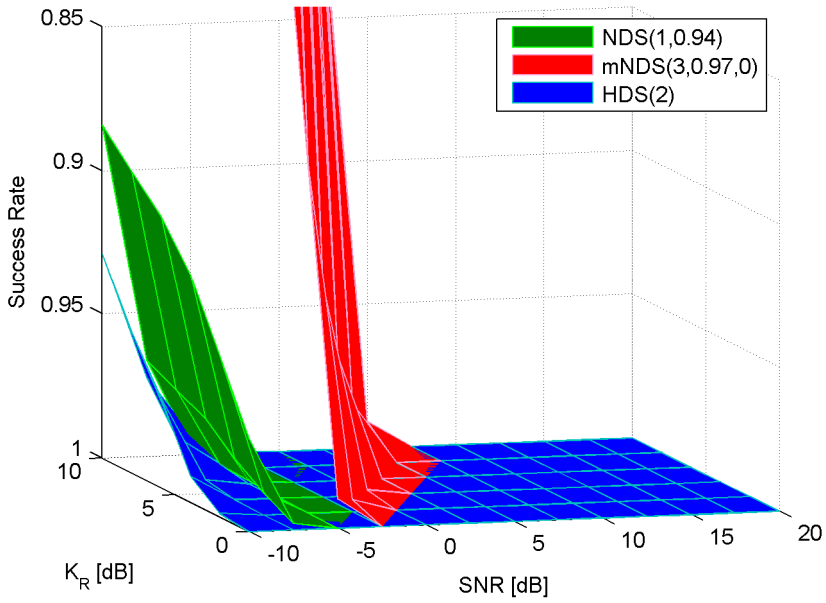

Figure A - 11: Success rate comparison of the Doppler spread estimators

(c) Derivation of the Zero-Frequency Spectral Component in the Jakes model

The total filter power is obtained from the normalized Jakes PSD in (5.6) as

$$S_J = \int_{-f_D}^{f_D} S_\mu(f)df = 1.$$

With $S_\mu(0) = 1/(\pi \cdot f_D)$ and the average PSD

$$\overline{S_\mu} = \frac{1}{2f_D} \int_{-f_D}^{f_D} S_\mu(f)df = \frac{1}{2f_D},$$

the relation between the zero frequency component and the average power is established as

$$S_\mu(0) = 2 \cdot \frac{\overline{S_\mu}}{\pi}.$$

(d) Additional Results for the Power Estimator Comparison

Based on the simulation settings outlined in Section 5.6.2.3, additional results comparing the performance of estimator A (see 5.6.2.1) and estimator B (see 5.6.2.2) are depicted in Figure A - 12, Figure A - 13, and Figure A - 14. Solid black lines indicate the respective normalized true value, dashed black lines indicate the appropriate NCRLB for the Rice channel (see 5.6.1) and red dashed lines indicate the appropriate NCRLB for AWGN conditions. Results of the estimator A are indicated in blue, those of estimator B in green; each of which are further distinguished according to the applied scatter model: RICE_{BW} results are marked as circlets and RICE_{J} results are marked as dots. The top plot in each figure compares the NMEV and the bottom plot compares the NMSE.

By detailed inspection of the figures, it is obvious that both estimators basically exhibit an equal performance. A deviation from the NMSE can be observed for the RICE_{J} results in the bottom plot of Figure A - 12 which stems from the fact that the NCRLB derives from a flat Doppler spread spectrum. Deviations from the analytical bounds can also be observed in the bottom plot of Figure A - 13 which eventually results from a bias effect.

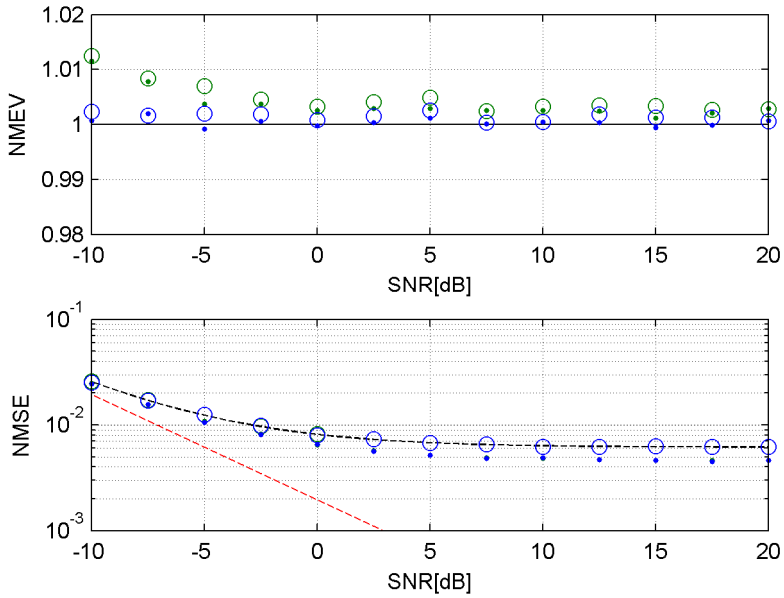

Figure A - 12: NMEV and NMSE evolution of the signal power estimation

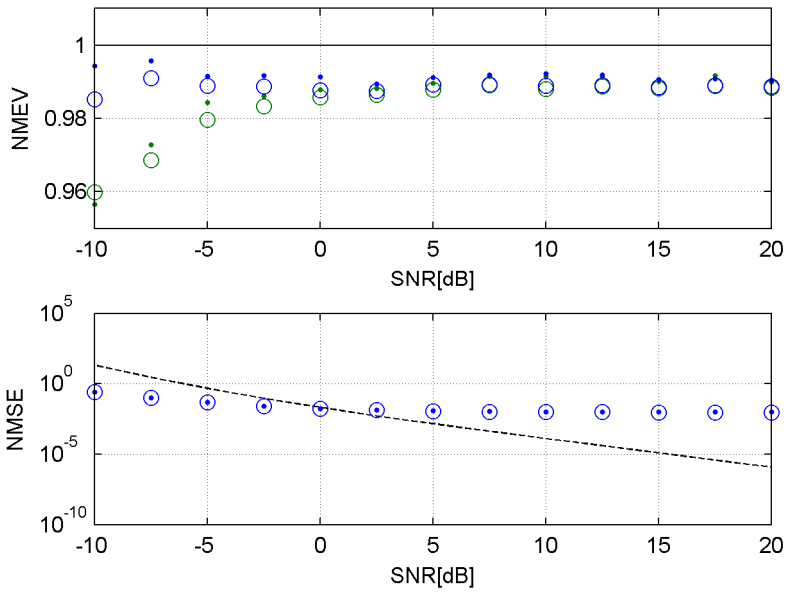

Figure A - 13: NMEV and NMSE evolution of the interference power estimation

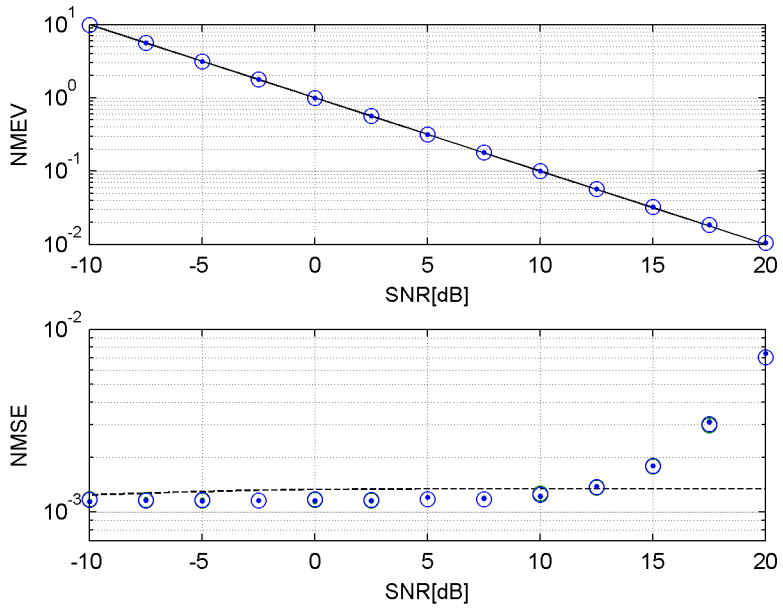

Figure A - 14: NMEV and NMSE evolution of
the noise power estimation

(e) Comparison of Power Ratio Estimates based on HDS and Genie

Figure A - 15 and Figure A - 16 visualize a benchmark for the SNR estimation performance and the K_R estimation performance in terms of NMSE for the HDS Doppler spread estimator. The results are plotted in blue and compared to results using ideal Doppler spread knowledge (Genie) indicated in ochre. A Doppler spread of $B_D T_S = 0.1$ on a RICE_{BW} channel with settings outlined in Section 5.2.4 was used.

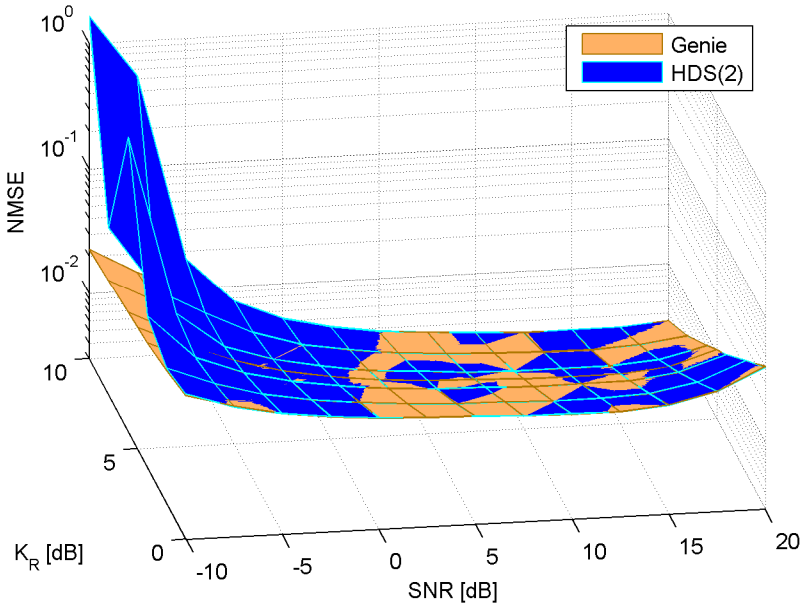

Figure A - 15: Benchmark of the normalized SNR jitter performance using HDS

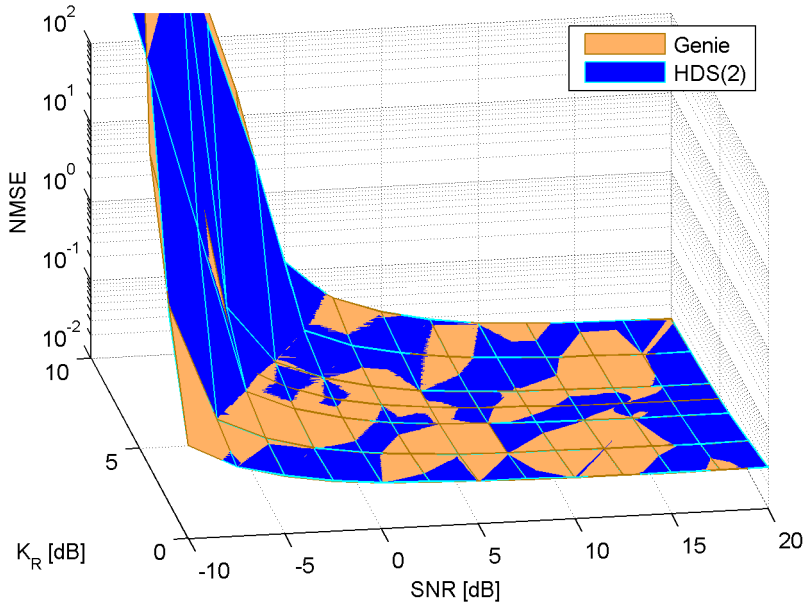

Figure A - 16: Benchmark of the normalized K_R jitter performance using HDS

Estimations relying on the HDS estimator perform quasi equivalent to those with known Doppler spread over a wide SNR range.

D Ad Chapter 6: Parameter Estimation on Land-Mobile Satellite Channels

(a) Two-Stage Doppler Spread Estimation Method

Since the LF channel exhibits at higher speeds a significant interference component originating from the shadowing process deteriorating the Doppler spread estimation, a two-stage approach consisting of consecutively linked HDS estimators is considered, where the first one (first stage) estimates the shadowing bandwidth, from which the second one (second stage) estimates the actual Doppler spread. For practical systems a relatively simple tracking algorithm could replace the first stage, since the mobile terminal speed may not vary significantly for consecutive data bursts.

Figure A - 17 depicts, according to the styles in Table 4, the jitter performance evolution of the Doppler spread for the described two stage approach after the second stage. In comparison with Figure 6.14, it is clear that it actually is less accurate, but according to the results in (b) it improves the accuracy of the power estimates in the higher SNR region. Obviously, this can be explained by the fact that the two-stage approach tends to overestimate the Doppler spread, nevertheless it is limited to the maximum speed.

State {1,2,3}→{black, blue, green}
$\dot{s}$ = {1,15,30} $\frac{m}{s}$ → Line/Marker = {dotted/dot, dash-dotted/diamond, solid/circlet}

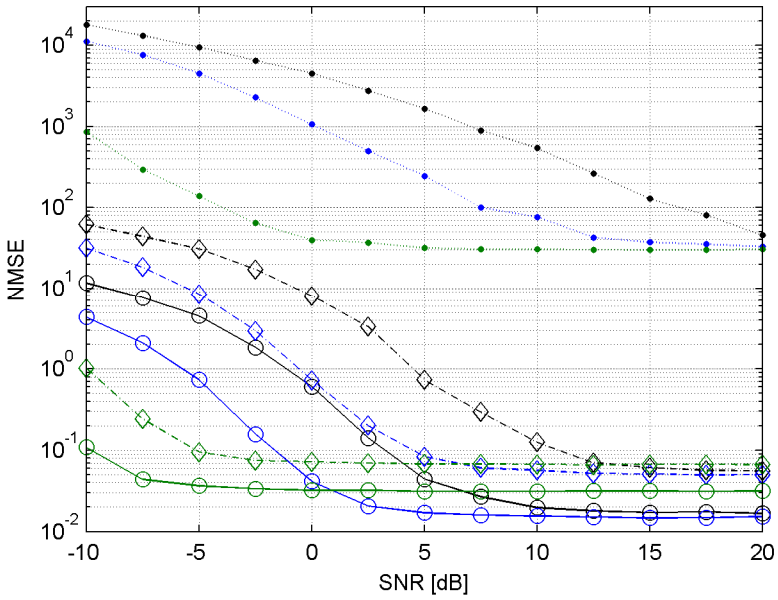

Figure A - 17: Jitter performance of the two-stage Doppler spread estimation

(b) Power Parameter Estimation Performance based on the Two-Stage Method

As a tribute to (a), Figure A - 18 and Figure A - 19 depict the jitter performance for SNR and SIR, respectively. The styles in Table 4 apply. In comparison with Figure 6.18 Figure 6.19, it is most evident that no performance degradations of the SNR estimates for high velocities occur in the high SNR regime.

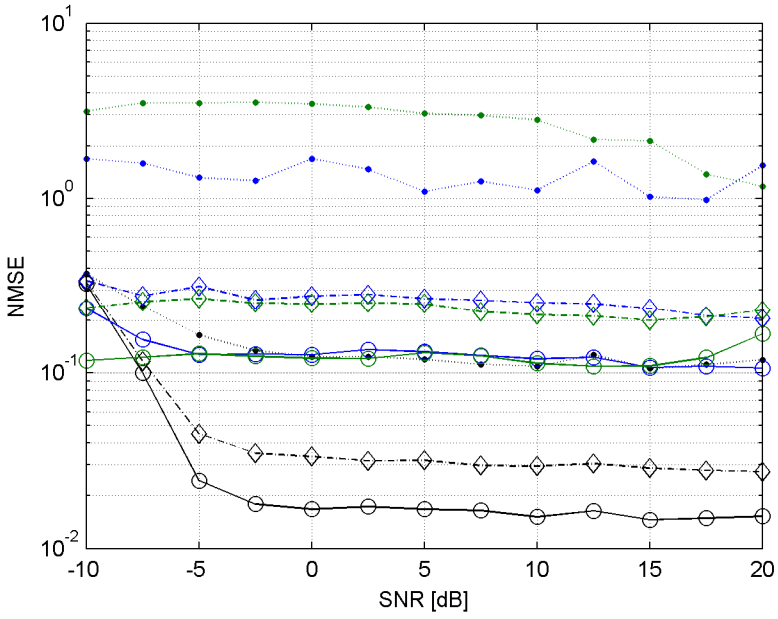

Figure A - 18: NMSE performance of SNR estimation, two-stage Doppler spread estimation

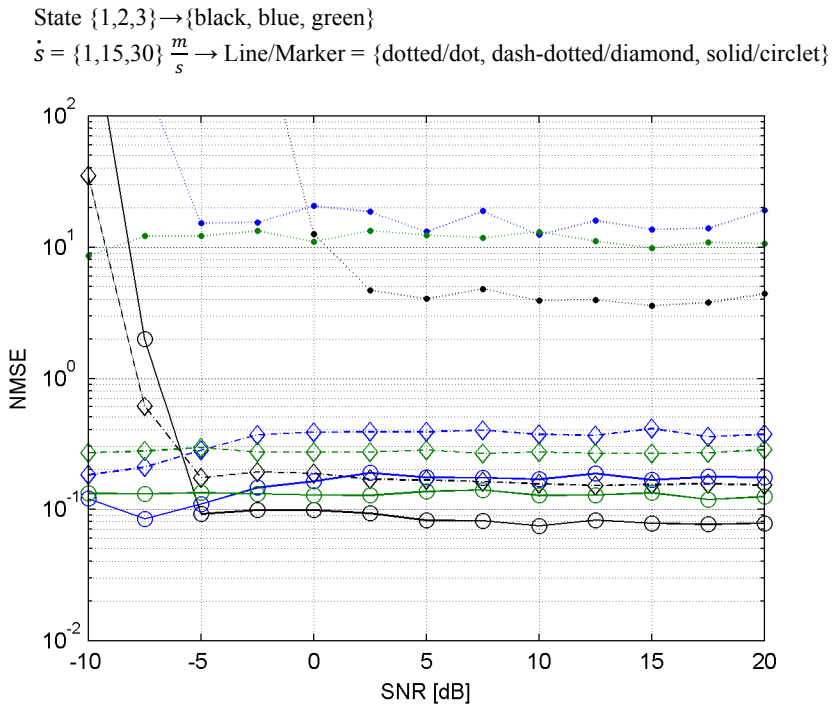

Figure A - 19: NMSE performance of SIR estimation,
two-stage Doppler spread estimation

E Publications, Achievements and Projects – a brief Overview

Within this section the author likes to give a brief overview of published work, project and additional experience gained throughout his doctoral studies at Graz University of Technology which, due to the narrow context of this thesis, were not completely incorporated. Additionally, the student projects and thesis supervised by the author are listed and briefly introduced.

(a) Overview of Conference Publications

This subsection provides a comprehensive list of conference publications (CPs) including direct quotes of the respective abstracts.

[CP1] M. Bergmann, W. Gappmair, B. Suesser-Rechberger and O. Koudelka. "Location-Aware Channel Estimation for Capacity Gains on MIMO Satellite Links", in *Proc. 63rd International Astronautical Congress*, Naples/Italy, B2-4-7, Oct. 2012.

> *"Bandwidth is an expensive and scarce resource, thus its efficient exploitation is of great interest. Recent communication satellites feature sophisticated spatial access strategies through spot beams providing total throughputs approaching 100 Gigabit per second. Next generations of communication satellites, as postulated in the Satellite Communications Network of Experts (SatNEx) III call off order (CoO) 2 activity, funded by the European Space Agency*

(ESA), require technological developments enabling throughputs of 1 Terabit per second. Multiple-input multiple-output (MIMO) system architectures, formed by a central gateway, a multibeam satellite, and an aggressive frequency reuse strategy can meet such ambitious design goals; interference problems are tackled by appropriate countermeasures such as (joint) precoding and beamforming on the forward link as well as multi-user detection on the return link; these methods require accurate and timely knowledge of the channel state information which in turn necessitates adequate channel estimation.
This paper addresses performance issues related to channel state estimation on the symbol-synchronous forward link and the frame-synchronous return link; it highlights for both links the potential performance gain by presuming a priori knowledge of the user position, as referred to as location-aware channel estimation."

[CP2] A. Vrolijk, M. Bergmann, M. V. Alonsoperez and T. Morris. "The Guidebook on Small Satellite Programs: Management of an International Team, Lessons Learned, and Future Visions", in *Proc. 63rd International Astronautical Congress*, Naples/Italy, B4-1-11, Oct. 2012.

"Small Satellite Programs have been a common way for countries, academia, industries and non-profit organizations to start a space program. Thus, based on experience from already pursued small satellite missions, expert knowledge in the field, and available literature, a team of 39 participants of the 2011 Space Studies Program of the International Space University (ISU) compiled a guidebook on small satellite programs aiming to support newcomers on the scene with their first steps. In this paper we describe the motivation, development, and main topics of this guidebook. We detail how a group of 39 people from 24 countries were coordinated and focused on a common goal within a short period of time, what difficulties arose and how these were tackled. Furthermore, we briefly answer the major questions addressed in the guidebook: Why small satellite programs? What can be accomplished? Who is involved? What legal and regulatory issues exist? How is the program concept envisioned? How is the mission concept implemented?"

[CP3] W. Gappmair, M. Bergmann and O. Koudelka. "Estimation of Carrier and Channel Parameters for Land Mobile Satellite Links", published at the *6th Advanced Satellite Mobile Systems Conference*, Baiona/Spain, Sep. 2012.

"Information about the channel state is particularly useful for adapting transmission parameters to different fading conditions. With slowly fading channels, the signal-to-noise ratio (SNR) is the most significant figure of merit to obtain the required goals in terms of availability and throughput. Using mobile satellite links, however, the situation may change within the round-trip time. Therefore, not just SNR estimates have to be delivered to the transmitter station in the context of an adaptive coding and modulation strategy, but also some additional information about the signal-to-interference ratio (SIR) and, perhaps more important, the Doppler spread of the mobile link, which determines the amount of variation in time. Assuming a channel determined by correlated Rician fading, an appropriate estimation framework for carrier frequency and phase, SNR, SIR, and Doppler spread will be discussed in the current paper. The signal model reflects in principle the conditions on a time-selective land-mobile satellite link, whereas frequency selectivity – as it is typical for multipath propagation – is considered to be negligible."

[CP4] J. Arnau-Yanez, M. Bergmann, E. A. Candreva, G. E. Corazza, R. De Gaudenzi, B. Devilliers, W. Gappmair, F. Lombardo, C. Mosquera, A. Perez-

Neira, I. Thibault, and A. Vanelli-Coralli. “Hybrid Space-Ground Processing for High-Capacity Multi-Beam Satellite Systems”, in *Proc. IEEE Globecom*, Houston/TX, pp. 1-6, Dec. 2011.

> *“Signal processing in satellite applications is usually performed either on-ground or on-board, i.e. at the gateway station or in the payload. Within the framework of the European Space Agency (ESA) SatNEx III study, an hybrid approach has been considered by splitting the processing between the satellite and the gateway, aiming to strike a better balance between performance and payload complexity. The design of a high-capacity multi-beam system has been carried out, to assess the potential applicability of a hybrid space-ground processing architecture (DIGISAT) for satellite broadband systems; this is achieved via hybrid space-ground beamforming, MIMO and MIMO-MUD, Precoding, and Digital Feeder link techniques.”*

[CP5] M. Bergmann, W. Gappmair, C. Mosquera, and O. Koudelka, “Channel Estimation on the Forward Link of Multi-Beam Satellite Systems”, in *Proc. 3rd International ICST Conference on Personal Satellite Services*, Malaga/Spain, pp. 250-259, Feb. 2011.

> *“Multi-beam concepts are an essential component of next generation broadband satellite systems. Due to aggressive design goals, full frequency reuse is suggested in this context so that appropriate interference mitigation techniques have to be applied on both forward and return links. In this respect, channel estimation is of paramount importance. Throughout this paper, we are focusing on channel estimation of the forward link with emphasis on orthogonal and non-orthogonal training sequences used for this purpose. By analytical and simulation results, it is confirmed that the former are best suited in terms of the obtained jitter performance. On the other hand, non-orthogonal codes are not restricted by their length, but it is shown that a linearly independent set of unique words is significantly affected by an amplification of the noise component – a result not available from the technical literature on this subject so far. Furthermore, it is demonstrated that a simple correlation procedure, which might be employed for any kind of non-orthogonal training sequences, produces a non-negligible jitter floor in the higher SNR regime, which is primarily given by the cross-correlation properties of the code.”*

[CP6] M. Bergmann, W. Gappmair, H. Schlemmer, and O. Koudelka, “Code-Aware Joint Estimation of Carrier Phase and SNR for Linear Modulation Schemes”, in *Proc. 5th Advanced Satellite Multimedia Systems Conference*, Cagliari/Italy, pp. 177-182, Sept. 2010.

> *“Depending on the length of the training sequence, data-aided parameter estimation requires some extra bandwidth. On the other hand, with non-data-aided solutions the payload symbols can be exploited as well, but the performance deviates significantly from the Cramer-Rao lower bound (CRLB) in the low signal-to-noise ratio (SNR) regime. In order to bridge this gap, recent activities concentrated more and more on code-aware (CA) algorithms so as to use the potential of error correction schemes, which usually form part of modern communication systems. In this context, methods for both carrier phase and SNR estimation have been published in the open literature. In the current paper, we extend this work by developing a CA algorithm for joint estimation of carrier phase and SNR; for comparison purposes, the CRLB of this joint approach is derived as the theoretical performance limit.”*

[CP7] M. Bergmann, P. Romano, O. Koudelka, and M. Wittig, "Generic Communication User and System Requirements for Future Space Science Missions", in *Proc. IEEE 5th International Workshop on Satellite and Space Comm.*, Siena/Italy, pp 295-299, Sept. 2009.

> *"Since space missions have been flown, a proper data return to Earth was inherently required. The complexity level and the number of space experiments have increased over the last decades. As a consequence, higher data rates have been required. The most limiting factor on achievable data rates for interplanetary communications is the distance. It imposes challenges on all parts of the communication system. Communication user and system requirements must be carefully defined to fulfill the mission needs. These requirements are expected to increase in the future. Hence, we studied 13 generic future ESA space mission scenarios comprising 5 Lunar missions, 5 Mars missions, and three missions to special targets (Lagrange point L2, NEO, and the Jovian satellite Europa) based on planned and already flown missions in order to derive communication user and system requirements. These requirements were classified, scaled, adapted and validated by calculations for these missions defined in [1]. Within this paper we will present how communication user and system requirements for future space science missions can be classified, scaled and applied. Therefore, after introducing a proper classification of communication requirements we will present recommendations by means of concrete examples assuming an Asteroid Sample Return mission scenario. Some practical hints will be provided as well."*

[CP8] M. Bergmann, P. Romano, T. Plank, P. Schrotter, and O. Koudelka, "Innovative Concepts for the Creation of Space Networks Relying on Hybrid RF and Optical Communication Links", in *Proc. 60th International Astronautical Congress*, Daejeon/South Korea, B2-4-2, Oct, 2009.

> *"With growing demands for space exploration missions there is a need for enhanced communications capabilities and increased inter-mission interaction. The creation of entire networks on exploration targets is desirable. Such networks will require high link availability, scalability, and high data transmission capabilities. Therefore, for future space missions the provision of networks on the remote targets should be taken into consideration. This paper investigates necessary developments for the creation of interplanetary networks. To support higher data rates, a move towards higher frequencies is required. The paper addresses in particular Ka-band and free-space optics systems for links from a space probe to the ground station. A trade-off between both technologies is made. Benefits of interplanetary networks with dedicated relay satellites to increase the availability are shown. Two communication topologies including key surface elements and orbiting spacecrafts for a near-Earth and a deep space network are presented. Recommendations for future space communication systems are provided."*

(b) Relevant Project Experience

Throughout his doctoral studies the author participated in several projects pursued at the *Institute of Communication Networks and Satellite Communications* of Graz University of Technology. In that respect he prepared, contributed to and/or reviewed several project reports, technical notes and proposals. Within the following, a brief overview of the

most relevant projects as well as the degree of involvement is provided. Furthermore the year of completion as well as the (most relevant) project partners and authorities are stated.

Interplanetary Communications I (2009): Throughout this project, 13 generic future space mission scenarios consisting of 5 Lunar missions, 5 Mars missions, and three missions to special targets were investigated. Communication user and system requirements were classified, scaled, and adapted accordingly as well as validated by calculations for the envisioned scenarios. In that context the author was key personnel responsible for coordination and investigative tasks. Project authorities and partners: ESA, EADS Astrium, Deimos Space.

Interplanetary Communications II (2011): The successor of the abovementioned project. Interplanetary Communication network architectures and protocols were investigated, as well as broadband radio communication strategies (RF and optical) were reviewed and benchmarked considering two generic missions. In that context the author was employed as reviewer. Project authorities and partners: ESA, EADS Astrium, Deimos Space, RUAG Aerospace.

SatNEx III CoO1 (2011): A brief introduction of this activity can be found at the beginning of Chapter 3, the author's task herein is detailed in that chapter. Project authorities and major partners: ESA, DLR, University of Vigo, University of Bologna.

SatNEx III CoO2 (2012): A brief introduction of this activity can be found at the beginning of Chapter 5, the authors task herein is detailed in Chapters 5 and 6. Project authorities and major partners: ESA, DLR, University of Vigo, University of Bologna.

TUGSAT-1 / BRITE-Austria (Phase 2) (on-going): The aim of this project is to bring the first Austrian satellite into space. The satellite is designed to observe brightness oscillations of stars, hence it is an ambitious scientific nano-satellite mission. The author was involved in the sub-system testing and was advisory to the ground station design team. Project authorities and major partners: FFG, University of Vienna, Vienna University of Technology, University of Toronto.

Global Educational Network for Satellite Operations (GENSO)-Graz (2012): The aim of this internal project was to set up a GENSO compatible ground station at the Institute's premises. The author was responsible for the project management including fundraising and supervision of students.

(c) Advanced Trainings

Within this section advanced trainings, which were attended in addition to the agreed curriculum in the field of space science and space communications, are briefly described.

Space Studies Program 2011 of the International Space University (ISU): This annually pursued program aims to foster space education providing an international, interdisciplinary, and intercultural mind-set. The international participants are educated in several space-related disciplines and are furthermore involved and challenged with competitive project work. In that context the author could achieve excellent grades, besides the basic training the he participated in the business and management department and in a team project tasked to compile a guidebook on small satellite programmes under supervision of the United Nations Office of Outer Space Affairs. The latter facilitated the author to foster and test his coordination skills as he was promoted a leading role in this international and interdisciplinary team; furthermore the author was awarded to participate and speak as representative of the ISU at the *49th Session of the Scientific and Technical Subcommittee of the United Nations Committee on the Peaceful Uses of Outer Space*.

Alpbach Summer School 2010 issuing "New Space Missions for Understanding Climate Change": The summer school comprises relevant multidisciplinary lectures in the field of space research, exploration and technology tailored to Master and doctoral students as well as fosters the participants by a highly competitive project work aiming to prepare a space mission fulfilling the default topic. In that respect the team the author was part of was awarded the best scientific case; in a follow-up activity the ideas were refined by former school mates and published in the Remote Sensing Journal.

SatNEx Summer School 2009 in Salzburg: Relevant advanced lectures tailored to Ph.D. students and scientific exchange in the realm of satellite communications.

SatNEx Summer School 2008 in Pisa: Relevant advanced lectures tailored to Ph.D. students and scientific exchange in the realm of satellite communications.

(d) (Co-)Supervised Student Projects and Theses

In the following a brief listing of student projects, Bachelor theses and Master theses is provided, which have been supervised and/or advised by the author. The titles were for convenience translated to English.

1. A. Gruber. Translated German title: "Implementation of an efficient simulator for Turbo codes ", B.Sc. thesis, Graz University of Technology, 2008: The goal of this work was the implementation of a Turbo code, as specified in the DVB-RCS standard in an Visual C++ simulation environment with focus on simulation speed whilst maintaining configurability of the implemented modules.
2. M. Petter. Translated German title: "Investigation and simulation of low-density parity-check codes", M.Sc. thesis, Graz University of Technology, 2012: The goal of this work was to provide an overview of the fundamentals of LDPC

codes and their decoding. Latest developments in that respect were summarized and a AWGN channel simulation of the DVB-S standard code implemented.

3. B. Suesser-Rechberger. "Position-based channel estimation on MIMO satellite forward links", B.Sc. thesis, Graz University of Technology, Austria, 2012: The goal of this thesis was to provide simulation results of the symbol-synchronous MIMO satellite link confirming and extending the results achieved by the author in his Ph.D thesis. Especially the influence of positioning inaccuracies on the LACE concept was investigated.
4. D. Holzleitner. Translated German title: "Revision of the digital modulation exercise for the laboratory tutorial in information technologies", B.Sc. thesis, Graz University of Technology, Austria, 2012: The goal of this thesis was to redesign a student laboratory unit elaborating on digital modulation and coding algorithms. The focus was to shift certain parts of this unit to MatLAB™ simulations, because in times of scarce resources it is difficult to hold timely hardware available.

Additionally to the already completed student theses the author (co-)supervises, at the time this work was handed in (2012), a number of student theses, which are:

- P. Strasser: The aim of his B.Sc. thesis is to construct and profile a GENSO ground station based on amateur radio equipment at the Institute's premises.
- B. Tittelbach: The aim of his M.Sc. thesis is to program overlay software that massively parallelizes the Institute's simulation software which was designed in collaboration with Joanneum Research; furthermore an LDPC code following the DVB-S standard is to be implemented and tested.
- B. A. Herbst: The aim of her B.Sc. thesis is to implement a simulation and visualization tool based on MatLAB™ to be used for education.
- P. R. Seebacher: The aim of his B.Sc. thesis is to implement a generic MIMO satellite channel in the Institute's simulation software.

(This page is intentionally left blank)

REFERENCES

[1] H. Potocnik Noordung. *The Problem of Space Travel: The Rocket Motor*, digital edition of English translation, Ljubliana, Slovenia: Cultural Centre of European Space Technologies (KSEVT), Dec. 2010.

[2] A. C. Clarke. "Extra-Terrestrial Relays: Can Rocket Stations Give World-wide Radio Coverage?", *Wireless World*, vol. 51, no. 10, pp. 305-308, Oct. 1945.

[3] J. R. Wertz, W. J. Larson (Ed.). *Space Mission Analysis and Design*, 3rd ed., El Segundo, CL: Microcosm Press, 1999.

[4] "Syncom-3", Internet: http://nssdc.gsfc.nasa.gov/nmc/spacecraftDisplay.do?id=1964-047A, [Aug. 15, 2012].

[5] D. J. Whalen. "Communications Satellites: Making the Global Village Possible", Internet: http://history.nasa.gov/satcomhistory.html, Nov. 30, 2010 [Aug. 15, 2012].

[6] "Early Bird: World's First Commercial Communications Satellite", Internet: http://www.boeing.com/defense-space/space/bss/factsheets/376/earlybird/ebird.html, [Aug. 15, 2012].

[7] "The Satellite Market", Internet: http://telecom.esa.int/telecom/www/object/index.cfm?fobjectid=456, Mar. 20, 2009 [Aug. 15, 2012]

[8] G. Maral and M. Bousquet. *Satellite Communications Systems: Systems, Techniques and Technology*. 3rd ed., Chichester, UK: John Wiley & Sons, 1998.

[9] G. D. Krebs. "TerreStar 1, 2", Internet: http://space.skyrocket.de/doc_sdat/terrestar-1.htm, Mar. 13, 2011 [Jun. 20, 2011].

[10] "ViaSat-1: Mission Overview", Internet: http://www.viasat.com/files/assets/web/datasheets/ViaSat-1%20Mission%20Overview%20r3.pdf, [Nov. 13, 2012].

[11] "SPACEWAY 3 North America: Bandwidth-on-Demand", Internet: http://www.boeing.com/defense-space/space/bss/factsheets/702/spaceway/spaceway3.html, [Jun. 20, 2011].

[12] "SPACEWAY: Technical Specifications", Internet: http://www.hughes.com/ProductsAndTechnology/spaceway/Pages/SpacewayTechnicalSpecification.aspx, [Feb. 13, 2012].

[13] "Performance, Power, Unique Capabilities: Spaceway 3", Internet: http://www.hughes.com/ProductsAndTechnology/spaceway/Pages/Spaceway.aspx, [Jun. 20, 2011].

[14] Avanti Communications Group. “HYLAS 2”, Internet: http://www.avantiplc.com/sites/default/files/hylas2_no_crops_0.pdf, [Jun 20, 2011].

[15] “KA-SAT :: 9° EAST”, Internet: http://www.eutelsat.com/satellites/9e_ka-sat.html, [Jun. 20, 2011].

[16] G. Ferrari, G. Colavolpe and R. Raheli. *Detection Algorithms for Wireless Communications*, Chichester, UK: John Wiley & Sons, 2004.

[17] ETSI EN 302 307. “Digital Video Broadcasting (DVB); Second generation framing structure, channel coding and modulation systems for Broadcasting Interactive Services, News Gathering and other broadband satellite applications (DVB-S2)”, European standard, v. 1.2.1, Aug. 2009.

[18] ETSI EN 301 545-2. “Digital Video Broadcasting (DVB); Second Generation DVB Interactive Satellite System (DVB-RCS2); Part2: Lower Layers for Satellite Standard”, European Standard, v. 1.1.1, Aug. 2011.

[19] E. L. Valles. *Timing Recovery and Carrier Synchronization Using LDPC Codes: Using Soft Decision Feedback to Aid Timing Recovery and Carrier Recovery*, Saarbrücken, Germany: VDM Verlag Dr. Müller, 2008.

[20] M. Bergmann, W. Gappmair, H. Schlemmer, and O. Koudelka. “Code-Aware Joint Estimation of Carrier Phase and SNR for Linear Modulation Schemes”, in *Proc. IEEE 5th Advanced Sat. Multimedia Syst. Conf. (ASMS) and the 11th Signal Processing for Space Commun. Workshop (SPSC)*, Cagliari/Italy, pp. 177-182, Sept. 2010.

[21] W. Gappmair. “Software-Defined Radios: Part 2: Synchronization and Parameter Estimation in Satellite Receivers”, Class Lecture, Institute of Communication Networks and Satellite Communications, Graz University of Technology, Graz, Austria, Mai 2009.

[22] U. Mengali and A. N. D’Andrea. *Synchronization Techniques in Digital Receivers*, New York, NY: Plenum Press, 1997.

[23] H. Meyr, M. Moeneclaey and S. A. Fechtel. *Digital Communication Receivers: Synchronization, Channel Estimation, and Signal Processing*, New York, NY: John Wiley & Sons, 1998.

[24] G. L. Stueber. *Principles of Mobile Communications*, Dortrecht, NL: Kluwer, 1996.

[25] L. Hanzo, T. H. Liew, and B. L. Yeap. *Turbo Coding, Turbo Equalization and Space-Time Coding*, Chichester, UK: John Wiley & Sons, 2002.

[26] S. M. Kay. *Fundamentals of Statistical Signal Processing: Estimation Theory*, Upper Saddle River, NJ: Prentice Hall, 1993.

[27] A. N. D' Andrea, U. Mengali and R. Reggiannini. "The Modified Cramer-Rao Bound and Its Application to Synchronization Problems", in *IEEE Trans. Commun.*, vol. 42, no. 2/3/4, pp. 1391-1399, Feb./Mar./Apr. 1994.

[28] "SatNEx, the European Satellite Communication Network of Excellence, continues with ESA support" Internet: http://telecom.esa.int/telecom/www/object/index.cfm?fobjectid=30236, Feb. 25, 2010 [Jun. 8, 2012].

[29] B. Devillers et al. "SatNEx III, CoO1 Task 2: Hybrid Space Ground Processing; TN 2.3 DigiSat Techniques Pre-Selection", ESA Technical Note, Contract No. RFQ/3-12859/09/NL/CLP, Issue 1, Rev. 1, Nov. 15, 2010.

[30] B. Devillers et al. "SatNEx III, CoO1 Task 2: Hybrid Space Ground Processing; TN 2.4 DigisatAnalysis and Trade-Offs", ESA Technical Note, Contract No. RFQ/3-12859/09/NL/CLP, Issue 1, Rev. 0, Nov. 12, 2010.

[31] B. Devillers et al. "SatNEx III, CoO1 Task 2: Hybrid Space Ground Processing; TN 2.5 Digisat Recommendations and Roadmap", ESA Technical Note, Contract No. RFQ/3-12859/09/NL/CLP, Issue 1, Rev. 0, Nov. 12, 2010.

[32] B. Devillers et al. "SatNEx III, CoO1 Task 2: Hybrid Space Ground Processing; Final Report", ESA Technical Note, Contract No. RFQ/3-12859/09/NL/CLP, Issue 1, Rev. 0, May 27, 2011.

[33] B. Devillers et al. "SatNEx III, CoO1 Task 2: Hybrid Space Ground Processing; Summary Report", ESA Contract No. RFQ/3-12859/09/NL/CLP, Issue 1, Rev. 0, May 27, 2011.

[34] M. Bergmann, W. Gappmair, C. Mosquera and O. Koudelka. "Channel Estimation on the Forward Link of Multi-Beam Satellite Systems", in *Proc. 3rd Int. ICST Conf. on Personal Satellite Service (PSATS)*, Malaga, Spain, pp. 1-10, 2011.

[35] J. Arnau-Yanez, M. Bergmann, E. A. Candreva, G. E. Corazza, R. de Gaudenzi, B. Devillers, W. Gappmair, F. Lombardo, C. Mosquera, A. Perez-Neira, I. Thibault and A. Vanelli-Coralli. "Hybrid Space-Ground Processing for High-Capacity Multi-beam Satellite Systems", in *IEEE Global Telecommun. Conf. (GLOBECOM 2011)*, Houston/TX, pp.1-6, Dec. 2011.

[36] G. Gallinaro. "Novel Intra-System Interference Mitigation Techniques & Technologies for Next Generations Broadband Satellite Systems: Executive Summary Report", ESA Final Report, Contract No. 18070/04/NL/US, Feb. 1, 2008.

[37] F. Lombardo et al. "SatNEx III, CoO1 Task 2: Hybrid Space Ground Processing; Internal TN on Antenna Model Analysis", ESA Technical Note, Contract No. RFQ/3-12859/09/NL/CLP, Issue 1, Rev. 0, Jun. 12, 2010.

[38] P. Angeletti, G. Gallinaro, M. Lisi and A. Vernucci. “On-Ground Digital Beamforming Techniques for Satellite Smart Antennas”, in *Proc. 19th AIAA*, Toulouse, France, pp. 1 – 8, April 2001.

[39] P. Angeletti and N. Alagha, “Space/Ground Beamforming Techniques for Emerging Hybrid Satellite Terrestrial Networks”, in *Proc. 27th AIAA*, Edinburgh, UK, pp. 1-6, June 2009.

[40] C.-C. J. Kuo, S-H. Tsai, L. Tadjpour and Y-H Chang. *Precoding Techniques for Digital Communication Systems*. New York, NY: Springer, 2010.

[41] M. H. M. Costa. “Writing on Dirty Paper”, in *IEEE Trans. Inf. Theory*, vol. IT-29, no. 3, pp. 439–441, May 1983.

[42] H. Weingarten, Y. Steinberg and S. Shamai. “The Capacity Region of the Gaussian Multiple-Input Multiple Output Broadcast Channel”, in *IEEE Trans. Inf. Theory*, vol. 52, no. 9, pp. 3936-3964, Sept. 2006.

[43] R. F. H. Fischer, C. Windpassinger, A. Lampe and J. B. Huber. “Tomlinson-Harashima Precoding in Space-Time Transmission for Low-Rate Backward Channel“, in *Proc. 2002 Int. Zurich Seminar on Broadband Commun.*, Zurich/Switzerland pp.7/1-7/6, 2002.

[44] B. Devillers et al. “SatNEx III, CoO1 Task 2: Hybrid Space Ground Processing; TN 2.1 DigiSat Techniques Review”, ESA Technical Note, Contract No. RFQ/3-12859/09/NL/CLP, Issue 1, Rev. 1, Jun. 1, 2010.

[45] A. Wiesel, Y. C. Eldar and S. Shamai. “Zero-Forcing Precoding and Generalized Inverses”, in *IEEE Trans. Signal Processing*, vol. 56, no. 9, pp. 4409-4418, Sept., 2008.

[46] G. Gallinaro et al. “Perspectives of Adopting Interference Mitigation Techniques in the Context of Broadband Multimedia Satellite Systems,” *23rd AIAA Int. Commun. Satellite Syst. Conf.* (ICSSC 2005), Rome/Italy, pp. 1-10, Sept. 2005.

[47] M. L. Honig et al, Ed. *Advances in Multiuser Detection*. New Jersey, NY: John Wiley & Sons, 2009.

[48] S. Verdu. *Multiuser Detection*. Cambridge, UK: Cambridge University Press, 1998.

[49] R. A. Horn and C. R. Johnson. *Matrix Analysis*, Cambridge, UK: Cambridge University Press, 1985.

[50] *“Physical Layer Standard for cdma2000 Spread Spectrum Systems”*, 3rd Generation Partnership Project 2 (3GPP2), Ver. 1.0, Rev. D, Feb. 13, 2004.

[51] R. Gold. “Optimal Binary Sequences for Spread Spectrum Multiplexing”, in *IEEE Trans. Info. Theory*, vol. 13, pp. 619-621, Oct., 1967.

[52] T. Kasami. “Weight Distribution Formula for some Class of Cyclic Codes”, Tech. Report R-285, Coordinated Science Laboratory, Univ. of Illinois, Apr., 1966.

[53] D. V. Sarwate and M. B. Pursley. “Crosscorrelation Properties of Pseudorandom and Related Sequences”, in *Proc. IEEE*, vol. 68, no. 5, pp.593-619, May, 1980.

[54] C. D. Ahlbrandt and A. C. Peterson. “Chapter 9.2: The Moore-Penrose Pseudo Inverse” in *Discrete Hamiltonian Systems: Difference Equations, Continued Fractions, and Riccati Equations*, Dordrecht, NL: Kluwer Academic Publishers, vol. 16, 2010.

[55] M. Luise and R. Reggiannini. “Carrier Frequency Recovery in All-Digital Modems for Burst Mode Transmissions”, in *IEEE Trans. Commun.*, vol. 45, no. 1, Jan., 1997.

[56] D. C. Rife and R. R. Boorstyn. “Single-Tone Parameter Estimation from Discrete-Time Observations”, in *IEEE Trans. Info. Theory*, vol. 20, no. 5, pp. 591-598, Sep., 1974.

[57] B. Süsser-Rechberger. “Position-based channel estimation on MIMO satellite forward links”, B.Sc. Thesis, Graz University of Technology, Austria, 2012.

[58] S. Xie, Z. Gu, S. Rahardja, J. C. Wong and Y. Xin. “Selection of Spreading Sequence Subsets for DS-CDMA Systems over Multipath Channels”, in *Proc. IEEE 5th Int. Conf. on Info., Commun. and Signal Processing* (ICICS 2005), Bangkok, Thailand, pp.1475-1479, Dec., 2005.

[59] U. Mengali and M. Morelli. “Data-Aided Frequency Estimation for Burst Digital Transmission”, in *IEEE Trans. Commun.*, vol. 43, no. 2/3/4, Feb./Mar./Apr., 1995.

[60] F. Lombardo, E. A. Candreva, I. Thibault, A. Vanelli-Coralli and G. E. Corazza. “Multi-User Interference Mitigation Techniques for Broadband Multi-Beam Satellite Systems”, in *IEEE Proc. of the 45th Asilomar Conference on Signals, Syst., and Computers*, Pacific Grove, CA, USA, pp. 1805-1809, Nov., 2011.

[61] A. L. Swindlehurst. "Time Delay and Spatial Signature Estimation Using Known Asynchronous Signals", in *IEEE Trans. Signal Processing*, vol. 46, no. 2, pp. 449-462, Feb., 1998.

[62] D. Dardari, E. Falletti and M. Luise (Eds.). *Satellite and Terrestrial Radio Positioning Techniques*. Oxford, UK: Elsevier, 2012.

[63] T. Menard and J. Miller. “Comparing the GPS Capabilities of the iPhone 4 and the iPhone 3G for Vehicle Tracking using FreeSim_Mobile”, in *2011 IEEE Intelligent Vehicles Symposium* (IV), Baden-Baden, Germany, pp.278-283, June, 2011.

[64] L. E. Frenzel, Ed. “GNSS Receiver Covers All Multi Constellation Standards”, Internet: http://mobiledevdesign.com/hardware_design/gnss-receiver-covers-all-multi-constellation-standards-0409/, Apr. 9, 2012 [June 1, 2012].

[65] M. Simic and P Pejovic. “Positioning in Cellular Networks” in *Cellular Networks - Positioning, Performance Analysis, Reliability*. A. Melikov Ed., Rijeka, Croatia: InTech, pp. 51-76, 2011.

[66] B. Nadel. “The TerreStar Genus keeps you connected via cell and satellite networks” Internet: http://www.computerworld.com/s/article/9206483/The_TerreStar_Genus_keeps_you_connected_via_cell_and_satellite_networks, Jan 27, 2011 [June 1, 2012].

[67] S. Gezici. “A Survey on Wireless Position Estimation” in *Wireless Personal Commun.*, vol. 44, no. 3, Springer Netherlands, pp. 263-282, 2008.

[68] A. J. Weiss. “Direct Position Determination of Narrowband Radio Frequency Transmitters”, in *IEEE Signal Processing Letters*, vol. 11, no. 5, pp. 513-516, May, 2004.

[69] D. K. Petraki, T. Taleb and A. V. Vasilakos, “Positioning in Multibeam Geostationary Satellite Networks”, in *Proc. IEEE Int. Conf. on Commun.* (ICC 2009), Dresden, Germany, pp. 1-5, June, 2009.

[70] M. S. Arulampalam, S. Maskell, N. Gordon and T. Clapp. “A Tutorial on Particle Filters for Online Nonlinear/Non-Gaussian Bayesian Tracking”, in *IEEE Trans. Signal Processing*, vol. 50, no. 2, pp.174-188, Feb., 2002.

[71] “SATellite Network of EXperts: Call off-Orders (COOs)”, Internet: http://www.satnex.com/index.php/call-off-order-coo, [Jul. 26, 2012].

[72] E. A. Candreva et al. “SatNEx III, CoO2-Task 3: Flexible and High Performance Adaptive Modulation and Coding Techniques for Satellite Multimedia Applications; TN 3.2 Initial Results”, ESA Technical Note, Contract No. 23089/10/NL/CLP, Issue 1, Rev. 0, Oct. 31, 2011.

[73] R. Baroni et al. “SatNEx III, CoO2-Task 3: Flexible and High Performance Adaptive Modulation and Coding Techniques for Satellite Multimedia Applications; Executive Summary Report”, ESA Final Report, Contract No. 23089/10/NL/CLP, Issue 1, Rev. 0, June 30, 2012.

[74] R. Baroni et al. “SatNEx III, CoO2-Task 3: Flexible and High Performance Adaptive Modulation and Coding Techniques for Satellite Multimedia Applications; Summary Report”, ESA Final Report, Contract No. 23089/10/NL/CLP, Issue 1, Rev. 0, June 30, 2012.

[75] R. Baroni et al. “SatNEx III, CoO2-Task 3: Flexible and High Performance Adaptive Modulation and Coding Techniques for Satellite Multimedia Applications; Final Report”, ESA Final Report, Contract No. 23089/10/NL/CLP, Issue 1, Rev. 0, June 30, 2012.

[76] W. Gappmair, M. Bergmann and O. Koudelka. “Estimation of Carrier and Channel Parameters for Land Mobile Satellite Links”, accepted for publication in *Proc. 6th Advanced Satellite Mobile Syst. Conf.*, Baiona, Spain, Sep. 2012.

[77] S. Cioni, R. De Gaudenzi and R. Rinaldo. “Channel estimation and physical layer adaptation techniques for satellite networks exploiting adaptive coding and modulation”, *Int. J. Satellite Commun. Network.*, vol. 26, pp. 157–188, March/April, 2008.

[78] S. Vassaki, A. D. Panagopoulos and P. Constantinou. “Effective Capacity and Optimal Power Allocation for Mobile Satellite Systems and Services”, in *IEEE Commun. Lett.*, vol. 16, no. 1, pp. 60–63, Jan., 2012.

[79] A. J. Goldsmith and P. P. Varaiya. “Capacity of Fading Channels with Channel Side Information”, in *IEEE Trans. Info. Theory*, vol. 43, no. 6, pp. 1986 – 1992, Nov., 1997.

[80] E. A. Candreva et al. “SatNEx III, CoO2-Task 3: Flexible and High Performance Adaptive Modulation and Coding Techniques for Satellite Multimedia Applications; TN 3.1 State of the art review and consolidation of system specifications”, ESA Technical Note, Contract No. 23089/10/NL/CLP, Issue 1, Rev. 1, Sept. 2, 2011.

[81] M. K. Simon and M.-S. Alouini. *Digital Communications over Fading Channels: A Unified Approach to Performance Analysis*. New York, NY: John Wiley & Sons, 2000.

[82] J. E. Allnutt. *Satellite-to-ground radiowave propagation.* London, UK: Peter Peregrinus, 1989.

[83] S. O. Rice. “Statistical properties of a sine wave plus random noise”, *Bell Syst. Tech. J.*, vol. 27, pp.109-157, Jan. 1948.

[84] F. Gini, M. Luise and R. Reggiannini. “Cramer-Rao Bounds in the Parametric Estimation of Fading Radiotransmission Channels”, in *IEEE Trans. Commun.*, vol. 46, no. 10, pp. 1390-1398, Oct., 1998.

[85] M. J. Gans. “A Power-Spectral Theory of Propagation in the Mobile-Radio Environment”, in *IEEE Trans. Vehicular Technol*., vol. VT-21, no. 1, Feb. 1972.

[86] R. H. Clarke. “A Statistical Theory of Mobile-Radio Reception”, *Bell Syst. Tech. J.*, pp. 957-1000, Jul.-Aug. 1968.

[87] K. E. Baddour and N. C. Beaulieu. “Nonparametric Doppler Spread Estimation for Flat Fading Channels”, in *Proc. IEEE Wireless Commun. and Networking Conf.*, New Orleans, LA, USA, pp. 953-958, May 2003.

[88] J. M. Holtzman and A. Sampath. “Adaptive Averaging Methodology for Handoffs in Cellular Systems”, in *IEEE Trans. Vehicular Technol*., vol. 44, no.1, pp. 59–66, Feb. 1995.

[89] M. Morelli, U. Mengali and G. M. Vitetta, “Further Results in Carrier Frequency Estimation for Transmissions Over Flat Fading Channels”, in *IEEE Commun. Lett.*, vol. 2, no. 12, pp. 327–330, Dec. 1998.

[90] C. Tepedelenlioglu and G. B. Giannakis. “On Velocity Estimation and Correlation Properties of Narrow-Band Mobile Communication Channels”, in *IEEE Trans. Vehicular Technol.*, vol. 50, no. 4, pp. 1039-1052, July 2001.

[91] K. E. Baddour and N. C. Beaulieu, “Robust Doppler Spread Estimation in Nonisotropic Fading Channels”, in *IEEE Trans. Wireless Commun.*, vol. 4, no. 6, pp. 2677–2682, Nov. 2005.

[92] K. E. Baddour and N. C. Beaulieu, “Robust Doppler Spread Estimation in Nonisotropic Scattering Environments”, in *Proc. 56th IEEE Vehicular Technol. Conf.* (VTC), Vancouver, Canada, vol. 4, pp. 2459-2464, Sept. 2002.

[93] W. Gappmair. “Cramer-Rao Bounds for Joint Parameter Estimation in Correlated Ricean Channels”, Internal document, Institute of Communication Networks and Satellite Communications, Graz University of Technology, Austria, 2011.

[94] F. Perez Fontan, M. Vazquez Castro, C. Enjamio Cabado, J. Pita Garcia and E. Kubista. “Statistical modeling of the LMS channel,” in *IEEE Trans. Vehicular Technol.*, vol. 50, pp. 1549–1567, Nov. 2001.

[95] C. Loo. “A statistical model for a land mobile satellite link,” in *IEEE Trans. Vehicular Technol.*, vol. 34, pp. 122–127, Aug. 1985.

[96] F. Perez-Fontan et al. “Complex Envelope Three-State Markov Model Based Simulation for the Narrow-Band LMS Channel”, *Int. J. Satellite Commun.*, vol. 15, issue 1, pp. 1-15, Jan. 1997.

[97] D. P. Bertsekas and J. N. Tsitsiklis (Fall 2000). “Markov Chains” in *Introduction to Probability*, Internet: http://www-sop.inria.fr/members/Giovanni.Neglia/proba11/bertsekas_tsitsiklis_probability.pdf, [Aug. 8, 2012].

[98] F. Perez-Fontan, M. A. Vazquez-Castro, S. Buonomo, J. P. Poiares-Baptista and B. Arbesser-Rastburg. „S-Band LMS propagation channel behavior for different environments, degrees of shadowing and elevation angles“, in *IEEE Trans. Broadcasting*, vol. 44, no. 1, Mar. 1998.

ABBREVIATIONS

3D	Three Dimensional
ACM	Adaptive Coding and Modulation
AFR	Array Fed Reflector
AOA	Angle Of Arrival
AWGN	Additive White Gaussian Noise
BC	Broadcast Channel
BOM	Bill Of Material
CA	Code-Aware
CoO	Call-off-Order
CP	Conference Publication
CRLB	Cramer-Rao Lower Bound
CSI	Channel State Information
DA	Data Aided
DBF	Digital BeamForming
DD	Decision Directed
DFT	Discrete Fourier Transform
DLR	Deutsches Zentrum für Luft- und Raumfahrt
DPC	Dirty Paper Coding
DTR	Deterministic Timing Recovery
DVB	Digital Video Broadcasting
DVB-S2	Second generation of DVB over Satellite
DVB-RCS2	Second generation DVB-Return Channel over Satellite
e.g.	*exempli gratia*
ESA	European Space Agency
ESTEC	European Space Research and Technology Centre
ETSI	European Telecommunications Standards Institute
EU	European Union
EVM	Error Vector Magnitude
FEC	Forward Error Correction
FFG	Die Österreichische ForschungsFörderungsGesellschaft
FFT	Fast Fourier Transform
FIM	Fisher Information Matrix
FIR	Finite Impulse Response

FSS	Fixed Satellite Service
GENSO	Global Educational Network for Satellite Operations
GEO	Geostationary Earth Orbit
GLONASS	Global Orbiting Navigation Satellite System
GNSS	Global Navigation Satellite System
GPS	Global Positioning System
HDS	Heuristic Doppler Spread
IC	Interference Cancellation
i.e.	*id est*
i.i.d.	independent and identically distributed
ISIC-A	Iterative SIC Method A
ISIC-B	Iterative SIC Method B
ISNR	Instantaneous SNR
ISU	International Space University
ITS	Intermediate Tree Shadowing
LACE	Location-Aware Channel Estimation
LDPC	Low-Density Parity-Check
LEO	Low Earth Orbit
LF	Loo-Fontan
LMMSE	Linear MMSE
LMS	Land-Mobile Satellite
LOS	Line-Of-Sight
LPF	Low Pass Filter
MAC	Multiple Access Channel
MAI	Multiple Access Interference
MCRB	Modified Cramer-Rao Bound
ME	Mean Error
MEO	Medium Earth Orbit
MIMO	Multiple-Input Multiple-Output
ML	Maximum Likelihood
MMSE	Minimum MSE
mNDS	modified NDS
MP	Mean Power
MSE	Mean Square Error
MSS	Mobile Satellite Service
MUD	Multi-User Detection

NASA	National Aeronautics and Space Administration
NCRLB	Normalized CRLB
NDA	Non-DA
NDS	Nonparametric Doppler Spread
NME	Normalized ME
NMSE	Normalized MSE
p.	Page
PDF	Probability Density Function
pp.	Pages
PRS	Pseudo-Random Sequence(s)
PSD	Power Spectral Density
QZSS	Quasi-Zenith Satellite System
RB	Rife-Boorstyn
RCI	Rate Conversion and Interpolation
RRC	Root-Raised Cosine
RSS	Received Signal Strength
RTT	Round-Trip Time
SatNEx I, II	Satellite Communication Network of Excellence I, II
SatNEx III	Satellite Communication Network of Experts III
SIC	Successive Interference Cancellation
SIR	Signal-to-Interference Ratio
SNIR	Signal-to-Noise-plus-Interference Ratio
TDMA	Time-Division Multiple Access
TDOA	Time Difference of Arrival
US	United States
UT	User Terminal
UW	Unique Word
WH	Walsh-Hadamard